Angular momentum polarisation effects in inelastic scattering

A thesis submitted for the degree of Doctor of Philosophy

Helen Chadwick



Jesus College, University of Oxford

Hilary Term, 2012

Angular momentum polarisation effects in inelastic scattering

Helen Chadwick, Jesus College
A thesis submitted for the degree of Doctor of Philosophy
Hilary Term, 2012

Abstract

In this thesis, a joint experimental and theoretical investigation of the vector properties that describe the inelastic scattering of a diatomic radical with an atomic collision partner is presented. A particular emphasis is placed on those correlations that include the final rotational angular momentum, $\boldsymbol{j}'$, of the radical.

The depolarisation of both NO(A) and OH(A) brought about through collisions with krypton has been studied, providing a measure of the $\boldsymbol{j}$-$\boldsymbol{j}'$ correlation, where $\boldsymbol{j}$ is the initial rotational angular momentum associated with the diatom. The total depolarisation cross-sections for both collisional disorientation and disalignment have been measured using quantum beat spectroscopy, and modelled theoretically using quasi-classical trajectory (QCT) calculations. The agreement between experiment and theory for NO(A)-Kr is excellent, but is not observed for OH(A)-Kr under thermal conditions. This has been attributed to the importance of electronic quenching in OH(A)-Kr. The depolarisation cross-sections have also been determined at a higher collision energy for OH(A)-Kr where electronic quenching is less significant, and the experimental results are in better agreement with those obtained theoretically. The NO(A)-Kr depolarisation cross-sections fall with increasing rotational quantum number, N, whereas for OH(A)-Kr, they exhibit less of an N dependence. This trend is mirrored in the elastic depolarisation cross-sections, which have also been determined experimentally for OH(A)-Kr. The significantly attractive and anisotropic nature of the OH(A)-Kr potential energy surface (PES) accounts for these observations.

The $\boldsymbol{j}$-$\boldsymbol{j}'$ correlation is extended to include the initial (relative) velocity ($\boldsymbol{k}$) in a new theoretical treatment of the $\boldsymbol{k}$-$\boldsymbol{j}$-$\boldsymbol{j}'$ correlation. The formalism developed is used with the results from the QCT calculations for NO(A)-Kr and OH(A)-Kr to provide further insight into the mechanism of depolarisation in the two systems. Collisions of NO(A) with krypton do not cause significant depolarisation due to their impulsive nature, and the projection of $\boldsymbol{j}$ onto the kinematic apse is conserved. In contrast, collisions of OH(A) with krypton effectively randomise the direction of $\boldsymbol{j}$, again showing the influence of the anisotropic and attractive nature of the PES. However, the projection of $\boldsymbol{j}$ onto the kinematic apse is still conserved.

The inelastic scattering of NO(X) with argon and krypton has also been investigated, using a crossed molecular beam apparatus. The initial Λ-doublet state of the NO(X) was selected using hexapole focussing, and the products of the collision detected using velocity mapped ion imaging. The state to state differential cross-sections (equivalent to the $\boldsymbol{k}$-$\boldsymbol{k}'$ correlation, where $\boldsymbol{k}'$ is the final relative velocity) have been measured for collisions which conserve the initial spin-orbit level of the NO(X) with krypton. The same parity dependent effects were seen as have been observed previously for NO(X)-Ar. The collision induced alignment (equivalent to the $\boldsymbol{k}$-$\boldsymbol{k}'$-$\boldsymbol{j}'$ correlation) of NO(X) as a result of scattering with argon has also been determined experimentally. The results can be explained classically by considering the conservation of the projection of $\boldsymbol{j}$ onto the kinematic apse.

Publications

1. Collisional depolarization of NO(A) by He and Ar studied by quantum beat spectroscopy.

M. Brouard, H. Chadwick, Y.-P. Chang, R. Cireasa, C. J. Eyles, A. O. La Via, N. Screen, F. J. Aoiz, and J. Kłos, *J. Chem. Phys.*, **131**, 104307, (2009).

2. Applications of Zeeman quantum beat spectroscopy to angular momentum polarization studies.

M. Brouard, H. Chadwick, Y.-P. Chang, R. Cireasa, and C. J. Eyles, *Physica Scripta*, **80**, 048120, (2009).

3. Elastic depolarization of OH(A) by He and Ar: a comparative study.

M. L. Costen, R. Livingstone, K. G. McKendrick, G. Paterson, M. Brouard, H. Chadwick, Y.-P. Chang, C. J. Eyles, F. J. Aoiz, and J. Kłos, *J. Phys. Chem. A*, **113**, 15156, (2009).

4. The $\boldsymbol{k}$-$\boldsymbol{j}$-$\boldsymbol{j}'$ vector correlation in inelastic scattering.

M. Brouard, H. Chadwick, C. J. Eyles, F. J. Aoiz, and J. Kłos, *J. Chem. Phys.*, **135**, 084305, (2011).

5. Collisional angular momentum depolarization of OH(A) and NO(A) by Ar: A comparison of mechanisms.

M. Brouard, H. Chadwick, Y.-P. Chang, C. J. Eyles, F. J. Aoiz, and J. Kłos, *J. Chem. Phys.*, **135**, 084306, (2011).

6. Fully Λ-doublet resolved state-to-state differential cross-sections for the inelastic scattering of NO(X) with Ar.

C. J. Eyles, M. Brouard, H. Chadwick, B. Hornung, B. Nichols, C. -H. Yang, J. Kłos, F. J. Aoiz, A. Gijsbertsen, A. E. Wiskerke and S. Stolte, *Phys. Chem. Chem. Phys.*, **14**, 5403, (2012).

7. The effect of parity conservation on the spin-orbit conserving and spin-orbit changing differential cross sections for the inelastic scattering of NO(X) by Ar.

C. J. Eyles, M. Brouard, H. Chadwick, F. J. Aoiz, J. Kłos, A. Gijsbertsen, X. Zhang and S. Stolte, *Phys. Chem. Chem. Phys.*, **14**, 5420, (2012).

8. *Ab Initio* studies of the interaction potential for the Xe-NO(X $^2\Pi$) van der Waals complex: Bound states and fully quantum and quasi-classical scattering.

J. Kłos, F. J. Aoiz, M. Menéndez, M. Brouard, H. Chadwick and C. J. Eyles, *J. Chem. Phys.*, (*Submitted*)

Future Publications

1. A new potential energy surface for OH(A $^2\Sigma^+$)-Kr: the van der Waals complex and inelastic scattering.

H. Chadwick, M. Brouard, Y. -P. Chang, C. J. Eyles, T. Perkins, S. A. Seamons, J. Kłos, M. H. Alexander and F. J. Aoiz.

2. Collisional depolarization of OH(A $^2\Sigma^+$) and NO(A $^2\Sigma^+$) with Kr: experiment and theory.

H. Chadwick, M. Brouard, Y. -P. Chang, C. J. Eyles, T. Perkins, S. A. Seamons, J. Kłos, M. H. Alexander and F. J. Aoiz.

3. Rotational Alignment Effects in NO(X)+Ar Inelastic Collisions-An Experimental Study.

M. Brouard, H. Chadwick, C. J. Eyles, B. Hornung, B. Nichols and S. Stolte.

4. Hyperfine structure of NO(A $^2\Sigma^+$).

M. Brouard, J. M. Brown, H. Chadwick, Y. -P. Chang, B. J. Howard, S. Marinakis, N. Screen and S. A. Seamons.

5. Collisional depolarization of OH(A)+H_2: Experiment versus theory.

F. J. Aoiz, J. Bowman, M. Brouard, H. Chadwick, J. Lawlor, T. Perkins, S. A. Seamons and P. Stevenson.

6. Collisional depolarization in electronically excited radicals.

M. Brouard, H. Chadwick, Y. -P. Chang and C. J. Eyles. *Invited article for International Reviews in Physical Chemistry.*

Acknowledgements

First and foremost I would like to thank my supervisor, Prof. Mark Brouard for all of his help, support, guidance and general encouragement over the last few years. You could not wish for a better or more enthusiastic supervisor and it really has been a pleasure to be a member of the group.

Secondly, I would like to thank all the members of the research group, both past and present, who have made the basement such a fun place to be (and made such good contributions to the Monday morning cake tradition). I would especially like to thank Dr. Chris Eyles for helping to tame the blue monster, Bethan Nichols for the truly expert monster sitting, and Dr. Yuan-Pin Chang for all his help and patience during my time on the LIF rig.

Much of the experimental work presented in this thesis would not have been possible without the expertise of the support staff based in the chemistry department. Therefore, thanks must be extended to all the members of staff in lab services, electronics, and both the PTCL and CRL workshops, for all their hard work in keeping the machines in the lab going.

I would also like to thank Prof. Javier Aoiz and Dr. Jacek Kłos, for all their help, particularly with the theoretical work presented in this thesis, and Prof. Steven Stolte, for allowing us to adopt the blue monster.

Finally, a huge thank you to all my friends and family for their unwavering support, as without that none of this would have been possible.

Contents

Abstract i

Publications ii

Acknowledgements iv

1 Introduction **1**

1.1 Atom-molecule collisions 2

1.2 Experimental methods 4

1.3 Potential energy surfaces 10

1.4 Theoretical methods 11

1.5 Outline of this thesis 12

2 Theoretical Background and Methods **14**

2.1 Atom-radical collisions 14

2.1.1 NO(X)-Ar/Kr 14

2.1.2 NO(A)-Kr and OH(A)-Kr 19

2.2 Vector correlations 22

2.2.1 Rotational angular momentum polarisation 22

2.2.2 Describing vector correlations 24

2.3 Calculation methods 28

2.3.1 Potential energy surfaces 28

2.3.2 Quasi-classical trajectories 31

2.3.3 Quantum mechanics 35

2.4 Observable properties 36

2.4.1 Integral cross-sections 37
2.4.2 Differential cross-sections 38
2.4.3 Depolarisation cross-sections 39
2.5 Tensor opacity formalism 41
2.6 Summary 45

3 Collisional depolarisation: Experimental methods 46
3.1 Creating polarised distributions 47
3.1.1 The effect of collisions 48
3.2 Quantum beat spectroscopy 50
3.2.1 Zeeman quantum beats 52
3.2.2 Hyperfine quantum beats 54
3.3 Experimental setup 54
3.3.1 Lasers 54
3.3.2 Chamber 55
3.3.3 Magnetic field 56
3.3.4 Monochromator 56
3.3.5 Detection 57
3.4 Data analysis 58
3.4.1 Hyperfine quantum beats 59
3.4.2 Zeeman quantum Beats 60
3.4.3 Error analysis 64
3.4.4 Converting rate constants to cross-sections 64
3.5 Experimental simulations 67
3.6 Summary 72

4 Collisional depolarisation of OH(A) and NO(A) with Kr 73
4.1 Calculation details 74
4.1.1 Quasi-classical trajectories 74

4.1.2 Quantum mechanics 75
4.2 Electronic quenching 75
4.3 Rotational energy transfer 77
4.3.1 Theoretical collision cross-sections 77
4.3.2 Experiment vs theory: Rotational energy transfer cross-sections for OH(A)+Kr 81
4.4 Collisional depolarisation 82
4.4.1 Theoretical depolarisation cross-sections 82
4.4.2 Experiment vs theory: Depolarisation cross-sections for NO(A)+Kr 84
4.4.3 Experiment vs theory: Depolarisation cross-sections for OH(A)+Kr 86
4.4.4 Elastic depolarisation cross-sections 91
4.4.5 Inelastic depolarisation cross-sections 94
4.5 Comparison of OH(A)-Kr vs NO(A)-Kr 97
4.5.1 Kinematics vs dynamics 97
4.5.2 Deflection functions: b vs θ 99
4.5.3 Opacity functions 101
4.6 The role of electronic quenching 103
4.7 Summary 107

5 The $\boldsymbol{k}$-$\boldsymbol{j}$-$\boldsymbol{j}'$ vector correlation 109

5.1 Describing correlated distributions 110
5.2 Symmetry considerations 111
5.3 Expansion coefficients 115
5.4 The $\boldsymbol{k}$-$\boldsymbol{j}'$ correlation 117
5.5 The $\boldsymbol{j}$-$\boldsymbol{j}'$ correlation 118
5.6 The $\boldsymbol{k}$-$\boldsymbol{k}'$ correlation 119
5.7 LAB frame distribution 119
5.8 Vector correlations in NO(A)-Kr and OH(A)-Kr 122

5.8.1 $\boldsymbol{k}$-$\boldsymbol{k}'$-$\boldsymbol{j}'$ vector correlation . . . 122
5.8.2 $\boldsymbol{k}$-$\boldsymbol{j}$-$\boldsymbol{j}'$ vector correlation . . . 125
5.9 Kinematic apse . . . 127
5.10 Summary . . . 133

6 Vector correlations in NO(X) 135
6.1 Hexapole state selection . . . 137
6.2 Experimental methods . . . 138
6.2.1 Molecular beams . . . 138
6.2.2 Vacuum system . . . 140
6.2.3 Lasers . . . 141
6.2.4 Detection . . . 141
6.3 Flux-density effects . . . 144
6.4 Kinematic apse model . . . 148
6.5 Data analysis: Differential cross-sections . . . 154
6.6 Differential cross-sections: NO(X)-Kr . . . 156
6.6.1 Calculation details . . . 156
6.6.2 Results . . . 156
6.7 Collision induced alignment: NO(X)-Ar . . . 162
6.7.1 Spin-orbit conserving transitions . . . 162
6.7.2 Spin-orbit changing transitions . . . 167
6.8 Summary . . . 168

7 Conclusions and future work 170
7.1 Conclusions . . . 170
7.2 Future work . . . 173
7.2.1 Atom-diatom scattering . . . 173
7.2.2 Diatom-diatom scattering . . . 177

Bibliography 182

Chapter 1

Introduction

Chemical processes are inherently anisotropic, whether this process is a reaction, photodissociation or simply a collision between the species involved. The field of reaction dynamics is concerned with obtaining a fundamental understanding of the interactions that govern these processes. Due to the complexity of many chemical systems it is not possible to determine (or necessary to understand) the microscopic properties of each individual collision. However, for smaller, simpler systems it is possible to gain an insight into the physics that underpins the chemical process. For this reason, reaction dynamics tends to focus on the study of small molecules in the gas phase, where it is possible to obtain a 'complete picture' of the process.

A central concept to reaction dynamics is that of a potential energy surface. This models the interaction between the species involved in a given process at a range of geometries. It can effectively be considered as describing the potential energy 'landscape' which governs the forces acting on the species throughout the process. A knowledge of the potential energy surface also allows theoretical calculations to be performed. Good agreement between experimental and theoretical results validates the theoretical methods used, and any disagreement between the two introduces the challenge to find a reason for the discrepancy.

In the present study, it is the inelastic scattering of diatomic open shell radicals with atomic collision partners that is under investigation. The properties of these are amenable

to both detailed experimental and theoretical determination, and a comparison between the two can yield new insights into the mechanism behind the collision.

1.1 Atom-molecule collisions

There are many factors that determine the outcome of a collision between an atom and a molecule. Some of these are related to scalar properties, for example whether the species have sufficient energy to bring about the process under investigation, and whether the species are in close enough proximity for the process to occur [1]. However other vector properties can also determine the outcome of the collision, for example the orientation of the molecule may increase (or decrease) the probability that there will be a reaction or energy transfer. Therefore, to obtain a complete picture of the scattering process it is essential to consider these vector properties.

Due to the complexity of the majority of chemical systems, it is unrealistic to consider all the vector correlations associated with all the degrees of freedom, and as such it is necessary to average over some of these, resulting in a loss of information. In contrast, collisions of small molecules have fewer degrees of freedom, and therefore more mechanistic insight can be obtained.

In the current study, it is the collision of diatomic radicals with rare gas atoms that is of interest. The vector properties that describe a collision between these two species are the initial relative velocity ($\boldsymbol{k}$), the final relative velocity ($\boldsymbol{k}'$), the initial angular momentum associated with the rotation of the nuclear framework of the radical ($\boldsymbol{j}$), and the final rotational angular momentum of the radical ($\boldsymbol{j}'$). These are shown in figure 1.1. Therefore, a consideration of the four vector $\boldsymbol{k}$-$\boldsymbol{k}'$-$\boldsymbol{j}$-$\boldsymbol{j}'$ correlation will completely describe the scattering process [2–8]. The direction of the diatom could equally be described in terms of the initial orientation of the bond axis ($\boldsymbol{r}$) and the orientation of this axis after the collision ($\boldsymbol{r}'$). This would give rise to the $\boldsymbol{k}$-$\boldsymbol{k}'$-$\boldsymbol{r}$-$\boldsymbol{r}'$ correlation, which would again provide a complete picture of the stereodynamics. It should be noted that the direction of $\boldsymbol{r}'$ cannot



Figure 1.1: A schematic representation of the vectors that can be used to completely describe the collision of an atom with a diatom. In this case, the orbital angular momentum would be directed perpendicular to the page.

be determined experimentally, and therefore this can only be considered theoretically. However, as the radical is likely to be rotating after the collision, considering the direction of $\boldsymbol{r}'$ provides less insight than determining the direction of $\boldsymbol{j}'$.

Whilst the four vector correlation discussed above completely describes the scattering process, information about the collision can also be obtained from lower order vector correlations, as will be the case throughout the current study. For example, the shapes of the differential cross-sections (equivalent to the $\boldsymbol{k}$-$\boldsymbol{k}'$ correlation), as considered in chapter 6, can provide insights into the mechanisms that govern the process under investigation. A strongly forward scattered differential cross-section corresponds to a more glancing blow collision, and points to the reaction or energy transfer occurring at larger separations. Backwards scattering corresponds to a more head-on collision, and suggests a more direct and impulsive encounter. The differential cross-section can also be used to directly infer information about the potential energy surface governing the process, for example, an isotropic differential cross-section may indicate the existence of an intermediate complex that survives for many rotational periods, before falling apart at any point during the rotation. This would suggest a significantly attractive potential. In inelastic scattering, the presence of a rainbow in the differential cross-section would again highlight the influence of an attractive interaction [9–12].

The other two vector correlation that will be considered extensively throughout the current study is the $\boldsymbol{j}$-$\boldsymbol{j}'$ correlation, which characterises the extent to which a collision

changes the plane of rotation of the radical. This can again provide information about the potential energy surface. If the direction of $\boldsymbol{j}$ is randomised after every collision, this would suggest a highly anisotropic and attractive potential, whereas if the direction of $\boldsymbol{j}'$ is similar to that of $\boldsymbol{j}$ the encounter is likely to be more impulsive. The $\boldsymbol{j}$-$\boldsymbol{j}'$ correlation is presented in chapters 3 and 4. It should be noted that the higher order $\boldsymbol{k}$-$\boldsymbol{k}'$-$\boldsymbol{j}'$ and $\boldsymbol{k}$-$\boldsymbol{j}$-$\boldsymbol{j}'$ correlations are also considered in this work in chapters 5 and 6.

1.2 Experimental methods

To be able to probe the vector properties of a collision discussed above experimentally, it is necessary to isolate the process of interest from other 'background' collisions. This can be achieved by operating under reasonably high vacuum conditions. It is also helpful to be able to select the initial (and final) quantum states that are studied, such that the properties observed are not averaged over the many populated states, resulting in a loss of information about the process of interest. The most common method for achieving this is through laser excitation, as will be used to select the initial states of NO(A) and OH(A) for the experiments presented in chapters 3 and 4. However, it is also possible to select the initial state using other methods, for example using an electric field, which will be considered in chapter 6 for NO(X). Throughout the rest of this section, some of the experimental methods available to determine the vector properties of collisions of these initial quantum state resolved species will be presented.

The simplest vector to control experimentally is that corresponding to the initial relative velocity, $\boldsymbol{k}$. This can be determined through the use of molecular beams, and many studies have made use of this, for example [13–47], and those given in reference [48]. Not only do these provide a well-defined direction of $\boldsymbol{k}$, the range of velocities in the molecular beam is usually relatively small, meaning the experiment is performed over only a narrow range of collision energies. The two molecular beams in most scattering experiments intersect at 90° as is the case in chapter 6, but some designs allow the angles to be changed,

with the effect that the collision energy can also be altered [13, 14, 31–33].

Having established the direction of $\boldsymbol{k}$, the determination of the direction of $\boldsymbol{k}'$ would allow the differential cross-section to be obtained. This could be achieved by moving the detector through different angles, to measure the extent to which scattering of the product occurred at that angle [34–36, 40–46]. The most universally applicable detection method is electron impact ionisation which is often coupled with time of flight mass spectrometry, see, for example references [48] and [49] (and references therein). Although this detection method gives good angular resolution, it is not always possible to determine the final quantum state of the scattered product, resulting in a loss of information about the scattering process. It is possible to achieve final state resolution with time of flight detection if the flight tube is sufficiently long to allow products with different translational energies to arrive at the detector at different times [50, 51]. This has the added advantage that all the populated product quantum states can be detected simultaneously.

An alternative method used to ionise the products in which final quantum state resolution is routinely achievable is through the use of lasers. The most commonly used technique is resonantly enhanced multi-photon ionisation (REMPI), which has been reviewed in reference [52]. This is a two step process, the first of which involves the absorption of one (or more) photon(s) to reach an electronically excited state of the molecule, before being ionised in the second step. REMPI transitions are labelled by two numbers, the first of which denotes the number of photons used for the excitation, and the second the number of photons for the ionisation. For example, Liu and co-workers combined a (1+1) REMPI scheme with Doppler resolved time of flight measurements to perform a detailed investigation of the reactive resonance in F+HD [34–36]. A (1+1′) ionisation scheme is employed in the experiments described in chapter 6 for the detection of NO(X), where the prime denotes the ionisation wavelength is different to that of the excitation wavelength.

A more recent development is that of Rydberg tagging [53–61]. In this scheme, the product is excited to a Rydberg state instead of being ionised. This has the advantage over ion based detection methods that the detected species is neutral (or alternatively

ionised just before detection), and therefore the final product distribution is unaffected by Coulomb repulsion, leading to very high resolution of the final velocity of the products, which can allow final quantum state resolution in favourable cases. Although this was originally developed for the detection of hydrogen atoms, it has since been applied to others, for example oxygen and sulfur [60, 61].

The advent of velocity mapped ion imaging [62, 63] removed the need to rotate the detector to be able to determine the direction of $\boldsymbol{k}'$, as the products scattered through all angles are detected simultaneously. The products are ionised (often by lasers), and are accelerated away from the interaction region by an electric field, tuned such that the ions with the same velocity are focussed onto the same point on a position sensitive detector. This can either be a delay line detector, where the ion impact produces a current and the time measured for it to reach a sink recorded (from which the position of the impact can be determined), or micro channel plates coupled with a phosphor screen, where the ion impact results in a flash that can then be recorded on a camera. There are many examples of measurements of differential cross-sections for both inelastic [9, 12, 19, 21–23, 37–39, 64–74] and reactive [31–33, 75–80] scattering, where this technique has been used. The differential cross-sections for the inelastic scattering of NO(X) with krypton which are presented in chapter 6 were obtained using this method.

In conventional ion imaging, the electric field that accelerates the ions up a time of flight tube towards the detector is tuned so as to compress the Newton sphere from the three dimensional scattering process into a two dimensional plane. If the electric field is instead tuned to elongate the Newton sphere along the time of flight axis, it is possible to detect only a 'slice' of the Newton sphere by pulsing the detector [31–33, 81–84]. This improves the resolution of the image, which can then allow pairwise correlations to be determined between the internal states populated as a result of the collision, as has been achieved in recent work on the reaction with F with deuterated forms of methane [31–33].

Whilst the introduction of molecular beams made it easier to perform experiments with a well-defined direction of $\boldsymbol{k}$, controlling the orientation of the molecule in atom-

molecule collisions is more difficult. In the case where the molecule has a dipole moment, it is possible to orient the bond axis, $\boldsymbol{r}$ with a static electric field, or control the direction of the initial rotational angular momentum $\boldsymbol{j}$ with a magnetic field [5, 85–95]. Many of these studies have focussed on orienting the carbon-halogen bond axis in the alkyl halides [86, 93–95], and determining the orientation dependence of the reaction with alkali metals [86, 93]. More recently, attention has turned to orienting the bond axis of diatomic molecules, with the inelastic scattering of both OH [25–27, 96] and NO [28, 47, 97–100] having been investigated. These studies have highlighted the steric asymmetry associated with inelastic scattering from either end of these radicals.

As mentioned above, it is possible to control the polarisation of $\boldsymbol{j}$ using magnetic fields. However, a more widely applied technique is using polarised laser light to create a polarised rotational angular momentum distribution (the direction of which could then be rotated using a magnetic field if required). For example, consider a perpendicular transition (corresponding to $\Sigma \leftarrow \Pi$ excitation, as used throughout this thesis). The transition dipole moment, $\boldsymbol{\mu}$, is perpendicular to both the bond axis and $\boldsymbol{j}$ for P and R branch excitation, and perpendicular to the bond axis but parallel to $\boldsymbol{j}$ for Q branch excitation, in the high j limit [5, 101, 102]. This is shown schematically in figure 1.2.

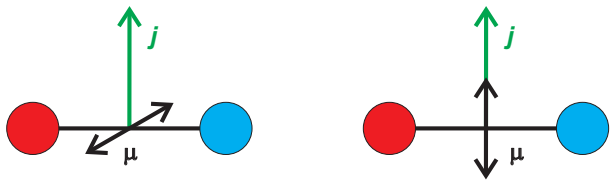


Figure 1.2: The correlation between $\boldsymbol{\mu}$ and $\boldsymbol{j}$ for $\Sigma \leftarrow \Pi$ transitions for P and R branch excitation (left) and Q branch excitation (right) [101].

The probability ($P(\theta_{\mu\varepsilon})$) that a molecule absorbs a photon of linearly polarised light is given classically by [5, 103]:

$$P(\theta_{\mu\varepsilon}) \propto |\boldsymbol{\varepsilon} \cdot \boldsymbol{\mu}|^2 \propto \cos^2 \theta_{\mu\varepsilon} \tag{1.1}$$

where $\boldsymbol{\varepsilon}$ is the direction of the linear polarisation, and $\theta_{\mu\varepsilon}$ is the angle between $\boldsymbol{\mu}$ and $\boldsymbol{\varepsilon}$.

Therefore, it is possible to create an electronically excited state ensemble of radicals with an aligned distribution of $\boldsymbol{\mu}$ from an isotropic distribution in the ground electronic state. Due to the correlation between $\boldsymbol{\mu}$ and $\boldsymbol{j}$ outlined above, it follows that the excited state molecules will also have an aligned distribution of $\boldsymbol{j}$.

The extent to which the atom-molecule interaction destroys this initial polarisation of $\boldsymbol{j}$ is characterised through the $\boldsymbol{j}$-$\boldsymbol{j}'$ correlation, where $\boldsymbol{j}'$ is the final rotational angular momentum associated with the molecule. Although this correlation cannot be measured directly in the same way as the $\boldsymbol{k}$-$\boldsymbol{k}'$ correlation discussed above, the measurement of the rates at which the polarisation is lost from the initially anisotropic distribution of $\boldsymbol{j}$ (or equivalently the cross-section for this process) allows information about the correlation to be determined. This has been the focus of many recent studies [104–134], and will be discussed further in chapters 3 and 4. Again, the collisional depolarisation of small open shell radicals has been the source of much of the interest, and there have been many studies on the OH radical in both the electronic ground state [104, 106, 108, 113, 114, 121, 122, 132–134], and first electronically excited state [108, 115, 116, 119, 120, 124], and to a lesser extent the NO radical in the ground [106, 110] and electronically excited state [109, 118–120, 123].

As already mentioned, the experimental determination of the direction of the bond axis of the molecule after the collision is not possible. However, the direction of $\boldsymbol{j}'$ can be determined, again through the use of polarised laser light. If the distribution of $\boldsymbol{j}'$ (and so consequently $\boldsymbol{\varepsilon}$) is anisotropic, then the probability that a photon is absorbed will be dependent on the direction of the laser polarisation. Therefore, performing experimental measurements with more than one laser polarisation can provide information about the direction of $\boldsymbol{j}'$ following the collision. When this is coupled with a crossed molecular beam set up and velocity mapped ion imaging as discussed above, it provides a means for measuring the $\boldsymbol{k}$-$\boldsymbol{k}'$-$\boldsymbol{j}'$ correlation. Chandler and co-workers have performed these measurements using both linearly polarised light [15, 16] and circularly polarised light [17] to determine the collision induced alignment and orientation of NO(X) following collisions with argon. The collision induced alignment of NO(X) with argon has also been measured

as part of the current study, but with full Λ-doublet resolution of the initial quantum state of the NO(X). These results are presented in chapter 6.

Information about the direction of $\boldsymbol{j}'$ can also be obtained from molecules in electronically excited states by recording their fluorescence. If the distribution of $\boldsymbol{j}'$ is anisotropic in the excited state, then the emitted fluorescence will also be polarised, due to the correlation between $\boldsymbol{\mu}$ and $\boldsymbol{j}$ discussed above. Therefore, recording the emission through suitable optics can provide a measure of the polarisation of $\boldsymbol{j}'$ [18, 124, 125, 135–137]. For example, the difference in fluorescence intensities recorded through a linear polariser following excitation using horizontal and vertical polarised light would reflect the degree of alignment in the sample (or equivalently, using one polarisation of the excitation laser and changing the detected polarisation from horizontal to vertical). The extent to which $\boldsymbol{j}'$ is oriented could be measured in the same way, but using circularly polarised light instead of linearly polarised light, and with the addition of a quarter waveplate to the detection optics. To achieve this with conventional laser induced fluorescence techniques, it is necessary for the laser to be directed along the detection axis. This can be avoided through the use of a magnetic field to rotate the distribution of $\boldsymbol{j}'$, as is the case in the Zeeman quantum beat spectroscopy experiments [108, 109, 115, 116, 119] which will be considered in chapters 3 and 4.

Polarisation spectroscopy [111, 130], as developed by McKendrick and co-workers, provides another method which can be used to probe the extent to which collisions cause a loss of polarisation in both the ground and electronically excited states [108, 110, 111, 114, 122, 130, 132–134]. This technique removes the need to change the polarisation of the pump laser which is necessary in the methods outlined above, but it is not possible to distinguish between the loss of population and polarisation as can be achieved with quantum beat spectroscopy. In the case of collisions of OH(A) with helium and argon, which have been studied using both polarisation spectroscopy and Zeeman quantum beat spectroscopy, it has been shown that the results obtained using the two different techniques are in excellent agreement [108, 138].

At the start of the previous section, a discussion was presented about the four vector correlations that would fully describe the stereodynamics of an atom-diatom collision. As has been shown, there have been considerable efforts to determine lower order vector correlations experimentally. By combining these techniques, it would be feasible to determine the full four vector correlation. This could be achieved by using a crossed molecular beam apparatus (to define $\boldsymbol{k}$) and velocity mapped ion imaging (to determine $\boldsymbol{k}'$). The direction of $\boldsymbol{r}$ (or $\boldsymbol{j}$) could be controlled using a static electric (or magnetic) field, and the direction of $\boldsymbol{j}'$ probed using a polarised laser. Although this would be a challenging experiment to perform, it would provide a complete picture of the scattering dynamics associated with the atom-diatom collision, and this is the longer term goal of the experiments described in chapter 6 of this thesis.

1.3 Potential energy surfaces

To obtain a complete understanding of an interaction between two species, it is necessary to consider both experimental observations and theoretical calculations. The link between the two is provided through the potential energy surface (PES). This characterises the interactions between the species involved in the collision at a range of geometries. Due to the large numbers of degrees of freedom that can be associated with the collision, one (or more) of these is often fixed. For example, the PES for the inelastic scattering of diatomic radicals with atoms, as considered here, is a function of the distance between the diatomic and atomic centre of mass, the angle of approach and the bond length of the radical. The PESs used throughout this study were obtained assuming that the bond length of the diatom was fixed at its equilibrium bond length.

The potential energy surface can be calculated by invoking the Born-Oppenheimer approximation [1, 139]. This states that the motion of the electrons is instantaneous on the timescales associated with nuclear motion, and therefore the motion of the two is separable. This allows the interaction potential to be calculated for a range of different posi-

tions of the nuclei (and the corresponding electron positions). If the Born-Oppenheimer approximation breaks down (*i.e.* the electrons are not necessarily found in their lowest energy configuration), then it is necessary to consider the motion of the nuclei across two (or more) adiabatic PESs, and the coupling that occurs between them. This is the case for the interactions of NO(X) (and OH(X)) with the rare gases, which are described by two potential energy surfaces. These will be presented for NO(X)-Ar and NO(X)-Kr in section 2.3.1.

Information regarding the potential energy surface can also be inferred from experimental observations [140]. In the case of reactive scattering, for example, the energy distribution in the products can point to whether the surface has an early or late barrier, with vibrationally excited products suggesting the presence of an early barrier. This forms the basis of Polanyi's rules [141]. Features of the PES can also be deduced from measurements made experimentally in the case of inelastic scattering. As discussed above, the features of the differential cross-section can provide insight into whether the interaction is attractive or repulsive. In the case where it is possible to observe and characterise the van der Waals complex, empirical potential energy surfaces can also be developed using these observations [142, 143].

1.4 Theoretical methods

Once the PES has been determined, then the forces acting on the species at every geometry sampled throughout the collision are known, allowing theoretical calculations to be performed. These can be run by modelling the motion of the atoms across the PES, using either classical mechanics or quantum mechanical (QM) methods. It would be expected that due to the inherently quantum mechanical nature of the scattering processes, Newtons laws of motion would not be applicable. However, there is often good agreement between the results from classical calculations, and the results from experimental observations (and the corresponding QM calculations). The advantage of using classical

mechanics over quantum mechanics is that the results provide a more intuitive picture of the scattering process, which in turn provides more insight into the mechanism behind the collision.

In systems where quantum effects are important, then the classical calculations will not provide an adequate description of the process under investigation. However, a comparison of the results from QM and classical calculations can highlight effects which are quantum mechanical in origin [144, 145]. Therefore discrepancies between the QM and classical calculations can arise due to tunnelling through a potential barrier, resonances and interference effects arising from the wave like nature of the particles. The classical calculations also do not consider any concept of quantisation of final rovibrational states, or of spin, although as discussed in this thesis these quantum considerations can be incorporated into 'classical' calculations.

The inelastic scattering of OH and NO with the rare gases, as considered here, is sufficiently simple to allow both detailed classical and QM calculations to be performed, and results from both will be presented throughout the current work. However, as the number of atoms involved in the scattering process increases, the QM calculations rapidly become too computationally expensive to perform. Therefore, for larger systems it is only feasible to run classical calculations, and even then it may be necessary to perform averaging over some of the degrees of freedom.

1.5 Outline of this thesis

Having outlined the motivations and goals of reaction dynamics in this chapter, the necessary theoretical methodology is presented in chapter 2. The first part of the chapter describes the angular momentum coupling schemes applicable to the radicals considered here, before the polarisation of rotational angular momentum distributions is introduced, which is a central theme to the current work. The focus will then move to considering the quasi-classical trajectory (QCT) and quantum mechanical calculations used to obtain

theoretical results which will be compared with those measured experimentally in later chapters.

Chapter 3 introduces the experimental methods used for measuring the rate of collisional depolarisation of OH(A) and NO(A) with krypton. The chapter begins with a brief introduction to the theory of the experimental method employed, before the experimental apparatus is described in section 3.3. The analysis used to obtain the quantities of interest from the experimental data is presented in section 3.4. A discussion of the experimental simulations that were also performed concludes the chapter. The experimental and theoretical results obtained using these methods are presented and discussed in chapter 4, with a particular emphasis on a comparison of the contrasting mechanisms of depolarisation that are seen in collisions of NO(A) and OH(A) with krypton. This theme is developed further in chapter 5 with a theoretical consideration of some of the three vector correlations that describe atom-diatom scattering. The main focus is the $\boldsymbol{k}$-$\boldsymbol{j}$-$\boldsymbol{j}'$ correlation, the equations for which have been developed as part of this work. The theoretical framework for this is presented in the first part of the chapter, and linked back to previous work on related correlations. This machinery is then used with the results from the QCT calculations for NO(A)-Kr and OH(A)-Kr to provide further insight into the scattering dynamics.

Chapter 6 describes the experimental determination of vector correlations of fully Λ-doublet state resolved NO(X) with argon and krypton. The first part of the chapter focusses on the apparatus used for the measurements, the theoretical aspects behind the experiment and the methods employed for data analysis. The results are then presented for the differential cross-sections for scattering of NO(X) with krypton in section 6.6 and the collision induced alignment of NO(X) through collisions with argon in section 6.7.

The final chapter summarises the principle conclusions of the current work, before presenting suggestions of future work that could develop and provide further insight to that which is presented here.

Chapter 2

Theoretical Background and Methods

In this chapter, the theoretical framework that underpins the work shown in this thesis is presented. In the first part of the chapter, the coupling of the angular momenta in OH and NO will be discussed. The focus of section 2.2 is the description of rotational angular momentum polarisation, and the formalism used for characterising vector correlations. Attention will then turn to the theoretical calculations, with both quasi-classical trajectory (QCT) and quantum mechanical methods described. The methods for obtaining the experimentally observable properties from these calculations will then be presented in section 2.4. In the final section of the chapter, the tensor opacity formalism for obtaining quasi-open shell results from the closed shell calculations for Σ radicals will be discussed.

2.1 Atom-radical collisions

In this section, the angular momentum coupling schemes applicable to both NO and OH in their electronic ground state and first electronically excited states will be presented.

2.1.1 NO(X)-Ar/Kr

The electronic ground state of the NO radical has one unpaired electron in a $\pi^\star$ orbital. Therefore, the electronic orbital angular momentum of the radical ($\boldsymbol{L}$) is 1, with projection Λ=$\pm$1 onto the internuclear axis, and the electronic spin angular momentum ($\boldsymbol{S}$) is $\frac{1}{2}$,

with projection $\Sigma{=}\pm\frac{1}{2}$ onto the same axis. The coupling of these angular momenta is best described by Hund's case (a). In this case, both $\boldsymbol{L}$ and $\boldsymbol{S}$ are strongly coupled to the internuclear axis, and there is strong spin-orbit coupling. The angular momentum associated with the rotation of the nuclei, $\boldsymbol{R}$, couples to the component of the total electronic angular momentum along the internuclear axis, Ω, to give the total angular momentum $\boldsymbol{j}$. The projection of $\boldsymbol{j}$ ($\Omega = \Sigma + \Lambda$) onto the internuclear axis can take absolute values of $\bar{\Omega}{=}\frac{1}{2}$ and $\bar{\Omega}{=}\frac{3}{2}$.

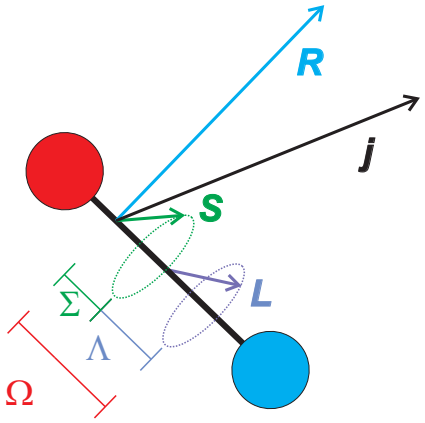


Figure 2.1: The angular momentum vector coupling scheme described by Hund's case (a).

Neglecting Λ-doubling, the total molecular Hamiltonian can be written as [102]:

$$\mathcal{H} = A(\boldsymbol{L}\cdot\boldsymbol{S}) + B(\boldsymbol{j}-\boldsymbol{S}-\boldsymbol{L})^2 \tag{2.1}$$

where the first term accounts for the spin-orbit coupling and the second the rotation of the nuclear framework ($\boldsymbol{R} = \boldsymbol{j}-\boldsymbol{S}-\boldsymbol{L}$). For the v=0 level of NO(X), the spin-orbit coupling constant, A, and the rotational constant, B, are given by $123.13\,\mathrm{cm}^{-1}$ and $1.6961\,\mathrm{cm}^{-1}$ respectively [146]. From the Hamiltonian, the energy of the rotational states can be worked out *via* [102]:

$$E(j) = B\left[(j-0.5)(j+1.5) \pm 0.5X\right] \tag{2.2}$$

where [102]:

$$X = \sqrt{4(j+0.5)^2 + Y(Y-4)} \tag{2.3}$$

and [102]:

$$Y = \frac{A}{B} \tag{2.4}$$

The $\pm$ sign in equation (2.2) distinguishes between the F_1 and F_2 spin-orbit manifolds. These correspond to the $^2\Pi_{\frac{1}{2}}$ and $^2\Pi_{\frac{3}{2}}$ states respectively, with the latter being the higher in energy by approximately $123\,\mathrm{cm}^{-1}$.

The wavefunctions for each Ω state are proportional to the Wigner rotation matrices defined in reference [102] and can be written as:

$$|j, m, \bar{\Omega}\rangle = \sqrt{\frac{2j+1}{4\pi}} D^j_{m\Omega}(\phi, \theta, 0)^\star \tag{2.5}$$

where m is the projection of $\boldsymbol{j}$ onto the space-fixed z axis. However, these states are not eigenfunctions of the Hamiltonian as they do not have a well-defined parity with respect to inversion [23]. Therefore, the rotational wavefunctions of NO(X) are described by linear combinations of the above states. In the case where Hund's case (a) fully describes the molecule, the states can be written as [102]:

$$|j, m, \bar{\Omega}, \epsilon\rangle = \frac{1}{\sqrt{2}} \left[|j, m, \bar{\Omega}\rangle + \epsilon |j, m, -\bar{\Omega}\rangle \right] \tag{2.6}$$

where $\epsilon{=}\pm1$. These states do have a well-defined parity with respect to inversion of the wavefunction, and this is given by $p{=}(-1)^{j-\epsilon/2}$ [147, 148]. The symmetric and antisymmetric combination of states corresponding to $\epsilon{=}\pm1$ are called Λ-doublets, with $\epsilon{=}+1$ referred to as e and $\epsilon{=}-1$ referred to as f. As well as these labels, the Λ-doublets are also given the symmetry labels A' and A'' which define whether the electronic part of the wavefunction is symmetric or antisymmetric with respect to reflection in the plane of rotation in the high j limit [149–151]. The A' label refers to the state where the unpaired electron is in a $\pi^\star$ orbital in the plane of rotation, and A'' when the orbital is perpendicular to the plane of rotation. The degeneracy of these two Λ-doublet levels is lifted through interactions with higher lying electronic states, especially those with Σ character. For

the $\bar{\Omega}$=0.5 manifold, the values of the energy gap range from 0.0118 cm^{-1} for j=0.5 to 0.1767 cm^{-1} for j=16.5 [152–154]. The splittings are smaller in the $\bar{\Omega}$=1.5 manifold, with it taking a value of 4×10^{-5} cm^{-1} for the lowest, j=1.5 state [155] and increasing with the third power of j [102].

As the radical rotates faster, Hund's case (a) starts to break down as $\boldsymbol{L}$ and $\boldsymbol{S}$ become uncoupled from the nuclear axis. Therefore at higher j, the wavefunctions should be written as [1, 30, 102]:

$$|F_1, j, m, \epsilon\rangle = a|j, m, \bar{\Omega} = 0.5, \epsilon\rangle + b|j, m, \bar{\Omega} = 1.5, \epsilon\rangle \quad (2.7)$$

$$|F_2, j, m, \epsilon\rangle = a|j, m, \bar{\Omega} = 1.5, \epsilon\rangle - b|j, m, \bar{\Omega} = 0.5, \epsilon\rangle \quad (2.8)$$

where the mixing coefficients a and b are given by:

$$a = \sqrt{\frac{X + (Y - 2)}{2X}} \quad (2.9)$$

$$b = \sqrt{\frac{X - (Y - 2)}{2X}} \quad (2.10)$$

where X and Y were defined in equations (2.3) and (2.4). It follows that at higher j, the coupling scheme tends towards that described by Hund's case (b), which is discussed in section 2.1.2. For the rotational levels used in this study, this mixing will be small [23, 98] and Hund's case (a) provides an adequate description of NO(X).

Spectroscopic transitions

For Hund's case (a), the spectroscopic transitions are labelled as [156]:

$$\Delta j_{f_\Sigma F_\Pi}(j'') \quad (2.11)$$

where j'' is the rotational quantum number of the ground state of the transition and Δj refers to the change in quantum number between the ground and excited state, where Δj=−1, 0, and +1 corresponds to P, Q and R branch excitation respectively. F_Π refers

to the spin-orbit manifold the excitation is from in the X $^2\Pi$ state, where F_1 is the $^2\Pi_{\frac{1}{2}}$ level and F_2 the $^2\Pi_{\frac{3}{2}}$ level. Analogously, f_Σ shows which spin-rotation level is populated in the excited state, where the f_1 level corresponds to $j = N + S$, and f_2 to $j = N - S$. This notation will be used throughout chapter 6.

Collision induced transitions

Throughout chapter 6, the inelastic transitions in NO(X) will be referred to as either conserving or changing the initially populated spin-orbit level, the parity, and the Λ-doublet level. Examples of transitions are shown schematically in figure 2.2, from the initially populated Ω=0.5, j=0.5 f level. The +/− labels refer to the parity of the associated Λ-doublet level, the upper of which is f and the lower e for each j [20]. Considering the

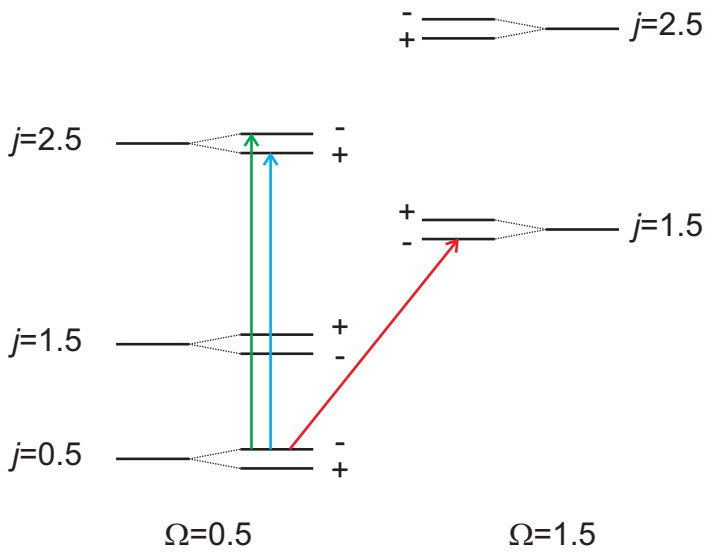


Figure 2.2: An energy level diagram of the rotational states in NO(X). The +/− labels denote the parity of the Λ-doublet level. The arrows show different types of transitions, as discussed in the text. It should be noted that the energy level separations are not to scale.

transitions shown in the figure, those shown by the blue and green arrows conserve the initially populated spin-orbit level, whereas the red arrow changes the spin-orbit level. The red and green arrows both show transitions in which the parity is conserved (*i.e.* final parity, p'=−1), and the blue to a transition where the parity changes (p'=+1). Although

the transitions shown by the red and green arrows both conserve the parity, the Λ-doublet level is conserved in the case of the green transition (*i.e.* the transition corresponds to *f*-*f*), and the Λ-doublet level changes in the red transition (corresponding to *f*-*e*).

2.1.2 NO(A)-Kr and OH(A)-Kr

The first electronically excited states of NO(A) and OH(A) have an unpaired electron in a $\sigma^\star$ orbital, giving rise to a $^2\Sigma$ state with a total electronic angular momentum of $\frac{1}{2}$. The angular momentum coupling in these radicals is best described by Hund's case (b), where the electron spin is not coupled to the internuclear axis [157].

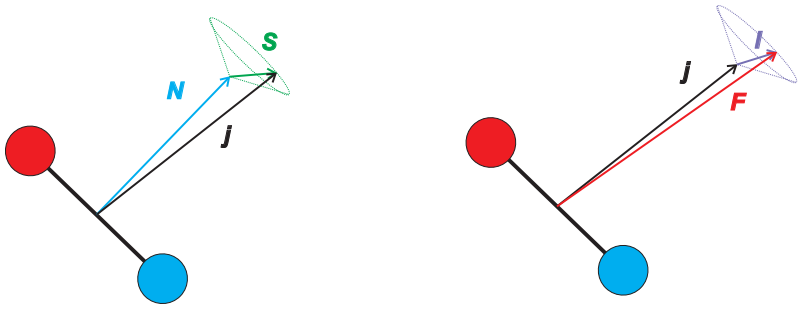


Figure 2.3: The angular momentum vector coupling scheme described by Hund's case (b). The left hand panel neglects the nuclear spin, and the right hand panel includes nuclear spin.

In this case, the rotational angular momentum of the nuclear framework $\boldsymbol{R}$ couples to the projection of the electronic orbital angular momentum Λ to give $\boldsymbol{N}$. As Λ=0 for both OH(A) and NO(A) it immediately follows that $\boldsymbol{R} \equiv \boldsymbol{N}$, and the 'closed shell' rotational angular momentum quantum number (*i.e.* neglecting the electron and nuclear spin) will be denoted N. The electron spin, $\boldsymbol{S}$ couples with $\boldsymbol{N}$ to produce $\boldsymbol{j}$. For both radicals under consideration here, $S=\frac{1}{2}$ so each rotational level is split into two spin-rotation levels, where $j = N \pm \frac{1}{2}$ (with the exception of N=0, where there is only the j=0.5 level). Each spin-rotation level is further split through the coupling of $\boldsymbol{j}$ to the nuclear spin, denoted as $\boldsymbol{I}$, which gives the total angular momentum of the radical, $\boldsymbol{F}$. There are $2I+1$ hyperfine sub-levels for each spin-rotation level. Therefore, in the case of OH(A), where $I=\frac{1}{2}$, there are two hyperfine levels, and in the case of NO(A) where I=1, each spin-rotation level is

split into three hyperfine levels. The degeneracy of these hyperfine levels is lifted in an applied magnetic field, where each level will split into $2F+1$ magnetic sublevels.

The molecular Hamiltonian can be written as [102]:

$$\mathcal{H} = B\boldsymbol{N}^2 + \gamma(\boldsymbol{N}\cdot\boldsymbol{S}) \tag{2.12}$$

where the first term accounts for the rotation of the nuclear framework and the second the spin-rotation coupling. For the v=0 level of NO(A), the rotational constant (B) is 1.99 cm^{-1} and the spin-rotation coupling constant (γ) is 0.12 cm^{-1} [158], and for the same vibrational level of OH(A), B=17.36 cm^{-1} and γ=0.226 cm^{-1} [159]. The energy of the rotational levels can then be obtained *via* [157]:

$$\begin{aligned} E(j,f_1) &= BN(N+1) + 0.5\gamma N \\ E(j,f_2) &= BN(N+1) - 0.5\gamma(N+1) \end{aligned} \tag{2.13}$$

where f_1 and f_2 refer to $j = N + S$ and $j = N - S$ respectively.

Spectroscopic transitions

Within Hund's case (b), spectroscopic transitions are labelled as [156]:

$$\Delta N_{f_\Sigma F_\Pi}(N'') \tag{2.14}$$

where N'' is the rotational quantum number of the ground state of the transition, F_Π and f_Σ are as defined in the previous section and ΔN refers to the change in quantum number between the ground and excited state. This can take values of -2, -1, 0, $+1$ and $+2$ which are labelled as O, P, Q, R and S respectively. This notation will be used throughout chapters 3 and 4.

Collision induced transitions

In chapters 3 and 4 transitions brought about by collisions will be referred to as either being elastic or inelastic. When considering the experimental results, an elastic transition is one where the final spin-rotation level is the same as the initially populated spin-rotation level, whereas an inelastic collision is one which changes the initially populated spin-rotation level. It follows that collisions which change the hyperfine level of the radical, but

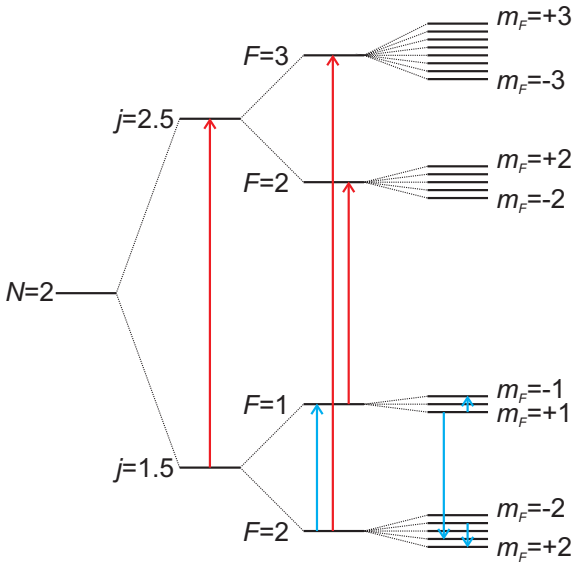


Figure 2.4: An energy level diagram of the rotational states in OH(A). The blue arrows correspond to elastic transitions and the red arrows to inelastic transitions. The energy level separations are not to scale.

preserve the initially populated spin-rotation level are still considered to be elastic. This is shown schematically in figure 2.4, where the blue arrows correspond to transitions that would be considered to be elastic, and red arrows to transitions that would be considered to be inelastic. Any collisions that change the initially populated N level would also be classed as an inelastic transition. The initially populated spin-rotation level in the figure is N=2, j=1.5.

2.2 Vector correlations

In this section, the concept of rotational angular momentum polarisation is introduced. A formalism for describing vector correlations will then be discussed, using both classical and quantum mechanical methods. This theme will be developed further in chapter 5.

2.2.1 Rotational angular momentum polarisation

Of particular interest in the current work is the polarisation of rotational angular momentum, $\boldsymbol{j}$. This is a property of an ensemble of molecules which have an anisotropic distribution of $\boldsymbol{j}$ with respect to a given reference axis or plane. In the present study, both orientation and alignment of $\boldsymbol{j}$ will be considered. An oriented distribution can be described classically as one in which the direction of $\boldsymbol{j}$ lies either parallel or antiparallel to the reference axis [18, 29, 101, 147]. This corresponds to molecules preferentially rotating clockwise or anticlockwise. If the distribution of $\boldsymbol{j}$ preferentially lies along the reference axis as opposed to the plane perpendicular to it, or vice versa, but without any preference for the direction of rotation, then that distribution is said to be aligned. This classical picture is shown in the top panels of figure 2.5, where the left hand panel corresponds to an oriented distribution of $\boldsymbol{j}$, and the right hand panel an aligned distribution.

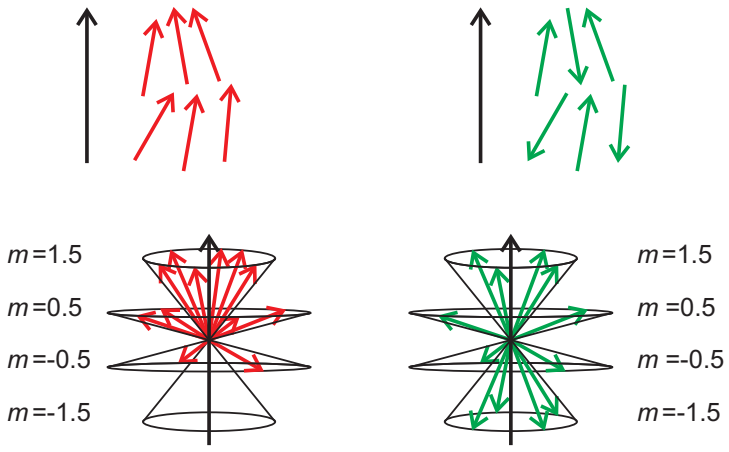


Figure 2.5: Pictorial representation of an oriented (left column) and an aligned (right column) rotational angular momentum distribution considered classically (top row) and quantum mechanically (bottom row). The direction of the red/green arrows show the direction of $\boldsymbol{j}$, and the black arrows the direction of the reference axis.

Quantum mechanically, the direction of $\boldsymbol{j}$ with respect to a given axis is quantised. $\boldsymbol{j}$ can have $2j+1$ projections onto that axis, which are denoted by the quantum number m. The relative populations of each of the $|jm\rangle$ states describes the distribution of $\boldsymbol{j}$. If the reference axis is taken as the quantisation axis, then a simple incoherent picture emerges, where the unequal population of these m states corresponds to $\boldsymbol{j}$ being polarised. For an oriented distribution, the population lies preferentially in, for example, $+m$ states as opposed to $-m$ states. An aligned distribution would correspond to one in which the population of the $+|m|$ level is the same as the $-|m|$ level, but where, for example, the populations in larger values of $|m|$ were bigger than those in smaller values of $|m|$. This is shown schematically in the bottom panels of figure 2.5, where the left hand panel corresponds to an oriented distribution and the right hand panel an aligned distribution.

In the general case, the anisotropic distribution of $\boldsymbol{j}$ is described by the unequal populations of the $|jm\rangle$ states and the coherences that exist between them. The distribution is then expressed in terms of its density matrix [5, 102, 160]. For a wavefunction that can be written as a linear combination of $|jm\rangle$ states $|\Psi\rangle = \sum_{m=-j}^{j} c_m|jm\rangle$, the density operator can be written as [160]:

$$\hat{\rho} = \sum_{m_1,m_2} c_{m_1} c^{\star}_{m_2} |jm_1\rangle\langle jm_2| \tag{2.15}$$

The density matrix elements are therefore given by [1, 160, 161]:

$$\begin{aligned} \langle jm|\hat{\rho}|jm'\rangle &= \sum_{m_1,m_2} c_{m_1} c^{\star}_{m_2} \langle jm|jm_1\rangle\langle jm_2|jm'\rangle \\ &= c_m c^{\star}_{m'} \end{aligned} \tag{2.16}$$

It follows that the diagonal elements of the density matrix describe the population of the $|jm\rangle$ state, whereas the off-diagonal elements characterise the coherences that exist between the $|jm\rangle$ and $|jm'\rangle$ states.

2.2.2 Describing vector correlations

Classical description

In the case where the distribution of $\boldsymbol{j}'$ is cylindrically symmetric about the reference axis, the correlation depends on only one angle. In chapters 3 and 4 the reference axis is taken to be the direction of the initial rotational angular momentum, $\boldsymbol{j}$. The distribution of $\boldsymbol{j}'$ with respect to $\boldsymbol{j}$ can be expanded using Legendre polynomials, $P_k(x)$:

$$P(\theta_{jj'}) = \frac{1}{2}\sum_k [k] a^{(k)} P_k(\cos\theta_{jj'}) \tag{2.17}$$

where $\theta_{jj'}$ is the angle between $\boldsymbol{j}$ and $\boldsymbol{j}'$, $[k] = 2k+1$, and $a^{(k)}$ are the expansion coefficients which are the expectation values of the associated Legendre moments [101]:

$$a^{(k)} = \langle P_k(\cos\theta_{jj'})\rangle \tag{2.18}$$

where $\langle\cdots\rangle$ is the ensemble average. It follows that for an isotropic distribution of $\boldsymbol{j}'$ about $\boldsymbol{j}$, $a^{(0)}$=1, and $a^{(k\neq 0)}$=0. In the case where the direction of $\boldsymbol{j}'$ is the same as $\boldsymbol{j}$, *i.e.* the collision does not cause any depolarisation, $a^{(k)}$=1 for all values of k.

Of particular interest to the current study are the moments when k=1 and k=2, which correspond to orientation and alignment respectively. These are given by:

$$\begin{aligned} a^{(1)} &= \langle P_1(\cos\theta_{jj'})\rangle &&= \langle \cos\theta_{jj'}\rangle \\ a^{(2)} &= \langle P_2(\cos\theta_{jj'})\rangle &&= \left\langle \frac{1}{2}(3\cos^2\theta_{jj'} - 1)\right\rangle \end{aligned} \tag{2.19}$$

Therefore $a^{(1)}$ can take values between +1 and −1, and $a^{(2)}$ can take values of between +1 and −0.5. The negative limits of these parameters correspond to distributions that are still oriented and aligned. When $a^{(1)}$ is negative the distribution of $\boldsymbol{j}'$ lies 180° away from $\boldsymbol{j}$, *i.e.* the collision has resulted in the radical rotating in the opposite sense to which it was rotating before the collision. If $a^{(2)}$ takes its negative limiting value, then the distribution

of $\boldsymbol{j}'$ is perpendicular to the initial distribution of $\boldsymbol{j}$.

The differential cross-section, which corresponds to the correlation between the initial velocity ($\boldsymbol{k}$) and final velocity ($\boldsymbol{k}'$), is considered in chapter 6. This can also be expanded in the same way as the $\boldsymbol{j}$-$\boldsymbol{j}'$ correlation discussed above, but using the scattering angle, $\theta_{kk'}$ as opposed to $\theta_{jj'}$. This is discussed further in section 2.4.2.

If the distribution of the vector under consideration is not cylindrically symmetric with respect to the reference axis, or the second vector is not restricted to a plane, then the correlation will also have an azimuthal dependence. This is the case that will be considered in chapters 5 and 6. In chapter 6 it is the $\boldsymbol{k}$-$\boldsymbol{k}'$-$\boldsymbol{j}'$ correlation that is considered. Therefore, the distribution of $\boldsymbol{j}'$ with respect to the $\boldsymbol{k}$-$\boldsymbol{k}'$ plane can be expanded using the complex conjugates of the modified spherical harmonics [8, 102, 162]:

$$P(\theta_{kj'}, \phi_{kj'}) = \frac{1}{4\pi} \sum_k \sum_q [k] a_q^{(k)} C_{kq}(\theta_{kj'}, \phi_{kj'})^\star \tag{2.20}$$

where $\theta_{kj'}$ is the angle between $\boldsymbol{k}$ and $\boldsymbol{j}'$, $\phi_{kj'}$ the azimuthal angle between $\boldsymbol{j}'$ and the $\boldsymbol{k}$-$\boldsymbol{k}'$ plane, and $a_q^{(k)}$ are the expansion coefficients, defined as the following expectation values:

$$a_q^{(k)} = \langle C_{kq}(\theta_{kj'}, \phi_{kj'}) \rangle \tag{2.21}$$

where $-k \leq q \leq +k$. The moments given above are complex, as are the basis functions. To obtain real expansion coefficients, which then have physical meanings, it is better to work within the Hertel-Stoll normalisation [163]:

$$\begin{aligned} a_{q+}^{(k)} &= \frac{1}{\sqrt{2}} \left[(-1)^q a_{+q}^{(k)} + a_{-q}^{(k)} \right] \\ a_{q-}^{(k)} &= \frac{1}{i\sqrt{2}} \left[(-1)^q a_{+q}^{(k)} - a_{-q}^{(k)} \right] \end{aligned} \tag{2.22}$$

where $0 \leq q \leq k$. Analogous expressions can also be used with the spherical harmonics basis functions, so that the basis sets for the expansion are also real.

The moments in equation (2.22) describe the distribution of $\boldsymbol{j}'$ with respect to the

scattering plane, with the $a^{(1)}_{q\pm}$ moments describing the orientation, and the $a^{(2)}_{q\pm}$ moments describing the alignment. When q=0, these moments are simply the $a^{(k)}$ expansion coefficients discussed above, and so describe the orientation and alignment of the distribution of $\boldsymbol{j}'$ with respect to $\boldsymbol{k}$. Defining $\boldsymbol{k}$ to lie along the z axis, and $\boldsymbol{k}'$ to lie in the zx plane (such that the scattering plane is the zx plane), the $a^{(1)}_{1-}$ moment of the distribution describes the orientation of $\boldsymbol{j}'$ perpendicular to the scattering plane (*i.e.* along the y axis), and the $a^{(1)}_{1+}$ moment the orientation along the x axis. As will be shown in chapter 5 (and also discussed in references [8] and [162]), the $a^{(1)}_{0}$ moment is necessarily zero for the $\boldsymbol{k}$-$\boldsymbol{k}'$-$\boldsymbol{j}'$ correlation, as are the $a^{(1)}_{1+}$, $a^{(2)}_{2-}$ and $a^{(2)}_{1-}$ moments, and so these do not contribute to the expansion. Therefore, the non-zero alignment moments are the $a^{(2)}_{2+}$ and $a^{(2)}_{1+}$ moments, where the $a^{(2)}_{2+}$ moment describes whether the alignment is along the y axis (perpendicular to the scattering plane) or x axis (lying in the scattering plane) and the $a^{(2)}_{1+}$ characterises the extent to which the $\boldsymbol{j}'$ distribution is tilted in the scattering plane, quantifying the extent to which it is parallel to the $\boldsymbol{x}+\boldsymbol{z}$ or $\boldsymbol{x}-\boldsymbol{z}$ vector.

Quantum mechanical description

Quantum mechanically it is not possible to specify the direction of $\boldsymbol{j}$ exactly. It is therefore convenient to consider the distribution of $\boldsymbol{j}$ in terms of its density matrix, as introduced in section 2.2.1. The expansion of the density matrix can be written as [161, 164]:

$$\langle jm|\hat{\rho}|jm'\rangle = \sum_{k=0}^{2j}\sum_{q=-k}^{k}\frac{2k+1}{2j+1}a^{(k)}_{q}\langle jm,kq|jm'\rangle \tag{2.23}$$

where $\langle jm,kq|jm'\rangle$ is a Clebsch-Gordan coefficient [102]. Using the orthogonality of the Clebsch-Gordan coefficients [102, 165] it is possible to invert the expression to obtain the following for the expansion coefficients [161, 164]:

$$a^{(k)}_{q} = \sum_{m=-j}^{j}\sum_{m'=-j}^{j}\langle jm|\hat{\rho}|jm'\rangle\langle jm,kq|jm'\rangle \tag{2.24}$$

It should be noted that these $a_q^{(k)}$ coefficients are the same as those in equation (2.20), and therefore, once the appropriate linear combinations are taken, have the same physical interpretation as already discussed.

Although it is not possible to define the direction of $\boldsymbol{j}$ precisely, it is possible to define a minimum uncertainty state $|\theta_j\phi_j\rangle$, where the direction of $\boldsymbol{j}$ is as localised as possible around the vector defined by the two angles, θ_j and ϕ_j [161]. The maximum localisation that can be obtained is when the projection of $\boldsymbol{j}$ onto that axis is maximum, corresponding to the state $|jj\rangle$. The minimum uncertainty state, $|\theta_j\phi_j\rangle$ can therefore be obtained by rotating the $|jj\rangle$ state to that direction [161, 164]:

$$|\theta_j\phi_j\rangle = R(\theta_j, \phi_j, 0)|jj\rangle = \sum_m |jm\rangle D^j_{mj}(\phi_j, \theta_j, 0) \tag{2.25}$$

where $D^j_{mj}(\phi_j, \theta_j, 0)$ is a Wigner rotation matrix, as defined in reference [102]. It follows that the overlap of a $|jm\rangle$ state with the minimum uncertainty state is given by [161]:

$$\langle jm|\theta_j\phi_j\rangle = D^j_{mj}(\phi_j, \theta_j, 0) \tag{2.26}$$

It is therefore now possible to define the population of this minimum uncertainty state as [161, 164]:

$$\begin{aligned} Q(\theta_j, \phi_j) &= \frac{\langle\theta_j\phi_j|\hat{\rho}|\theta_j\phi_j\rangle}{\mathrm{Tr}(\hat{\rho})} \\ &= \frac{1}{4\pi}\sum_{k=0}^{2j}\sum_{k=-q}^{q}[k]\langle jj, k0|jj\rangle a_q^{(k)} C_{kq}(\theta_j, \phi_j)^\star \end{aligned} \tag{2.27}$$

This is the same as equation (2.20), other than the $\langle jj, k0|jj\rangle$ Clebsch-Gordan coefficient. This restricts the extent to which the distribution of $\boldsymbol{j}$ can be polarised, reflecting the uncertainty with which the direction of $\boldsymbol{j}$ can be defined. In the high j limit, the Clebsch-Gordan coefficient tends to unity, and the direction of $\boldsymbol{j}$ tends to that defined by the minimum uncertainty state, with the result that the expression given above is then iden-

tical to the one in equation (2.20).

2.3 Calculation methods

In the first part of this section, the potential energy surfaces used in the scattering calculations are discussed. Then, the theoretical methods for modelling the motion of the atoms across the potential energy surface are presented, with both quasi-classical trajectory and quantum mechanical methods described.

2.3.1 Potential energy surfaces

NO(X)-Ar/Kr

The interactions of NO(X) with Ar and Kr are described by two non-degenerate potential energy surfaces. As discussed in section 2.1.1, NO(X) has an unpaired electron in a $\pi^\star$ orbital. Therefore, the approach of the rare gas atom can break the cylindrical symmetry of the radical. The A' symmetry corresponds to the π orbital containing the unpaired electron lying in the triatomic plane, and the A'' to the orbital lying perpendicular to the triatomic plane [1, 166] (note the different definitions of A' and A'' here and in section 2.1.1). In the Hund's case (a) limit, Alexander has shown that spin-orbit conserving collisions are governed by a potential described by [166, 167]:

$$V_{\text{sum}} = \frac{1}{2}\left[V(A'') + V(A')\right] = \sum_{l=0}^{l_{\max}} V_{l0}(R) d^l_{00}(\gamma) \tag{2.28}$$

whereas spin-orbit changing collisions occur on a potential energy surface (PES) given by [166, 167]:

$$V_{\text{diff}} = \frac{1}{2}\left[V(A'') - V(A')\right] = \sum_{l=2}^{l_{\max}} V_{l2}(R) d^l_{20}(\gamma) \tag{2.29}$$

where $d^l_{\lambda 0}(\gamma)$ are reduced Wigner rotation matrix elements [102] and $V_{l\lambda}(R)$ are the radially dependent expansion coefficients [150, 166].

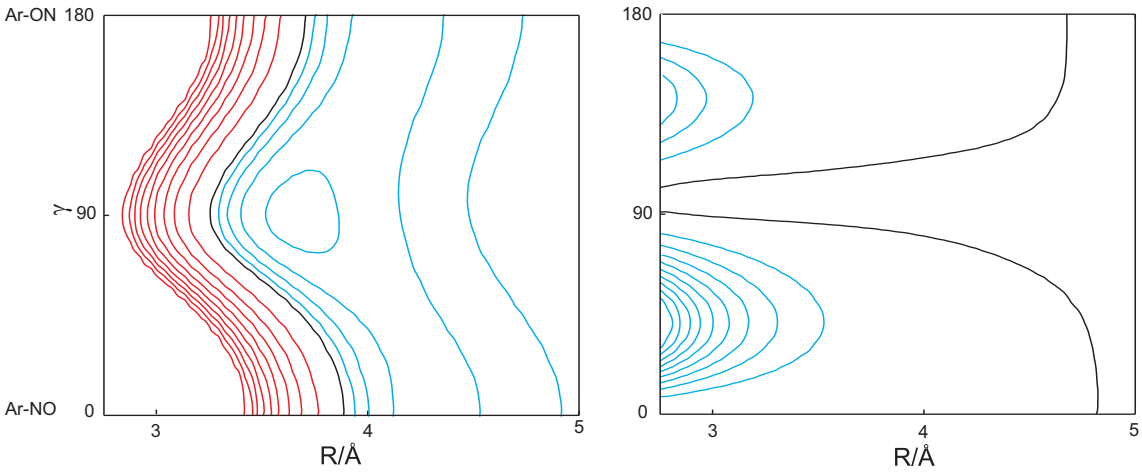


Figure 2.6: The potential energy surfaces corresponding to V_{sum} (left panel) and V_{diff} (right panel) calculated by Alexander [168] for NO(X)-Ar. The black contour corresponds to an energy of $0\,cm^{-1}$, red contours show repulsive regions of the PES and blue contours the attractive regions. For V_{sum} the repulsive contours are spaced by $100\,cm^{-1}$, and the attractive by $25\,cm^{-1}$, and for V_{diff} they are spaced by $100\,cm^{-1}$. $\gamma = 0°$ corresponds to the Ar-NO geometry, and $\gamma = 180°$ corresponds to Ar-ON.

The PESs for NO(X)-Ar calculated by Alexander [168] using the CCSD(T) level of theory are shown in figure 2.6, as a function of distance between the atomic and diatomic centre of mass, R, and angle of approach, γ. The bond length of the NO(X) was fixed at its equilibrium value of 1.15 Å [169]. As can be seen, the V_{sum} PES is significantly more repulsive and isotropic than the V_{diff} PES, which has deep attractive potential wells in two approach geometries. V_{diff} is also more anisotropic, with the potential varying rapidly as a function of angle of approach of the argon. As the potential which corresponds to $V(A'')$ is very similar to that for $V(A')$, it would be anticipated that the determination of V_{diff} would be less accurate than the determination of V_{sum}.

The V_{sum} PES for NO(X)-Kr is shown in the left hand panel of figure 2.7, and the V_{diff} PES is shown in the right hand panel. This was calculated by Alexander and co-workers [170] again at the CCSD(T) level of theory, with the NO(X) bond length fixed at its equilibrium value. Both the V_{sum} and V_{diff} potentials are longer range and more attractive for NO(X)-Kr than for NO(X)-Ar. The V_{sum} potential is also more symmetric about the T-shaped geometry for the heavier rare gas, reflecting the more homonuclear character of the NO(X)-Kr PES. The V_{diff} potential is again significantly more anisotropic than the

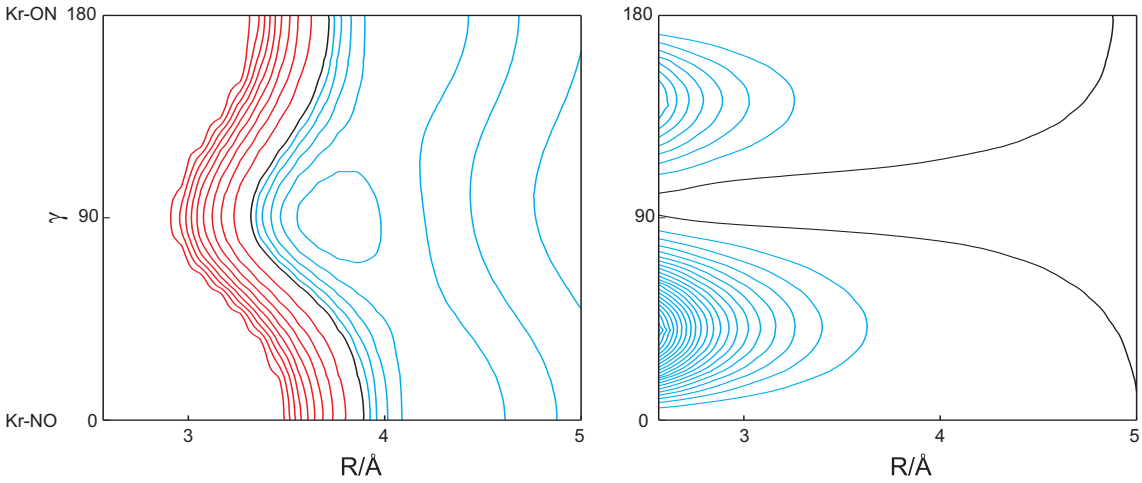


Figure 2.7: The potential energy surfaces corresponding to V_{sum} (left panel) and V_{diff} (right panel) for NO(X)-Kr calculated by Alexander and co-workers [170]. The black contour corresponds to an energy of $0\,cm^{-1}$, red contours show repulsive regions of the PES and blue contours the attractive regions. For V_{sum} the repulsive contours are spaced by $100\,cm^{-1}$, and the attractive by $25\,cm^{-1}$, and for V_{diff} they are spaced by $100\,cm^{-1}$. $\gamma = 0°$ corresponds to the Kr-NO geometry, and $\gamma = 180°$ corresponds to Kr-ON.

V_{sum} potential.

NO(A)-Kr and OH(A)-Kr

The first electronically excited state of NO lies approximately $44200\,cm^{-1}$ above the ground state [171]. Unlike for NO(X), the interactions between NO(A) and krypton (and OH(A) with krypton) can be described by a single, adiabatic PES. For NO(A)-Kr, the latest *ab initio* PES of Kłos *et al.* [171] was used, which is shown in the left hand panel of figure 2.8. The PES was calculated at the RCCSD(T) level of theory, and the bond length of the NO radical was fixed at its equilibrium value of 1.064Å [169]. In comparison to the NO(X)-Kr PES considered in the previous section, the dependence of the NO(A)-Kr potential as a function of the angle of approach is markedly different. The minimum in the ground state corresponds to a T-shaped geometry, whereas in the excited state there are two minima in the surface which correspond to linear approaches of the Kr. The global minimum is in the Kr–NO geometry and has a depth of $137.8\,cm^{-1}$ at a distance of 4.2 Å. The other, local minima is in the Kr–ON geometry, and this has a well depth of $63\,cm^{-1}$ at a distance of 5.2 Å.

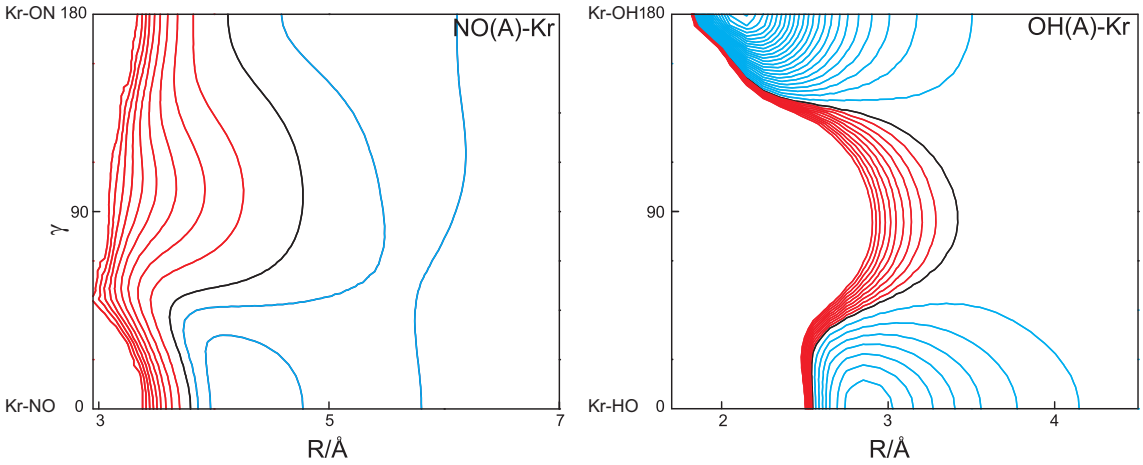


Figure 2.8: Potential energy surfaces for NO(A $^2\Sigma^+$)-Kr [171] (left hand panel) and OH(A $^2\Sigma^+$)-Kr [172] (right hand panel). The black contour corresponds to an energy of $0\,\mathrm{cm}^{-1}$, red contours show repulsive regions of the PES and blue contours the attractive regions. The red contours are spaced by $100\,\mathrm{cm}^{-1}$ in both cases, whereas the blue contours are spaced by $50\,\mathrm{cm}^{-1}$ for NO(A)-Kr in the left hand panel, and $250\,\mathrm{cm}^{-1}$ for OH(A)-Kr in the right hand panel. $\gamma = 0°$ corresponds to the Kr approaching the N or H end of the radical, and $\gamma = 180°$ corresponds to the Kr approaching the O end of the radical.

In contrast, the OH(A)-Kr PES is significantly more anisotropic and attractive than the NO(A)-Kr PES. The PES employed was the latest *ab initio* PES of Kłos *et al.* [172], which is depicted in the right hand panel of figure 2.8. This was also calculated at the RCCSD(T) level of theory, and the bond length of the OH radical was fixed at its equilibrium value of 1.004Å [169]. The global minimum in the surface corresponds to the linear Kr–OH geometry, and has a well depth of $6079\,\mathrm{cm}^{-1}$ at a distance of 2.10 Å. There is also a local minimum of $1949\,\mathrm{cm}^{-1}$ at a distance of 2.84 Å in the Kr–HO geometry. There is a saddle point with a depth of $80\,\mathrm{cm}^{-1}$ at a distance of 3.94 Å, and therefore there is a significant barrier to rotation of approximately $1850\,\mathrm{cm}^{-1}$. Consequently, linear approach geometries are the most favoured.

2.3.2 Quasi-classical trajectories

Quasi-classical trajectory (QCT) calculations were performed for NO(A)-Kr and OH(A)-Kr using the PESs described above. The paths of the nuclei across the PES were de-

termined using Newtons laws of motion, and as such were governed solely by classical mechanics. As the outcome of an individual trajectory depends on the initial conditions, it is necessary to average over a large number of trajectories to determine any dynamical information about the system of interest.

If the cartesian co-ordinates for the atom, A with mass m_A, and diatom BC (where the individual atoms have masses m_B and m_C) are given by x_i, and the conjugate momenta as P_{xi}, where i=1,2,3 corresponds to A, i=4,5,6 to B and i=7,8,9 to C, then the Hamiltonian for the system is given by [173]:

$$\mathcal{H} = \sum_{i=1}^{3} \frac{P_{xi}^2}{2m_A} + \sum_{i=4}^{6} \frac{P_{xi}^2}{2m_B} + \sum_{i=7}^{9} \frac{P_{xi}^2}{2m_C} + V(x_1, x_2 \ldots, x_9) \tag{2.30}$$

where the first three terms give the total kinetic energy and $V(x_1, x_2 \ldots, x_9)$ the potential energy. In using Cartesian co-ordinates, it is necessary to specify nine variables (associated with the x, y and z co-ordinates of each atom). However, the trajectories are run in a space fixed frame, as shown in figure 2.9, where the centre of mass of the diatom is taken as the origin of the co-ordinate system. The co-ordinates of the system are also expressed in terms of Jacobi co-ordinates, as only six variables are needed. In this case, q_1, q_2 and q_3 define the position of C with respect to B ($\boldsymbol{r}$), and q_4, q_5 and q_6 define the position of the atom A with respect to the centre of mass of the radical BC ($\boldsymbol{R}$). The conjugate

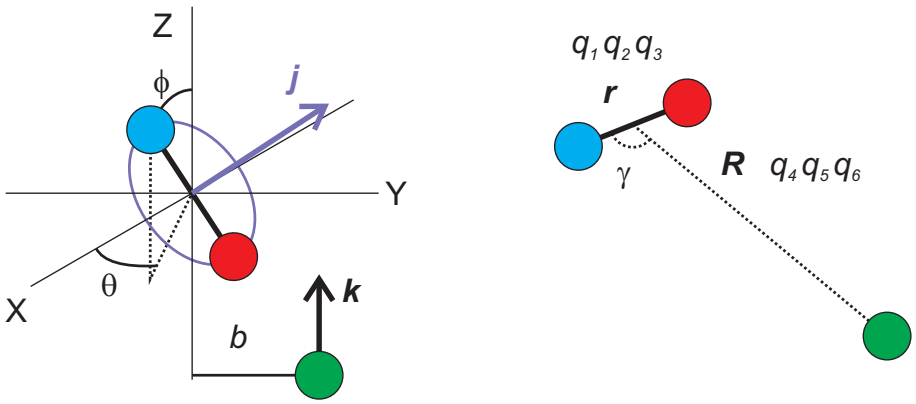


Figure 2.9: The space fixed frame used for running the QCT calculations (left hand panel), and the corresponding Jacobi co-ordinates (right hand panel).

momenta for each co-ordinate is given by p_{qi}. The angle (γ) between $\boldsymbol{R}$ and $\boldsymbol{r}$ can then be calculated using:

$$\cos\gamma = \frac{R_x.r_x + R_y.r_y + R_z.r_z}{|\boldsymbol{R}||\boldsymbol{r}|} = \frac{q_1.q_4 + q_2.q_5 + q_3.q_6}{\sqrt{q_1^2+q_2^2+q_3^2}\,\sqrt{q_4^2+q_5^2+q_6^2}} \tag{2.31}$$

The Hamiltonian for the system can then be expressed as:

$$\mathcal{H} = \sum_{i=1}^{3} \frac{p_{qi}}{2\mu_{BC}} + \sum_{i=4}^{6} \frac{p_{qi}}{2\mu_{A,BC}} + V(R,r,\gamma) \tag{2.32}$$

where the first term accounts for the kinetic energy of the diatom BC, the second the kinetic energy associated with the relative motion of atom A with respect to BC, and the final term the potential energy when the radical, with a bond length r, is at a distance of R from the atom, and the angle between $\boldsymbol{r}$ and $\boldsymbol{R}$ is given by γ.

The trajectories are run by solving Hamilton's equations of motion across the PES. These are given by [173]:

$$\frac{\mathrm{d}q_i}{\mathrm{d}t} = \frac{\partial\mathcal{H}}{\partial p_i} = \frac{\partial T}{\partial p_i} \tag{2.33}$$

$$\frac{\mathrm{d}p_i}{\mathrm{d}t} = -\frac{\partial\mathcal{H}}{\partial q_i} = -\frac{\partial V}{\partial q_i} = -\left(\frac{\partial V}{\partial R}\frac{\partial R}{\partial q_i} + \frac{\partial V}{\partial r}\frac{\partial r}{\partial q_i} + \frac{\partial V}{\partial\cos\gamma}\frac{\partial\cos\gamma}{\partial q_i}\right) \tag{2.34}$$

As mentioned above, it is necessary to run large numbers of trajectories to obtain dynamical information about the system of interest. For each trajectory, the collision energy was either set to a fixed initial value, or randomly and uniformly sampled between two user defined limits. It should be noted that it would also be possible to sample the collision energy according to some other distribution, for example the Boltzmann distribution.

The impact parameter for the trajectory, b, was also sampled uniformly between 0 and $b_{\max}^2$. The value of $b_{\max}$ was chosen for each initial rotational state such that there is no inelastic scattering or elastic depolarisation at higher values of b. As the incoming relative velocity of the atom is defined as being parallel to the z axis, and lies in the yz plane, this is simply the initial distance of the atom from the z axis. It also follows that the initial

orbital angular momentum is directed along the x axis.

The initial rovibrational state of the diatom could either be sampled from a distribution, or, as here, could be input by the user. If the bond length is allowed to vary, then it is set to a value that corresponds to one of the turning points of the vibration. The orientation of $\boldsymbol{r}$, (or equivalently initial rotational angular momentum, $\boldsymbol{j}$) is chosen by random sampling of the angles θ, ϕ and η. θ and ϕ are the polar and azimuthal angles describing the direction of $\boldsymbol{r}$ (or $\boldsymbol{j}$), and η defines the rotational phase of the radical.

At t=0, the trajectory starts with the atom and diatom at a sufficiently large separation such that the interaction between them is negligible. In the case that the bond length is allowed to vary, this is adjusted slightly for each trajectory to allow randomisation of the initial vibrational phase. This was not necessary in the current calculations, as the method of Lagrangian multipliers [174] was used to enforce a fixed bond length. The trajectory is then propagated by solving the equations of motion given above, until the separation is again large and the interaction negligible, at which point the trajectory is deemed to be over. The final positions and momenta are then recorded, from which the quantities of interest can be calculated.

The 'quasi' nature of the trajectories refers to the fact that the initial rotational quantum number, N, is quantised. It is also necessary to quantise the final rotational angular momentum N', as this can vary continuously as there is no restriction imposed on it during the trajectory calculation. N' is histogram binned to the nearest integer *via* $|\boldsymbol{N'}| = \hbar\sqrt{N'(N'+1)}$. Trajectories where $N' = N \pm 0.5$ were considered to be elastic.

Observable properties can be obtained from the QCT calculations as an ensemble average over a large number of (typically $\approx 1 \times 10^5$) trajectories. For example, the total inelastic cross-section ($\sigma^{(0)}$) can be obtained *via*:

$$\sigma^{(0)} = \sum_{N' \neq N} \sigma^{(0)}_{NN'} = \sum_{N' \neq N} \frac{\mathcal{N}_{NN'}}{\mathcal{N}_{\text{tot}}} \pi b^2_{\text{max}} \tag{2.35}$$

where $\sigma^{(0)}_{NN'}$ is the cross-section for a given N to N' transition, $\mathcal{N}_{NN'}$ is the number of

trajectories for a given initial N with final rotational angular momentum N', and $\mathcal{N}_{\text{tot}}$ is the total number of trajectories for initial state N.

It should be noted that it is not possible to converge the elastic (velocity changing) cross-sections in QCT calculations. As the value of b_{max} is increased the fraction of trajectories that are deemed to be elastic also increases. As can be seen from equation (2.35), this will result in $\sigma^{(0)}$ changing with the value of b_{max} used. Also, the calculations are governed solely by classical mechanics and so do not include any quantum mechanical effects, for example tunnelling or resonances. They are also inherently closed shell and so do not include any concept of electron or nuclear spin. For Σ radicals, this can be incorporated using the tensor opacity formalism [118, 175], which will be described in section 2.5.

2.3.3 Quantum mechanics

The quantum mechanical (QM) calculations run for this study were performed using HIBRIDON [176], using the same OH(A)-Kr potential energy surface [172] as the QCT calculations described previously, and using the NO(X)-Kr PES [170] presented in section 2.3.1. This propagates the wavefunction by solving the close-coupled quantum mechanical equations [177], using the Log-Derivative method [178] in the short range region, and the airy propagator [179, 180] in the long range region. The output of this is the scattering, or $\hat{S}$ matrix, from which the observable properties of the system can be calculated.

Considering wavefunctions where the total angular momentum of the system, J, is fixed, $\hat{S}$ is defined such that:

$$\hat{S}|\Psi^J_{\text{in}}\rangle = |\Psi^J_{\text{out}}\rangle \tag{2.36}$$

where in the case of pure, coherent states both $|\Psi^J_{\text{in}}\rangle$ and $|\Psi^J_{\text{out}}\rangle$ can be written as a linear combination of rovibrational eigenstates that describe the system:

$$|\Psi^J_{\text{in}}\rangle = \sum_i c_i|\psi^J_i\rangle \tag{2.37}$$

$$|\Psi^J_{\text{out}}\rangle = \sum_f c_f|\psi^J_f\rangle \tag{2.38}$$

where $\sum_i |c_i|^2 = 1$ and $\sum_f |c_f|^2 = 1$ to ensure the wavefunctions are properly normalised.

It is useful to define the transition operator, $\hat{T}$, as $\hat{1} - \hat{S}$, as this is more directly related to properties that can be observed experimentally:

$$\begin{aligned} \hat{T}|\Psi_{\text{in}}\rangle &= (\hat{1} - \hat{S})|\Psi_{\text{in}}\rangle \\ &= |\Psi_{\text{in}}\rangle - |\Psi_{\text{out}}\rangle \end{aligned} \tag{2.39}$$

The probability for scattering from an initial state $|\psi_i^J\rangle$ to final state $|\psi_f^J\rangle$ for a given value of J is then given by $|T_{if}^J|^2$ [23, 181]. This is simply equivalent to the opacity function, $P_{if}(J)$, from which the observable properties of interest can be calculated. For example, the integral cross-section can be found *via* [23, 181]:

$$\sigma^{(0)} = \frac{\pi}{k_i^2} \sum_J \frac{2J+1}{2j+1} [2\min(J, j') + 1] P_{if}(J) \tag{2.40}$$

where $k_i = p/\hbar$ is the initial wavevector and the sum is over all partial waves. Although this sum is infinite, there is some maximum J above which the opacity function falls to 0, allowing the cross-sections to be converged. It should also be noted that it is possible to converge the elastic cross-sections in the QM calculations.

2.4 Observable properties

In the chapters that follow, the measurements recorded experimentally will be compared with those obtained theoretically using either QM or QCT calculations. In this section, the methods for obtaining the observable properties from either the $\hat{S}$ matrix or trajectories will be outlined.

2.4.1 Integral cross-sections

For inelastic scattering between an atom and diatom, the integral cross-section can be considered to be the effective target area in which the atom and diatom have to collide in order to bring about a transition from an initial state to a final state. This can be calculated *via* [1, 139]:

$$\begin{aligned} \sigma^{(0)} &= \int_0^{2\pi} \int_0^{b_{\max}} P(b) b \mathrm{d}b \mathrm{d}\phi \\ &= \int_0^{b_{\max}} P(b) 2\pi b \mathrm{d}b \end{aligned} \tag{2.41}$$

where b is the impact parameter, defined as the distance of closest approach between the atom and diatom in the absence of a potential, and $P(b)$ is the opacity function, which gives the probability of the scattering between the two states occurring at b. In the simplest case, where $P(b) = 1$ for $b \leq b_{\max}$, the resulting cross-section is:

$$\sigma^{(0)} = \pi b_{\max}^2 \tag{2.42}$$

As discussed above, the integral cross-sections can be calculated from the QCT calculations using equation (2.35), and from the QM calculations using equation (2.40).

In the present work rate constants are measured, as opposed to the cross-sections directly. The two quantities are linked, at a fixed collision energy, *via* $k^{(0)}{=}\sigma^{(0)} v_{\mathrm{rel}}$, where v_{rel} is the relative velocity. Therefore, the rate constants effectively correspond to the number of collisions that occur in a cylinder with a cross-section of $\sigma^{(0)}$ and length v_{rel} in a second. However, the results are presented as cross-sections as these provide more insight into the mechanisms under consideration, and make comparisons between different systems easier to interpret.

2.4.2 Differential cross-sections

The differential cross-section (DCS) gives the dependence of the integral cross-section discussed above on the scattering angle, and can be written as:

$$\frac{\mathrm{d}\sigma^{(0)}}{\mathrm{d}\omega_{kk'}} = \frac{1}{4\pi}\frac{1}{\sin\theta_{kk'}}\frac{\mathrm{d}^2\sigma^{(0)}}{\mathrm{d}\theta_{kk'}\mathrm{d}\phi_{kk'}} \tag{2.43}$$

where $\mathrm{d}\omega_{kk'} = \sin\theta_{kk'}\mathrm{d}\theta_{kk'}\mathrm{d}\phi_{kk'}$. The differential cross-section can be considered to be the cross-section associated with scattering through an angle $\theta_{kk'} + \mathrm{d}\theta_{kk'}$, $\phi_{kk'} + \mathrm{d}\phi_{kk'}$. It follows that the total integral cross-section can be obtained by integrating over the surface of a sphere, which corresponds to all the directions that scattering can occur through [1, 139]:

$$\sigma^{(0)} = \int_0^{2\pi}\int_0^{\pi}\frac{\mathrm{d}\sigma^{(0)}}{\mathrm{d}\omega_{kk'}}\sin\theta_{kk'}\mathrm{d}\theta_{kk'}\mathrm{d}\phi_{kk'} \tag{2.44}$$

As the scattering process is cylindrically symmetric about the direction of the initial velocity, $\boldsymbol{k}$, the DCS is independent of the azimuthal scattering angle, $\phi_{kk'}$, and is only dependent on $\theta_{kk'}$.

The DCS can be obtained for a given N to N' transition from the QCT calculations by histogram binning the trajectories into bins of width $\Delta\cos\theta_{kk'}$ *via* [23, 139]:

$$\frac{\mathrm{d}\sigma^{(0)}_{NN'}}{\mathrm{d}\omega_{kk'}} = \frac{\mathcal{N}_{NN'}(\theta_{kk'})}{\mathcal{N}_{\mathrm{tot}}}\frac{\pi b^2_{\mathrm{max}}}{2\pi\Delta\cos\theta_{kk'}} \tag{2.45}$$

where $\mathcal{N}_{NN'}(\theta_{kk'})$ is the number of trajectories for a given N to N' transition that are scattered through the angle range between $\cos\theta_{kk'}$ and $\cos\theta_{kk'} + \Delta\cos\theta_{kk'}$. A very large number of trajectories are required to obtain a smooth DCS with a sufficiently good angular resolution using this method. Instead, it is possible to describe the distribution using a Legendre polynomial expansion, as introduced in section 2.2.2:

$$\frac{\mathrm{d}\sigma^{(0)}_{NN'}}{\mathrm{d}\omega_{kk'}} = \frac{\sigma^{(0)}_{NN'}}{4\pi}\sum_k [k]a^{(k)}(k,k')P_k(\cos\theta_{kk'}) \tag{2.46}$$

where $P_k(\cos\theta_{kk'})$ is the k^{th} Legendre polynomial, and the expansion coefficients are the expectation values of the associated Legendre moments. These can be calculated from the QCT calculations using:

$$a^{(k)}(k,k') = \frac{1}{\mathcal{N}_{NN'}} \sum_{i=0}^{\mathcal{N}_{NN'}} P_k(\cos\theta^i_{kk'}) \tag{2.47}$$

where $\theta^i_{kk'}$ is the scattering angle for the i^{th} trajectory that is scattered from state N to state N'.

Quantum mechanically, the DCS for scattering from an initial state $|\psi_i\rangle$ to a final state $|\psi_f\rangle$ can be determined from the $\hat{T^J_{if}}$ matrix elements discussed previously using [23, 181]:

$$\begin{aligned}\frac{\mathrm{d}\sigma^{(0)}_{if}}{\mathrm{d}\omega_{kk'}} &= \frac{1}{4k_i^2}\sum_{JJ'}\frac{2J+1}{2j+1}\frac{2J'+1}{2j+1}[2\mathrm{min}(J,j)+1] \\ &\times [2\mathrm{min}(J',j)+1]T^J_{if}T^{J'\star}_{if}P_J\cos(\theta_{kk'})P_{J'}(\cos\theta_{kk'})\end{aligned} \tag{2.48}$$

It should be noted that the double summation over J and J' in this expression leads to the possibility of interference between different partial waves. This can give rise to oscillatory structure in the DCS.

2.4.3 Depolarisation cross-sections

The DCSs discussed in the previous section provide a measure of the $\boldsymbol{k}$-$\boldsymbol{k}'$ correlation. It is also possible to consider the correlation between the initial and final rotational angular momentum of the diatom (the $\boldsymbol{j}$-$\boldsymbol{j}'$ correlation).

In the same way that it was possible to obtain the DCS from the QCT calculations by histogram binning the value of $\theta_{kk'}$ as in equation (2.45), the $\boldsymbol{j}$-$\boldsymbol{j}'$ correlation could be obtained by binning trajectories using the value of $\theta_{jj'}$. However, it would again be more appropriate to consider a Legendre polynomial expansion. As discussed in section 2.2.2, the (probability) distribution of the direction of $\boldsymbol{j}'$ with respect to $\boldsymbol{j}$ following a collision

can be written as:

$$\begin{aligned} P(\theta_{jj'}) &= \frac{2\pi}{\sigma^{(0)}}\frac{\mathrm{d}\sigma^{(0)}}{\mathrm{d}\omega_{jj'}} \\ &= \frac{1}{2}\sum_k [k] a^{(k)} P_k(\cos\theta_{jj'}) \end{aligned} \tag{2.49}$$

where $a^{(k)}$ are the depolarisation moments which are again simply given by the expectation values of the associated Legendre moments.

It is the depolarisation cross-sections ($\sigma^{(k)}$) that are considered in chapters 3 and 4. These can be calculated from the integral cross-sections and depolarisation moments discussed above *via* [104, 109, 111, 116]:

$$\sigma^{(k)} = \sigma^{(0)}(1 - a^{(k)}) \tag{2.50}$$

As previously mentioned, the depolarisation moments can take negative values, and therefore the depolarisation cross-section can be larger than the collision cross-section.

The depolarisation cross-section for a given N to N' transition can be calculated from the QCT calculations as:

$$\sigma^{(k)}_{NN'} = \frac{\mathcal{N}_{NN'}}{\mathcal{N}_{\mathrm{tot}}}\pi b^2_{\mathrm{max}}\left(1 - \frac{1}{\mathcal{N}_{NN'}}\sum_i P_k(\cos\theta^i_{NN'})\right) \tag{2.51}$$

These cross-sections reflect the extent to which collisions cause depolarisation. Therefore if the direction of $\boldsymbol{j}$ is not changed by the collision, the depolarisation cross-section is zero (as $a^{(k)}$=1). It is also possible to define the tensor cross-section, which reflects the amount of polarisation that remains after the collision. The tensor cross-section ($\sigma^{(k)}_{\mathrm{T}}$) can be calculated *via*:

$$\sigma^{(k)}_{\mathrm{T}} = a^{(k)}\sigma^{(0)} = \sigma^{(0)} - \sigma^{(k)} \tag{2.52}$$

Therefore, if $a^{(k)}$=1 the tensor cross-section has the same value as the integral cross-section (as all the polarisation is transferred), but if the collision causes complete depolarisation

so that $a^{(k)}$=0, then the corresponding tensor cross-section is also zero.

The tensor cross-sections for scattering from the initial state j to final state j' can be found quantum mechanically using [111, 182–186]:

$$\sigma_{\mathrm{T}}^{(k)} = \frac{\pi}{k_i^2} \sum_{JJ'} \sum \ell\ell'(-1)^{\ell-\ell'-j-j'-2J} \begin{Bmatrix} j & j & k \\ J & J' & \ell \end{Bmatrix} \begin{Bmatrix} j' & j' & k \\ J & J' & \ell' \end{Bmatrix} T^{J}_{j\ell j'\ell'} T^{J'\star}_{j\ell j'\ell'} \qquad (2.53)$$

where ℓ is the initial orbital angular momentum, and ℓ' the final orbital angular momentum. There is a double summation over J and J', as seen in equation (2.48) for the DCS, meaning that it is again possible for interference to occur between different partial waves.

2.5 Tensor opacity formalism

As discussed in section 2.3.2, the QCT calculations are inherently closed shell, and contain no concept of spin. However, both NO and OH are open shell radicals. For Σ radicals (*i.e.* OH(A) and NO(A)), the spin can be factored in using the tensor opacity formalism, as will be discussed in this section. This allows quasi-open shell properties of the system to be determined from the QCT calculations, which can then be compared with results obtained experimentally, as will be considered in chapter 4.

The tensor opacities ($P^K(N, N')$) are independent of spin, and contain all the dynamical information for the system. They can, therefore, be obtained by considering the results from both classical and quantum mechanical closed shell theoretical calculations. It should be emphasised that the methods described in this section are only applicable to the Σ radicals under consideration here. For OH(A) and NO(A), the direction of the electron and nuclear spin cannot be changed by the collision, as the potential is electrostatic in origin, and therefore the spin can be treated as spectators to the collision [183]. The same formalism cannot be used for NO(X $^2\Pi$), as the electron and nuclear spin have a fixed projection on the intermolecular axis, as discussed in section 2.1.1, and consequently cannot be considered to be spectators to the collision.

Quantum mechanically, the tensor opacities are defined as [175, 182, 183, 185]:

$$P^K(N, N') = \frac{1}{[K]} \sum_{\ell\ell'} |\langle N'\ell' || T^K || N\ell \rangle|^2 \tag{2.54}$$

where ℓ and ℓ' are the initial and final orbital angular momentum respectively, and the reduced $\hat{T}$ matrix elements have been defined in references [182], [183] and [185]. The open shell rotational energy transfer (RET) cross-sections ($\sigma^{(0)}_{jj'}$) can then be calculated using [182, 183, 187, 188]:

$$\sigma^{(0)}_{jj'} = \frac{\pi}{k_i^2}[j'] \sum_K \begin{Bmatrix} N' & N & K \\ j' & j & S \end{Bmatrix}^2 P^K(N, N') \tag{2.55}$$

In the closed shell (classical) case, when $N = j$ and $S = 0$, this expression reduces to [175]:

$$\sigma^{(0)}_{NN'} = \frac{\pi}{k_i^2} \sum_K \frac{P^K(N, N')}{[N]} = \sum_K \sigma^{(0)}_{NN'}(K) \tag{2.56}$$

where $\sigma^{(0)}_{NN'}(K)$ is the cross-section for a given N to N' transition where an angular momentum of K is transferred. Therefore, the tensor opacities can be calculated classically using:

$$P^K(N, N') = \frac{k_i^2}{\pi}[N]\sigma^{(0)}_{NN'}(K) \tag{2.57}$$

It follows that the tensor opacity can be considered to be proportional to the probability that an angular momentum of magnitude K, is transferred in a collision from an initial state N to final state N'. Substituting equation (2.57) into equation (2.55) yields:

$$\sigma^{(0)}_{jj'} = [j'][N] \sum_K \begin{Bmatrix} N' & N & K \\ j' & j & S \end{Bmatrix}^2 \sigma^{(0)}_{NN'}(K) \tag{2.58}$$

In the limit where the electron and nuclear spin are spectators to the collision, the transferred angular momentum, $\boldsymbol{K}$, reflects the extent to which the direction of $\boldsymbol{N}$ is changed by the collision *i.e.* $\boldsymbol{K} = \boldsymbol{N'} - \boldsymbol{N}$. Therefore, the modulus of $\boldsymbol{K}$ can be calculated

via:

$$|\boldsymbol{K}|^2 = |\boldsymbol{N}|^2 + |\boldsymbol{N'}|^2 - 2|\boldsymbol{N}||\boldsymbol{N'}|\cos\theta_{NN'} \tag{2.59}$$

where

$$\cos\theta_{NN'} = \frac{\boldsymbol{N}\cdot\boldsymbol{N'}}{|\boldsymbol{N}||\boldsymbol{N'}|} \tag{2.60}$$

The value of K can then be obtained by using the semi classical quantisation rule $|\boldsymbol{K}| = \hbar\sqrt{K(K+1)}$, as used previously to determine the value of N' in the QCT calculations.

By analogy with equation (2.35), $\sigma^{(0)}_{NN'}(K)$ can be obtained using the QCT calculations *via*:

$$\begin{aligned}\sigma^{(0)}_{NN'}(K) &= \frac{\mathcal{N}_{NN'}(K)}{\mathcal{N}_{\text{tot}}}\pi b^2_{\text{max}} \\ &= \frac{\mathcal{N}_{NN'}(K)}{\mathcal{N}_{NN'}}\sigma^{(0)}_{NN'}\end{aligned} \tag{2.61}$$

where $\mathcal{N}_{NN'}(K)$ is the number of trajectories for a given N to N' transition, where the magnitude of the change in rotational angular momentum is K. Therefore, once these cross-sections have been determined from the QCT calculations, they can be combined with equation (2.58) to obtain quasi-open shell RET cross-sections. It is also possible to determine quasi-open shell depolarisation moments, which can be written as [118, 175]:

$$a^{(k)} = (-1)^{k-j-j'}[j]^{\frac{1}{2}}[j']^{\frac{1}{2}}\frac{\sum_K (-1)^K \begin{Bmatrix} j & j & k \\ j' & j' & K \end{Bmatrix}\begin{Bmatrix} N & N' & K \\ j' & j & S \end{Bmatrix}^2 \sigma^{(0)}_{NN'}(K)}{\sum_K \begin{Bmatrix} N & N' & K \\ j' & j & S \end{Bmatrix}^2 \sigma^{(0)}_{NN'}(K)} \tag{2.62}$$

As the nuclear spin can also be treated as a spectator to the collision, this can be treated in the same way [184]. The equivalent expressions for these hyperfine state resolved cross-sections and depolarisation moments can be found in reference [175].

For the Σ radicals considered in this study, the main focus is the determination of the depolarisation cross-sections, as discussed in section 2.4.3. In the closed shell case, the

quantum mechanical expression for the depolarisation cross-section for a given N to N' transition ($\sigma^{(k)}_{NN'}$) can be written as [118, 175]:

$$\sigma^{(k)}_{NN'} = \sum_{K>0} \sigma_{NN'}(K) \left(1 - (-1)^{k-K-N-N'} [N]^{\frac{1}{2}} [N']^{\frac{1}{2}} \begin{Bmatrix} N & N & k \\ N' & N' & K \end{Bmatrix} \right) \tag{2.63}$$

where $\{\cdots\}$ is a 6-j symbol [102]. The K=0 term is not included, as this corresponds to pure elastic scattering where ΔK=ΔN=0, meaning that the direction of $\boldsymbol{N}$ does not change. It therefore does not contribute to the depolarisation cross-section. This also means that it is possible to calculate the elastic depolarisation cross-sections from the QCT calculations, as the only contribution that cannot be converged is that where ΔK=ΔN=0. This is because it is possible to define a value of $b_{\max}$ above which no angular momentum transfer occurs, *i.e.* there are only trajectories with $K < 0.5$.

Using the Racah formula [165, 189], valid when N, N', $K \gg k$ it can be shown that:

$$\begin{Bmatrix} N & N & k \\ N' & N' & K \end{Bmatrix} \sim \frac{(-1)^{k+K+N+N'}}{[N]^{\frac{1}{2}} [N']^{\frac{1}{2}}} P_k(\cos\theta_{NN'}) \tag{2.64}$$

Using the above two expressions gives:

$$\sigma^{(k)}_{NN'} = \sum_{K>0} \sigma^{(0)}_{NN'}(K)[1 - P_k(\cos\theta_{NN'})] \tag{2.65}$$

Substituting equation (2.61) into the above expression yields:

$$\sigma^{(k)}_{NN'} = \sigma^{(0)}_{NN'} \left[1 - \frac{1}{\mathcal{N}_{NN'}} \sum_{K>0} \mathcal{N}_{NN'}(K) P_k(\cos\theta_{NN'}) \right] \tag{2.66}$$

which is the same as equation (2.51). In the limit where $\boldsymbol{N}$ and $\boldsymbol{N'}$ have definite values, there then exists a one to one correspondence between $\boldsymbol{K}$ (and therefore K) and $\cos\theta_{NN'}$

[118]. Considering this correspondence produces the expression:

$$\sigma^{(k)}_{NN'} = \sigma^{(0)}_{NN'}[1 - \langle P_k(\cos\theta_{NN'})\rangle] \tag{2.67}$$

where $\langle P_k(\cos\theta_{NN'})\rangle = a^{(k)}$, and therefore this is simply the same as equation (2.50). The open shell depolarisation cross-sections, $\sigma^{(k)}_{jj'}$, can consequently be obtained by substituting equations (2.58) and (2.62) into equation (2.67).

2.6 Summary

In this chapter the theoretical framework that underpins the rest of the work discussed in the subsequent chapters has been presented. In sections 2.1.1 and 2.1.2 Hund's case (a) and Hund's case (b) were discussed, which characterise the angular momentum coupling in the electronic ground and excited states of NO and OH. The concept of rotational angular momentum polarisation was introduced in section 2.2.1, before the methods for describing these distributions were presented in the following section. In section 2.3, both the quasi-classical trajectory and quantum mechanical methods employed throughout the present study were discussed, alongside the potential energy surfaces that were used for the calculations. A description of the methods used to obtain the experimentally observable properties from the results of these calculations was then presented in section 2.4, before the tensor opacity formalism was discussed. The results from both the quasi-classical trajectory and quantum mechanical calculations will be compared with those obtained experimentally in chapters 4 and 6, and also used to discuss vector correlations in chapter 5.

Chapter 3

Collisional depolarisation: Experimental methods

The inelastic scattering of the NO and OH radicals with rare gases has been the subject of many previous studies. Both radicals are considered to be a prototype for studying collisions of open shell species [29]. Earlier studies tended to focus on scalar properties, for example, there has been considerable interest in the rotational energy transfer (RET) cross-sections in both the ground [72, 97–100, 168, 190–197] and first electronically excited state [108, 198–205]. More recently, attention has turned to considering the vector correlations that describe the collision dynamics, and the additional information that can be obtained from these.

Studies of the correlation between the initial rotational angular momentum, $\boldsymbol{j}$, and final rotational angular momentum, $\boldsymbol{j}'$, can provide a fundamental insight into the dynamics that govern both elastic and inelastic scattering. This collisional depolarisation of the rotational angular momentum of simple open shell molecules with a range of collision partners has been the focus of many recent studies [104–106, 108–122, 124, 131–134, 175, 206, 207]. Here, the collisional depolarisation of NO(A) and OH(A) with krypton will be considered. As previously for NO(A)-He and NO(A)-Ar [109], OH(A)-Ar [108, 116, 119] and OH(A)-H_2O [115], the rates of collisional depolarisation for the two radicals with krypton will be determined using quantum beat spectroscopy [208–210].

In this chapter, the experimental methods employed for recording the Zeeman and hyperfine quantum beat data for NO(A)-Kr and OH(A)-Kr are presented, and the analysis used to obtain the depolarisation cross-sections from the data is discussed. The methods used to obtain the RET and electronic quenching cross-sections for OH(A)-Kr are also described. In the final section, the simulations of the experiment performed using the quasi-classical trajectory calculations are presented, with a particular emphasis on the further insight they provide into the results obtained experimentally.

3.1 Creating polarised distributions

Consider an isotropic distribution of closed shell molecules which absorb a photon of polarised light, which results in excitation from the $|j''m''\rangle$ level in the ground electronic state, to the $|jm\rangle$ level in an excited electronic state. Following the absorption of the light, the laboratory (LAB) frame distribution of the rotational angular momentum, $\boldsymbol{j}$, can be written as [85, 211–213]:

$$P(\Theta_j, \Phi_j) = N\,[j] \sum_{m''} \begin{pmatrix} j'' & 1 & j \\ m'' & q & -m \end{pmatrix}^2 |D^j_{mj}(\Phi_j, \Theta_j, \chi_j)|^2 \tag{3.1}$$

where N is a normalisation constant, $(\cdots)$ is a 3-j symbol [102] and $[j] = 2j + 1$. The angles Θ_j and Φ_j define the direction of the minimum uncertainty state (as discussed in section 2.2.2 and references [161, 164]), which in the high j limit corresponds to the direction of $\boldsymbol{j}$ with respect to the polarisation of the laser, $\boldsymbol{\varepsilon}$. χ_j defines the phase of the rotation and $D^j_{mj}(\Phi_j, \Theta_j, \chi_j)$ is a Wigner rotation matrix element, as defined in reference [102]. When linearly polarised light is used for the excitation, q=0, and the resulting distribution in the high j limit can be written as [138]:

$$P(\Theta_j, \Phi_j) = \frac{1}{2}\left[1 + 5A^{(2)}P_2(\cos\Theta_j)\right] \tag{3.2}$$

where $P_2(\cos\Theta_j)$ is the 2nd order Legendre polynomial, and $A^{(2)}$ is an extrinsic polarisation parameter that reflects the magnitude of the alignment initially created in the sample by the absorption of the light. This depends on both j and the excitation branch used [214, 215]. When circularly polarised light is used to create the polarised ensemble, q=±1. The distribution for $\boldsymbol{j}$ in the high j limit can be written as [138]:

$$P(\Theta_j, \Phi_j) = \frac{1}{2}\left[1 + 3A^{(1)}P_1(\cos\Theta_j) + 5A^{(2)}P_2(\cos\Theta_j)\right] \tag{3.3}$$

Here, the k=1 term corresponds to the distribution of $\boldsymbol{j}$ being oriented. It should be noted that whilst it is possible to create a sample in the excited electronic state that is purely aligned through the absorption of linearly polarised light, the absorption of circularly polarised light results in the excited state distribution of $\boldsymbol{j}$ being both oriented and aligned. Therefore, when making the orientation measurements, the experimental geometry is chosen such that the aligned component of the distribution does not contribute.

3.1.1 The effect of collisions

When the polarised sample considered above undergoes a collision, the interaction may result in the loss of the initially prepared polarisation. The distribution of the final rotational angular momentum, $\boldsymbol{j}'$, with respect to $\boldsymbol{j}$ can be written as:

$$P(\theta_{jj'}, \phi_{jj'}) = \frac{1}{4\pi}\sum_k [k] a^{(k)} C_{k0}(\theta_{jj'}, \phi_{jj'})^\star \tag{3.4}$$

where $C_{k0}(\theta_{jj'}, \phi_{jj'})$ is a modified spherical harmonic. As the $\boldsymbol{j}$-$\boldsymbol{j}'$ distribution is cylindrically symmetric, q has been set to zero. The case where the distribution is not cylindrically symmetric is considered in section 5.7. As q=0, this expansion can simply be rewritten in

terms of Legendre polynomials, as discussed in section 2.2.2:

$$\begin{aligned} P(\theta_{jj'}) &= 2\pi P(\theta_{jj'}, \phi_{jj'}) \\ &= \frac{1}{2}\sum_k a^{(k)} P_k(\cos\theta_{jj'}) \end{aligned} \tag{3.5}$$

where the $a^{(k)}$ expansion coefficients (referred to as the depolarisation moments) reflect the extent to which the direction of $\boldsymbol{j}$ is changed by the collision. These are simply given as the expectation values of the associated Legendre moments, *i.e.* $a^{(k)} = \langle P_k(\cos\theta_{jj'})\rangle$.

To obtain the LAB frame distribution of $\boldsymbol{j'}$ after a single collision, the initially polarised distribution of $\boldsymbol{j}$ has to be convoluted by the extent to which the collision changes the direction of $\boldsymbol{j}$. It follows that the LAB frame distribution of $\boldsymbol{j'}$ after a single collision can be written as [119, 175]:

$$P(\Theta_{j'}, \Phi_{j'}) = \int_0^{2\pi}\int_0^{\pi} P(\Theta_j, \Phi_j) P(\theta_{jj'}, \phi_{jj'}) \mathrm{d}\Theta_j \mathrm{d}\Phi_j \tag{3.6}$$

Using the spherical harmonic addition theorem [102] yields the result:

$$P(\Theta_{j'}, \Phi_{j'}) = \frac{1}{4\pi}\sum_{kq} [k] a^{(k)} A^{(k)} C_{kq}(\Theta_{j'}, \Phi_{j'})^{\star} \tag{3.7}$$

In the case where the initially polarised distribution is created with circularly polarised light, the above reduces to:

$$P(\Theta_{j'}) = \frac{1}{2}\left[1 + 3a^{(1)}A^{(1)}P_1\cos(\Theta_{j'}) + 5a^{(2)}A^{(2)}P_2(\cos\Theta_{j'})\right] \tag{3.8}$$

It follows that the polarisation moments after a collision, $\mathcal{P}^{(k)}$, can be related to the initial polarisation of the distribution and the depolarisation moment *via*:

$$\mathcal{P}^{(k)} = a^{(k)} A^{(k)} \tag{3.9}$$

It is the rate at which collisions destroy the initially polarised distribution of $\boldsymbol{j}$ that is of interest in this and the following chapter. This reflects the magnitude of $a^{(k)}$, which provides insight into the $\boldsymbol{j}$-$\boldsymbol{j}'$ correlation.

3.2 Quantum beat spectroscopy

Quantum beat spectroscopy involves the coherent excitation of at least two closely-spaced energy levels in an atom or molecule. The quantum beat is observed as an oscillation of intensity over time in the resultant fluorescence decay. This phenomenon can be modelled by considering a simple four level system, as shown in figure 3.1 [208]. At t=0, the

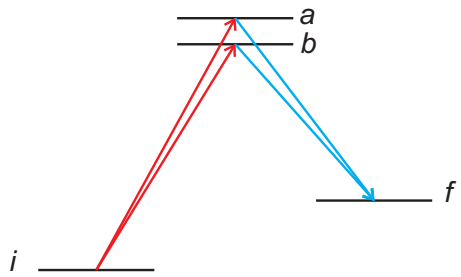


Figure 3.1: The four level system used to model the coherent superposition of states that produces quantum beats.

wavefunction of the excited state can be written as:

$$|\Psi(0)\rangle = c_a|\psi_a\rangle + c_b|\psi_b\rangle \tag{3.10}$$

The time evolution of the wavefunction can be obtained by solving the Schrödinger equation, the solution of which for an eigenstate $|\psi_n\rangle$ is given by:

$$|\psi_n\rangle = |\psi_n(0)\rangle \mathrm{e}^{-i\omega_n t} \tag{3.11}$$

It follows that:

$$|\Psi(t)\rangle = c_a|\psi_a\rangle \mathrm{e}^{-i\omega_a t} + c_b|\psi_b\rangle \mathrm{e}^{-i\omega_b t} \tag{3.12}$$

If the excitation light intensity is constant over the energy range that encompasses $|\psi_a\rangle$ and $|\psi_b\rangle$, then the associated coefficients are proportional to the transition dipole matrix elements *i.e.* $c_n \propto \langle\psi_n|\hat{\boldsymbol{\mu}}|\psi_i\rangle = \mu_{ni}$. It is also necessary to introduce a phenomenological rate constant, γ_n, to account for the decay of population of the excited state as fluorescence is emitted. Therefore the total wavefunction can now be written as:

$$|\Psi(t)\rangle \propto \mu_{ai}|\psi_a\rangle \mathrm{e}^{-i(\omega_a+\gamma_a/2)t} + \mu_{bi}|\psi_b\rangle \mathrm{e}^{-i(\omega_b+\gamma_b/2)t} \tag{3.13}$$

The intensity of fluorescence observed from the two states if they fluoresce to state $|\psi_f\rangle$ is simply proportional to $|\langle\psi_f|\hat{\boldsymbol{\mu}}|\Psi(t)\rangle|^2$. Therefore:

$$\begin{aligned} I(t) &\propto |\mu_{ai}|^2|\mu_{fa}|^2 \mathrm{e}^{-\gamma_a t} + |\mu_{bi}|^2|\mu_{fb}|^2 \mathrm{e}^{-\gamma_b t} \\ &+ |\mu_{ai}\mu_{bi}\mu_{af}\mu_{bf}| \mathrm{e}^{-((\gamma_a+\gamma_b)t)/2} \cos(\omega_{ab}t + \phi) \end{aligned} \tag{3.14}$$

where the substitutions $\langle\psi_f|\hat{\boldsymbol{\mu}}|\psi_n\rangle = \mu_{fn}$ and $\omega_{ab} = |\omega_a - \omega_b|$ have also been made. The first two terms in equation (3.14) account for the decay of population of states $|\psi_a\rangle$ and $|\psi_b\rangle$ respectively. It is the last term that accounts for the coherence between the two states which gives rise to the quantum beat which has a frequency ω_{ab}. The factor of ϕ which has also been introduced accounts for the phase at the start of the quantum beat.

Assuming that the transition moments and fluorescence rates are the same for both coherently excited states, equation (3.14) simplifies to:

$$I(t) \propto \left[1 + \cos(\omega_{ab}t + \phi)\right] \mathrm{e}^{-\gamma t} \tag{3.15}$$

In this expression, the amplitude of the quantum beat is the same as the amplitude of the fluorescence decay. This is often not the case, and another factor is introduced to reduce the beat amplitude.

$$I(t) \propto \left[1 + A^{(k)} \cos(\omega_{ab}t + \phi)\right] \mathrm{e}^{-\gamma t} \tag{3.16}$$

As discussed above, $A^{(k)}$ indicates the magnitude of the polarisation created in the OH(A) or NO(A) radical. Therefore the extent to which the distribution of $\boldsymbol{j}$ is polarised is reflected in the beat amplitude. As this polarisation is lost through collisions the magnitude of the quantum beat decreases, with the rate reflecting the extent to which collisions cause depolarisation. This loss of polarisation is measured using either Zeeman quantum beats or hyperfine quantum beats, each of which will now be considered in turn.

3.2.1 Zeeman quantum beats

The interaction energy of a magnetic dipole with a magnetic field is given by [102]:

$$E = -\boldsymbol{\mu} \cdot \boldsymbol{B} \tag{3.17}$$

In the case of NO(A) and OH(A), the main contribution to the magnetic dipole arises from the electron spin, $\boldsymbol{S}$, as there is no orbital angular momentum. The magnetic dipole is therefore given by:

$$|\boldsymbol{\mu}_\mathrm{e}| = -g_\mathrm{e}\mu_\mathrm{B}\sqrt{S(S+1)} \tag{3.18}$$

where g_e is the Landé g value for the electron (≈ 2.002) and μ_B is the bohr magneton. As discussed in section 2.1.2, the angular momentum coupling in NO(A) and OH(A) is best described by Hund's case (b). Therefore, $\boldsymbol{S}$ couples to $\boldsymbol{N}$ to give $\boldsymbol{j}$. It follows that the time averaged magnetic moment is then directed along $\boldsymbol{j}$. The projection of this onto the magnetic field axis is then given by:

$$\mu_j = \mu_\mathrm{B} g_j m_j \tag{3.19}$$

where

$$g_j = g_\mathrm{e}\frac{j(j+1) + S(S+1) - N(N+1)}{2j(j+1)} \tag{3.20}$$

In the Hund's case (b) framework, $\boldsymbol{j}$ then couples to the nuclear spin $\boldsymbol{I}$ through the hyperfine interaction. Therefore the time averaged magnetic moment is then directed

along $\boldsymbol{F}$, the total angular momentum for the radical. It follows that the final projection of the magnetic dipole moment onto the field axis is given by:

$$\mu_F = \mu_B g_F m_F \tag{3.21}$$

where

$$g_F = g_j \frac{F(F+1) + j(j+1) - I(I+1)}{2F(F+1)} \tag{3.22}$$

In the applied magnetic field, the $2F+1$ Zeeman levels associated with a single hyperfine level are no longer degenerate. The energy of this Zeeman splitting can be obtained by substituting the above expression into equation (3.17):

$$E = -g_F \mu_B m_F B \tag{3.23}$$

The applied magnetic field also causes the angular momentum to precess around the field direction. When circularly polarised light is used, which creates an oriented distribution, the magnetic quantum number selection rule is, Δm_F=1 [138]. It follows that the precession frequency is given by:

$$\omega_{L_F} = \frac{\Delta E}{\hbar} = \frac{g_F \mu_B B}{\hbar} \tag{3.24}$$

For an initially aligned sample which is created by absorption of linearly polarised light, Δm_F=2 [138]. It follows that the frequency is given by [216–219]:

$$\omega_{L_F} = \frac{2 g_F \mu_B B}{\hbar} \tag{3.25}$$

Therefore, the frequency at which an initially aligned sample precesses is double that at which an initially oriented sample precesses. This reflects the fact that an aligned distribution (which can be considered as a double headed arrow) requires a 180° rotation before the original distribution is recovered, whereas an oriented distribution (a single

headed arrow) needs to be rotated by 360°.

3.2.2 Hyperfine quantum beats

When the hyperfine energy level splitting is sufficiently small allowing the levels to be coherently excited, it is possible to observe a quantum beat in the absence of an applied magnetic field. The polarisation initially created in $\boldsymbol{j}$ cycles between $\boldsymbol{j}$ and $\boldsymbol{I}$ due to the coupling between the two vectors discussed in section 2.1.2. The time dependence of the polarisation of $\boldsymbol{j}$ is given by [220]:

$$A^{(k)}(t) = G^{(k)}(t)\, A^{(k)}(0) \tag{3.26}$$

where [220]:

$$G^{(k)}(t) = \sum_{FF'} \frac{(2F+1)(2F'+1)}{(2I+1)} \begin{Bmatrix} F' & F & k \\ j & j & I \end{Bmatrix}^2 \cos\left[\frac{(E_F - E_{F'})t}{\hbar}\right] \tag{3.27}$$

where E_F are the energies of the hyperfine levels. It follows that the beat amplitude will be largest when j and I are of similar magnitudes, as the polarisation can be completely transferred between $\boldsymbol{j}$ and $\boldsymbol{I}$.

3.3 Experimental setup

3.3.1 Lasers

For the NO(A)-Kr experiments, the probe laser was a Scanmate tunable dye laser pumped with the third harmonic of an Nd:YAG pulsed laser (corresponding to 355 nm). The dye used was Coumarin 2 in methanol, which lases around 452 nm, which was then frequency doubled to wavelengths in the region of 226 nm. The wavelength could then be tuned to the NO(A $\leftarrow$ X) rovibrational transition of interest. In this study, the f_2 spin-rotation level of N=2, 5, 7, 9 and 14 was excited using the S_{21} and R_{22} branches.

An ArF excimer (Lambda Physik EMG MSC 103) was used to photolyse H_2O_2 at a wavelength of 193 nm to produce translationally excited OH(X) radicals [221–223]. After a time delay of 250 ns for the superthermal measurements and 9 μs for the thermal measurements these were then excited using an LPD3000 tunable dye laser, which was pumped using the second harmonic of an Nd:YAG pulsed laser (corresponding to 532 nm). The dye used was Rhodamine b in methanol, which lases in the region of 590 nm-620 nm. This is frequency doubled and tuned to the OH(A $\leftarrow$ X) transition of interest. For the total depolarisation measurements, OH(A) was produced using $R_{22}(1)$, $R_{22}(4)$, $R_{22}(7)$ and $R_{11}(13)$ excitation.

Before entering the chamber, the laser was passed through a Glan-Taylor polariser to improve the polarisation of light, which was determined to be better than 95% on exiting the chamber. A photoelastic modulator (PEM) was used to flip the polarisation of the laser on alternate shots, between horizontal and vertical linear polarisation for the alignment measurements, and between left and right circularly polarised light for the orientation measurements.

The power of the dye lasers used to excite the OH(X) and NO(X) was determined to be below 100 μJ at the entrance of the chamber. In both cases, the bandwidth of the laser is sufficient to coherently excite the Zeeman sub levels of a given hyperfine level, which are non-degenerate in the applied magnetic field. For NO(A), the hyperfine levels at low N are closely spaced, and therefore can also be coherently excited, allowing hyperfine beats to be observed.

3.3.2 Chamber

The vacuum chamber was pumped by a rotary vane pump, which achieved pressures of the order of 0.1 mTorr. For the NO(A)-Kr experiments, a flow of <1 mTorr of NO was maintained through the chamber, and the maximum pressure of krypton used was approximately 700 mTorr. For the OH(A)-Kr experiments, a flow of <2 mTorr of a 50:50 H_2O_2:H_2O was mixture was used, and photolysed to produce OH(X) radicals. A time delay

of 250 ns between the pump and probe lasers was used for the superthermal measurements, and a maximum quencher gas pressure of 400 mTorr, to minimise the effects of translational cooling. For the thermal measurements, the time delay between the pump and probe lasers was set to 9 μs, and the maximum pressure of the quenching gas was approximately 700 mTorr.

3.3.3 Magnetic field

A pair of matched Helmholtz coils produce a tunable, pulsed magnetic field in the interaction region. The coils were surrounded by μ metal shielding to remove the influence of stray magnetic fields that would destroy the polarisation created in the sample by causing radicals at different points to precess at different frequencies [112]. For the alignment measurements, the field axis was parallel to the detection direction [115], whilst for the orientation measurements, the magnetic field axis was aligned perpendicular to both the laser propagation and detection axes [117]. The fields employed ranged between 0 Gauss and 30 Gauss.

3.3.4 Monochromator

Before the fluorescence is detected, it is passed through a monochromator. This allowed either P, Q or R branch emission to be recorded (where P, Q and R refer to Δj in this section as opposed to ΔN), resulting in a larger quantum beat amplitude. For the alignment measurements, the beats in the P and R branch are of the same phase, and opposite to those in the Q branch. In this case, a beat is still observable in the unresolved emission, as the beat amplitude in the Q branch is larger than those in the P and R branch, and some of the total disalignment data presented here was recorded with the monochromator at the minimum resolution. However, for the orientation measurements it was essential to use a monochromator, as there is little or no beat in the Q branch emission, and the beats in the P and R branch are of equal magnitude and out of phase. Therefore, if the emission was unresolved the beat would be lost due to the averaging over

the P and R branch.

The maximum resolution achievable with the monochromator was approximately 1Å [108]. This allowed the fluorescence from only the initially populated spin-rotation level of OH(A) to be recorded, meaning elastic depolarisation and rotational energy transfer cross-sections could be determined. This resolution was not sufficient for NO(A), as the rotational lines are less well separated due to the smaller rotational constant associated with the radical.

3.3.5 Detection

The fluorescence from the radical is passed through a quarter waveplate if orientation is being measured, and a linear polariser before being detected using a UV sensitive photomultiplier tube. The signal is then passed to a digital oscilloscope which has two channels, one to record the fluorescence decay associated with each polarisation of the probe laser. The oscilloscope averages the decays over a number of laser shots, before passing them to

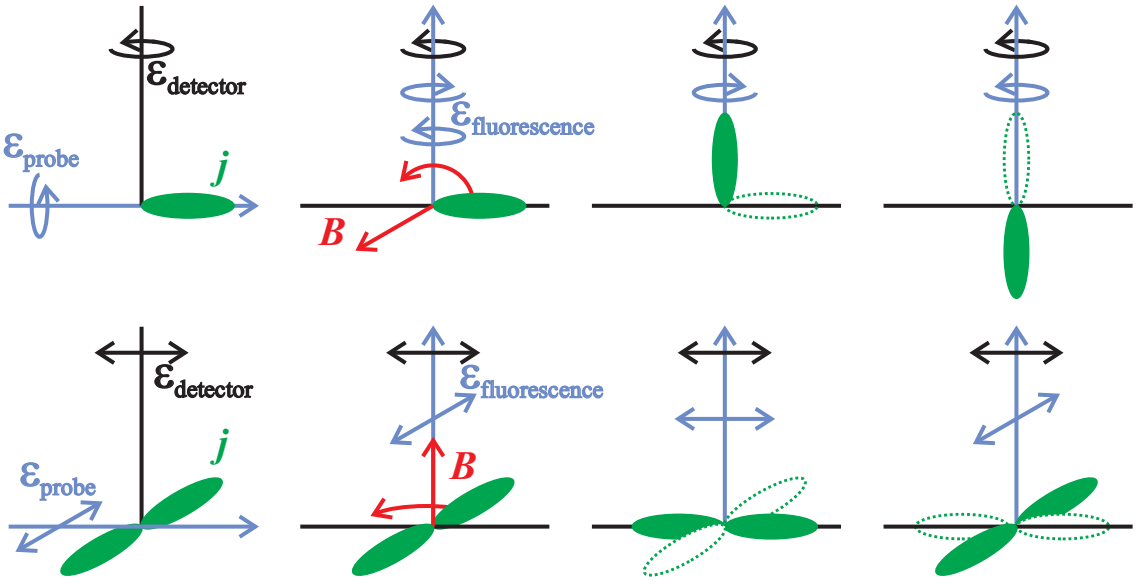


Figure 3.2: The geometries used in the Zeeman quantum beat experiments. The top panel shows how an initially oriented angular momentum distribution, created by absorption of circularly polarised light, precesses in the applied magnetic field, and the polarisation of the emitted fluorescence. The bottom panel shows the same thing, but for an aligned distribution created with linearly polarised light.

a computer, where 12 to 24 such decays are averaged to give the final trace. This was repeated for between six and eight pressures of quencher gas, for each transition recorded.

Figure 3.2 shows the experimental geometries employed for the orientation and alignment measurements. The geometry used for the orientation measurements is shown in the top panel of the figure. The circularly polarised probe laser creates an oriented distribution along the propagation direction of the laser. This distribution is then rotated by the applied field, and the fluorescence recorded after passing through a quarter wave plate and linear polariser. As the emission from the distribution is circularly polarised, the intensity of the signal oscillates as the fluorescence polarisation is the same and opposite to that of the detection optics.

The bottom panel of the figure shows the geometry used for the alignment measurements. A beat is only seen when the polarisation of the probe laser is perpendicular to the detection direction. In this case, the aligned distribution created precesses in the applied magnetic field, and the decay passes through a series of maxima and minima when the fluorescence is parallel and perpendicular to the detector polarisation.

3.4 Data analysis

The fluorescence decays obtained from the quantum beat experiments can be described by:

$$I(t) = I(0)\mathrm{e}^{-k_\mathrm{p}\,t}\left(1 + \mathrm{e}^{-k_\mathrm{d}\,t}\sum_F C_F\cos(k\,\omega_{L_F}t + \phi)\right) \tag{3.28}$$

C_F is the beat amplitude and ω_{L_F} the Larmor frequency (as defined in equation (3.24)) associated with the F^{th} hyperfine level. ϕ accounts for the phase at the start of the beat, and is dependent on the excitation branch, the emission branch and whether orientation (k=1) or alignment (k=2) is being measured. The sum is over all the hyperfine levels that contribute to the quantum beat signal. The rate constants k_p and k_d describe the loss of population and the loss of the initially prepared polarisation respectively, and they can both be written in terms of a sum of rate constants associated with collisional and

non-collisional processes:

$$k_{\mathrm{p}} = k_0 + k_1[Q] \tag{3.29}$$

$$k_{\mathrm{d}} = k_2 + k_3^{(k)}[Q] \tag{3.30}$$

where $[Q]$ is the concentration of the quencher gas. k_0 is simply the fluorescence rate constant. In the case where measurements are made with the minimum monochromator resolution, k_1 is the rate constant associated with electronic quenching. In the case where the emission is resolved with the monochromator, this will also include a contribution from RET. k_2 accounts for the loss of polarisation in the absence of collisions, which may be caused, for example, by field inhomogeneities which would cause the radicals to precess at slightly different frequencies, leading to a loss of the quantum beat. The main focus of this work is obtaining $k_3^{(k)}$ which accounts for the loss of the initially prepared polarisation through collisions.

The fit was performed using a genetic algorithm, and all the decays measured experimentally at different pressures were fit globally. The values of k_0, k_1, k_2, $k_3^{(k)}$, C_F, ϕ and ω_{L_F} were sampled randomly between two limits, and the goodness of the fit determined using [23]:

$$\chi^2 = \frac{1}{n_{\max}} \sum_n \int (I^n_{\mathrm{expt}}(t) - I^n_{\mathrm{fit}}(t))^2 \mathrm{d}t \tag{3.31}$$

$I^n_{\mathrm{expt}}(t)$ is the experimental fluorescence intensity for the n^{th} pressure decay, and the sum is over the number of decays recorded at different pressures. The returned values of the parameters correspond to those which result in the minimum value of χ^2.

3.4.1 Hyperfine quantum beats

The disalignment cross-section for NO(A)-Kr for N=2 was obtained using hyperfine quantum beat spectroscopy. Typical fluorescence decays that were obtained are shown in figure 3.3 (dashed black lines), along with the fits to the data (solid red lines), along with

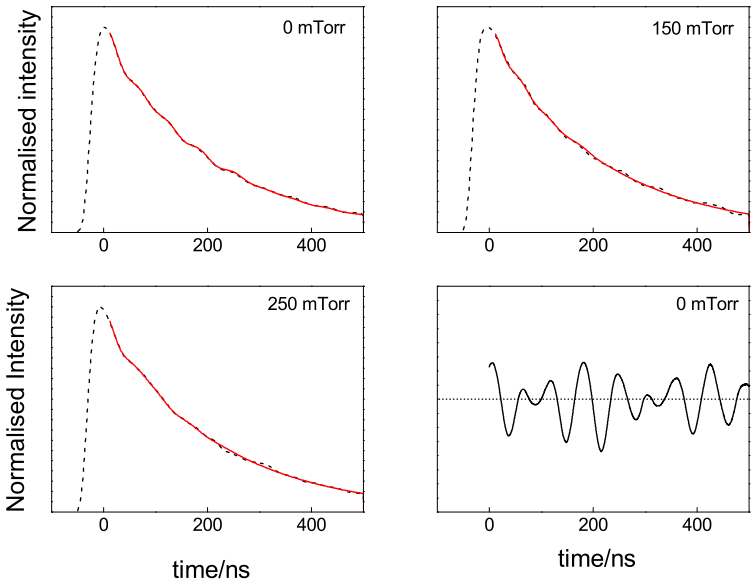


Figure 3.3: An alignment hyperfine quantum beat recorded for NO(A)-Kr using $S_{21}(0)$ excitation (black line) and a fit to the data (red line) for a range of pressures of krypton (top row and bottom left), and the resultant hyperfine beat for the 0 mTorr data (bottom right).

an example of a hyperfine beat in the bottom right panel (solid black line). In this case, the full decay was fitted using equation (3.28), where ω_{L_F} are the hyperfine splitting frequencies of NO(A). As these were allowed to vary in the fit, (as were the hyperfine beat amplitudes C_F), the returned values could also be used as a test of the goodness of the fit.

3.4.2 Zeeman quantum Beats

Orientation

As mentioned previously, a PEM was used to flip the polarisation of the laser between left (I_L) and right (I_R) circularly polarised light on alternate shots when making the orientation measurements. Therefore two fluorescence decays were recorded simultaneously, one for each polarisation. This makes it possible to separate the polarisation decay from the population decay by taking the normalised difference between the two polarisations:

$$\frac{I_L - I_R}{I_L + I_R} = \mathrm{e}^{-(k_2 + k_3^{(1)}[Q])\,t} \sum_F C_F \cos(\omega_{L_F} t + \phi) \tag{3.32}$$

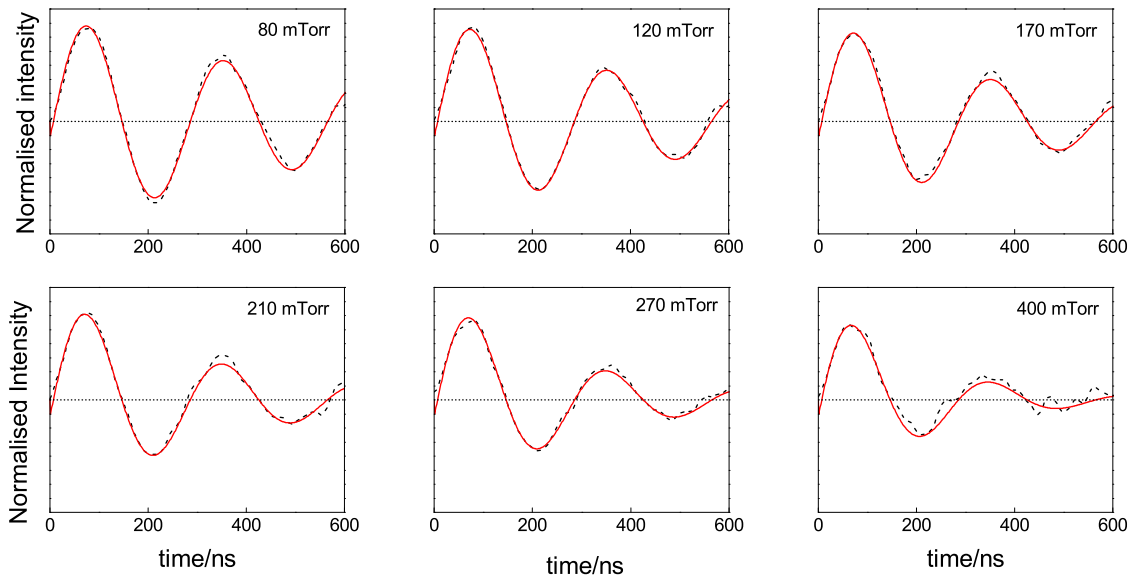


Figure 3.4: An orientation Zeeman quantum beat recorded for OH(A)-Kr using $R_{22}(7)$ excitation (black line) and a fit to the data (red line) for a range of pressures of krypton. The magnetic field used was approximately 20 Gauss, and the emission was recorded on the P_{22} branch.

The resultant quantum beats are shown as black dashed lines in figure 3.4 for six pressures of krypton. As the pressure of the quencher gas is increased, the beat amplitude drops more quickly with time reflecting the increased depolarisation occurring at higher pressures. The solid red lines show the fit to the data using equation (3.32), from which $k_3^{(1)}$ can be determined. It should be noted that at t=0 there is no orientation, and therefore the magnetic field is required to rotate it so it is parallel to the direction of detection.

Alignment

The alignment measurements were also made using a PEM, and therefore two fluorescence decays were again recorded with two orthogonal linear polarisations. As in the case of the orientation measurements, it is possible to separate out the decay of the population from the decay of the polarisation using:

$$\frac{I_{\parallel} - I_{\perp}}{I_{\perp}} = \frac{\mathrm{e}^{-(k_2+k_3^{(2)}[Q])\,t} \sum_F C_F \cos(2\omega_{L_F} t + \phi)}{1 + \mathrm{e}^{-(k_2+k_3^{(2)}[Q])\,t} \sum_F C_F} \tag{3.33}$$

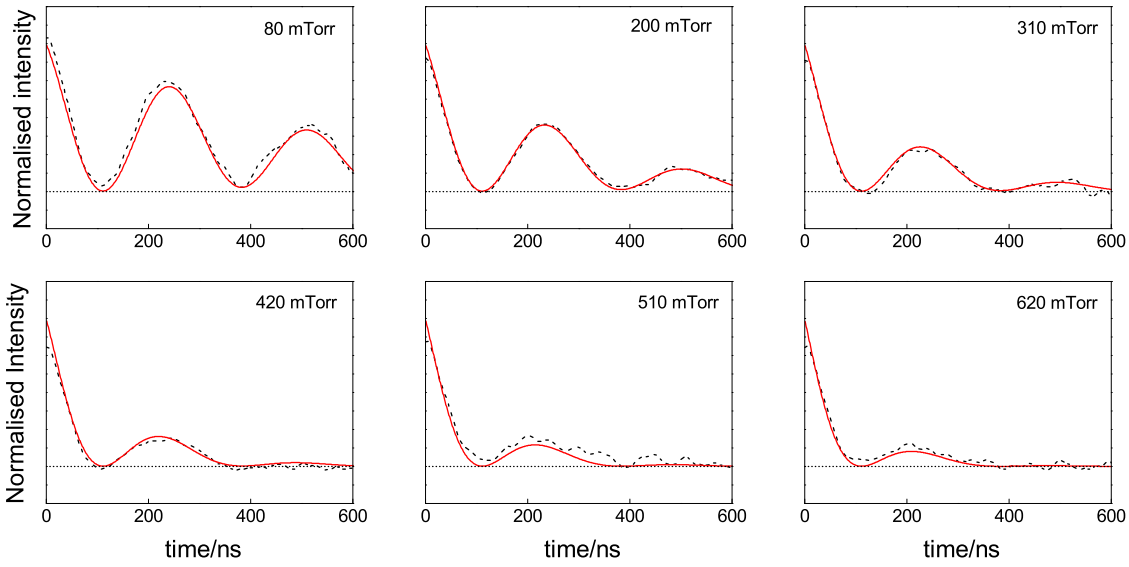


Figure 3.5: An alignment Zeeman quantum beat recorded for OH(A)-Kr using $R_{22}(7)$ excitation (black line) and a fit to the data (red line) for a range of pressures of krypton. The magnetic field used was approximately 10 Gauss.

where $I_{\parallel}$ is the fluorescence intensity when the polarisation is parallel to the detection axis, and $I_{\perp}$ the intensity when it is perpendicular. The resultant Zeeman quantum beats are shown as black dashed lines in figure 3.5 for six pressures of krypton. Again, the beat structure decays more quickly at higher pressures of krypton. The solid red lines show the fits to the data using equation (3.33). For alignment measurements, the beat amplitude is a maximum at t=0 which allows disalignment measurements to be made without the applied magnetic field. This method was employed to record some of the elastic disalignment data. In this case, $k_3^{(2)}$ could be determined by fitting $(I_{\parallel} - I_{\perp})/(I_{\parallel} + 2I_{\perp})$, which again is only dependent on the decay of the polarisation.

Rotational energy transfer and electronic quenching

As mentioned previously, k_1 contains information on the electronic quenching and the rotational energy transfer rate constants, depending on the resolution with which the fluorescence decays were recorded. In the case of the totally unresolved measurements, k_1 gives a direct measure of the electronic quenching rate constant. It would be possible to determine this rate constant by fitting one of the fluorescence decays associated with a

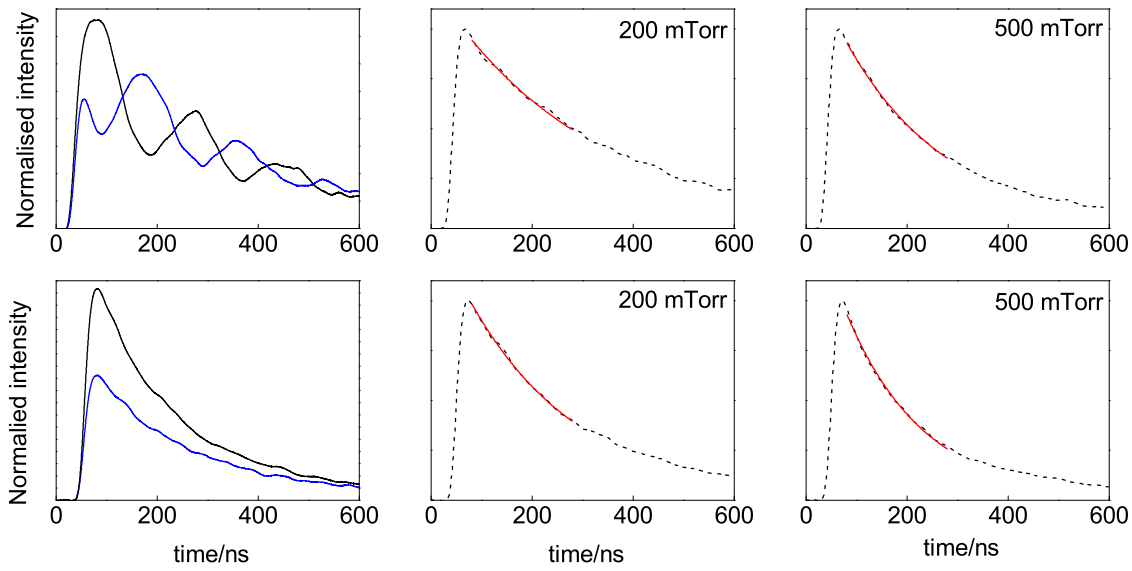


Figure 3.6: The fluorescence decays recorded experimentally for orientation using left and right circularly polarised light (top left) and for alignment using linearly polarised light (bottom left), and the corresponding summed decays (black dashed lines) and the fits (red lines) used to obtain the RET cross-sections.

particular polarisation with equation (3.28). However, it is again possible to obtain just the population decays. For the orientation measurements this corresponds to the sum of the two fluorescence decays, $I_L + I_R$, and for the alignment measurements made without a magnetic field, to $I_{\parallel} + 2I_{\perp}$.

The fluorescence decays recorded for the elastic depolarisation measurements can also be fit in the same way. Examples of this are presented in figure 3.6, with the top row showing the orientation data, and the bottom row the alignment data. The left hand panels show the fluorescence decays recorded using the two polarisations, and the middle and right hand panels the summed experimental decays (dashed black line), with the fits to the data (red line). The values of k_1 obtained from the resolved measurements are the sum of the RET and electronic quenching rate constants. As the electronic quenching rate constant can be obtained from the unresolved data as described above, the RET rate constant can be found as the difference between the two.

3.4.3 Error analysis

The errors for the experimental data are determined using a Monte Carlo procedure. Random values of the coefficients used in the fitting equations were selected, and χ^2 calculated using equation (3.31). If the returned value of χ^2 was lower than a predetermined value, it was deemed to be an acceptable alternative fit. From the spread of the values from the alternative fits, it is possible to calculate the standard deviation, from which the error can be determined. All error bars represent 95% confidence limits.

As the RET rate constants and inelastic depolarisation cross-sections were not measured directly, the errors associated with these values could not be determined as described above. The errors associated with the RET rate constants (δ_{RET}) were calculated *via*:

$$\delta_{\mathrm{RET}} = \sqrt{\delta^2_{\mathrm{RET+EQ}} + \delta^2_{\mathrm{EQ}}} \tag{3.34}$$

where $\delta_{\mathrm{RET+EQ}}$ is the error for the sum of the RET and electronic quenching rate constant, and δ_{EQ} that for the electronic quenching rate constant. An equivalent expression is valid for the inelastic depolarisation cross-section, which was determined as the difference between the total and elastic depolarisation cross-sections.

3.4.4 Converting rate constants to cross-sections

The values obtained from the fit are depolarisation rate constants, but the values presented in the next chapter are depolarisation cross-sections. Assuming that the depolarisation cross-section is independent of the relative velocity (v_{rel}), the rate constants can be converted to cross-sections ($\sigma^{(k)}$) *via*:

$$\sigma^{(k)} = \frac{k_3^{(k)}}{v_{\mathrm{rel}}} \tag{3.35}$$

In the case of the thermal measurements, the relative velocity is given as the mean of the Maxwell-Boltzmann distribution [1, 139]:

$$v_{\mathrm{rel}} = \sqrt{\frac{8k_{\mathrm{B}}T}{\pi\mu}} \tag{3.36}$$

where T=300 K and μ is the reduced mass for the system. The value of v_{rel} used to obtain the cross-sections for NO(A)-Kr was 482 ms^{-1}, and for OH(A)-Kr was 668 ms^{-1}.

For the superthermal OH(A)-Kr measurements, the system is not in thermal equilibrium so the above expression cannot be used. A simple hard sphere model of the scattering process was used to estimate the extent of translational moderation of the OH that took place at a range of time delays and pressures [115]. A value of the hard-shell cross-section of 17 $\mathrm{Å}^2$ was approximated using the OH(A)-Kr PES [172], and it was assumed that the scattering process was isotropic [115, 120, 224]. The resulting velocity distributions are shown in figure 3.7. The left hand panel of the figure shows the effect of increasing the

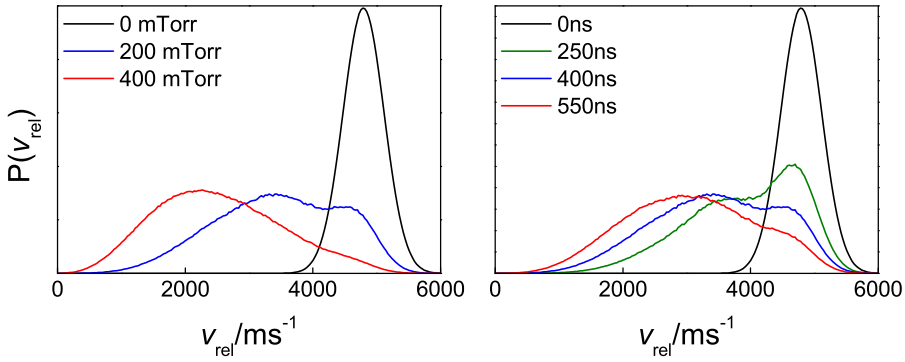


Figure 3.7: Velocity distributions for OH(A)-Kr following photolysis of H_2O_2 at 193 nm for a range of pressures of krypton after a time delay of 400 ns (left panel) and for a range of time delays for a fixed pressure of Kr of 200 mTorr (right panel).

pressure of Kr on the v_{rel} distribution, with all distributions calculated 400 ns after the photodissociation of the peroxide, and the right hand panel shows the effect of increasing the time, with all distributions calculated at 200 mTorr of krypton. As expected, as the pressure of krypton increases, and as the time after the photodissociation increases, there is more translational moderation due to the fact there are more collisions between the OH

and the Kr. To minimise the effects of this, only the first 500 ns of the decay was fit, and a maximum pressure of 400 mTorr of krypton was used. This model was also employed to verify that 9 μs was a sufficiently long delay to allow translational moderation of the OH to thermal equilibrium.

To obtain an estimate of v_{rel} for the superthermal measurements, the continuous energy QCT calculations described in chapter 2 were used, to determine how the depolarisation cross-sections varied over the energy range that was sampled experimentally. The excitation functions obtained from these calculations are shown in figure 3.8. As can be seen,

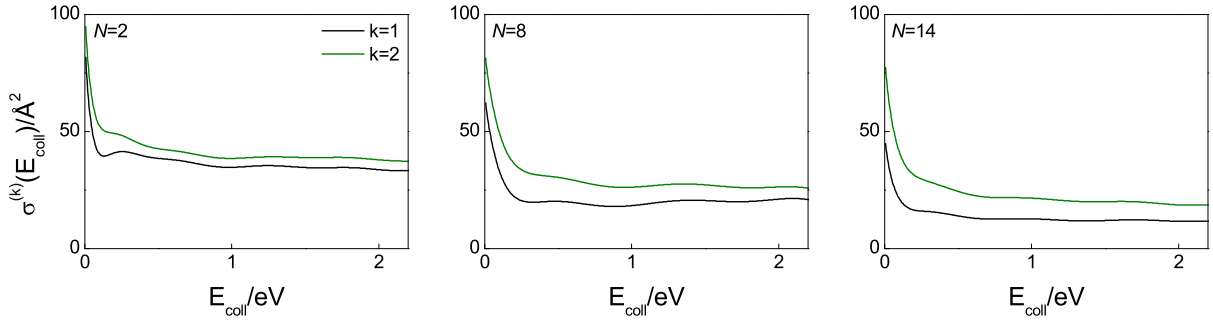


Figure 3.8: Excitation functions for OH(A)-Kr for disorientation (black) and disalignment (green) for N=2 (left panel), N=8 (middle panel) and N=14 (right panel).

the depolarisation cross-sections vary only very slowly over the range of collision energies sampled experimentally. A rate constant was obtained from the velocity distribution and excitation function described above *via* [1, 139]:

$$k_3^{(k)} = \int_0^\infty \sigma^{(k)}(E_{\mathrm{coll}}) v_{\mathrm{rel}} P(v_{\mathrm{rel}}) \mathrm{d}v_{\mathrm{rel}} \tag{3.37}$$

The velocity distribution used was that for the middle pressure recorded experimentally, and the middle time delay. As mentioned above, most decays were fit for 500 ns, and therefore a time delay of 500 ns was used, to also include the 250 ns between the pump and probe pulses during which moderation could occur. The value of the rate constant determined from equation (3.37) was then used with the fixed energy QCT cross-section to obtain an estimate of v_{rel}. The value obtained was 3600 ms^{-1}, which corresponds to a

mean collision energy of approximately 0.9 eV.

Although these superthermal measurements were not performed at a sharply defined collision energy, the simulations presented in figure 3.8 show that the depolarisation cross-sections are not expected to vary significantly over the range of collision energies sampled experimentally. Therefore, these measurements provide a qualitative picture of the effect that increasing the collision energy has on the depolarisation process.

3.5 Experimental simulations

It was possible to simulate the LIF decays from the Zeeman quantum beat experiments using a Monte Carlo method to integrate the kinetic equations associated with the loss of population and polarisation [225, 226]. For an initial state, j, the change in population is given by [23, 109]

$$\frac{\mathrm{d}N_j(t)}{\mathrm{d}t} = \sum_{j' \neq j} \left(k_{j'j} N_{j'}(t) - k_{jj'} N_j(t) \right) [Q] - k_{0j} - k_{1j}[Q] \tag{3.38}$$

where $N_j(t)$ is the population at time t, $[Q]$ is the concentration of the quencher gas, k_{ab} is the RET rate constant for transfer of population from state a to state b, k_{0j} is the fluorescence rate constant, and k_{1j} is the electronic quenching rate constant. Therefore, to run the simulations it is necessary to input a matrix of the state to state RET cross-sections, as well as the fluorescence lifetimes [156], and the quenching rate constants [172, 227]. The RET cross-sections used are those obtained from the fixed energy QCT calculations using the tensor opacity formalism described in section 2.5.

The loss of polarisation ($P_j^{(k)}(t)$) for the state j is given by [23, 109]:

$$\frac{\mathrm{d}P_j^{(k)}(t)}{\mathrm{d}t} = \sum_{j' \neq j} \left(k_{j'j}^{(k)} N_{j'}(t) - k_{jj'}^{(k)} N_j(t) \right) [Q] - k_{jj}^{(k)}[Q] - k_{2j} \tag{3.39}$$

$k_{jj}^{(k)}$ is the rate constant for elastic depolarisation, and k_{2j} is the rate constant that accounts for the loss of the beat amplitude not brought about by collisions. As mentioned above,

this accounts for factors including inhomogeneity of the magnetic field experimentally, and for the simulations it is set to zero.

From the input rate constants, the probability that the molecule would fluoresce, change state, or be quenched was calculated at each time step. In the event that the molecule was quenched, the radical could no longer contribute to the fluorescence decay, so the trajectory was deemed to be finished. If the molecule changed state, then the phase of the quantum beat remains unchanged. However, the beat amplitude is multiplied by $a_{jj'}^{(k)}$ to account for the depolarisation that changing state will have caused. The value of ω_{L_F} will also change from that of the initial level to that of the final level. It follows that it is also necessary to input the g_F values for each quantum state, and a matrix of the state to state $a_{jj'}^{(k)}$ values into the simulation. Even in the absence of depolarisation, these state changing collisions can lead to a loss of the quantum beat. Figure 3.9 shows a quantum

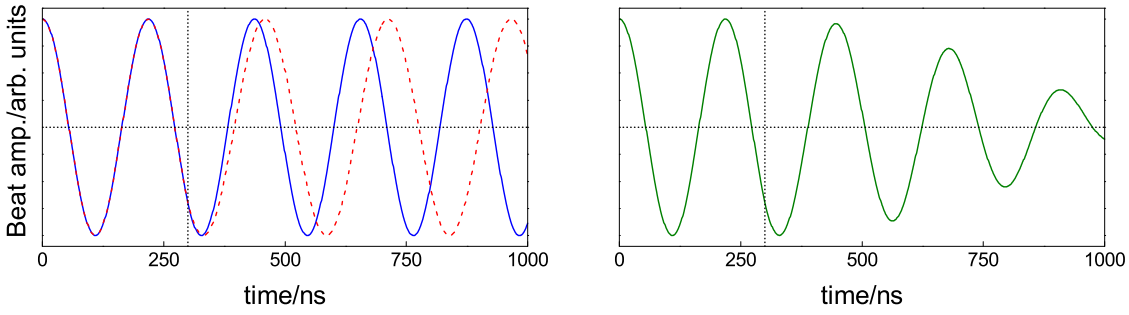


Figure 3.9: Two quantum beats (left) and the total (right) to show the effects of dephasing on the experimental signal.

beat from two states in the left hand panel. Initially, the beats are for the same state, and so the amplitude of the total, in the right hand panel, remains the same. At t=300 ns, RET occurs, and so one of the beats changes frequency due to the change in the g_F value that this brings about. This change of state does not result in any depolarisation, so the beat amplitude remains the same. However, as can be seen in the right hand panel of the figure, the amplitude of the sum of the two beats now decays, due to the different precession frequencies of the two states. This loss of the beat structure in the absence of depolarisation will be referred to as 'dephasing', and this is indistinguishable from de-

polarisation experimentally. However, the experimental simulations allows the extent to which this contributes to the experimentally observed cross-sections to be estimated.

The importance of dephasing depends on the extent to which collisions populate different final states, and the extent to which these collisions cause depolarisation. Collisions which change the spin-rotation state of the radical contribute most to dephasing. These collisions result in a quantum state being populated which precesses in the opposite direction to the initially populated state in the applied magnetic field. However, as $\boldsymbol{S}$ and $\boldsymbol{I}$ can be treated as spectators to the collision, these transitions are brought about by a large change in direction of $\boldsymbol{N}$ which causes significant depolarisation. Collisions which change N but conserve S and I contribute less to dephasing, as the g_F values for consecutive states do not change significantly. The largest difference between g_F values is at low N, so the contribution dephasing makes will be largest at low N.

If the molecule fluoresces, then it is necessary to increase the fluorescence intensity for that time step. The intensity increase for a molecule in state j fluorescing to a state j'' in the electronic ground state is given by:

$$I_j(t) = \sum_{\Delta j=-1,0,1} S_{jj''} W_{jj''} \left[1 + C^{(k)}_{jj''}(t)\cos(\phi(t))\right] \tag{3.40}$$

where the sum is over all six possible emission branches ($\Delta j = j - j''$), and $S_{jj''}$ is the emission coefficient for the transition [156, 228]. $C^{(k)}_{jj''}(t)$ is the beat amplitude at time t. If the molecule has not undergone any collisions, this will simply be the magnitude of the polarisation created, $A^{(k)}(0)$, which depends on both the excitation and emission branches. However, if the molecule has undergone n collisions before it fluoresces, $C^{(k)}_{jj''}(t) = A^{(k)}(0)\prod_n a^{(k)}_{j_{n-1}j'_n}$. This can be rationalised as follows. As the molecule undergoes a collision and causes depolarisation, this leads to a reduction in the beat amplitude (which reflects the amount of polarisation remaining in the sample, as given by equation (3.9)). Each collision would result in a reduction of the beat amplitude by a factor of $a^{(k)}_{jj'}$, which is the depolarisation moment associated with the j to j' transition. Therefore the final beat

amplitude is the product of the initial beat amplitude and the depolarisation moments associated with each collision that the radical has undergone, each of which decreases the beat amplitude by its associated depolarisation moment.

$\phi(t)$ is the phase of the quantum beat at time t. Again, if the molecule has not undergone any collisions, this is simply given by $\phi(t) = \omega_{L_F} t + \phi(0)$. If the molecule has undergone n collisions, this will be given by $\phi(t) = \phi(0) + \sum_n \omega_{L_{Fn-1}} \Delta t_{n-1n}$. Each term in the sum is simply the angle that the angular momentum precesses through between each collision, and therefore $\phi(t)$ is the 'total' phase.

The $W_{jj''}$ term is a weighting factor to account for the probability of detecting the fluorescence due to the monochromator. It follows that if the simulation is 'unresolved' $W_{jj''} = 1$ for all j. If the fluorescence is resolved, the weighting is modelled as a Gaussian distribution, and is given by:

$$W_{jj''} = \exp\left(-2\left(\frac{\lambda_{jj''} - \lambda_{\text{mono}}}{2\sigma}\right)^2\right) \tag{3.41}$$

$\lambda_{jj''}$ is the position of the emission branch [156], λ_{mono} is the monochromator position and σ is proportional to the monochromator band width. The addition of this monochromator weighting has allowed simulations to be run to determine the effects that satellite lines have on the elastic depolarisation measurements, and the detection probabilities of different emission branches on the superthermal measurements. These will be discussed further in the following chapter.

The final fluorescence decays are obtained using 1×10^7 such trajectories, and the total intensity at a given time is simply the sum of the intensity at that time over all final states populated. The decays are simulated for a number of pressures of quencher gases, and these decays can then be fit using equation (3.28) to obtain a value of $k_3^{(k)}$.

Experimentally, two fluorescence decays are recorded with either orthogonal linearly polarised light in the case of alignment, or left and right circularly polarised light for orientation. It is possible to simulate the two decays by making small changes to equa-

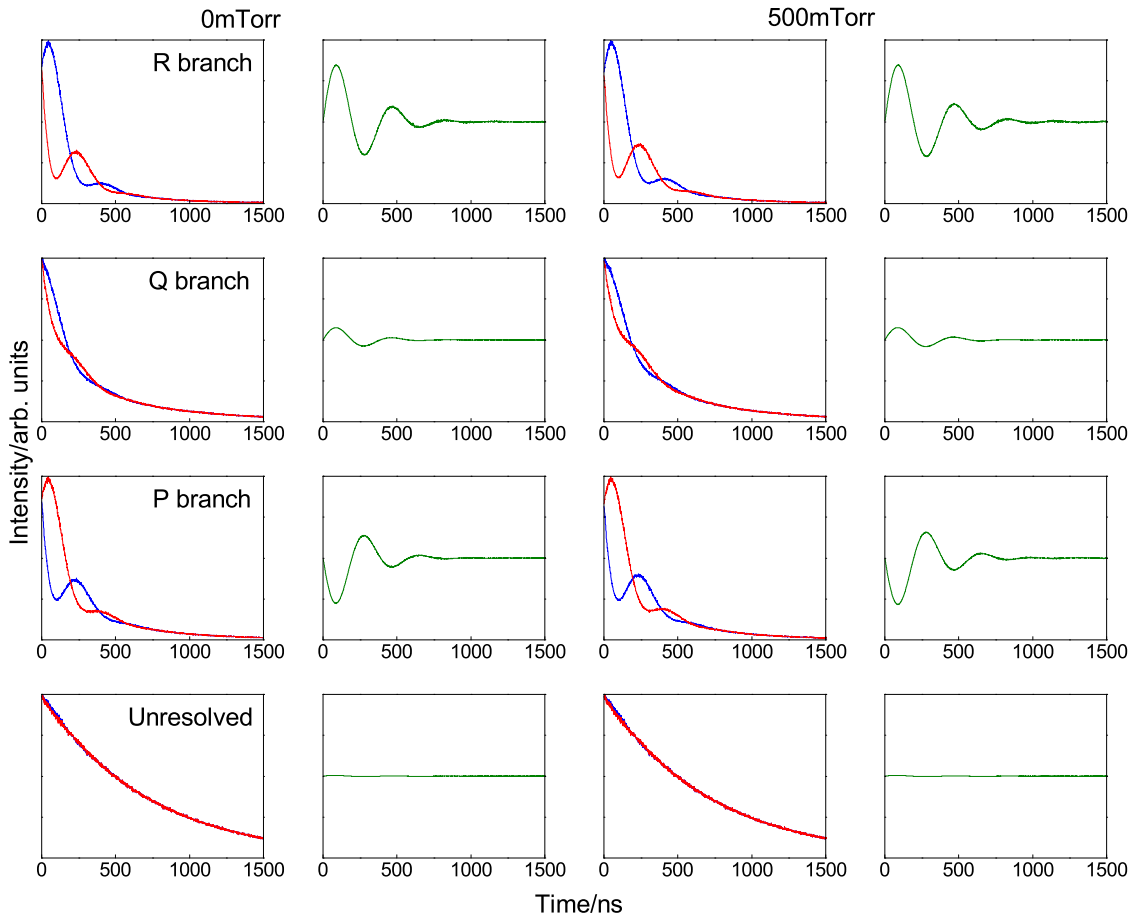


Figure 3.10: Simulated resolved orientation fluorescence decays (first and third columns) and the resulting quantum beats (second and fourth columns) for OH(A) following $R_{22}(4)$ excitation with the emission being resolved on the R_{22} (top row), Q_{22} (second row), P_{22} (third row) branches, and when the emission is unresolved (bottom row). The first two columns show the decays in the absence of a quencher, and the last two the decays with 500 mTorr krypton. The field used was 10 Gauss.

tion (3.40). For the alignment simulations, it is necessary to replace $\phi(t)$ by $\phi(0)$ in one of the decays, corresponding to the aligned distribution being created parallel to the detection axis. For the orientation measurements, both decays can be simulated as outlined above, but require the value of $\phi(t)$ to be different by π. Simulated decays are shown in figure 3.10 for orientation following $R_{22}(4)$ excitation in OH. The fluorescence intensity is shown simulating either R_{22} branch emission (top row), Q_{22} branch emission (second row), P_{22} branch emission (third row) and unresolved emission (bottom row). The two polarisations are shown in the first and third column, and the resulting quantum beat in the second and fourth column. The first two columns correspond to the intensity in the

absence of a quencher, and the last two to the intensity with 500 mTorr Kr.

It is therefore possible to do full simulations of the quantum beat experiment, where the pressures of quencher gas used experimentally, along with the magnetic field strength, the monochromator position and slit width can be used as inputs. This also allows simulations to be run to determine the RET cross-sections and electronic quenching cross-sections using the same methods outlined above. As these are inputs to the simulations, the values obtained are dependent on those defined by the user. However, the values of the cross-sections obtained from the simulations are the same as those input, validating the experimental and analysis methods used to measure the values of these cross-sections.

3.6 Summary

A description of how both initially oriented and aligned rotational angular momentum distributions can be created by the absorption of polarised light has been presented. The subsequent time evolution of the distribution in the presence of a quencher gas has been discussed, and quantum beat spectroscopy introduced as a way of measuring the rate at which collisions destroy the initially prepared polarisation. For OH(A), experimental methods for obtaining both the total depolarisation cross-sections at two collision energies, and the (thermal) elastic depolarisation cross-sections with the use of a monochromator have been described, as well as the data analysis which also allows both the rotational energy transfer cross-sections and electronic quenching cross-sections to be determined.

A method for simulating the fluorescence decays using results from the QCT calculations discussed in section 2.3.2 has been described. These simulations will allow the importance of dephasing to be determined on the NO(A)-Kr and OH(A)-Kr depolarisation results presented in the following chapter. They will also allow the influence of dispersing the fluorescence through a monochromator on the returned values of the depolarisation cross-sections to be determined.

Chapter 4

Collisional depolarisation of OH(A) and NO(A) with Kr

The results presented in this chapter build on previous work on the collisional depolarisation of OH(A) and NO(A) with helium and argon, [108, 109, 116, 118, 119], and also related studies of the collisional depolarisation of the same radicals in the ground state [104–106, 108, 110, 113, 114, 121, 122, 132–134]. It has been shown that collisions of NO(A) with helium and argon are impulsive encounters, and do not cause significant depolarisation [109, 118, 119]. In comparison, the collisions of OH(A) with argon cause very efficient depolarisation [116, 119]. The OH(A)-Kr potential energy surface (PES) is significantly more attractive and anisotropic than that for OH(A)-Ar, with well depths of 6000 cm^{-1} [172] and 1700 cm^{-1} [206] respectively, whereas the NO(A)-Kr potential is more isotropic and has a much shallower well depth (approximately 140 cm^{-1} [171]) and is therefore similar to that for NO(A)-Ar [171]. The different strengths of the interactions reflects both the differences in the dipole moments of the radicals and the polarisabilities of the species involved, and also that open shell molecules can form strong interactions through electron correlation effects [202]. Due to the different underlying potentials, it is anticipated that different dynamical behaviour will be observed in collisions of NO(A) and OH(A) with krypton.

The PESs that describe the interactions between NO and OH in their electronic ground

state are more similar in nature to those that describe the NO(A)-rare gas systems than the OH(A)-rare gas systems [122, 168, 170, 229]. It has been shown theoretically that in the ground state, elastic depolarisation is brought about by collisions that probe the more repulsive part of the potential as opposed to the long range attractive region [104–106]. In contrast, the attractive part of the potential does play a role in the elastic depolarisation of OH(A) through collisions with Ar [108]. Determining the influence of the more attractive and anisotropic nature of the OH(A)-Kr PES on elastic depolarisation will therefore provide further insight into the role that these play in the corresponding mechanism.

In this chapter, the cross-sections for both collisional disorientation and disalignment obtained from the quantum beat spectroscopy experiments described in the previous chapter are presented for NO(A)-Kr and OH(A)-Kr. For OH(A)-Kr, rotational energy transfer, electronic quenching and elastic depolarisation cross-sections have been measured, alongside the total depolarisation cross-sections at two different collision energies. A detailed comparison is made between these results and those obtained from the theoretical, quasi-classical trajectory (QCT) calculations. In section 4.5, the mechanism of depolarisation in OH(A)-Kr and NO(A)-Kr is considered. The results from the QCT calculations are compared to provide further insight into the differences between the two systems.

4.1 Calculation details

4.1.1 Quasi-classical trajectories

For the QCT calculations, batches of approximately 1×10^5 trajectories were run for selected rotational levels between N=0 and N=16 for NO(A)-Kr and OH(A)-Kr at a fixed collision energy of 39 meV, which corresponds to the mean thermal collision energy at 300 K, using the latest *ab initio* PESs of Kłos *et al.* [171, 172]. Calculations were also run for OH(A)-Kr at fixed collision energies of 0.9 eV and 1.5 eV, which is the range of energies considered to be sampled experimentally considering the effects of translational moderation

discussed in section 3.4.4. The maximum impact parameter was chosen such that no inelastic scattering or elastic depolarisation occurred above it. The initial conditions for each trajectory were sampled as described in section 2.3.2, and the trajectories analysed using the methods discussed in sections 2.4 and 2.5.

4.1.2 Quantum mechanics

For OH(A)-Kr, close-coupled QM calculations were also performed at a collision energy of 39 meV using the HIBRIDON suite of codes [176], for N=2, 5, 8 and 12. The Log-Derivative propagation [178] was performed from 3 a_0 to 9 a_0 and Airy propagation [179, 180] to 30 a_0. To converge the cross-sections, it was necessary to include partial waves up to J=300, and a rotational basis set of OH(A) up to and including N=29. It should be noted that these scattering calculations were run by J. Kłos.

4.2 Electronic quenching

By fitting the summed fluorescence decays from the unresolved total depolarisation measurements, it is possible to obtain the electronic quenching rate constants as discussed in section 3.4.2. The results obtained are presented in figure 4.1 as filled triangles, where the

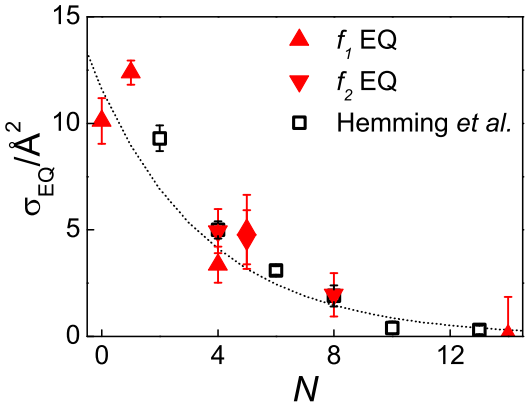


Figure 4.1: Experimentally determined electronic quenching cross-sections for the f_1 (upward pointing triangles) and f_2 (downward pointing triangles) spin-rotation levels. The results are compared with those from a previous study by Hemming *et al.* (open squares) [227].

upwards pointing triangles are for the f_1 spin-rotation level, and the downward pointing triangles the f_2 spin-rotation level. The results from the present study are compared with those obtained previously by Hemming *et al.* [227] (open squares). There is excellent agreement between the two sets of results. The cross-sections presented from the Zeeman quantum beat experiments are for electronic quenching from a single spin-rotation (j) level within a rotational (N) level, whereas those from reference [227] are only resolved in N. This is equivalent to recording the average quenching associated with both spin-rotation levels. The electronic quenching cross-sections do not show a strong dependence on spin-rotation level, as shown in the figure for N=4 and N=5, where the cross-sections measured for both spin-rotation levels are the same (within the errors). Therefore it is reasonable to compare the two sets of data.

It should also be noted that the larger variation in the values of the electronic quenching cross-sections obtained here is due to the experimental method employed. The purpose of the experiments was to obtain the collisional depolarisation cross-sections, and not the electronic quenching cross-sections. However, these could be obtained from the analysis of the data, as has been presented here.

The electronic quenching cross-sections are seen to decrease as N increases. This is consistent with quenching occurring on an attractive, anisotropic PES [227, 230], as is the case for OH(A)-Kr [172]. The angular dependence of the OH(A)-Kr PES at R=2.1 Å (corresponding to the distance of the global minimum in the HO-Kr geome-

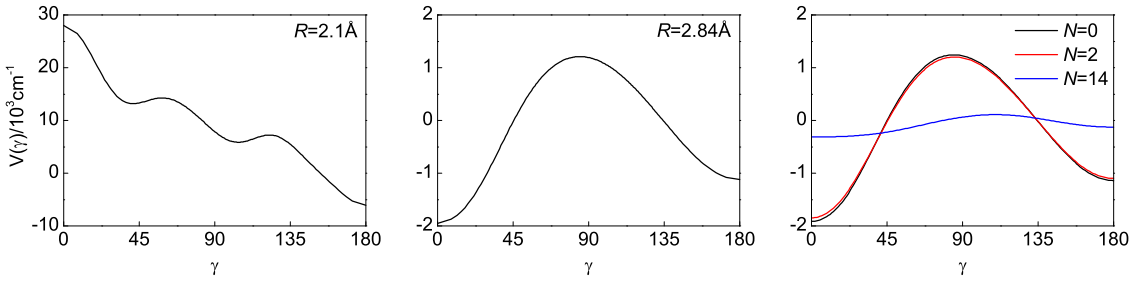


Figure 4.2: Cuts through the OH(A)-Kr PES [172] at R=2.1 Å (left panel) and R=2.84 Å (middle panel), and rotationally averaged between R=2.75 Å and R=2.95 Å for a range of rotational states (right panel).

try) and R=2.84 Å (the position of the local minimum in the OH-Kr geometry) are shown in the left and middle panels of figure 4.2 respectively. The potential varies rapidly as a function of the angle of approach, and has regions of both attraction and repulsion at the two distances considered. As N increases, and the rotation of the radical is faster, the potential that the krypton experiences will be rotationally averaged, and therefore less anisotropic. The right hand panel of the figure shows the effect that this rotation of the radical has on the potential on the region of the potential between 2.75 Å and 2.95 Å (*i.e.* the region around the local minimum). To determine the extent to which the potential is averaged by rotation, the angular frequency (ω) of the radical has to be calculated. This can be found by equating $\frac{1}{2}I\omega^2$ to the rotational energy of the radical, $BN(N+1)$, where I is the moment of inertia ($I = \mu r^2$), and B is the rotational constant. For N=2, $\omega \approx 1.6 \times 10^{13}\,\mathrm{rads}^{-1}$ and for N=14, $\omega \approx 9.6 \times 10^{13}\,\mathrm{rads}^{-1}$. It follows that, in the time it takes for the krypton to travel 0.2 Å, (*i.e.* between 2.75 Å and 2.95 Å) the OH will have rotated through approximately 30° if the rotational state of the radical is N=2, and 160° if it is N=14, assuming a relative velocity of $668\,\mathrm{ms}^{-1}$. As can be seen in the figure, the rotational averaging for N=2 does not significantly alter the anisotropy of the potential that the krypton experiences, whereas for N=14, the potential is significantly more isotropic and less attractive. This has the result that the krypton is less likely to sample the attractive region of the PES where quenching can occur, leading to a reduction in the quenching cross-sections.

4.3 Rotational energy transfer

4.3.1 Theoretical collision cross-sections

A comparison of the OH(A)-Kr rotational energy transfer (RET) cross-sections obtained from fixed energy QM (open squares) and QCT (open circles) calculations performed at 39 meV is presented in figure 4.3. The top row corresponds to cross-sections for N=2, the middle N=5 and the bottom N=8, and the results are resolved into final rotational state,

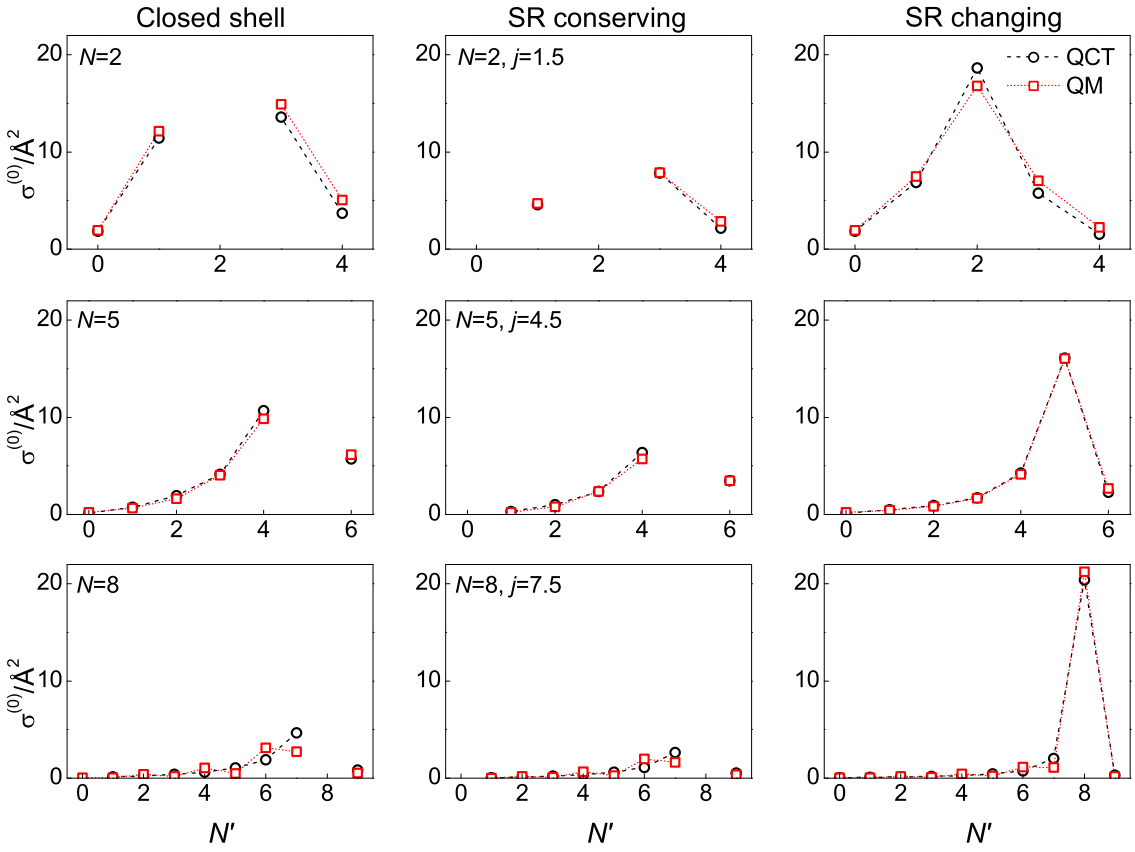


Figure 4.3: Comparison of the thermal OH(A)-Kr RET cross-sections obtained from QM (open squares) and QCT (open circles) calculations for N=2 (top row), N=5 (middle row) and N=8 (bottom row). The left hand column shows the results for the closed shell calculations, and the middle and right hand columns open shell results for the f_2 spin-rotation level. The middle column shows the spin-rotation (SR) conserving cross-sections and the right hand column the spin-rotation changing cross-sections.

N'. The left hand column of the figure shows the results from the closed shell calculations, the two sets of calculations are in good agreement. As $\Delta N(=N-N')$ increases, the RET cross-sections decrease. As mentioned above, the energy of the rotational levels of OH(A) is given by $E_{\rm rot} = B\,N(N+1)$, and therefore as ΔN increases, more energy transfer is required to bring about the transition. As translational to rotational energy transfer is more efficient at smaller impact parameters, this results in smaller cross-sections. By the same argument, the cross-sections also decrease as the initial rotational quantum number increases due to the increased rotational energy level separation of adjacent levels, and fewer rotational levels are populated after the collision for higher initial rotational states, as fewer rotational levels are energetically accessible.

As the electron spin can be treated as a spectator to the collision, (quasi-)open shell QCT cross-sections can be obtained using the tensor opacity formalism discussed briefly in section 2.5 and in detail in references [118] and [175]. These open shell QCT cross-sections are compared with their QM counterparts in the middle and right hand column of figure 4.3. The cross-sections are presented for the f_2 ($N - S$) spin-rotation level, and are resolved into cross-sections which conserve (middle column) and change the initially populated spin-rotation level (right hand column). Again there is excellent agreement between the two sets of calculation results, and the trends seen are identical to the closed shell case. It should be noted that averaging the open shell results over the two spin-rotation levels returns the closed shell cross-sections. The good agreement between the QM and QCT cross-sections means that throughout the rest of this section only the results from QCT calculations are considered.

The contribution that spin-rotation conserving and spin-rotation changing collisions make to the total RET cross-sections is shown in figure 4.4 for NO(A)-Kr (left panels), thermal OH(A)-Kr (middle panels) and superthermal OH(A)-Kr (right panels). The top section of the bar shows the contribution made by pure spin-rotation changing collisions ($\Delta N = 0$, $\Delta j = \pm 1$), the middle section to collisions which change both N and the spin-rotation level ($\Delta N \neq \Delta j \neq 0$) and the bottom section of the bar to those which change N but conserve the spin-rotation level ($\Delta N = \Delta j \neq 0$). The top row corresponds to the f_1 spin-rotation level, and the bottom row the f_2 spin-rotation level. It should be noted that there is no $N - S$ level for the N=0 rotational level, and therefore no purely spin-rotation changing collisions are seen for the N=0, f_1 level.

The total height of the bar corresponds to the total RET cross-sections. These are larger for NO(A)-Kr than OH(A)-Kr, both under thermal and superthermal conditions. The rotational constant of NO(A) is approximately $1.99\,\mathrm{cm}^{-1}$ [158], whereas for OH(A) it is approximately $17.36\,\mathrm{cm}^{-1}$ [159] due to the different moments of inertia of the two radicals. Therefore, in NO(A) the rotational states are significantly closer in energy than in OH(A), meaning less energy needs to be transferred for RET to take place. This results

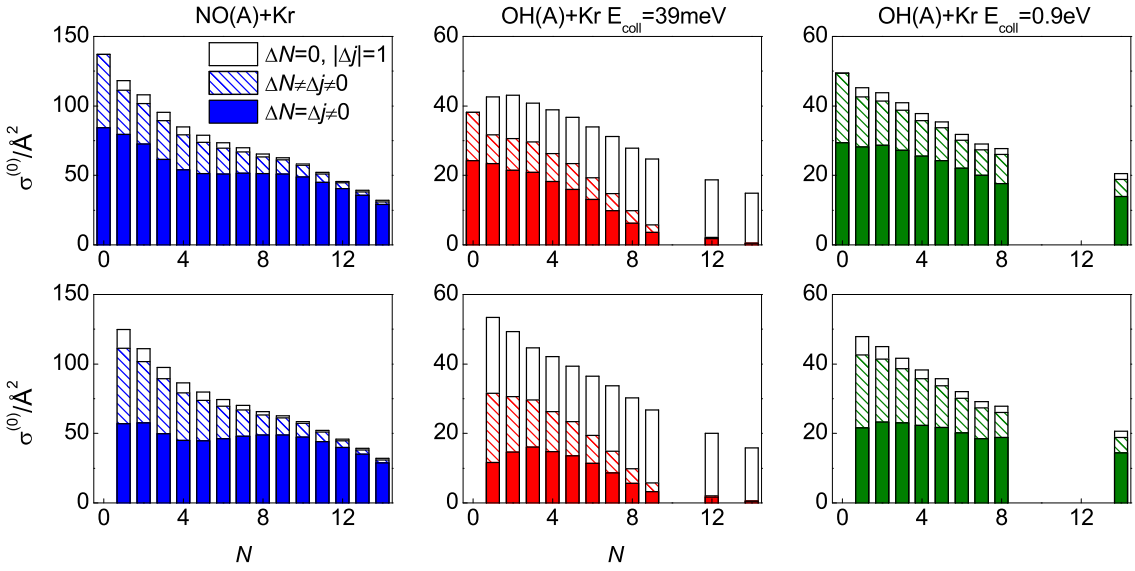


Figure 4.4: RET cross-sections for NO(A)-Kr (left panels), thermal OH(A)-Kr (middle panels) and superthermal OH(A)-Kr (right panels) for the f_1 $(N+S)$ spin-rotation level (top row) and the f_2 $(N-S)$ spin-rotation level (bottom row), resolved into contributions from different processes. The total height of the bar shows the total RET cross-section. The top (white) section of the bar corresponds to pure spin-rotation changing collisions ($\Delta N = 0$, $\Delta j = \pm 1$), the middle (striped) section of the bar to collisions which change both N and the spin-rotation state ($\Delta N \neq \Delta j \neq 0$) and the bottom (solid) section of the bar to collisions which change N but conserve the spin-rotation state ($\Delta N = \Delta j \neq 0$).

in larger RET cross-sections. The total cross-sections for OH(A)-Kr under thermal and superthermal conditions are of a comparable magnitude, even though more rotational levels will be energetically accessible at the higher collision energy. The total height of the bottom two sections of the bar shows the cross-sections for collisions which change the rotational state. As can be seen, this makes a larger contribution to the total RET cross-sections under superthermal conditions than under thermal conditions, and therefore collisions which change the rotational state are more prevalent at the higher collision energy. This is particularly apparent for N=14, where the only contribution to the RET cross-section under thermal conditions is from spin-rotation state changing collisions, whereas collisions which change N are still seen under superthermal conditions. It should be noted that at 39 meV, there is insufficient energy to increase the rotational state of OH(A) from N=14 to N'=15. Under the approximations made spin-rotation changing collisions do not require a change in energy, only a large change in the direction of $\boldsymbol{N}$, as the electron

spin is considered to be a spectator to the collision. The attractive and anisotropic nature of the PES is sufficient for these to occur, and therefore, this is the main contribution for OH(A) under thermal conditions. For NO(A)-Kr and OH(A)-Kr under superthermal conditions, where significantly more rotational levels are energetically accessible, spin-rotation conserving collisions dominate. As these collisions are more impulsive in nature, they are not accompanied by a significant change in the direction of $\boldsymbol{N}$.

4.3.2 Experiment vs theory: Rotational energy transfer cross-sections for OH(A)+Kr

The RET cross-sections could be obtained experimentally for OH(A)-Kr under thermal conditions by fitting the summed fluorescence decays from the elastic depolarisation measurements as discussed in section 3.4.2. The results are presented in figure 4.5, where the experimental results (filled triangles) are compared with those from QCT calculations (open circles). The left hand panel shows the results for the f_1 spin-rotation level, and the right hand panel the results for the f_2 spin-rotation level. There is good agreement between the experimental and theoretical values of the RET cross-sections, although the QCT calculations tend to underestimate the RET cross-sections slightly at low N. When fitting the data to obtain the RET cross-sections, only the first 100 ns were used in the analysis to avoid including effects of secondary collisions which result in the repopulation

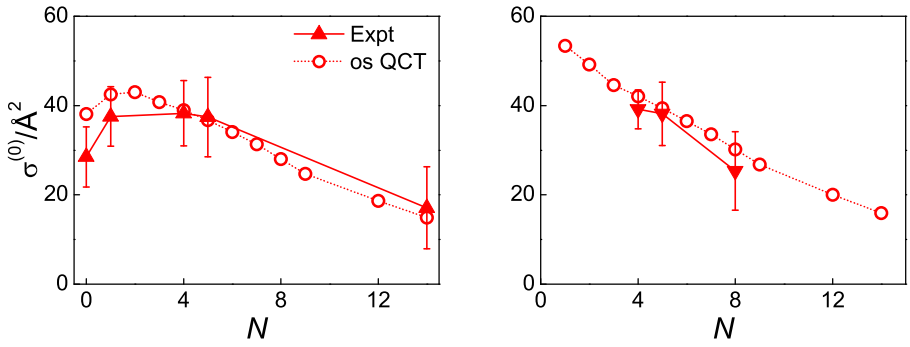


Figure 4.5: Total RET cross-sections for recorded under thermal conditions for OH(A)-Kr for the f_1 (left panel) and f_2 (right panel) spin-rotation levels. The experimental results (filled triangles) are compared with those from QCT (open circles) calculations.

of the initially populated spin-rotation level. This population back transfer is likely to be most significant at low N, which could lead to the small discrepancy between the experimental and theoretical values. It is also possible that as the QCT calculations do not include the effects of electronic quenching, this may contribute to the slight disagreement between the RET cross-sections at low N.

4.4 Collisional depolarisation

4.4.1 Theoretical depolarisation cross-sections

A comparison of the OH(A)-Kr disalignment cross-sections obtained from fixed energy QM (open squares) and QCT (open circles) calculations run at 39 meV is presented in

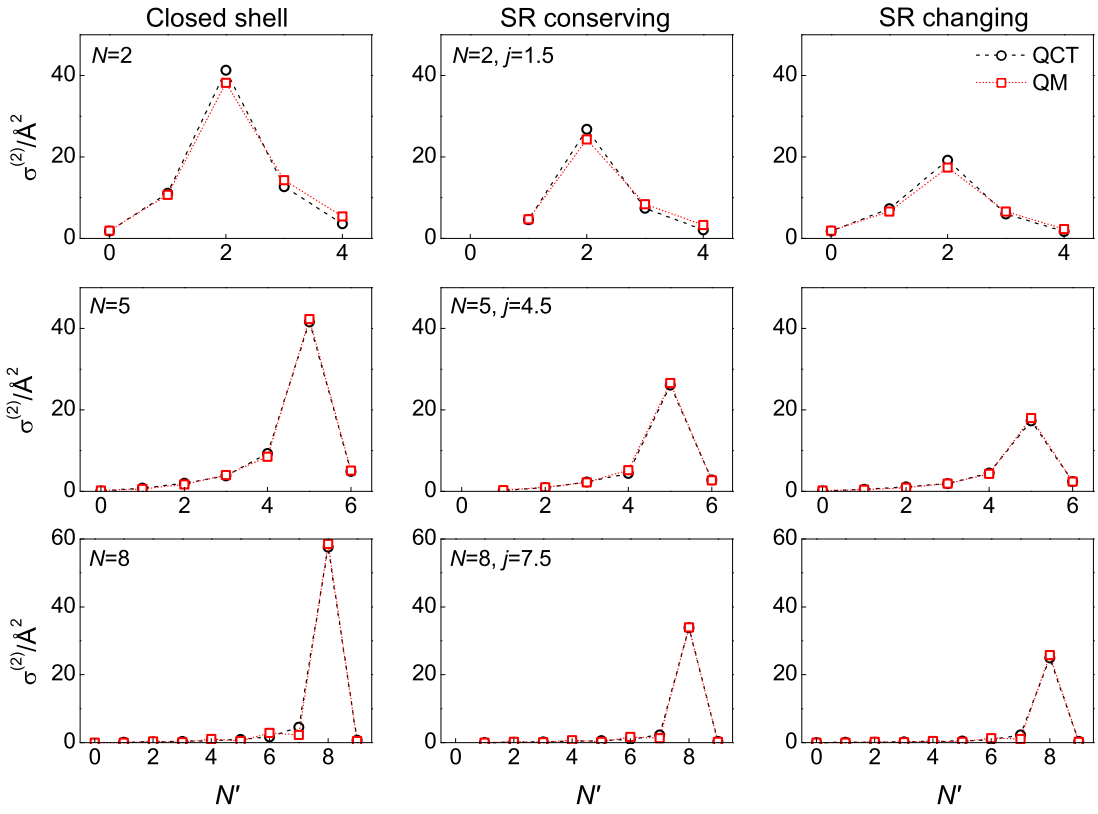


Figure 4.6: Comparison of the thermal OH(A)-Kr disalignment cross-sections obtained from QM (open squares) and QCT (open circles) calculations for N=2 (top row), N=5 (middle row) and N=8 (bottom row). The left hand column shows the results for the closed shell calculations, and the middle and right hand columns open shell results for the f_2 spin-rotation level. The middle column shows the spin-rotation (SR) conserving cross-sections and the right hand column the spin-rotation changing cross-sections.

figure 4.6. The top row corresponds to cross-sections for N=2, the middle N=5 and the bottom N=8, and the results are resolved into final rotational state, N'. The closed shell results are presented in the left hand column, and there is again good agreement between the results from the QCT and QM calculations. Similarly good agreement is seen in a comparison of the open shell results in the middle and right hand column, where the open shell QCT cross-sections have been obtained using the tensor opacity formalism described previously. The results are presented for the f_2 $(N-S)$ spin-rotation level, with the middle column showing the cross-sections for collisions which conserve the spin-rotation level, and the right hand column cross-sections for spin-rotation changing collisions. It should be noted that although only the disalignment results for the f_2 spin-rotation level are presented here, there is also excellent agreement for the f_1 level, and for the disorientation cross-sections. The level of agreement again validates the use of the QCT calculations, and therefore only these will be compared with the experimental results presented throughout the rest of this chapter.

The experimental depolarisation cross-sections were measured for either the f_1 or f_2

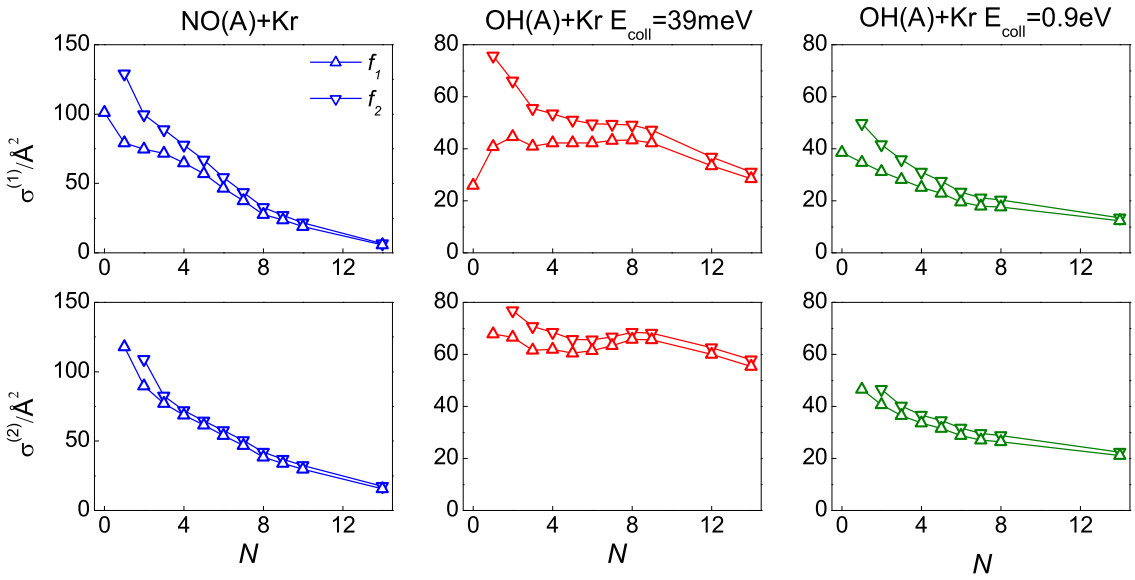


Figure 4.7: Total disorientation (top row) and disalignment (bottom row) cross-sections obtained from QCT calculations for the f_1 (upwards pointing triangles) and f_2 (downwards pointing triangles) spin-rotation levels for NO(A)-Kr (left hand column), thermal OH(A)-Kr (middle column) and superthermal OH(A)-Kr (right hand column).

spin-rotation level, for a given N. Therefore it is instructive to consider the differences in cross-section for the two spin-rotation levels before considering the experimental results. The disorientation (top row) and disalignment (bottom row) cross-sections obtained from fixed energy QCT calculations are shown in figure 4.7 for NO(A)-Kr (left column), thermal OH(A)-Kr (middle column) and superthermal OH(A)-Kr (right column). The upwards pointing triangles are for the f_1 spin-rotation level, and the downwards pointing triangles for the f_2 spin-rotation level. It should be noted that it is not possible to align j=0.5. The cross-sections tend to be larger for the f_2 spin-rotation level, with this difference most pronounced at low N. As has been mentioned previously, the electron spin can be treated as a spectator to the collision, meaning the direction of the electron spin cannot be changed by the collision. It follows that a given change in the direction of $\boldsymbol{N}$ causes more depolarisation for the f_2 $(N - S)$ spin-rotation level than for the f_1 $(N + S)$ level, and that this difference will be more pronounced at lower N.

4.4.2 Experiment vs theory: Depolarisation cross-sections for NO(A)+Kr

The total depolarisation cross-sections determined experimentally are shown as filled triangles in figure 4.8. The left hand panel shows the disorientation cross-sections, and the right hand panel the disalignment cross-sections. All cross-sections presented are for the f_2 spin-rotation level. In both cases, the cross-sections tend to decrease as N increases. As discussed previously, the RET cross-sections also drop as N increases. The (inelastic) depolarisation cross-sections are related to the RET cross-sections *via* $\sigma^{(k)} = \sigma^{(0)}(1-a^{(k)})$. Therefore (and neglecting elastic depolarisation), the drop in depolarisation cross-sections is partly due to the decrease in the RET cross-sections. However, there is another factor, $a^{(k)}$, which reflects the extent to which collisions cause depolarisation. At higher N, a larger momentum transfer is required to change the direction of $\boldsymbol{N}$ through a given angle. Therefore, collisions tend to become less depolarising as N increases, which again results in a decrease in the depolarisation cross-sections. Both the drop in RET cross-sections

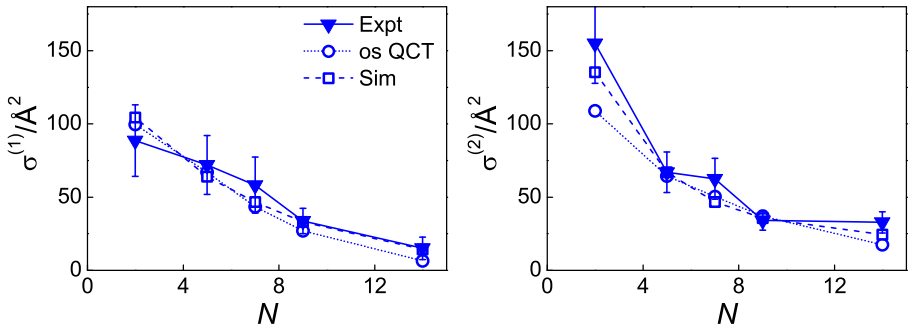


Figure 4.8: Comparison of the NO(A)-Kr depolarisation cross-sections determined experimentally (filled triangles) with those from QCT calculations (open circles) and experimental simulations (open triangles). The left hand panel presents the disorientation cross-sections, and the right hand panel the disalignment cross-sections. All data are shown for the f_2 $(N-S)$ spin-rotation level.

and the less depolarising nature of collisions will contribute to the observed decrease in depolarisation cross-sections.

It should also be noted that the disorientation cross-sections tend to be smaller than the disalignment cross-sections for the same N. This is because it is easier to change the plane of rotation of the molecule (*i.e.* cause disalignment) than it is to change the direction of rotation of the molecule (*i.e.* cause disorientation).

The experimental results are also compared with results from QCT calculations (shown as open circles) in figure 4.8. As can be seen, there is in general good agreement between the experimental and theoretical values of the depolarisation cross-sections, although the QCT results tend to underestimate the disalignment cross-sections at low N. These calculations do not include any correction for dephasing effects which are indistinguishable from depolarisation experimentally. As discussed in section 3.5, dephasing occurs because each hyperfine level of the radical has a different value of g_F. Therefore, when different hyperfine levels are populated by collisions, each hyperfine level will precess at a different frequency in the applied magnetic field ($\omega_{L_F} \propto g_F$). This means the total recorded signal is a sum of many beat signals with slightly different frequencies, which leads to a loss of the quantum beat even in the absence of depolarisation.

As discussed in the previous chapter, the importance of dephasing depends on the

extent to which collisions populate different hyperfine levels. At low N, the g_F values vary more quickly for different states. As shown in figure 4.3, RET populates more N' states at low N, meaning dephasing is likely to be more important. However, the main contribution to dephasing is from collisions which change the spin-rotation level of the radical (in this case corresponding to populating the f_1 state). This results in the radical precessing in the opposite direction in the applied magnetic field to those in the initially prepared state. As shown in figure 4.4 spin-rotation changing collisions are also more prevalent at lower N. Therefore, it is expected that dephasing would be more significant at lower N. The results from experimental simulations which include this effect are shown as open squares in figure 4.8. The difference between the QCT results and the simulation results reflect the contribution that dephasing is expected to make to the depolarisation cross-sections. As can be seen, the difference between the two sets of results is small showing dephasing makes only a minor contribution to the depolarisation cross-sections. However, inclusion of this effect does bring the theoretical and experimental disalignment cross-sections into better agreement.

4.4.3 Experiment vs theory: Depolarisation cross-sections for OH(A)+Kr

Thermal

The total depolarisation cross-sections measured experimentally for OH(A)-Kr under thermal conditions (filled triangles) are presented in figure 4.9. The left hand panel shows the disorientation cross-sections, and the right hand panel the disalignment cross-sections. The trend in the depolarisation cross-sections is significantly different to that in NO(A)-Kr discussed in the previous section, as the cross-sections increase to N=8 before dropping slightly to N=14. This is not due to the different spin-rotation levels used to record the cross-sections, as the lower states were recorded using the f_2 spin-rotation levels (downwards pointing triangles), and only N=14 was recorded using the f_1 spin-rotation level

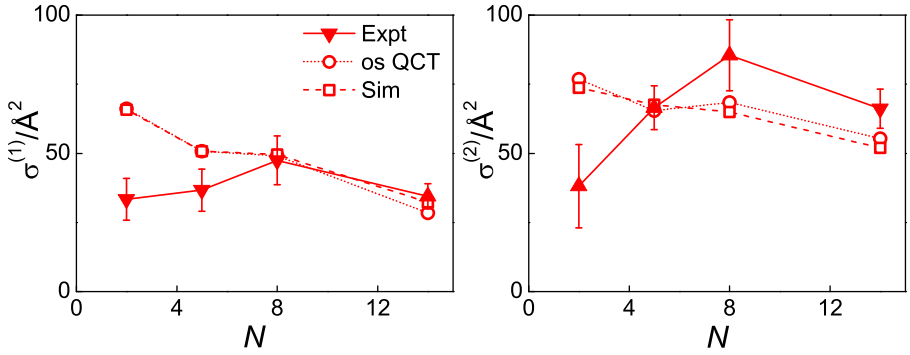


Figure 4.9: Comparison of the total thermal OH(A)-Kr disorientation (left panel) and disalignment (right panel) cross-sections determined experimentally (filled triangles) with those from QCT calculations at a fixed collision energy of 39 meV (open circles), and from full experimental simulations (open squares). The experimental results for the f_1 spin-rotation level are shown as upwards pointing triangles, and the f_2 spin-rotation levels as downwards pointing triangles. The results from the theoretical calculations are for the same spin-rotation level as that observed experimentally.

(upwards pointing triangle). As shown in figure 4.7, there is no significant difference between the f_1 and f_2 cross-sections at high N.

The results from the QCT calculations (open circles) are also included in the figure, for the same spin-rotation level as observed experimentally. The QCT calculations fail to capture the unusual trends seen in the experimental depolarisation cross-sections. This is not a failure of the QCT method, as shown in figures 4.3 and 4.6, the results from the QM and QCT calculations are in excellent agreement.

A possible reason for the disagreement between the experimental and theoretical calculations is that electronic quenching leads to significant loss of the excited state population in OH(A)-Kr. This effect is not included in the theoretical calculations, which only consider adiabatic trajectories across the excited state PES. As shown in figure 4.1, the electronic quenching cross-sections decrease as N increases. The agreement between the experimental and theoretical cross-sections tends to be better at higher N, where electronic quenching is less significant. This agreement for higher N states where electronic quenching could be neglected, as it has been in the previous studies [108, 109, 116, 119], suggests this could be the source of the discrepancy between the experimental and theoretical depolarisation cross-sections at lower N.

Experimental simulations were also performed to determine the contribution that dephasing makes to the depolarisation cross-sections. These are shown in figure 4.9 as open squares. Again, the difference between the QCT calculations and the simulations shows the significance of dephasing. As can be seen, the two sets of results are indistinguishable, showing that dephasing does not make a contribution to the depolarisation cross-sections. Due to the anisotropy of the PES, every collision causes complete depolarisation under thermal conditions, meaning that the states populated after collision are effectively unpolarised and so do not contribute to the polarisation signal.

Superthermal

It is possible to increase the collision energy of the OH(A)-Kr collisions experimentally by decreasing the time delay between the pump and probe lasers. The results from this are presented in figure 4.10, with the left hand panel again showing the disorientation cross-sections, and the right hand panel the disalignment cross-sections. In both cases, the experimental results (filled triangles) tend to fall with increasing N.

The experimental cross-sections are compared with the results from fixed energy QCT calculations performed at 0.9 eV (open squares) and 1.5 eV (open circles). The results

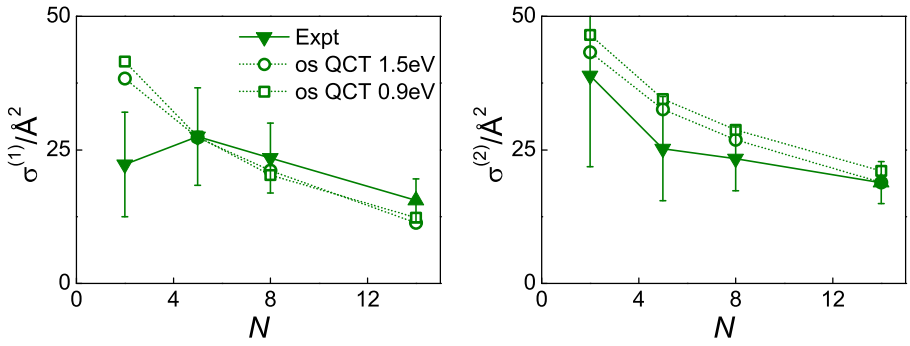


Figure 4.10: Comparison of the total superthermal OH(A)-Kr disorientation (left panel) and disalignment (right panel) cross-sections determined experimentally (filled triangles) with those from QCT calculations at a fixed collision energy of 0.9 eV (open squares) and 1.5 eV (open circles). The experimental results for the f_1 spin-rotation level are shown as upwards pointing triangles, and the f_2 spin-rotation levels as downwards pointing triangles. The results from the theoretical calculations are for the same spin-rotation level as that observed experimentally.

for the cross-sections at these two collision energies are very similar, showing that the depolarisation cross-sections do not change significantly over the range of collision energies sampled experimentally. There is, in general, better agreement between the experimental results and the results from the QCT calculations than observed under thermal conditions, although the QCT calculations tend to overestimate the experimental disalignment cross-sections. However, given the uncertainties in the collision energy of these experiments, the agreement between the experimental and theoretical cross-sections is reasonable.

The QCT calculations also significantly overestimate the N=2 disorientation cross-section. To measure the disorientation cross-sections, it was necessary to disperse the fluorescence with a monochromator. Therefore, emission branches at the edge of the monochromators bandwidth are less likely to be detected, which could lead to a decrease in the disorientation cross-section measured experimentally. As at low N there is more RET, collisions are likely to populate more N' levels. To determine whether this is the source of the discrepancy for N=2, experimental simulations were performed where the emission was appropriately weighted to account for this, as discussed in section 3.5. However, this did not lead to a significant reduction in the returned cross-sections, and so is not the reason for the disagreement. It should be noted that this does not need to be considered for the alignment measurements, as the monochromator was used with the minimum possible resolution.

Thermal vs superthermal

The effect that collision energy has on the total depolarisation cross-sections can now be considered. Figure 4.11 presents the RET (left panel), disorientation (middle panel) and disalignment (right panel) cross-sections for OH(A)-Kr under thermal (red triangles) and superthermal (green triangles) conditions. Experimental results have been used as far as possible, but for the N=2 thermal RET cross-section and all the superthermal RET cross-sections, the results from the QCT calculations have been used. As the collision energy is increased, the depolarisation cross-sections tend to decrease, as can be seen from

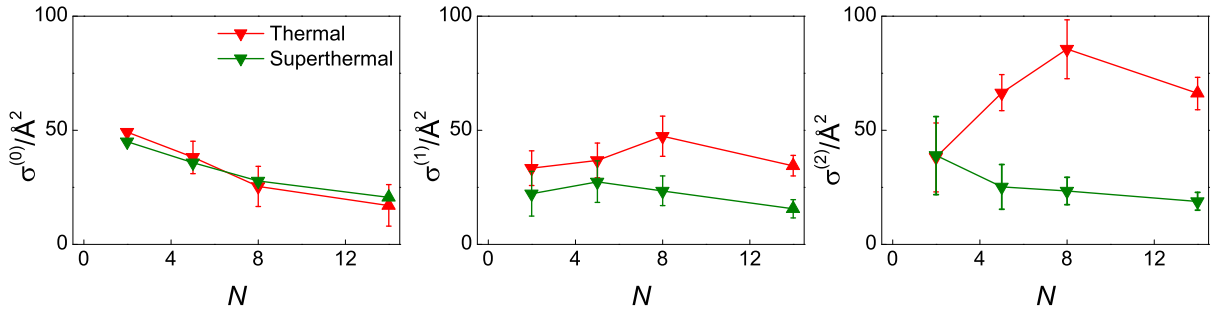


Figure 4.11: RET (left panel), disorientation (middle panel) and disalignment (right panel) cross-sections for OH(A)-Kr under thermal (red triangles) and superthermal (green triangles) conditions. All the cross-sections are experimental results other than the N=2 thermal RET cross-section, and the superthermal RET cross-sections which have been taken from QCT calculations.

the middle and right panels of the figure. The (inelastic) depolarisation cross-sections are related to the RET cross-sections *via* $\sigma^{(k)} = \sigma^{(0)}(1 - a^{(k)})$. As shown in the left hand panel of the figure, the RET cross-sections are approximately the same at the two collision energies. It follows that as the collision energy is increased, the collisions become less depolarising, *i.e.* $a^{(k)}$ is closer to unity. This is as expected, as at the higher collision energy, the krypton will be travelling too quickly to fully sample the attractive potential well, and therefore the collisions will cause less depolarisation.

Previous studies have shown that the collisional quenching cross-sections also fall with increasing collision energy [230–232]. This is consistent with the collisions becoming less depolarising, as both observations suggest that the krypton samples the deep potential wells less as the collision energy is increased. Consequently, the importance of electronic quenching under superthermal conditions will be less than that under thermal conditions. As the agreement between the theoretical and experimental values of the depolarisation cross-sections is better at the higher collision energy, this again suggests that the discrepancy is due to the role of electronic quenching.

4.4.4 Elastic depolarisation cross-sections

The rotational energy levels are sufficiently spaced in OH(A)-Kr to allow the measurement of the elastic depolarisation cross-sections to be made under thermal conditions using a monochromator. This allows the fluorescence to be recorded from just the initially populated spin-rotation level, and consequently elastic depolarisation cross-sections to be determined. The disorientation (top row) and disalignment (bottom row) cross-sections are presented in figure 4.12 for the f_1 (left column) and f_2 (right column) spin-rotation level. The experimental results (filled triangles) are compared with those from QCT calculations (open circles). There is, in general, good agreement between the experimental and theoretical values of the depolarisation cross-sections although the QCT results show less of an N dependence than the values obtained experimentally. It should be noted that the N=0, j=0.5 disorientation cross-section is necessarily zero. The only contribution to the

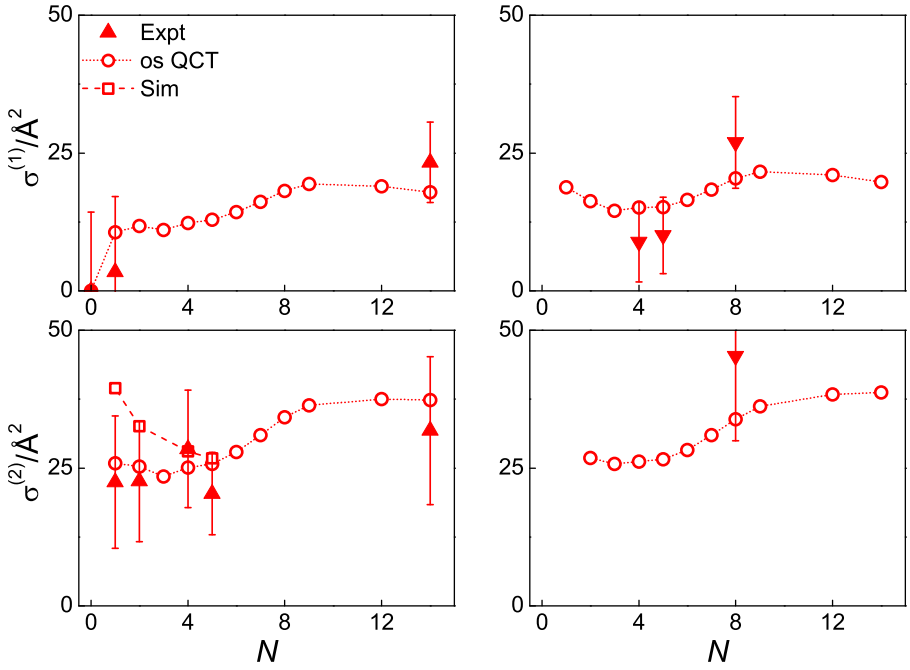


Figure 4.12: Comparison of the elastic thermal OH(A)-Kr disorientation (top row) and disalignment (bottom row) cross-sections measured experimentally (filled triangles) with those from QCT (open circles) calculations. The left hand column presents the results for the f_1 spin-rotation level, and the right hand column those for the f_2 spin-rotation level. The results for full experimental simulations which take into account the effects of satellite lines are shown in the bottom left panel as open squares.

rotational angular momentum for this state is the electronic spin (neglecting the nuclear spin, although the same argument applies). As the spin is a spectator to the collision, it is not possible for the collision to change its direction, and therefore no depolarisation can occur. This results in the depolarisation cross-sections being zero within the errors.

The elastic depolarisation cross-sections appear to increase as N increases. Efficient elastic depolarisation occurs through 'following' type trajectories [104, 105, 108], where the OH(A) and krypton are trapped in a collision complex due to the attractive nature of the PES, which survives for several rotational periods. At higher N, the radical rotates faster, resulting in the krypton sampling an averaged potential, as shown in figure 4.2. However, to cause elastic depolarisation the krypton needs to approach out of the plane of the radicals rotation, reducing the extent to which the potential is averaged. Consequently, this averaging is not sufficient to suppress the anisotropy and attractive nature of the PES, with the result that elastic depolarisation is maintained to high N.

The elastic disalignment cross-sections for N=1, 2, 4 and 5 were recorded with Q_{11} excitation and emission. The resolution of the monochromator for these states was not sufficient to separate out the fluorescence from only the initially populated state, with the result that the recorded signal contained contributions from unresolved satellite lines. These correspond to emission from the other spin-rotation level of the initially populated N level. Population of this state is a spin-rotation level changing collision which results in significant dephasing as the radical precesses in the applied magnetic field in the opposite direction to the initially prepared state. Detailed experimental simulations were run to account for this, the results from which are shown as open squares in figure 4.12. Including this effect increases the depolarisation cross-sections, particularly at low N, and makes the agreement between the theoretical and experimental disalignment cross-sections worse. It should be noted that the disalignment cross-sections for N=8 and 14 were recorded using P branch excitation and emission, and therefore satellite lines did not contribute to the signal, so this correction was not considered.

Although it is not possible to measure the elastic depolarisation cross-sections for

NO(A)-Kr or OH(A)-Kr under superthermal conditions, values can be obtained from the QCT calculations. The contribution that elastic depolarisation makes to the total depolarisation cross-sections is shown in figure 4.13. The middle column shows the thermal OH(A)-Kr total (filled triangles) and elastic (open triangles) depolarisation cross-sections determined experimentally, the left hand column the total NO(A)-Kr depolarisation cross-sections measured experimentally (filled triangles), and the elastic depolarisation cross-sections obtained from QCT calculations (open circles), and the right hand column the total experimental superthermal OH(A)-Kr cross-sections (filled triangles), and the elastic cross-sections determined from QCT calculations (open circles). The top row presents the results for the disorientation cross-sections, and the bottom row the results for the disalignment cross-sections. For NO(A)-Kr, elastic depolarisation makes a far smaller

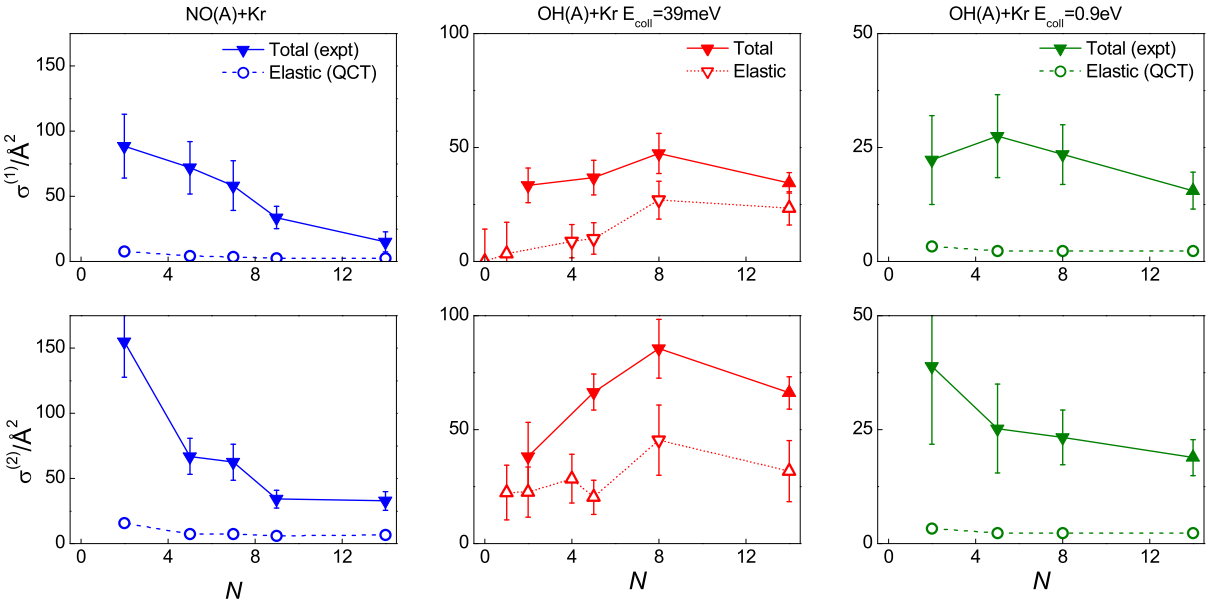


Figure 4.13: Comparison of the total depolarisation cross-sections (filled triangles) and elastic depolarisation cross-sections (open triangles) measured experimentally for OH(A)-Kr under thermal conditions (middle column), and the total experimental depolarisation cross-sections for NO(A)-Kr (left column) and superthermal OH(A)-Kr (right column) with the elastic depolarisation cross-sections from QCT calculations (open circles). The top row shows the disorientation cross-sections, and the bottom row the disalignment cross-sections. The experimental results for the f_1 spin-rotation level are shown as upwards pointing triangles, and the f_2 spin-rotation levels as downwards pointing triangles. The results from the theoretical calculations are for the same spin-rotation level as that observed experimentally.

contribution to the total depolarisation cross-sections than for OH(A)-Kr at the same collision energy. This again reflects the smaller rotational energy level spacing in NO(A) compared to OH(A), which makes inelastic transitions more probable in NO(A) than in OH(A), and the more impulsive nature of NO(A)-Kr collisions. As the collision energy is increased, elastic depolarisation plays less of a role as more rotational energy levels become energetically accessible. The collisions also become more impulsive, as the krypton is travelling too quickly to fully sample the attractive part of the PES, meaning that they become less depolarising. However, in all cases elastic depolarisation becomes more significant as N increases, as more energy is required to bring about an inelastic transition. Perhaps the most striking feature in the plots is that the total depolarisation cross-sections mirror the trends in the elastic depolarisation cross-sections. Therefore, the unusual trend in the total thermal OH(A)-Kr depolarisation cross-sections discussed previously can be attributed to the importance of elastic depolarisation for OH(A), and the anisotropy of the PES which is sufficient to allow efficient depolarisation to occur even at high N.

4.4.5 Inelastic depolarisation cross-sections

From a knowledge of the total depolarisation cross-sections and the elastic depolarisation cross-sections it is possible to calculate the inelastic depolarisation cross-sections as the difference between the two. The errors associated with the inelastic cross-sections were determined as discussed in section 3.4.3. The experimental inelastic depolarisation cross-sections for thermal OH(A)-Kr (filled triangles) are compared with those from the QCT calculations (open circles) in figure 4.14. As the elastic disorientation cross-section for N=2 has not been measured experimentally, a value has been estimated to allow the inelastic disorientation cross-section for N=2 to be included. Again, there is disagreement between the experimental and theoretical values of the cross-sections, with the theoretical cross-sections dropping more significantly with N than is observed experimentally. The largest discrepancy is again at low N, where the krypton will experience the full anisotropy of the PES. As discussed previously, the faster rotation of the radical at higher N averages

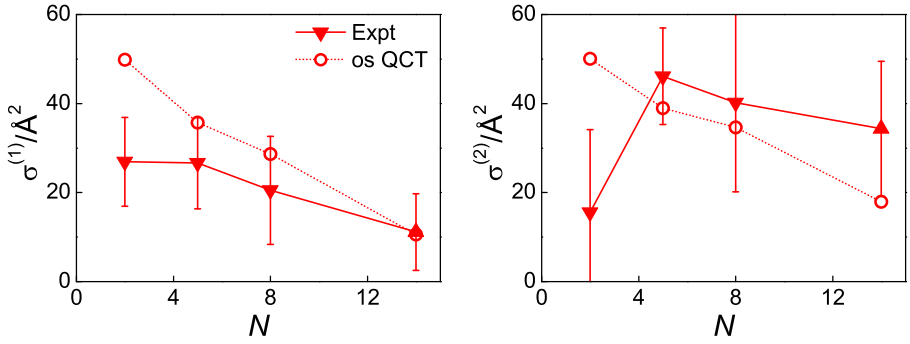


Figure 4.14: Comparison of the inelastic thermal OH(A)-Kr disorientation (left panel) and disalignment (right panel) cross-sections determined experimentally (filled triangles) with those from QCT calculations at a fixed collision energy of 39 meV (open circles). The experimental results for the f_1 spin-rotation level are shown as upwards pointing triangles, and the f_2 spin-rotation levels as downwards pointing triangles. The results from the theoretical calculations are for the same spin-rotation level as that observed experimentally.

the potential that the krypton experiences. Therefore at lower N the potential will play a more significant role, where any inaccuracies in the attractive part of the PES will be magnified.

Another possibility is that electronic quenching is more significant at low N, and this is not taken into account in the theoretical calculations. As the inelastic depolarisation cross-sections and the RET cross-sections are related *via* $\sigma^{(k)} = \sigma^{(0)}(1-a^{(k)})$, the good agreement between the experimental and theoretical RET cross-sections shown in figure 4.5 implies that the discrepancy between experiment and theory for the inelastic depolarisation cross-sections lies in the extent to which collisions cause depolarisation. Collisions which sample the deep potential well of the PES would be expected to cause significant depolarisation. However, as discussed in section 4.2, the OH(A) would also be more likely to be quenched if it samples the attractive well and forms a complex with the krypton. Therefore, these collisions would not contribute to the experimentally measured rate of depolarisation, but would be included in the theoretical calculations, which would give rise to the observed disagreement between the two sets of data at low N. As the agreement between the elastic depolarisation cross-sections measured experimentally and calculated theoretically is generally better than observed in this case, the main source of the disagreement between

the experiment and theory for the total depolarisation cross-sections can be attributed to the contribution inelastic depolarisation makes.

To determine the extent to which collisions cause depolarisation for each of the systems considered here, a comparison of the RET and inelastic depolarisation cross-sections is presented in figure 4.15. The RET (open diamonds for f_1, open squares for f_2), inelastic disorientation (filled triangles) and inelastic disalignment (open triangles) cross-sections are shown for NO(A)-Kr (left panel), thermal OH(A)-Kr (middle panel) and superthermal OH(A)-Kr (right panel). As far as possible experimental data has been used, but where this is not possible the results from QCT calculations have been used. For NO(A)-Kr, the inelastic depolarisation cross-sections tend to be smaller than the RET cross-sections. This corresponds to $a^{(k)} > 0$, and depolarisation is relatively inefficient compared to RET. As the well depth of the NO(A)-Kr PES is approximately 140 cm^{-1} [171] which is less than the collision energy ($\frac{3}{2}k_{\mathrm{B}}T \approx 300\,\mathrm{cm}^{-1}$), the collisions are expected to be impulsive and will not cause significant depolarisation, as observed. In contrast, under thermal conditions the inelastic disorientation cross-sections for OH(A)-Kr are of a comparable magnitude to the RET cross-sections. Therefore, $a^{(1)} \approx 0$ and each collision effectively randomises

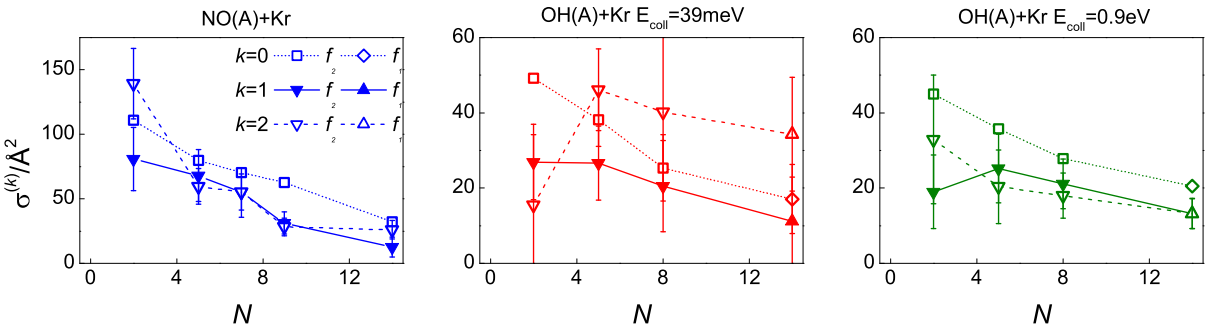


Figure 4.15: Comparison of the experimental RET (open diamonds for f_1, open squares for f_2) and inelastic depolarisation cross-sections (triangles) for OH(A)-Kr under thermal conditions (middle panel), and the theoretical RET (open diamonds for f_1, open squares for f_2) and experimental inelastic depolarisation cross-sections (triangles) for NO(A)-Kr (left panel) and OH(A)-Kr under superthermal conditions (right panel). The disorientation cross-sections are shown as filled triangles, and the disalignment cross-sections as open triangles. Experimental data has been used as far as possible, but where this is not available, QCT data has been used. The experimental depolarisation cross-sections for the f_1 levels are presented as upward pointing triangles, and those for the f_2 levels as downwards pointing triangles.

the direction of $\boldsymbol{j}$, and RET is accompanied by efficient depolarisation. The inelastic disalignment cross-sections are larger than the corresponding RET cross-sections. This results from the rate of disalignment being larger than the collision rate, and $a^{(2)} < 0$. The well depth of the OH(A)-Kr PES (approximately 6000 cm^{-1} [172]) is significantly larger than the collision energy and this deep potential well and associated anisotropy will lead to significant depolarisation. As the collision energy is increased, the trajectories will sample the deep potential well less, and the magnitude of the inelastic depolarisation cross-sections decreases compared to the RET cross-sections. This results in the inelastic depolarisation cross-sections being smaller than the RET cross-sections, so $a^{(k)} > 0$, as is observed in the case of NO(A)-Kr.

4.5 Comparison of OH(A)-Kr vs NO(A)-Kr

In this section, the results from the fixed energy QCT calculations for NO(A)-Kr and OH(A)-Kr at 39 meV, and OH(A)-Kr at 0.9 eV will be used to provide an insight into the different mechanisms of depolarisation. Particular emphasis will be placed on the role that the different PESs and mass combinations have on this, and the effect of the collision energy. All the results presented in this section treat NO(A) and OH(A) as closed shell radicals, and therefore N and j can be used interchangeably. Therefore, throughout this section an elastic transition is classed as one where $\Delta N \leq 0.5$.

4.5.1 Kinematics vs dynamics

To determine whether the differences in the RET cross-sections and depolarisation cross-sections for NO(A)-Kr and OH(A)-Kr are due to kinematic effects or due to their different potential energy surfaces, QCT calculations were run for N=2 using the OH-Kr masses on the NO-Kr PES (denoted ^{1}NO-Kr) and the NO-Kr masses on the OH-Kr PES (denoted O^{14}H-Kr). The results from these calculations are presented alongside those from the correct mass and PES combinations (denoted as ^{14}NO-Kr and O^{1}H-Kr) in figure 4.16. On

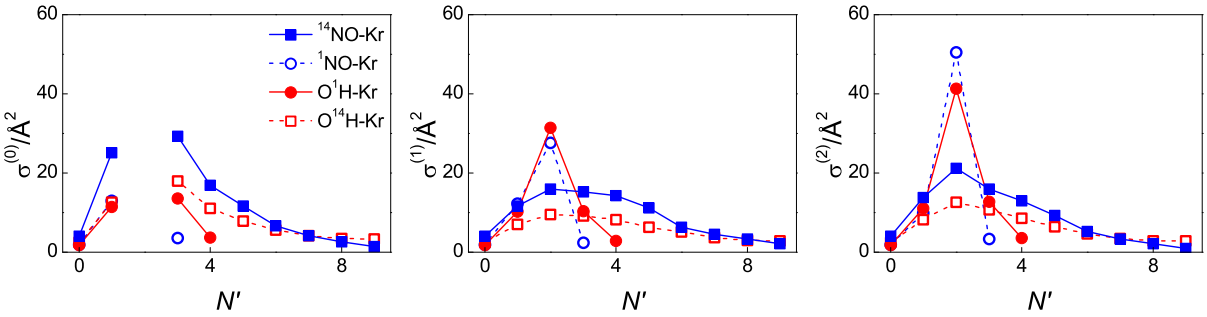


Figure 4.16: Closed shell RET (left panel), disorientation (middle panel) and disalignment (right panel) cross-sections from fixed energy QCT calculations showing the effects of kinematics vs dynamics. The results are for N=2 resolved into N', for the NO-Kr masses on the NO-Kr PES (^{14}NO-Kr), the NO-Kr masses on the OH-Kr PES (O^{14}H-Kr PES), the OH-Kr masses on the OH-Kr PES (O^{1}H-Kr) and the OH-Kr masses on the NO-Kr PES (^{1}NO-Kr).

changing from the OH mass to the NO mass (*i.e.* on going from ^{1}NO-Kr to ^{14}NO-Kr), both the RET cross-sections and the final number of rotational levels populated increases, as shown in the left hand panel of the figure. This is due to the different moments of inertia associated with each of the mass combinations, which results in the rotational energy level spacing being closer in ^{14}NO than ^{1}NO. For the same reason, elastic depolarisation is more important in ^{1}NO than ^{14}NO, as more energy transfer is required to bring about an inelastic collision. Changing the PES also influences the RET and depolarisation cross-sections. On going from O^{14}H-Kr to ^{14}NO-Kr (*i.e.* changing from the OH-Kr PES to the NO-Kr PES) the RET cross-sections increase, reflecting the longer range of the NO-Kr PES. However, making the same change for the OH masses (*i.e.* from O^{1}H-Kr to ^{1}NO-Kr) results in a decrease of the RET cross-sections. Therefore, the NO-Kr PES is too isotropic to bring about efficient RET when the rotational energy level spacing of the radical is larger. The magnitude of the RET cross-sections and depolarisation cross-sections are similar when the OH-Kr PES is used, whereas for the NO-Kr PES the depolarisation cross-sections are smaller than the RET cross-sections. Therefore, collisions on the OH-Kr PES cause more depolarisation, as would be expected due to the significantly more anisotropic and attractive nature of the PES.

4.5.2 Deflection functions: b vs θ

Scatter plots of the scattering angle θ as a function of impact parameter b are presented in figure 4.17 for NO(A)-Kr (left column), thermal OH(A)-Kr (middle column) and superthermal OH(A)-Kr (right column) for N=2 (top row), N=8 (middle row) and N=14 (bottom row). Elastic trajectories are shown in blue, and inelastic trajectories are shown in red. At large impact parameters the trajectories tend to be elastic, as the collisions are too 'glancing blow' to bring about RET. The maximum impact parameter at which RET occurs also decreases as N increases, reflecting the need for greater energy transfer to bring about RET at higher N. As the impact parameter is decreased, the collisions become more

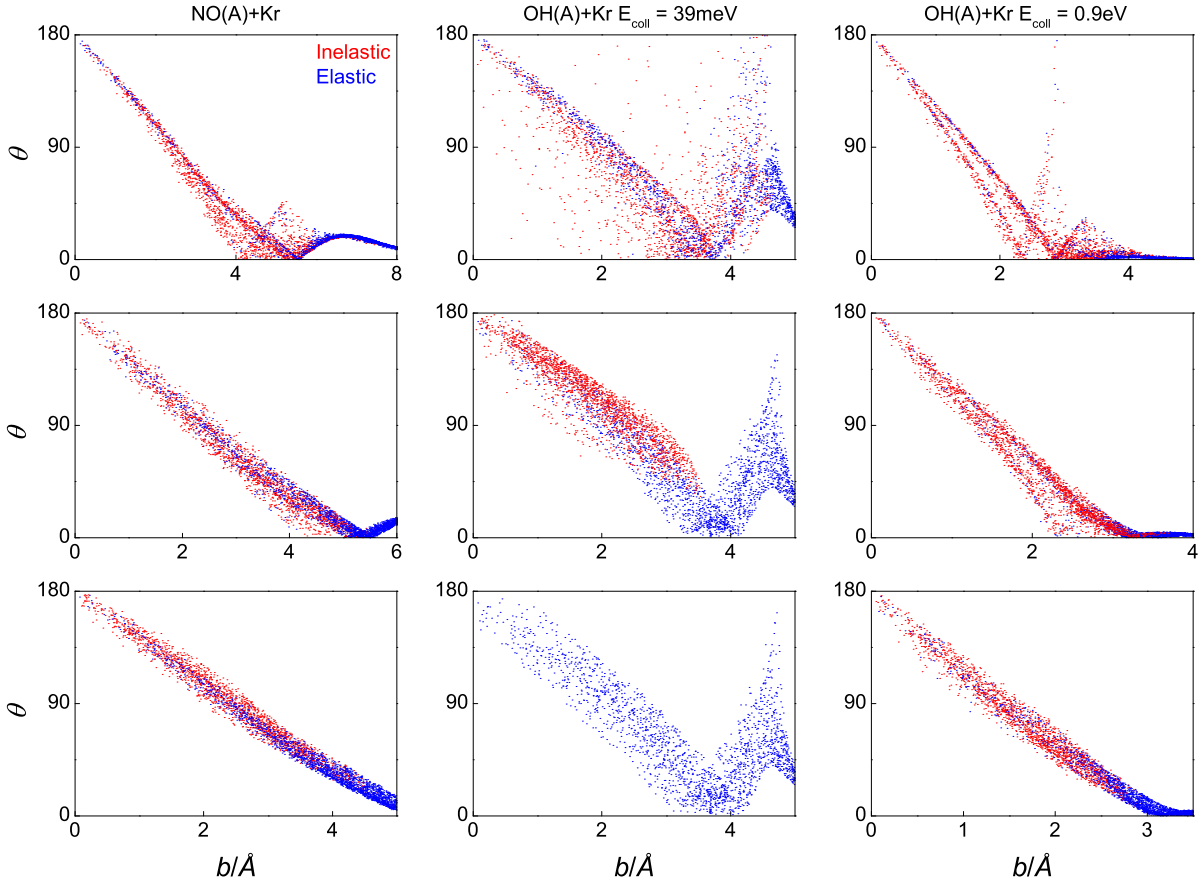


Figure 4.17: Scatter plots of scattering angle vs impact parameter for NO(A)-Kr (left column), thermal OH(A)-Kr (middle column) and superthermal OH(A)-Kr (right column) for N=2 (top row), N=8 (middle row) and N=14 (bottom row). Elastic trajectories are shown in blue, and inelastic trajectories in red. It should be noted that in the closed shell case presented here, there are no inelastic trajectories for N=14 for thermal OH(A)-Kr.

'head on' and the interaction between the radical and krypton is purely repulsive, leading to larger scattering angles. However, it should be noted that these collisions can still lead to elastic scattering.

As the impact parameter is increased, the attractive part of the PES starts to play a role. This is seen as a maximum in the deflection functions. The position of this maximum reflects the different positions of the most attractive parts of the PES, which gives rise to the maximum deflection. This maximum is not observed in the deflection functions for superthermal OH(A)-Kr for N=8 and N=14 as the krypton is travelling too quickly to fully sample the attractive part of the PES. Under thermal conditions, the influence of the attractive part of the potential is clearly visible for all N. The deep potential well allows complexes to form, where the krypton is trapped by the OH(A) and the motion of the Kr drags the radical around. As these complexes can fall apart at any point in the rotation, this leads to the band structure observed in the deflection functions. These trajectories will also lead to efficient depolarisation. As at higher N these trajectories are all elastic, and the trend in the elastic depolarisation cross-sections were attributed to the anisotropy and attractive nature of the PES, this supports the conclusions reached in section 4.4.4.

Unlike in OH(A)-Ar, where only the H end of the radical traps the Ar in a complex [119], both ends of the radical can trap the krypton, as shown in the middle panel of

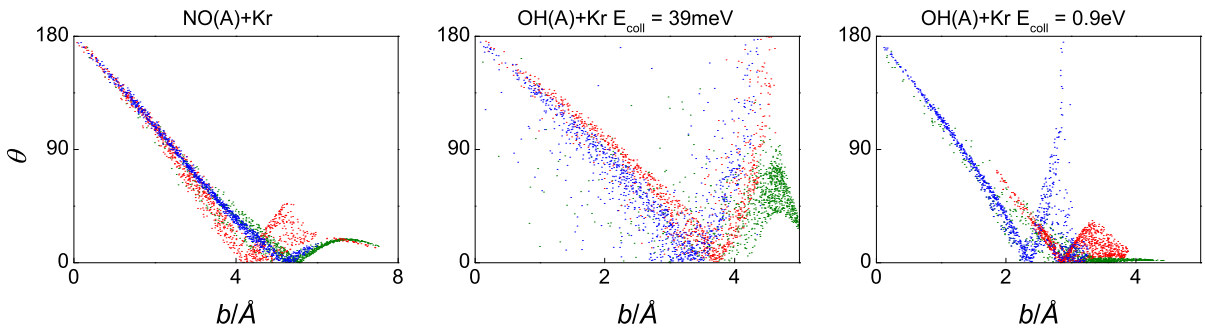


Figure 4.18: Scatter plots of scattering angle vs impact parameter for NO(A)-Kr (left), thermal OH(A)-Kr (middle) and superthermal OH(A)-Kr (right) for N=2. Trajectories that collide with the N/H end of the radical are shown in red, trajectories that collide with the O end in blue, and those corresponding to T-shaped approaches in green. No distinction has been made between elastic and inelastic trajectories in this figure.

figure 4.18, where the red and blue points correspond to the krypton colliding with the H and O ends of the radical respectively. Evidence for orbiting trajectories can also be clearly seen under superthermal conditions for N=2. Even at this higher collision energy (approximately 7200 cm^{-1}), the significant attractive potential well of the PES is still sufficient to trap the krypton, with the complex forming with the O end of the radical (well depth $\approx$ 6000 cm^{-1} [172]). Finally, this figure also shows that the double band structure observed in the deflection functions for OH(A)-Kr under superthermal conditions corresponds to the krypton interacting with either end of the OH(A) radical. This is not observed at the lower collision energy, as the anisotropy of the PES blurs out the structure, or in the case of the more symmetric NO(A) radical. However this does show that in NO(A)-Kr the two maxima in the deflection functions correspond to the krypton sampling either the N end or O end of the radical, a point which will be discussed further in section 5.8.1.

4.5.3 Opacity functions

The closed shell opacity functions obtained from the QCT calculations are shown in figure 4.19 for NO(A)-Kr (left column), thermal OH(A)-Kr (middle column) and superthermal OH(A)-Kr (right column) for N=2 (top row), N=8 (middle row) and N=14 (bottom row). The continuous red and blue lines show the opacity functions for inelastic and elastic collisions respectively. These necessarily sum to unity, as they represent the probability that a collision is inelastic or elastic, and as discussed previously in section 2.3.2 it is not possible to converge the elastic cross-sections in QCT. Therefore, at larger b all collisions are considered elastic, and the corresponding opacity function goes to unity. Inelastic collisions are more probable in NO(A) than in OH(A) under thermal conditions. As has been discussed previously, this can be attributed to the different moments of inertia of the two radicals which lead to the rotational levels being closer in energy in NO(A) than in OH(A). As the collision energy is increased, more rotational energy levels become energetically accessible, and inelastic collisions become more probable in OH(A). The range

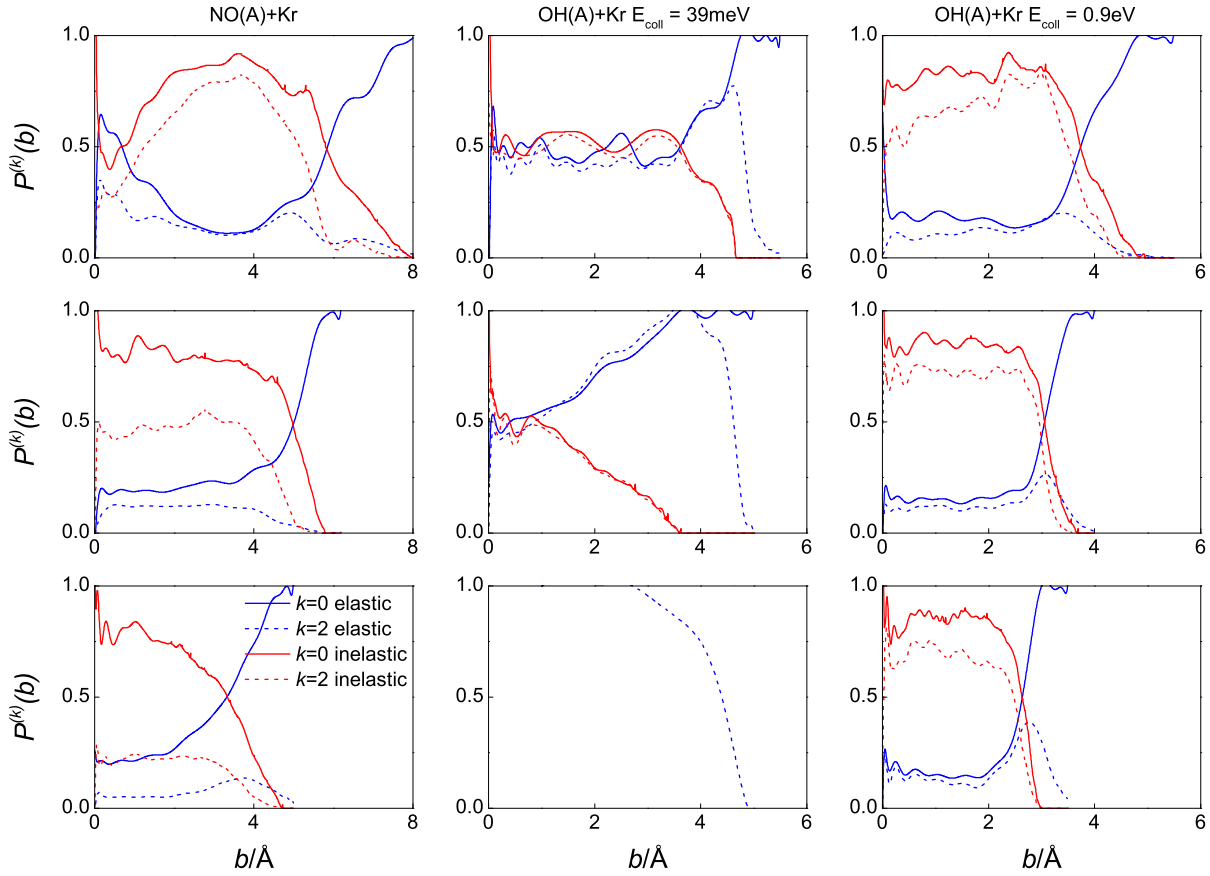


Figure 4.19: Closed shell QCT opacity functions for elastic (solid blue) and inelastic (solid red) collisions for NO(A)-Kr (left column), thermal OH(A)-Kr (middle column) and superthermal OH(A)-Kr (right column) for rotational states N=2 (top row), N=8 (middle row) and N=14 (bottom row). The dashed lines show the corresponding disalignment opacity functions. It should be noted that in the closed shell case presented here, there are no inelastic trajectories for N=14 for thermal OH(A)-Kr.

over which RET occurs is also greater in NO(A)-Kr than in OH(A)-Kr, both under thermal and superthermal conditions. This reflects the longer range of the NO(A)-Kr PES compared to the OH(A)-Kr PES. As noted in the preceding section, the range over which RET occurs decreases as N increases, as more energy transfer is required at higher N. Therefore, elastic collisions become more important as N increases, to the point where for N=14 in OH(A)-Kr under thermal conditions there are only elastic collisions.

The dashed red and blue lines show the extent to which the inelastic and elastic collisions cause disalignment respectively. These have been calculated using:

$$P^{(2)}(b) = P^{(0)}(b)(1 - a^{(2)}(b)) \tag{4.1}$$

As $a^{(2)}(b)$ can be negative, it immediately follows that the depolarisation opacity functions can be greater than one, and that, therefore the inelastic and elastic contributions do not sum to unity. It should also be noted that it is possible to converge the elastic values of $P^{(2)}(b)$ in the QCT calculations, as there is an impact parameter above which no elastic depolarisation will occur. For NO(A)-Kr, the collisions do not cause significant levels of depolarisation, with the collisions becoming less depolarising as N increases. There is also a small range of impact parameters over which RET occurs which is not accompanied by depolarisation. This also reflects the very impulsive nature of the collisions between NO(A) and krypton. In contrast, every collision in OH(A)-Kr under thermal conditions leads to a complete randomisation in the direction of $\boldsymbol{N}$. This efficient depolarisation is maintained over all impact parameters at which RET occurs, for all N. Elastic depolarisation also occurs over a larger range of impact parameters than RET at all N, and the maximum value of b at which there is elastic depolarisation is relatively insensitive to N. Therefore, elastic depolarisation is influenced by the long range part of the PES under thermal conditions. These observations can again be attributed to the attractive and highly anisotropic nature of the OH(A)-Kr PES. As the collision energy is increased, the collisions become less depolarising and the range over which depolarisation occurs decreases as N increases. At the higher collision energy, the collisions will become more impulsive in nature and probe the repulsive wall of the PES, and therefore the trends start to resemble those observed in NO(A)-Kr.

4.6 The role of electronic quenching

In this section, the possible reasons for the observed disagreement between the experimental and theoretical depolarisation cross-sections for OH(A)-Kr will be presented. To provide further insight into this, it is helpful to consider the results obtained previously for the collisional depolarisation for NO(A) with helium and argon [23, 116, 138], and for OH(A) with argon [23, 109, 119, 138]. These are presented in figure 4.20 for the collisional

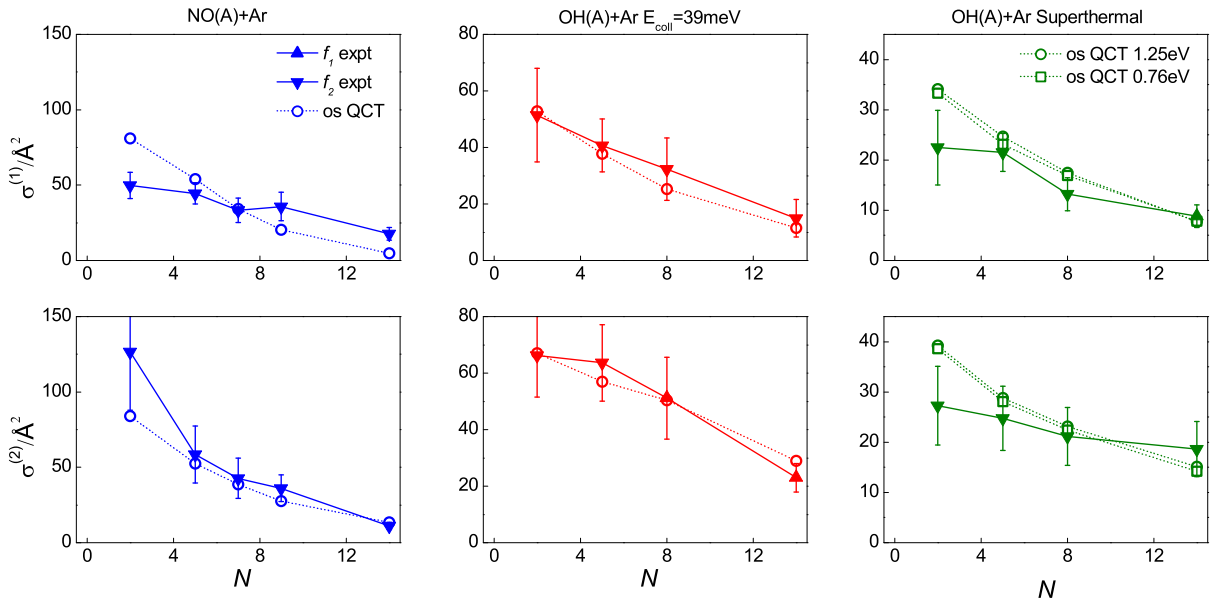


Figure 4.20: Comparison of the total disorientation (top row) and disalignment (bottom row) cross-sections determined experimentally (filled triangles) with those from QCT calculations (open symbols) for NO(A)-Ar (left column), thermal OH(A)-Ar (middle column) and superthermal OH(A)-Ar (right hand column). The experimental results for the f_1 spin-rotation level are shown as upwards pointing triangles, and the f_2 spin-rotation levels as downwards pointing triangles. The results from the theoretical calculations are for the same spin-rotation level as that observed experimentally. For the thermal data, the QCT results correspond to 39 meV (open circles) whereas for the superthermal data, the results from the QCT calculations at 0.76 eV (open squares) and 1.25 eV (open circles). Data taken from references [23, 109, 116, 119, 138, 233].

disorientation (top row) and collisional disalignment (bottom row) of NO(A) with argon (left column), OH(A) with argon under thermal conditions (middle column) and OH(A) with argon under superthermal conditions (right column) following photolysis of H_2O_2 at 193 nm. The experimental results are shown as filled triangles, with upwards pointing triangles corresponding to the f_1 spin-rotation level, and the downwards pointing triangles to the f_2 spin-rotation level. The total depolarisation cross-sections fall with increasing N, as observed in NO(A)-Kr. The results from the QCT calculations (open circles) run at 39 meV for NO(A)-Ar and OH(A)-Ar are compared with the experimental results in the left hand and middle column respectively. As can be seen, the results from the theoretical calculations are in excellent agreement with those observed experimentally. In the right hand column, the results from fixed energy calculations run at 0.76 eV (open squares) and

1.25 eV (open circles) are compared with the experimentally determined cross-sections. These energies are considered to represent the range sampled experimentally, which is different to that sampled in the OH(A)-Kr superthermal experiments, due to the different extent that collisions of Ar and Kr cause translational moderation (see section 3.4.4). Given the uncertainty in the collision energy, the agreement between the experiment and theory is again observed to be good. It should be noted that similarly good agreement between the theoretical calculations is observed in NO(A)-He [109], and in OH(A)-Ar following photolysis of H_2O_2 at 248 nm [119]. Therefore, good agreement between the experimental and theoretical calculations has been observed in all the cases studied other than OH(A)-Kr.

A possible reason for the disagreement between experiment and theory for OH(A)-Kr is that the OH(A) bond length is assumed to be fixed at its equilibrium values in the calculations. This assumption was also used in the NO(A)-Kr calculations presented in section 4.4.2, and for NO(A) with He and Ar [23, 109, 138] as well as for OH(A)-Ar [23, 108, 116, 119, 138], and as discussed above the agreement between the experimental and theoretical results has been good in all cases. The NO(A)-rare gas PESs have well depths of $<150\,\mathrm{cm}^{-1}$ [171] and for OH(A)-Ar the well depth is approximately $1700\,\mathrm{cm}^{-1}$ [206]. In comparison, the well depth of the OH(A)-Kr PES is approximately $6000\,\mathrm{cm}^{-1}$ [172], so the bond length of the radical is likely to change significantly when the Kr samples the deep potential well. However, if this was the source of the disagreement it would be expected that there would also be some evidence of this in the OH(A)-Ar results, as the depth of the potential well is a factor of five greater than the collision energy in the case of the thermal measurements. Therefore, although this assumption could contribute to the disagreement, it is unlikely to be the main reason for the disagreement between the two sets of results.

Another possible reason for the discrepancy between the experimental and theoretical depolarisation cross-sections is due to the importance of electronic quenching in OH(A)-Kr, as has been suggested throughout the chapter. For both the NO(A)-rare gas systems

[234, 235] and OH(A)-Ar [231, 232, 236, 237] the electronic quenching cross-sections are negligible under the conditions sampled in the quantum beat experiments. The effects of electronic quenching are not included in the QCT calculations, and as shown good agreement is observed between the experimental and theoretical depolarisation cross-sections where this can be neglected. This is not the case for OH(A)-Kr. The agreement between the two sets of results is better under superthermal conditions than thermal conditions, where the relative contribution of electronic quenching to the collision dynamics is smaller. The agreement is also observed to be better in the thermal case at higher N, where the electronic quenching cross-sections are smaller. Therefore, the contribution of electronic quenching is a more likely explanation for the disagreement between the experimental and theoretical depolarisation cross-sections seen in OH(A)-Kr.

Cuts through the PES for OH(A $^2\Sigma$)-Kr and OH(X $^2\Pi$)-Kr are shown in figure 4.21, for $\gamma = 0°$ (left panel) and $\gamma = 180°$ (right panel), based on provisional calculations performed by J. Kłos [238]. These correspond to the Kr-HO and Kr-OH approach geometries respectively. As can be seen, there is a curve crossing in the Kr-OH geometry, meaning that collisions that sample this deep potential well can be quenched. To sample the region

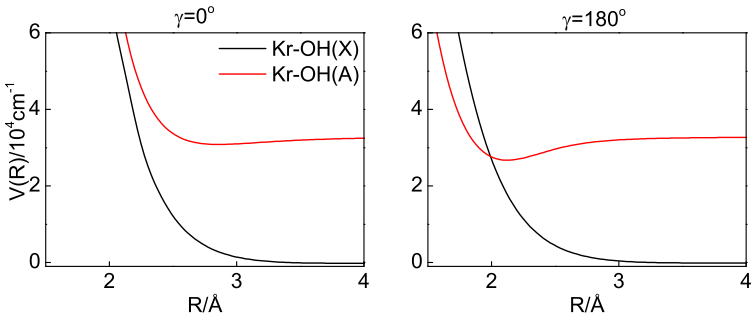


Figure 4.21: Cuts through the OH(X)-Kr and OH(A)-Kr potential energy surfaces corresponding to the Kr-HO ($\gamma = 0°$, left panel) and Kr-OH ($\gamma = 180°$, right panel) approach geometries [238].

of the potential corresponding to $\gamma = 180°$ the krypton has to approach the OH(A) in its plane of rotation. As the radical rotates faster, the potential that the krypton will experience would then be averaged over the attractive linear geometries, and repulsive T-shaped geometries, as shown in the right hand panel of figure 4.2. Consequently at higher

N, the krypton would be less likely to sample the deep potential well, and less likely to be quenched, leading to a decrease in the quenching cross-sections as was observed to be the case in section 4.2.

The presence of the curve crossing between the ground and electronically excited states means that the system cannot be properly characterised using one adiabatic PES, as has been considered here. As shown throughout the chapter, this leads to disagreement between the experimental and theoretical depolarisation cross-sections. However, the agreement between the two sets of RET cross-sections presented in section 4.3.2 was observed to be very good. This raises the question whether RET is influenced by electronic quenching and the attractive part of the PES. The results presented in this chapter would suggest not. However the curve crossing is likely to change the shape of the potential in the region of the well, so the good agreement between the experiment and theory in the case of the RET cross-sections is likely to be fortuitous.

4.7 Summary

A joint experimental and theoretical study of the collisional depolarisation of NO(A)-Kr and OH(A)-Kr has been presented. The experimental results were obtained using quantum beat spectroscopy, which allowed measurements of the total depolarisation cross-sections for NO(A)-Kr and OH(A)-Kr under thermal conditions, and OH(A)-Kr under superthermal conditions to be made, as well as electronic quenching, RET and elastic depolarisation cross-sections for OH(A)-Kr under thermal conditions. These results were compared with those from fixed energy QCT calculations. For NO(A)-Kr, the theoretical and experimental depolarisation cross-sections were found to be in excellent agreement, although this was not the case for thermal OH(A)-Kr. Separating the total depolarisation cross-sections into contributions made by elastic and inelastic depolarisation showed that there is disagreement between the theoretical and experimental values in both, which is compounded in the total depolarisation cross-sections. However, the main source of the discrepancy seemed

to arise from the inelastic depolarisation cross-sections. Due to the good agreement between the theoretical and experimental RET cross-sections, the disagreement between the experimental and theoretical depolarisation cross-sections was attributed to the different extent collisions were found to cause depolarisation in the two cases. Reasons for the disagreement between experiment and theory have been suggested. As has been shown, the QCT calculation results agree well with those from QM calculations, and so the reason for the discrepancy is not a failure of the QCT method. The most likely reason for the disagreement is due to the importance of electronic quenching in OH(A)-Kr, which is not accounted for in the theoretical calculations. This has been shown to be less important at high N and higher collision energies where the agreement between the the experimental and QCT results is observed to be better.

A consideration of the mechanism of depolarisation has also been presented. It has been shown that in NO(A)-Kr, depolarisation is inefficient compared to RET, reflecting the impulsive nature of the collisions due to the isotropic nature of the PES. In contrast, under thermal collision energies, RET is accompanied by efficient depolarisation in OH(A)-Kr, where every collision effectively randomises the direction of $\boldsymbol{j}$. Elastic depolarisation is also more significant in OH(A)-Kr than NO(A)-Kr, reflecting the different rotational energy level spacings in the two radicals. Elastic depolarisation is maintained to high rotational levels due to the significant anisotropy of the PES, which allows complexes to form. The unusual trend in the total depolarisation cross-sections is mirrored in the elastic depolarisation cross-sections, and therefore the trend in the total depolarisation cross-sections has been attributed to the significance of elastic depolarisation in OH(A)-Kr, and also the anisotropy and attractive nature of the PES which allows significant elastic depolarisation at high N. As the collision energy is increased, and the collisions start to probe the repulsive wall of the PES, the trends in OH(A)-Kr start to resemble those observed in NO(A)-Kr. However, orbiting trajectories are still observed for N=2 in OH(A)-Kr under superthermal conditions, showing that the attractive part of the potential still influences the dynamics even at the elevated collision energy considered here.

Chapter 5

The $\boldsymbol{k}$-$\boldsymbol{j}$-$\boldsymbol{j}'$ vector correlation

As discussed in the first chapter, a collision between a closed shell atom and a diatom can be completely defined by four vectors, $\boldsymbol{k}$, $\boldsymbol{k}'$, $\boldsymbol{j}$ and $\boldsymbol{j}'$, where $\boldsymbol{k}$ and $\boldsymbol{k}'$ are the initial and final relative velocities, and $\boldsymbol{j}$ and $\boldsymbol{j}'$ are the initial and final rotational angular momenta of the molecule. In this chapter, a theoretical consideration of some of the three vector correlations that describe the stereodynamics of the collision will be presented. The main focus will be on the $\boldsymbol{k}$-$\boldsymbol{j}$-$\boldsymbol{j}'$ correlation, the description of which has been developed as part of the current work. Integrating this distribution over the direction of $\boldsymbol{k}$ yields the $\boldsymbol{j}$-$\boldsymbol{j}'$ distribution, as considered in the preceding chapter for OH(A)-Kr and NO(A)-Kr.

The $\boldsymbol{k}$-$\boldsymbol{j}$-$\boldsymbol{j}'$ correlation will be compared to previous theoretical work on the $\boldsymbol{k}$-$\boldsymbol{k}'$-$\boldsymbol{j}'$ correlation [8, 162]. This three vector correlation has already been the focus of earlier experimental studies [15–17] and will be considered experimentally in the following chapter, for collisions of NO(X) with argon. If the direction of $\boldsymbol{j}'$ is undetermined, then the familiar differential cross-section, or the $\boldsymbol{k}$-$\boldsymbol{k}'$ correlation, is recovered. This will also be considered in the next chapter for collisions of NO(X) with krypton.

In the first part of this chapter, the theoretical framework for the $\boldsymbol{k}$-$\boldsymbol{j}$-$\boldsymbol{j}'$ correlation will be presented, in both the $\boldsymbol{k}$-$\boldsymbol{j}$ reference frame, and the laboratory (LAB) frame. From the three vector correlation, it will be shown how expressions for the lower order vector correlations can be obtained. The discussion will then be extended to the $\boldsymbol{a}$-$\boldsymbol{j}$-$\boldsymbol{j}'$ vector correlation in section 5.9, where $\boldsymbol{a}$ is the kinematic apse [18]. The vector

correlations considered will be presented for NO(A)-Kr and OH(A)-Kr in the second part of the chapter, to provide further insight into the mechanism of depolarisation considered in the previous chapter.

5.1 Describing correlated distributions

The reference frame used for expanding the ***k*-*j*-*j′*** correlation is shown in the right hand panel of figure 5.1. ***k*** is taken to lie along the $+z$ axis, and ***j*** lies in the $+zx$ plane. The

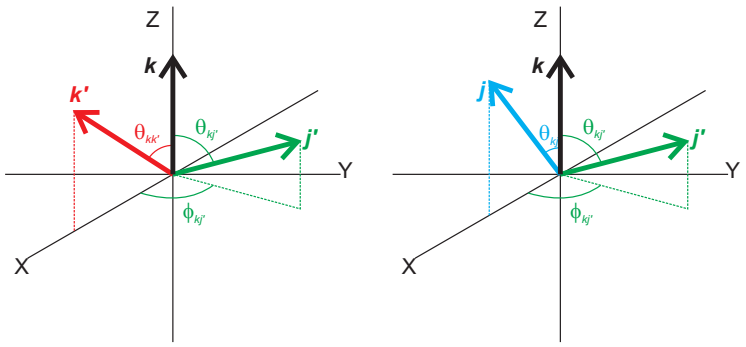


Figure 5.1: The ***k*-*k′*** reference frame used for the ***k*-*k′*-*j′*** correlation (left panel) and the ***k*-*j*** reference frame used for the ***k*-*j*-*j′*** correlation (right panel).

direction of ***j′*** is then described by the angles $\theta_{kj'}$ and $\phi_{kj'}$. Using this frame of reference, it is possible to expand the ***k*-*j*-*j′*** correlation using bipolar harmonics [8]:

$$\begin{aligned} P(\omega_{kj},\omega_{kj'}) &\equiv P(\theta_{kj},\phi_{kj},\theta_{kj'},\phi_{kj'}) \\ &= \frac{1}{16\pi^2}\sum_{KQ}\sum_{k_1k_2}[k_1][k_2]\,h_Q^K(k_1k_2)\,B_Q^K(k_1k_2;\omega_{kj},\omega_{kj'})^\star \end{aligned} \tag{5.1}$$

where $[n]=2n+1$, the expansion coefficients of the distribution, $h_Q^K(k_1k_2)$, are the expectation values of the bipolar harmonics $\langle B_Q^K(k_1k_2;\omega_{kj},\omega_{kj'})\rangle$, and the (complex conjugate) bipolar harmonics are defined as [102, 212]:

$$B_Q^K(k_1k_2;\omega_{kj},\omega_{kj'})^\star = \sum_{q_1q_2}(-1)^{K-Q}[K]^{1/2}\begin{pmatrix} k_1 & K & k_2 \\ q_1 & -Q & q_2 \end{pmatrix} C_{k_1q_1}(\theta_{kj},\phi_{kj})^\star\, C_{k_2q_2}(\theta_{kj'},\phi_{kj'})^\star \tag{5.2}$$

where $(\cdots)$ is a 3-j symbol and $C_{kq}(\theta,\phi)$ is a modified spherical harmonic [102]. As the reference frame is defined so that $\boldsymbol{j}$ lies in the $+xz$ plane, $\phi_{kj} = 0°$. Therefore for the distribution to be real, Q must equal zero [8, 118, 212]. It follows that the expression for the correlation becomes:

$$P(\omega_{kj},\omega_{kj'}) = \frac{1}{16\pi^2}\sum_{K}\sum_{k_1k_2}[k_1][k_2]\,h_0^K(k_1k_2)\,B_0^K(k_1k_2;\omega_{kj},\omega_{kj'})^\star \tag{5.3}$$

where the bipolar harmonics are defined as [102]:

$$B_0^K(k_1k_2;\omega_{kj},\omega_{kj'})^\star = \sum_q (-1)^K[K]^{1/2}\begin{pmatrix} k_1 & K & k_2 \\ -q & 0 & q\end{pmatrix} C_{k_1-q}(\theta_{kj},0)^\star\, C_{k_2q}(\theta_{kj'},\phi_{kj'})^\star \tag{5.4}$$

5.2 Symmetry considerations

Next it is necessary to consider the properties of the $\boldsymbol{k}$-$\boldsymbol{k}'$-$\boldsymbol{j}$-$\boldsymbol{j}'$ distribution when it is reflected in the $\boldsymbol{k}$-$\boldsymbol{k}'$ plane. The reference frame used to describe the correlation is shown in the left hand panel of figure 5.2. In this frame, $\boldsymbol{k}$ is defined as lying along the z axis, and $\boldsymbol{k}'$ lies in the $+zx$ plane. The direction of $\boldsymbol{j}$ is then defined by θ_{kj} and ϕ_{kj}, and $\boldsymbol{j}'$ by $\theta_{kj'}$ and $\phi_{kj'}$, where the azimuthal angle is the angle between the vector and the $\boldsymbol{k}$-$\boldsymbol{k}'$

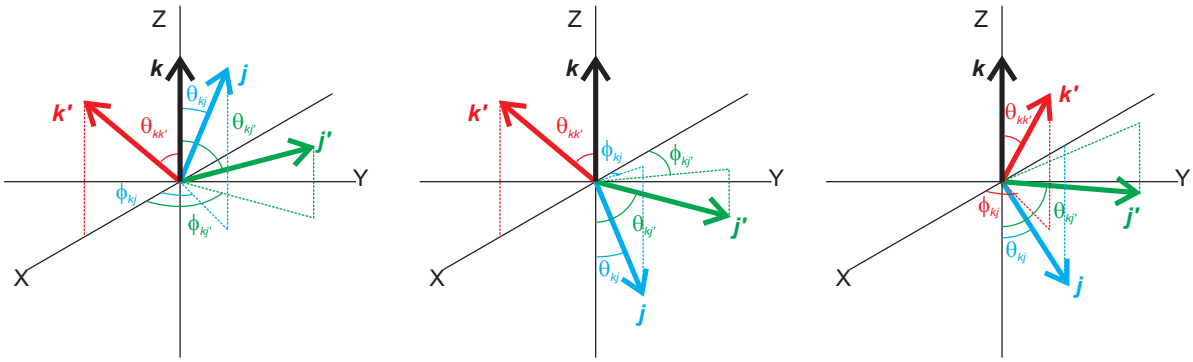


Figure 5.2: The effect of a reflection in the $\boldsymbol{k}$-$\boldsymbol{k}'$ plane on the $\boldsymbol{k}$-$\boldsymbol{k}'$-$\boldsymbol{j}$-$\boldsymbol{j}'$ correlation, followed by a rotation into the $\boldsymbol{k}$-$\boldsymbol{j}$ plane.

plane. The distribution can be written as [118]:

$$P(\omega_{kk'}, \omega_{kj}, \omega_{kj'}) = P(\theta_{kk'}, 0, \theta_{kj}, \phi_{kj}, \theta_{kj'}, \phi_{kj'}) \tag{5.5}$$

If the collision process is achiral, the distribution of the internuclear axes is invariant to reflection in the scattering plane. As both $\boldsymbol{j}$ and $\boldsymbol{j'}$ behave as pseudo vectors, the j_x and j_z components of $\boldsymbol{j}$ change sign when reflected, but the j_y component remains unchanged [160]. The effect of reflecting the distribution in the $\boldsymbol{k}$-$\boldsymbol{k'}$ plane is shown in the central panel in figure 5.2. Therefore, the effect of the reflection symmetry operator $\hat{\mathcal{S}}$ on the $\boldsymbol{k}$-$\boldsymbol{k'}$-$\boldsymbol{j}$-$\boldsymbol{j'}$ correlation can be written as:

$$\hat{\mathcal{S}}\left[P(\omega_{kk'}, \omega_{kj}, \omega_{kj'})\right] = P(\theta_{kk'}, 0, \pi - \theta_{kj}, \pi - \phi_{kj}, \pi - \theta_{kj'}, \pi - \phi_{kj'}) \tag{5.6}$$

Due to the invariance under reflection of the distribution in the scattering plane, this is the same as the original distribution $P(\omega_{kk'}, \omega_{kj}, \omega_{kj'})$. In the case where the direction of $\boldsymbol{j}$ is undefined, invariance under reflection for the $\boldsymbol{k}$-$\boldsymbol{k'}$-$\boldsymbol{j'}$ distribution reads:

$$\hat{\mathcal{S}}\left[P(\omega_{kk'}, \omega_{kj'})\right] = P(\theta_{kk'}, 0, \pi - \theta_{kj'}, \pi - \phi_{kj'}) \tag{5.7}$$

which is the case discussed previously in references [8] and [162].

The $\boldsymbol{k}$-$\boldsymbol{j}$ plane is defined such that $\boldsymbol{j}$ lies in the zx plane, and not $\boldsymbol{k'}$. This can be achieved by rotating the distribution shown in the middle panel around the z axis through the angle ϕ_{kj} to obtain the distribution shown in the right hand panel of the figure. The effect of this rotation (denoted by the operator $\hat{\mathcal{R}}$) on the distribution can be written as:

$$\begin{aligned} & \hat{\mathcal{R}}\left[P(\theta_{kk'}, 0, \pi - \theta_{kj}, \pi - \phi_{kj}, \pi - \theta_{kj'}, \pi - \phi_{kj'})\right] \\ = \;& P(\theta_{kk'}, \phi_{kj}, \pi - \theta_{kj}, \pi - \phi_{kj} + \phi_{kj}, \pi - \theta_{kj'}, \pi - \phi_{kj'} + \phi_{kj}) \\ = \;& P(\theta_{kk'}, \phi_{kj}, \pi - \theta_{kj}, \pi, \pi - \theta_{kj'}, \pi - \phi_{jj'}) \end{aligned} \tag{5.8}$$

where $\phi_{jj'} = \phi_{kj'} - \phi_{kj}$. As the azimuthal angles are currently defined with respect to the $-x$ axis instead of the $+x$ axis, the final step is just a simple rotation through $-\pi$ to yield:

$$P(\omega_{kk'}, \omega_{kj}, \omega_{kj'}) = P(\theta_{kk'}, -\pi + \phi_{kj}, \pi - \theta_{kj}, 0, \pi - \theta_{kj'}, -\phi_{jj'}) \tag{5.9}$$

It follows that the reflection of the $\boldsymbol{k}$-$\boldsymbol{k'}$-$\boldsymbol{j}$-$\boldsymbol{j'}$ correlation in the scattering plane in the $\boldsymbol{k}$-$\boldsymbol{j}$ frame can be written as:

$$P(\theta_{kk'}, \phi_{kj}, \theta_{kj}, 0, \theta_{kj'}, \phi_{jj'}) = P(\theta_{kk'}, \phi_{kj} - \pi, \pi - \theta_{kj}, 0, \pi - \theta_{kj'}, -\phi_{jj'}) \tag{5.10}$$

For the $\boldsymbol{k}$-$\boldsymbol{j}$-$\boldsymbol{j'}$ correlation, the direction of $\boldsymbol{k'}$ is unresolved. Therefore, invariance under reflection for this distribution in the $\boldsymbol{k}$-$\boldsymbol{j}$ frame reads:

$$P(\omega_{kk'}, \omega_{kj'}) = P(\pi - \theta_{kj}, 0, \pi - \theta_{kj'}, -\phi_{jj'}) \tag{5.11}$$

It should be noted that exactly the same result is obtained by directly reflecting the $\boldsymbol{k}$-$\boldsymbol{j}$-$\boldsymbol{j}'$ distribution in the $\boldsymbol{k}$-$\boldsymbol{j}$ plane, as long as the $+zx$ plane is always defined as that containing $\boldsymbol{j}$.

To impose the invariance of the $\boldsymbol{k}$-$\boldsymbol{j}$-$\boldsymbol{j'}$ distribution to reflection given in equation (5.11), the following properties of the spherical harmonics can be used [102]:

$$C_{kq}(\theta, 0) = (-1)^{k+q} C_{kq}(\pi - \theta, 0) = C_{kq}(\theta, 0)^\star \tag{5.12}$$

$$C_{kq}(\theta, \phi)^\star = (-1)^{k+q} C_{kq}(\pi - \theta, -\phi) \tag{5.13}$$

The bipolar moments after reflection can therefore be written as:

$$\begin{aligned} B_0^K(k_1 k_2; \pi - \theta_{kj}, \pi - \theta_{kj'}, -\phi_{kj'})^\star &\propto C_{k_1 -q}(\pi - \theta_{kj}, 0)^\star \, C_{k_2 q}(\pi - \theta_{kj'}, -\phi_{kj'})^\star \\ &\propto (-1)^{k_1+q} C_{k_1 -q}(\theta_{kj}, 0)(-1)^{k_2+q} C_{k_2 q}(\theta_{kj'}, \phi_{kj'}) \\ &= (-1)^{k_1+k_2} B_0^K(k_1 k_2; \theta_{kj}, \theta_{kj'}, \phi_{kj'}) \end{aligned} \tag{5.14}$$

And therefore:

$$\hat{\mathcal{S}} B_0^K(k_1k_2;\omega_{kj},\omega_{kj'})^\star = (-1)^{k_1+k_2} B_0^K(k_1k_2;\omega_{kj},\omega_{kj'}) \tag{5.15}$$

As the distribution has to be real [8, 118]:

$$h_0^K(k_1k_2)^\star = (-1)^{k_1+k_2+K} h_0^K(k_1k_2) \tag{5.16}$$

$$B_0^K(k_1k_2;\omega_{kj},\omega_{kj'})^\star = (-1)^{k_1+k_2+K} B_0^K(k_1k_2;\omega_{kj},\omega_{kj'}) \tag{5.17}$$

which when combined with equation (5.15) leads to:

$$\hat{\mathcal{S}} B_0^K(k_1k_2;\omega_{kj},\omega_{kj'})^\star = (-1)^K B_0^K(k_1k_2;\omega_{kj},\omega_{kj'})^\star \tag{5.18}$$

By the same method:

$$h_0^K(k_1k_2) = (-1)^K h_0^K(k_1k_2) \tag{5.19}$$

It follows that K must be even, and:

$$h_0^K(k_1k_2)^\star = (-1)^{k_1+k_2} h_0^K(k_1k_2) \tag{5.20}$$

The invariance of the $\boldsymbol{k}$-$\boldsymbol{k}'$-$\boldsymbol{j}'$ distribution to reflection can be considered in the same way. This is as expressed in equation (5.7). Again, by making use of the property of the spherical harmonics [102, 165]:

$$C_{kq}(\theta,\phi) = (-1)^k C_{kq}(\pi-\theta,\pi-\phi)^\star \tag{5.21}$$

it can be shown that the bipolar moments after reflection can be written as:

$$\begin{aligned} \hat{\mathcal{S}} B_0^K(k_1k_2;\theta_{kk'},\theta_{kj'},\phi_{kj'})^\star &= B_0^K(k_1k_2;\theta_{kk'},\pi-\theta_{kj'},\pi-\phi_{kj'})^\star \\ &= (-1)^{k_2} B_0^K(k_1k_2;\theta_{kk'},\theta_{kj'},\phi_{kj'}) \end{aligned} \tag{5.22}$$

Therefore k_2 must be even. Again, the distribution has to be real, and combining the above result with that given in equation (5.17) yields the property that for the ***k*-*k*′-*j*′** correlation $k_1 + K$ must be even [8].

5.3 Expansion coefficients

A more convenient way to expand the distribution is in terms of angle dependent moments which are analogous to the polarisation dependent differential cross-sections [8, 239, 240]. The distribution can then be written as:

$$P(\omega_{kj}, \omega_{kj'}) = \frac{1}{4\pi} \sum_{k_2} \sum_{q=-k_2}^{q=k_2} [k_2]\, S_{k_2 q}(\theta_{kj}) C_{k_2 q}(\theta_{kj'}, \phi_{kj'})^\star \tag{5.23}$$

where:

$$S_{k_2 q}(\theta_{kj}) = \langle C_{k_2 q}(\theta_{kj'}, \phi_{kj'}) \rangle = (-1)^q S_{k_2 -q}(\theta_{kj})^\star \tag{5.24}$$

where use has been made of:

$$C_{kq}(\theta, \phi) = (-1)^q C_{k-q}(\theta, \phi)^\star \tag{5.25}$$

and the $\langle \cdots \rangle$ is the average over all angles. Comparing equation (5.3) and equation (5.23), the $S_{k_2 q}(\theta_{kj})$ expansion coefficients are given by [8, 162]:

$$S_{k_2 q}(\theta_{kj}) = \frac{1}{2} \sum_{k_1 \geq |q|} [k_1] s^{k_1}_{k_2 q} C_{k_1 - q}(\theta_{kj}, 0) \tag{5.26}$$

with:

$$s^{k_1}_{k_2 q} = \sum_k (-1)^K [K]^{1/2} \begin{pmatrix} k_1 & K & k_2 \\ -q & 0 & q \end{pmatrix} h^K_0(k_1 k_2) \tag{5.27}$$

These may be calculated as the following expectation values:

$$s^{k_1}_{k_2 q} = \langle C_{k_1 - q}(\theta_{kj}, 0) C_{k_2 q}(\theta_{kj'}, \phi_{kj'}) \rangle \tag{5.28}$$

For the $\boldsymbol{k}$-$\boldsymbol{j}$-$\boldsymbol{j}'$ correlation, K must be even as already discussed. From equations (5.27) and (5.20) it follows that:

$$s^{k_1}_{k_2q} = (-1)^{(k_1+k_2)} s^{k_1\star}_{k_2q} = (-1)^{(k_1+k_2)} s^{k_1}_{k_2-q} \tag{5.29}$$

Therefore, when $k_1 + k_2$ is even the $s^{k_1}_{k_2q}$ moments are real, and when $k_1 + k_2$ is odd, the $s^{k_1}_{k_2q}$ moments are imaginary. It immediately follows that:

$$\begin{aligned} s^{k_1}_{k_2q} &= \langle C_{k_1-q}(\theta_{kj},0) C_{k_2q}(\theta_{kj'},0)\cos q\phi_{kj'}\rangle \qquad k_1+k_2 \text{ even} &(5.30)\\ &= i\langle C_{k_1-q}(\theta_{kj},0) C_{k_2q}(\theta_{kj'},0)\sin q\phi_{kj'}\rangle \qquad k_1+k_2 \text{ odd} &(5.31)\end{aligned}$$

To obtain real moments for the distribution, it is helpful to work within the Hertel-Stoll normalisation [163]:

$$\begin{aligned} S_{k_2q+}(\theta_{kj}) &= \frac{1}{\sqrt{2}}\left[(-1)^q S_{k_2+q}(\theta_{kj}) + S_{k_2-q}(\theta_{kj})\right] &(5.32)\\ S_{k_2q-}(\theta_{kj}) &= \frac{1}{i\sqrt{2}}\left[(-1)^q S_{k_2+q}(\theta_{kj}) - S_{k_2-q}(\theta_{kj})\right] &(5.33)\end{aligned}$$

It should be noted that in these equations $q \geq 0$. By making use of equation (5.29), it can be shown that the moments for the $\boldsymbol{k}$-$\boldsymbol{j}$-$\boldsymbol{j}'$ correlation may be written as:

$$\begin{aligned} S_{k_2q+}(\theta_{kj}) &= \frac{1}{2\sqrt{2}}\sum_{k_1}[k_1] C_{k_1q}(\theta_{kj},0) s^{k_1}_{k_2q}\left[1+(-1)^{k_1+k_2}\right] &(5.34)\\ S_{k_2q-}(\theta_{kj}) &= \frac{1}{2i\sqrt{2}}\sum_{k_1}[k_1] C_{k_1q}(\theta_{kj},0) s^{k_1}_{k_2q}\left[1-(-1)^{k_1+k_2}\right] &(5.35)\end{aligned}$$

Finally, making use of these real expansion coefficients allows the distribution given in equation (5.23) to be written as:

$$\begin{aligned} P(\omega_{kj},\omega_{kj'}) &= \frac{1}{4\pi}\sum_{k_2}[k_2]\Bigg[S_{k_20}(\theta_{kj}) C_{k_20}(\theta_{kj'},0) + \sqrt{2}\sum_{q>0} C_{k_2-q}(\theta_{kj'},0)\\ &\times \left\{S_{k_2q+}(\theta_{kj})\cos q\phi_{kj'} + S_{k_2q-}(\theta_{kj})\sin q\phi_{kj'}\right\}\Bigg] &(5.36)\end{aligned}$$

5.4 The $\boldsymbol{k}$-$\boldsymbol{j}'$ correlation

The $\boldsymbol{k}$-$\boldsymbol{j}'$ correlation in the $\boldsymbol{k}$-$\boldsymbol{j}$-$\boldsymbol{j}'$ reference frame described above can be obtained by integrating equation (5.3) or equation (5.23) over the direction of $\boldsymbol{j}$. The resulting distribution can be written as [118]:

$$P(\omega_{kj'}) = \frac{1}{4\pi}\sum_{k_2 q}[k_2]a_q^{(k_2)}C_{k_2 q}(\theta_{kj'},\phi_{kj'})^{\star} \tag{5.37}$$

where the expansion coefficients can be written as:

$$\begin{aligned} a_q^{(k_2)} &= \langle C_{k_2 q}(\theta_{kj'},\phi_{kj'})\rangle \\ &= \int_{-1}^{1} S_{k_2 q}(\theta_{kj})\,\mathrm{d}\cos\theta_{kj} \\ &= \frac{1}{2}\sum_{k_1\geq|q|}[k_1]s_{k_2 q}^{k_1}\int_{-1}^{1} C_{k_1 -q}(\theta_{kj},0)\,\mathrm{d}\cos\theta_{kj} \end{aligned} \tag{5.38}$$

When $q=0$, $a_0^{(k_2)} = s_{k_2 0}^0 = h_0^{k_2}(0k_2)$. For the distribution to be real and planar symmetric, only the $a_0^{(k_2)}$ moments when k_2 are even are non-zero. To determine which of the $a_q^{(k_2)}$ moments are non-zero when $q \neq 0$, it is again better to work within the Hertel-Stoll normalisation [163]. The distribution can be written as:

$$\begin{aligned} P(\omega_{kj'}) &= \frac{1}{4\pi}\sum_{k_2}[k_2]\Bigg\{a_0^{(k_2)}P_{k_2}(\cos\theta_{kj'}) \\ &+ \sqrt{2}\sum_{q>0}C_{k_2 -q}(\theta_{kj'},0)[a_{q+}^{(k_2)}\cos q\phi_{kj'} + a_{q-}^{(k_2)}\sin q\phi_{kj'}]\Bigg\} \end{aligned} \tag{5.39}$$

where (from equations (5.34) and (5.35)):

$$a_{q+}^{(k_2)} = \frac{1}{2\sqrt{2}}\sum_{k_1}[k_1]s_{k_2 q}^{k_1}\left[1+(-1)^{k_1+k_2}\right]\int_{-1}^{1} C_{k_1 q}(\theta_{kj},0)\,\mathrm{d}\cos\theta_{kj} \tag{5.40}$$

$$a_{q-}^{(k_2)} = \frac{1}{2i\sqrt{2}}\sum_{k_1}[k_1]s_{k_2 q}^{k_1}\left[1-(-1)^{k_1+k_2}\right]\int_{-1}^{1} C_{k_1 q}(\theta_{kj},0)\,\mathrm{d}\cos\theta_{kj} \tag{5.41}$$

The integrals over $C_{k_1 q}(\theta_{kj}, 0)$ are only non-zero when $k_1 + q$ is even. Combining this with the restrictions on k_1 and k_2 discussed previously implies that within the Hertel-Stoll normalisation, the $a_{q+}^{(k_2)}$ moments are non-zero when $q + k_2$ is even, and the $a_{q-}^{(k_2)}$ moments are non-zero when $q + k_2$ is odd. These expansion coefficients can be written as the following expectation values:

$$a_{q+}^{(k_2)} = (-1)^q \sqrt{2} \langle C_{k_2|q|}(\theta_{kj'}, 0) \cos q\phi_{kj'} \rangle \qquad k_2 + q \text{ even} \tag{5.42}$$

$$a_{q-}^{(k_2)} = (-1)^q \sqrt{2} \langle C_{k_2|q|}(\theta_{kj'}, 0) \sin q\phi_{kj'} \rangle \qquad k_2 + q \text{ odd} \tag{5.43}$$

If the $\boldsymbol{k}$-$\boldsymbol{j}$ plane is undefined, the resulting $\boldsymbol{k}$-$\boldsymbol{j}'$ distribution can be obtained by integrating over $\phi_{kj'}$. This leads to a Legendre polynomial expansion:

$$P(\theta_{kj'}) = \frac{1}{2} \sum_{k_2} [k_2] a_0^{(k_2)} P_{k_2}(\cos \theta_{kj'}) \tag{5.44}$$

where $a_0^{(k_2)} \equiv h_0^{k_2}(0k_2)$, and only terms with even k_2 are non-zero. It should be noted that the same result would be obtained by integrating the $\boldsymbol{k}$-$\boldsymbol{k}'$-$\boldsymbol{j}'$ correlation over $\theta_{kk'}$ and $\phi_{kj'}$.

5.5 The $\boldsymbol{j}$-$\boldsymbol{j}'$ correlation

The $\boldsymbol{j}$-$\boldsymbol{j}'$ correlation can be obtained from the $\boldsymbol{k}$-$\boldsymbol{j}$-$\boldsymbol{j}'$ distribution by restricting all the $K \neq 0$ moments to zero in equation (5.3). This implies $k_1 = k_2 = k$. The resulting distribution may be written as [8]:

$$P(\theta_{jj'}) = \frac{1}{2} \sum_{k} (-1)^k [k]^{3/2} h_0^0(kk) \sum_{q} C_{kq}(\theta_{kj}, 0) C_{kq}(\theta_{kj'}, \phi_{kj'})^\star \tag{5.45}$$

where $\theta_{jj'}$ is the angle between $\boldsymbol{j}$ and $\boldsymbol{j'}$. Using the spherical harmonic addition theorem [102], the distribution can be rewritten as:

$$\begin{aligned} P(\theta_{jj'}) &= \frac{1}{2}\sum_k (-1)^k [k]^{3/2} h_0^0(kk) C_{kq}(\theta_{jj'}, 0) \\ &= \frac{1}{2}\sum_k [k] a^{(k)} P_k(\cos\theta_{jj'}) \end{aligned} \tag{5.46}$$

This is simply a Legendre polynomial expansion as given in equation (2.17), where the $a^{(k)}$ moments are the same moments considered in chapter 4.

5.6 The $\boldsymbol{k}$-$\boldsymbol{k'}$ correlation

Integration of the $\boldsymbol{k}$-$\boldsymbol{k'}$-$\boldsymbol{j'}$ correlation over the direction of $\boldsymbol{j'}$, $\theta_{kj'}, \phi_{kj'}$, yields the $\boldsymbol{k}$-$\boldsymbol{k'}$ distribution, or the differential cross-sections (DCSs), which are considered in chapter 6. In this case $k_2 = q = 0$, and the distribution can be written as:

$$P(\theta_{kk'}) = \frac{1}{2}\sum_{k_1} [k_1] h_0^{k_1}(k_1 0) P_{k_1}(\cos\theta_{kk'}) \tag{5.47}$$

The bipolar moments $h_0^{k_1}(k_1 0) = s_{00}^{k_1} = a^{(k)}(k, k')$ are just the expansion coefficients for the differential cross-section considered in chapter 6.

5.7 LAB frame distribution

In this section, the vector correlations discussed above will be considered in the laboratory (LAB) frame. When linearly polarised light is used, the Z-axis in this frame is defined as being along the direction of the polarisation of the laser, and the direction of propagation is along the X-axis. If circularly polarised light is used, then it is the direction of propagation of the laser that defines the Z-axis. In the LAB frame, the distribution of $\boldsymbol{k}$ may be

characterised as:

$$P(\Theta_k, \Phi_k) = \frac{1}{4\pi} \sum_{k'q'} [k'] \, g_{q'}^{(k')} \, C_{k'q'}(\Theta_k, \Phi_k)^\star = \frac{1}{8\pi^2} \sum_{k'q'} [k'] \, g_{q'}^{(k')} \, D_{q'0}^{k'}(\Phi_k, \Theta_k, \chi_k)^\star \qquad (5.48)$$

where $g_{q'}^{(k')}$ is the expansion coefficient, $D_{q'0}^{k'}(\Phi_k, \Theta_k, \chi_k)$ is a Wigner rotation matrix element [102], Θ_k and Φ_k define the LAB frame direction of $\boldsymbol{k}$, and the angle χ_k is arbitrarily defined. To obtain the distribution of $\boldsymbol{j}$ and $\boldsymbol{j}'$ in the LAB frame, it is necessary to rotate the bipolar harmonics into the LAB frame, and integrate over all directions of $\boldsymbol{k}$:

$$\begin{aligned} P(\Omega_j, \Omega_{j'}) &= \int P(\Theta_k, \Phi_k) P(\omega_j, \omega_{j'}) \mathrm{d}\Omega_k \\ &= \frac{1}{16\pi^2} \sum_K \sum_{k_1 k_2} [k_1][k_2] \, h_0^K(k_1 k_2) \int P(\Theta_k, \Phi_k) \\ &\times \sum_P D_{P0}^K(\Phi_k, \Theta_k, \chi_k) \left[B_P^K(k_1 k_2; \Theta_j, \Phi_j, \Theta_{j'}, \Phi_{j'}) \right]^\star \mathrm{d}\Omega_k \end{aligned} \qquad (5.49)$$

The orthogonality of the rotation matrices leads to:

$$P(\Omega_j, \Omega_{j'}) = \frac{1}{16\pi^2} \sum_K \sum_{k_1 k_2} [k_1][k_2] \, h_0^K(k_1 k_2) \sum_{q'} g_{q'}^K \left[B_{q'}^K(k_1 k_2; \Theta_j, \Phi_j, \Theta_{j'}, \Phi_{j'}) \right]^\star \qquad (5.50)$$

In the LAB frame, the distribution of $\boldsymbol{k}$ would normally be cylindrically symmetric about the Z-axis, and therefore $q' = 0$. If the distribution of $\boldsymbol{k}$ is also isotropic, then $K = q' = 0$, and consequently $k_1 = k_2 = k$. In this case, equation (5.50) reduces to equation (5.45), and can therefore be written as a Legendre expansion in $\Theta_{jj'} = \theta_{jj'}$.

To complete the transformation of the distribution to the LAB frame, it is necessary to convolute equation (5.50) with the LAB frame (*i.e.* extrinsic) distribution of $\boldsymbol{j}$. This can be written as [175]:

$$P(\Omega_j) = \frac{1}{4\pi} \sum_{k''q''} [k''] \, A_{q''}^{(k'')} \, C_{k''q''}(\Theta_j, \Phi_j)^\star \qquad (5.51)$$

The resulting distribution of $\boldsymbol{j}'$ in the LAB frame can therefore be written as:

$$\begin{aligned} P(\Omega_{j'}) &= \int P(\Theta_j, \Phi_j)\, P(\Omega_j, \Omega_{j'})\, \mathrm{d}\Omega_j \\ &= \frac{1}{4\pi} \sum_K \sum_{k''k_2} [k''][k_2] h_0^K(k''k_2) \\ &\times \sum_{q'q''q_2} g_{q'}^{(K)} (-1)^{K-q'-q''} [K]^{1/2} \begin{pmatrix} k'' & K & k_2 \\ -q'' & -q' & q_2 \end{pmatrix} A_{q''}^{(k'')}(j) C_{k_2q_2}(\Theta_{j'}, \Phi_{j'})^\star \\ &= \frac{1}{4\pi} \sum_{k_2q_2} [k_2] C_{k_2q_2}(\Theta_{j'}, \Phi_{j'})^\star \sum_{k''q''} A_{q''}^{(k'')} a_{q_2q''}^{k_2k''} \end{aligned} \tag{5.52}$$

where:

$$a_{q_2q''}^{k_2k''} = [k''] \sum_K \sum_{q'} g_{q'}^{(K)}\, (-1)^{K+q_2} [K]^{1/2} \begin{pmatrix} k'' & K & k \\ -q'' & -q' & q_2 \end{pmatrix} h_0^K(k''k_2) \tag{5.53}$$

It follows that the expansion coefficients of the distribution, $\mathcal{P}_{q_2}^{(k_2)}$, are given by:

$$\mathcal{P}_{q_2}^{(k_2)} = \sum_{k''q''} a_{q_2q''}^{k_2k''} A_{q''}^{(k'')} \tag{5.54}$$

This is consistent with the quantum mechanical expressions obtained in references [185] and [186], and the expressions obtained in chapter 3.

If the direction of $\boldsymbol{k}$ is isotropic, then $K = q' = 0$, $k_2 = k'' = k$ and $q_2 = q'' = q$. It follows that the distribution of $\boldsymbol{j}'$ in the LAB frame can be written as:

$$P(\Omega_{j'}) = \frac{1}{4\pi} \sum_{kq} [k] A_q^{(k)} a_q^{(k)} C_{kq}(\Theta_{j'}, \Phi_{j'})^\star \tag{5.55}$$

where:

$$a_q^{(k)} \equiv a_{q_2q''}^{k_2k''} = (-1)^k [k]^{1/2}\, h_0^0(kk)\, \delta_{k_2k''} \delta_{q_2q''} \tag{5.56}$$

In the case where the distribution of $\boldsymbol{j}'$ is cylindrically symmetric in the LAB frame, $q = 0$.

It follows that the distribution of $\boldsymbol{j}'$ in the LAB frame can be written as:

$$\begin{aligned} P(\Theta_{jj'}) &= \frac{1}{4\pi}\sum_k [k]A^{(k)}a^{(k)}C_{k0}(\Theta_{j'},\Phi_{j'})^\star \\ &= \frac{1}{2}\sum_k [k]A^{(k)}a^{(k)}P_k(\cos\Theta_{j'}) \end{aligned} \tag{5.57}$$

This is the same result as obtained in section 3.1.1, when considering the LAB frame distribution of $\boldsymbol{j}'$ following collisions in the Zeeman quantum beat experiments.

5.8 Vector correlations in NO(A)-Kr and OH(A)-Kr

The methodology for considering vector correlations presented in the first part of the chapter will now be used to provide a further insight into the mechanism of depolarisation of NO(A) and OH(A) with krypton discussed in the previous chapter. All the plots of the vector correlations shown are calculated using the results from the fixed energy quasi-classical trajectories.

5.8.1 $\boldsymbol{k}$-$\boldsymbol{k}'$-$\boldsymbol{j}'$ vector correlation

The $\boldsymbol{k}$-$\boldsymbol{k}'$-$\boldsymbol{j}'$ correlations for N=2 to N'=3 for NO(A)-Kr (top row) and OH(A)-Kr (bottom row) are presented in figure 5.3. The reference frame used is that shown in the left hand panel of figure 5.1, where $\boldsymbol{k}$ is defined as lying along the $+z$ axis, and $\boldsymbol{k}'$ lies in the $+zx$ plane. From left to right, the scattering angle, $\theta_{kk'}$ is 0°, 45°, 90°, 135° and 180°. In both cases, the distribution of $\boldsymbol{j}'$ is broad, suggesting that the direction of $\boldsymbol{j}'$ is distributed over a wide range of angles after the collision. The most strongly polarised distributions are observed in the case where $\theta_{kk'} = 0°$ and $\theta_{kk'} = 180°$, where there is a propensity for $\boldsymbol{j}'$ to be parallel to the z-axis. The distributions for these two scattering angles are cylindrically symmetric, as is necessary as both $\boldsymbol{k}$ and $\boldsymbol{k}'$ lie along the z axis and therefore the zx plane is undefined. $\theta_{kk'} = 0°$ and $\theta_{kk'} = 180°$ correspond to forwards and backwards scattered products respectively, and these contribute less to the scattering process than those that

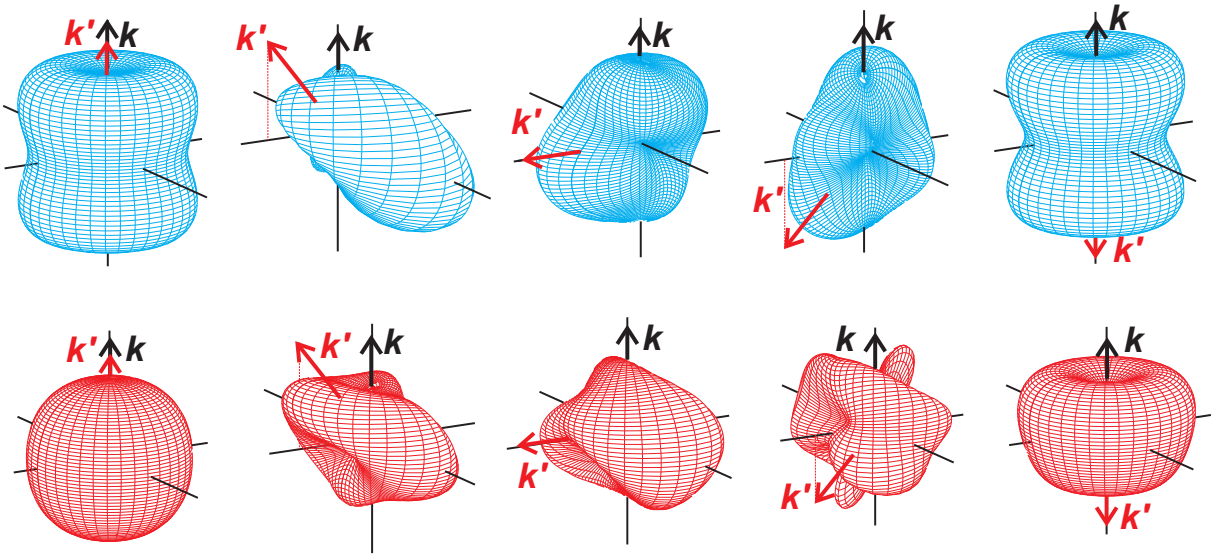


Figure 5.3: The $\boldsymbol{k}$-$\boldsymbol{k}'$-$\boldsymbol{j}'$ distribution for N=2 to N'=3 for NO(A)-Kr (top row) and OH(A)-Kr (bottom row). The plots, from left to right are for $\theta_{kk'} = 0°$, $\theta_{kk'} = 45°$, $\theta_{kk'} = 90°$, $\theta_{kk'} = 135°$ and $\theta_{kk'} = 180°$.

are sideways scattered. This is due to the $\sin\theta_{kk'}$ weighting that must be applied, which corresponds to the products being scattered over the surface of a sphere.

The extent to which each scattering angle contributes to the integrated $\boldsymbol{k}$-$\boldsymbol{j}'$ distribution also depends on the probability that the product is scattered through $\theta_{kk'}$. This is simply the DCS. As previously mentioned, the DCS (or $\boldsymbol{k}$-$\boldsymbol{k}'$ distribution) can be obtained by integrating the $\boldsymbol{k}$-$\boldsymbol{k}'$-$\boldsymbol{j}'$ correlation over all directions of $\boldsymbol{j}'$ (*i.e.* $\theta_{kj'}$ and $\phi_{kj'}$). These are shown in figure 5.4 for NO(A)-Kr (left panel) and OH(A)-Kr (right panel) for the transition N=2 to N'=3. The DCSs are strongly peaked at $\theta_{kk'}$=0° in both cases, corresponding

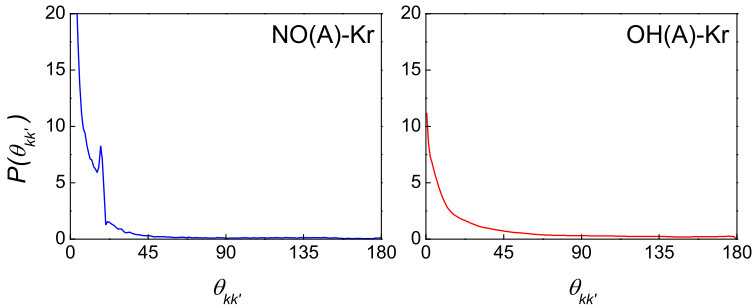


Figure 5.4: The $\boldsymbol{k}$-$\boldsymbol{k}'$ correlation for N=2 to N'=3 for NO(A)-Kr (left panel) and OH(A)-Kr (right panel).

to forward scattering, although the NO(A)-Kr DCS is more strongly peaked than the OH(A)-Kr DCS. As discussed previously, less energy transfer is required to bring about this transition in NO(A) than OH(A). To conserve energy this is accompanied by a change in the velocity of the atom. Smaller changes in velocity can be brought about by more 'glancing blow' collisions, which tends to result in strong forward scattering. Consequently the NO(A)-Kr DCS is more strongly peaked at $\theta_{kk'} = 0°$ than the OH(A)-Kr DCS.

There is also a second peak in the NO(A)-Kr DCS at approximately 20°. This corresponds to rainbow scattering, and shows the influence of the attractive part of the potential energy surface (PES). This can also be seen in the deflection function plots shown for the same transition in figure 5.5, where the left hand panel is for NO(A)-Kr and the right hand panel OH(A)-Kr. As can be seen for NO(A)-Kr, there is a clear maximum in the

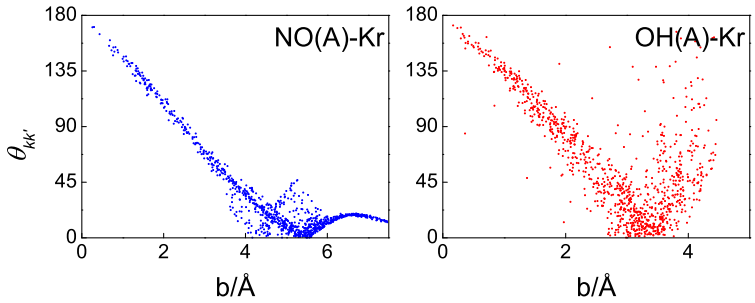


Figure 5.5: Scatter plots of scattering angle vs impact parameter for the N=2 to N'=3 transition for NO(A)-Kr (left panel) and OH(A)-Kr (right panel).

deflection function at an impact parameter of about 6.5 Å, at a value of $\theta_{kk'} = 20°$, which was shown in figure 4.18 to be due to the krypton scattering from the O end of the NO radical. Therefore, the probability of scattering at this angle is greater, giving rise to a maximum in the DCS. It should be noted that this does not correspond to the maximum in the deflection function, which is at $b \approx 5$ Å. This can be attributed to scattering from the N end of the radical, as shown in figure 4.18. By considering the plot of the PES in figure 2.8, it can be seen that the collisions corresponding to $b \approx 5$ Å can be associated with the deeper well on the PES (in the Kr-NO geometry), and so will give rise to larger deflections. However, scattering through this angle is less likely, and so no maximum is

observed in the DCS. Although the OH(A)-Kr PES is significantly more attractive, this structure is not observed as the Kr is trapped in a complex with the OH(A), which leads to orbiting trajectories. Consequently there is no maximum in the deflection function, and instead a band structure is observed as the complex can fall apart at any point in its rotation.

5.8.2 *k*-*j*-*j*′ vector correlation

The plots of the ***k***-***j***-***j***′ correlation are more revealing. These are presented in figure 5.6 for the same transition as in figure 5.3. Again, the NO(A)-Kr distribution is shown in the top row, and the OH(A)-Kr distribution in the bottom row. The reference frame used is that shown in the right hand panel of figure 5.1, where $\boldsymbol{k}$ lies along the $+z$ axis and $\boldsymbol{j}$ lies in the $+zx$ plane. As can be seen the direction of $\boldsymbol{j}'$ is more strongly polarised along the direction

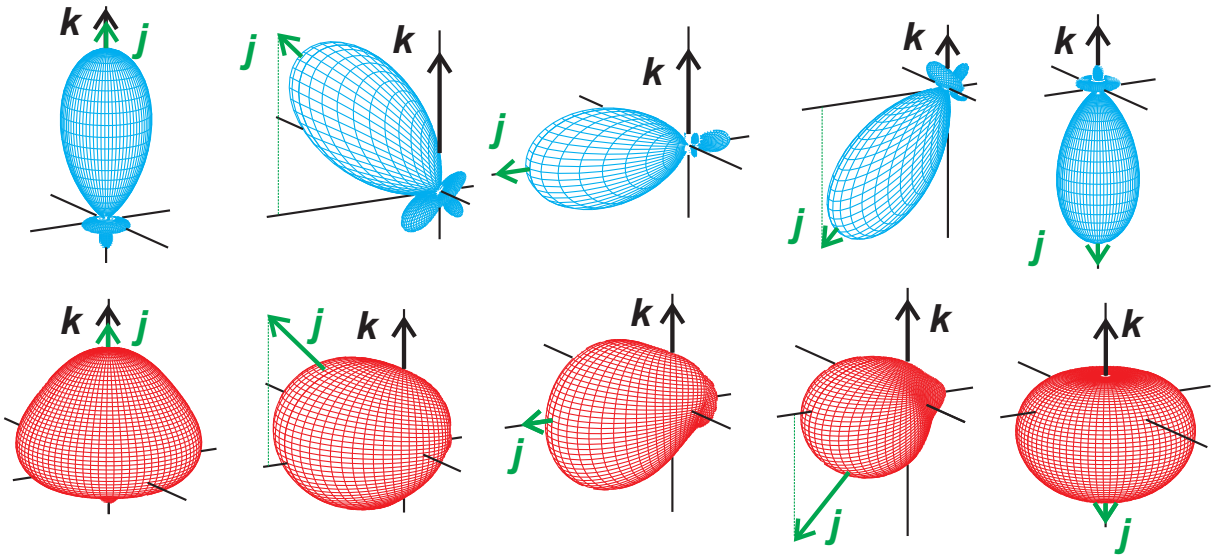


Figure 5.6: The ***k***-***j***-***j***′ distribution for N=2 to N'=3 for NO(A)-Kr (top row) and OH(A)-Kr (bottom row). The plots, from left to right are for $\theta_{kj} = 0°$, $\theta_{kj} = 45°$, $\theta_{kj} = 90°$, $\theta_{kj} = 135°$ and $\theta_{kj} = 180°$.

of $\boldsymbol{j}$ in NO(A)-Kr than in OH(A)-Kr, where the distribution of $\boldsymbol{j}'$ is spread over a larger range of angles. This again reflects the less depolarising nature of collisions in NO(A)-Kr, where the direction of $\boldsymbol{j}$ is not significantly altered by the collision. In contrast, collisions of krypton with OH(A) cause significant depolarisation, resulting in the distribution of

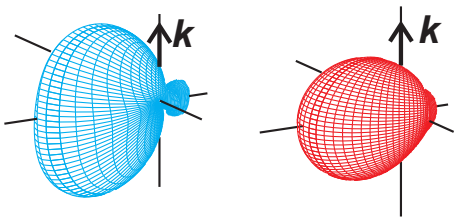


Figure 5.7: The $\boldsymbol{k}$-$\boldsymbol{j}$-$\boldsymbol{j}'$ distribution for N=2 to N'=3 for NO(A)-Kr (left panel) and OH(A)-Kr (right panel). The distributions are integrated over θ_{kj}, but $\boldsymbol{j}$ is still defined as lying in the $+zx$ plane.

$\boldsymbol{j}'$ being more isotropic with respect to the direction of $\boldsymbol{j}$, as is clearly evident from the correlations presented here.

The $\boldsymbol{k}$-$\boldsymbol{j}'$ distribution obtained by integrating the distribution over the direction of $\boldsymbol{j}$ (*i.e.* θ_{kj}) is shown in figure 5.7. The left hand panel corresponds to the distribution for NO(A)-Kr, and the right hand panel to the distribution for OH(A)-Kr. As shown in figure 5.8, all θ_{kj} angles contribute roughly equally to the integrated $\boldsymbol{k}$-$\boldsymbol{j}'$ distribution (where the left hand panel again corresponds to NO(A)-Kr and the right hand panel OH(A)-Kr). The integrated $\boldsymbol{k}$-$\boldsymbol{j}'$ correlation is less informative than when considered resolved into θ_{kj}. However, it is apparent there is still a strong propensity for $\boldsymbol{j}'$ to lie in the same plane as $\boldsymbol{j}$ in NO(A)-Kr, again reflecting the less depolarising nature of the collisions. For OH(A)-Kr, the distribution of $\boldsymbol{j}'$ is more isotropic, which would be expected as the collisions cause more significant depolarisation. This conclusion is supported by the two vector $\boldsymbol{j}$-$\boldsymbol{j}'$ correlation presented in figure 5.9 for the same transition. The left hand panel is for NO(A)-Kr and the right hand panel OH(A)-Kr. The distribution for NO(A)-

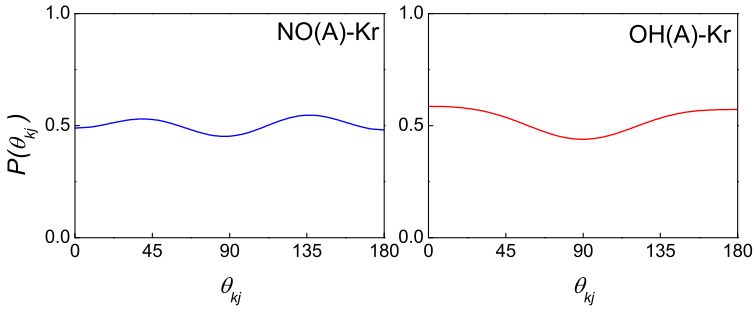


Figure 5.8: The $\boldsymbol{k}$-$\boldsymbol{j}$ correlation for N=2 to N'=3 for NO(A)-Kr (left panel) and OH(A)-Kr (right panel).

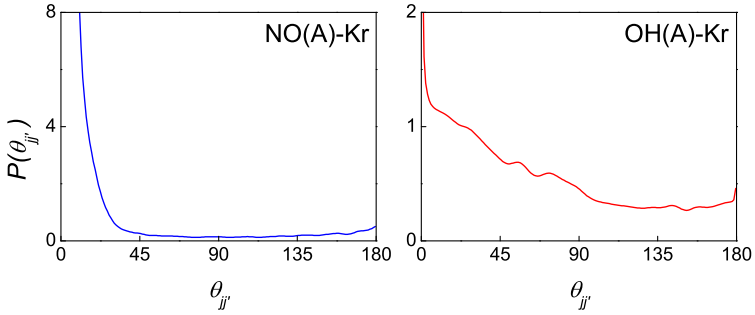


Figure 5.9: The $\boldsymbol{j}$-$\boldsymbol{j}'$ correlation for N=2 to N'=3 for NO(A)-Kr (left panel) and OH(A)-Kr (right panel).

Kr is strongly peaked at $\theta_{jj'} = 0°$ showing the collisions do not significantly change the direction of $\boldsymbol{j}$, and consequently do not cause depolarisation. As shown by the DCS in figure 5.4, the collisions that bring about the transition are relatively 'glancing blow', and so would not be expected to cause significant depolarisation. In contrast, collisions in OH(A)-Kr are more depolarising, as shown by the more isotropic distribution in the right hand panel of figure 5.9. These collisions also lead to forward scattering, but the anisotropy of the potential energy surface still leads to the randomisation of the direction of $\boldsymbol{j}$.

5.9 Kinematic apse

The kinematic apse is defined as [18]:

$$\hat{\boldsymbol{a}} = \frac{\boldsymbol{k}' - \boldsymbol{k}}{|\boldsymbol{k}' - \boldsymbol{k}|} \tag{5.58}$$

For a purely impulsive interaction between a hard sphere and a rigid ellipsoid, there can only be a change in rotational angular momentum perpendicular to the scattering plane. This leads to the propensity rule that the projection of $\boldsymbol{j}$ onto the kinematic apse is conserved throughout the collision [18, 241, 242]. Scatter plots showing the projection of $\boldsymbol{j}$ (m_j^a) and $\boldsymbol{j}'$ ($m_{j'}^a$) onto the kinematic apse are presented in figure 5.10 for NO(A)-Kr (left column), OH(A)-Kr at a fixed collision energy of 39 meV (middle column) and OH(A)-Kr at a fixed collision energy of 0.9 eV (right column). The top row corresponds to N=2,

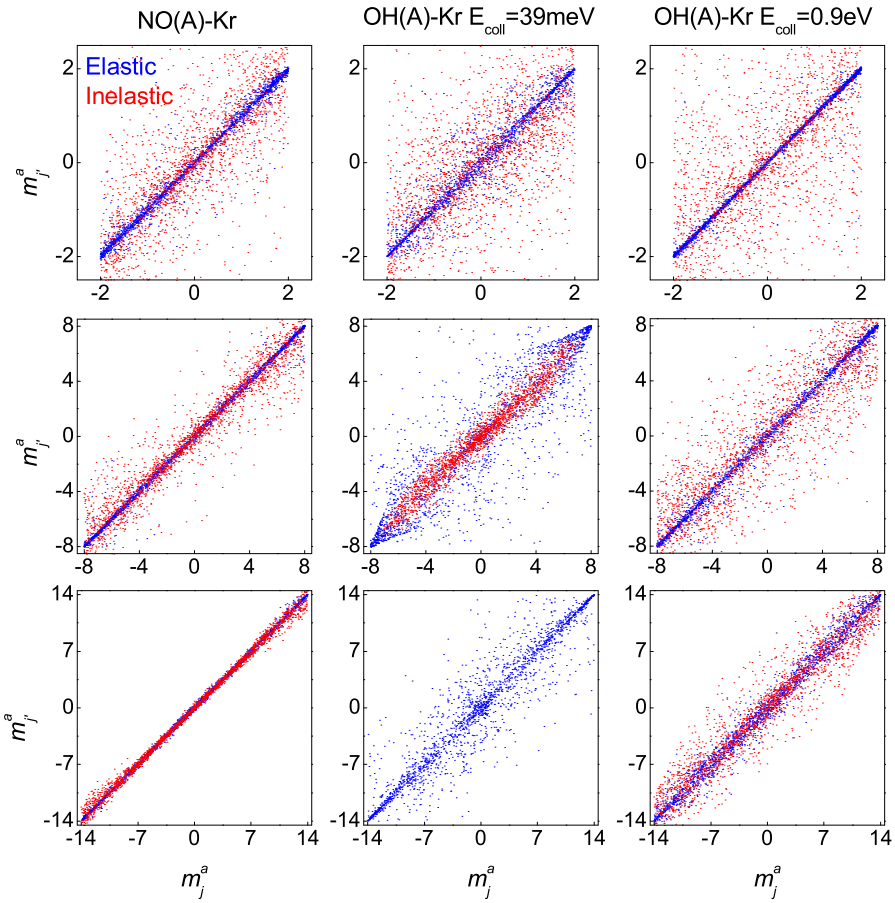


Figure 5.10: Scatter plots showing the projection of $\boldsymbol{j}$ (m_j^a) and $\boldsymbol{j}'$ ($m_{j'}^a$) onto the kinematic apse for NO(A)-Kr (left column), thermal OH(A)-Kr (middle column) and superthermal OH(A)-Kr (right hand column). The top row corresponds to N=2, the middle N=8 and the bottom N=14. Elastic trajectories are shown in blue, and inelastic trajectories are shown in red. It should be noted that under thermal conditions there are no inelastic trajectories for N=14 OH(A)-Kr.

the middle row to N=8 and the bottom row to N=14. Inelastic trajectories are shown in red, and elastic trajectories are shown in blue. Here, an elastic trajectory is defined as $\Delta j \leqslant 0.5$ but $\Delta K \geqslant 0.5$ *i.e.* the trajectory leads to elastic depolarisation. It should be noted that there are no inelastic trajectories in OH(A)-Kr under thermal conditions for N=14. For all the transitions and systems considered here, there is good conservation of the projection of $\boldsymbol{j}$ onto the kinematic apse. The conservation is stronger for elastic transitions than for inelastic, as would be expected as rotational energy transfer (RET) is more likely to be accompanied by a larger change in the direction of $\boldsymbol{j}$ than an elastic collision. The conservation is also seen to be better in NO(A)-Kr than OH(A)-Kr under

thermal conditions. This is not surprising, as collisions in NO(A)-Kr are significantly more impulsive than in OH(A)-Kr, where the significant potential well gives rise to orbiting trajectories. As N increases, the conservation of the projection of $\boldsymbol{j}$ onto the kinematic apse is also seen to improve. At higher N, the collisions sample the more repulsive part of the potential, and therefore become more impulsive, leading to the observed better conservation.

As the collision energy is increased, the projection of $\boldsymbol{j}$ is less well conserved. It would be expected that the conservation should be better at the higher collision energy as the collisions become more impulsive and are less likely to be influenced by the attractive potential well. However, there is significantly more RET at higher collision energies, which means to conserve the projection of $\boldsymbol{j}$ onto the kinematic apse the direction would have to change significantly. This would also lead to significant depolarisation. As shown in the previous chapter, collisions of OH(A) with krypton become less depolarising as the collision energy is increased. Therefore, the direction of $\boldsymbol{j}$ is not altered significantly by the collision, and consequently the projection of $\boldsymbol{j}$ onto the apse is less well conserved.

It is possible to consider the $\boldsymbol{a}$-$\boldsymbol{j}$-$\boldsymbol{j}'$ correlation using the same formalism as presented earlier in the chapter for the $\boldsymbol{k}$-$\boldsymbol{j}$-$\boldsymbol{j}'$ correlation. In the kinematic apse frame, the apse is defined as lying along the $+z$ axis, and $\boldsymbol{j}$ as lying in the $+zx$ plane. Considering again the four vector $\boldsymbol{k}$-$\boldsymbol{k}'$-$\boldsymbol{j}$-$\boldsymbol{j}'$ correlation, the apse will lie in the scattering plane. Therefore, to make $\boldsymbol{a}$ the $+z$ axis, as opposed to $\boldsymbol{k}$, all that is required is a rotation about the y axis (which is perpendicular to the scattering plane) through an angle of θ_{ak}, which is the angle between $\boldsymbol{k}$ and $\boldsymbol{a}$. The equations derived are equally valid when $\boldsymbol{a}$ is the $+z$ axis, as they were obtained by considering the effects of reflecting the distribution in the zx plane, which corresponded to the scattering plane. After the rotation through θ_{ak} about the y axis, the scattering plane is still the zx plane, and therefore the results of considering the reflection of the distribution will still be the same. However, the angles defining the directions of $\boldsymbol{j}$ and $\boldsymbol{j}'$ should be defined with respect to $\boldsymbol{a}$ as opposed to $\boldsymbol{k}$. Therefore, the direction of $\boldsymbol{j}$ is defined by the polar and azimuthal angles θ_{aj} and ϕ_{aj}, and the direction

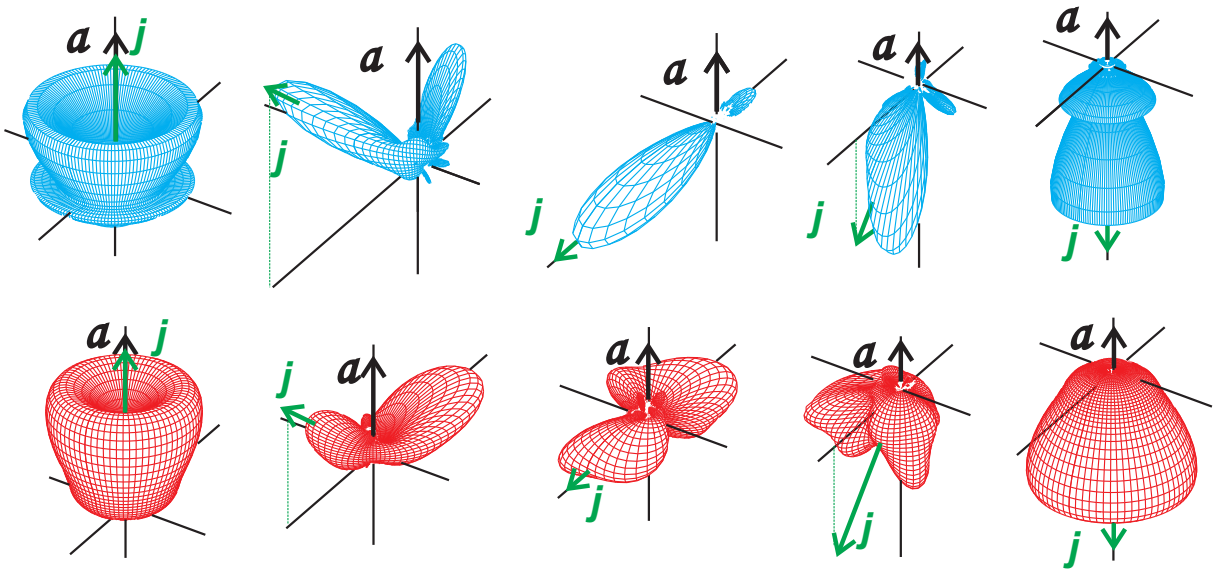


Figure 5.11: The $\boldsymbol{a}$-$\boldsymbol{j}$-$\boldsymbol{j}'$ distribution for N=2 to N'=3 for NO(A)-Kr (top row) and OH(A)-Kr (bottom row). The plots, from left to right are for $\theta_{aj} = 0°$, $\theta_{aj} = 45°$, $\theta_{aj} = 90°$, $\theta_{aj} = 135°$ and $\theta_{aj} = 180°$.

of $\boldsymbol{j}'$ by the angles $\theta_{aj'}$ and $\phi_{aj'}$.

The $\boldsymbol{a}$-$\boldsymbol{j}$-$\boldsymbol{j}'$ correlations are presented in figure 5.11 for N=2 to N'=3 for NO(A)-Kr (top row) and OH(A)-Kr (bottom row). As previously, the distributions are shown for $\theta_{aj} = 0°$, 45°, 90°, 135° and 180°. These plots again illustrate the good conservation of the projection of $\boldsymbol{j}$ onto the kinematic apse. This is particularly apparent in the plots where $\theta_{aj} = 0°$. As the transition under consideration is N=2 to N'=3, for $\boldsymbol{j}'$ to have the same projection as $\boldsymbol{j}$ onto the apse, it is necessary for $\boldsymbol{j}'$ to lie in a cone around the z axis. The cylindrical symmetry observed at this angle is again a result of the $+zx$ plane being undefined, as both $\boldsymbol{a}$ and $\boldsymbol{j}$ lie along the z axis. However in general the distributions are not cylindrically symmetric. Although cylindrically symmetric distributions would allow the projection of $\boldsymbol{j}$ to be conserved, as has been shown previously collisions in NO(A)-Kr cause little depolarisation, and consequently $\theta_{jj'}$ is small. Therefore the distribution of $\boldsymbol{j}'$ is strongly polarised around the direction of $\boldsymbol{j}$. The distributions for OH(A)-Kr are broader, again reflecting the more depolarising nature of the collisions which results in a less polarised distribution of $\boldsymbol{j}'$.

The most striking difference between the $\boldsymbol{a}$-$\boldsymbol{j}$-$\boldsymbol{j}'$ plots presented for NO(A)-Kr and

OH(A)-Kr is that for NO(A)-Kr the $\boldsymbol{j}'$ distribution tends to lie in a cone around $\boldsymbol{j}$, whilst for OH(A)-Kr $\boldsymbol{j}'$ can also lie in a distribution over a specific range of other angles. This was also observed in the $\boldsymbol{a}$-$\boldsymbol{j}$-$\boldsymbol{j}'$ distributions for OH(A)-Ar which are shown in the bottom row of figure 5.12 [119]. However the structure is absent from the NO(A)-Ar distributions, presented in the top row of figure 5.12, and also was not observed in NO(A)-He [118]. For example, when $\boldsymbol{j}$ lies perpendicular to the apse, as shown in the middle panels of

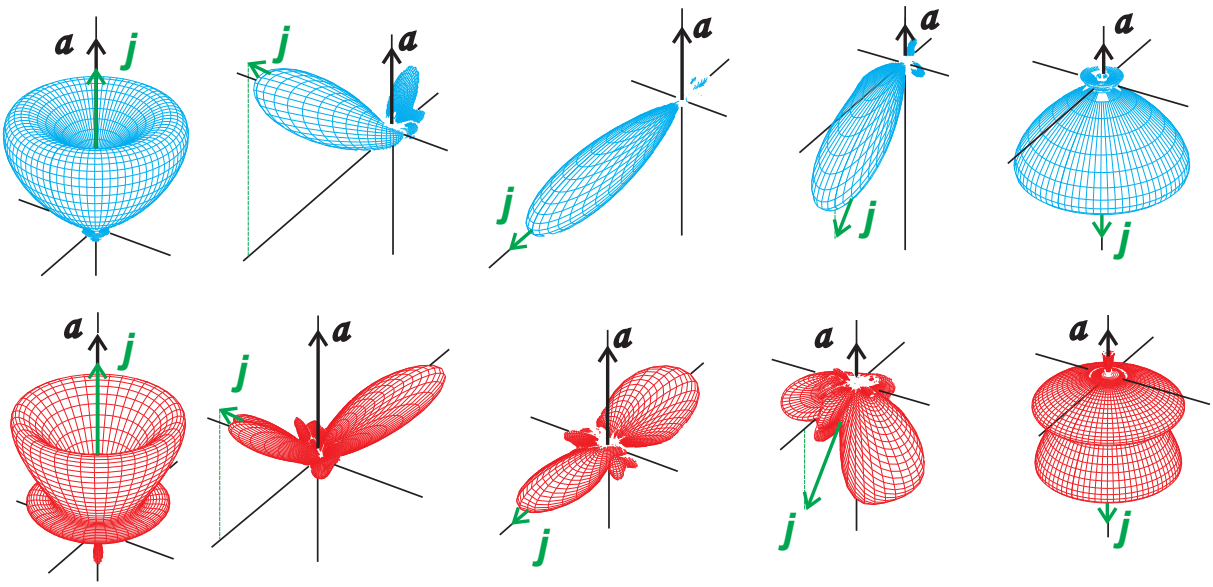


Figure 5.12: The $\boldsymbol{a}$-$\boldsymbol{j}$-$\boldsymbol{j}'$ distribution for N=2 to N'=3 for NO(A)-Ar (top row) and OH(A)-Ar (bottom row). The plots, from left to right are for $\theta_{aj} = 0°$, $\theta_{aj} = 45°$, $\theta_{aj} = 90°$, $\theta_{aj} = 135°$ and $\theta_{aj} = 180°$. Adapted from reference [119].

the figures, for NO(A)-Ar and NO(A)-Kr the resulting distributions of $\boldsymbol{j}'$ are strongly polarised along the direction of $\boldsymbol{j}$. In the equivalent plots for OH(A)-Ar and OH(A)-Kr, $\boldsymbol{j}'$ can also lie along $\boldsymbol{j}$, but it is approximately equally likely to lie anti-parallel to $\boldsymbol{j}$. Whilst this conserves the projection of $\boldsymbol{j}$ onto the apse, it means the diatom is rotating in the opposite sense as a result of the collision. This can be attributed to the significantly more attractive nature of the interactions of OH(A) with krypton and argon, and also the kinematics of the OH(A) radical. As the rare gas atom approaches, it is possible for the attraction between the radical and rare gas to change the direction of rotation of the radical. In the case of OH(A)-Ar, this is exclusively attraction between the H end of the

radical and the argon, as the lightness of the H atom allows the H to swing around and meet the incoming Ar before it has chance to sample the deeper potential well in the Ar–OH geometry [206]. As shown, for OH(A)-Kr the krypton samples both the H end and O end of the radical. However, there is a substantial barrier to rotation which means that the direction of rotation of the radical can change to allow a favoured linear approach. Therefore, in the case when $\boldsymbol{j}$ lies perpendicular to the apse, such that the forces primarily act in the plane of rotation of the diatomic, two different types of trajectories can be envisaged. In the first case, the motion of the rare gas is the same as the sense of rotation of the OH(A), and the attraction accelerates the rotation of the radical from N=2 to N'=3. This will result in $\boldsymbol{j}'$ being parallel to $\boldsymbol{j}$. The component of the distribution where $\boldsymbol{j}'$ is antiparallel to $\boldsymbol{j}$ arises from trajectories where the sense of rotation of the radical is opposite to the motion of the incoming rare gas atom. In this case, the attraction of the argon to the H end of the radical, or the krypton to either end of the radical is sufficient to induce rotation in OH(A) in the opposite direction. When $\boldsymbol{j}$ lies at an angle other than 90° to the apse, the forces do not act purely in the OH(A) rotational plane. The strong attraction of the rare gas to the OH(A) can then lead to a reorientation of the plane of rotation, which leads to the double lobe structure observed when $\theta_{aj} = 45°$ and $\theta_{aj} = 135°$. Due to the importance of the attractive interaction in determining the distribution of $\boldsymbol{j}'$, it is perhaps surprising that the encounters still lead to good conservation of the projection of $\boldsymbol{j}$ onto the apse.

As mentioned above, the double lobe structure is almost entirely absent from the NO(A)-rare gas $\boldsymbol{a}$-$\boldsymbol{j}$-$\boldsymbol{j}'$ correlation plots [118, 119]. The potential energy surfaces for these systems are significantly more isotropic than those for OH(A)-Ar and OH(A)-Kr, and also much less attractive. Therefore, the interaction between the radical and atom is insufficient to significantly change the motion of the radical unless the collision is a direct, impulsive interaction. It follows that the distribution of $\boldsymbol{j}'$ is solely determined by the direction in which the impulse acts, leading to the oriented distributions observed.

The effect of increasing the collision energy on the $\boldsymbol{a}$-$\boldsymbol{j}$-$\boldsymbol{j}'$ distributions for OH(A)-

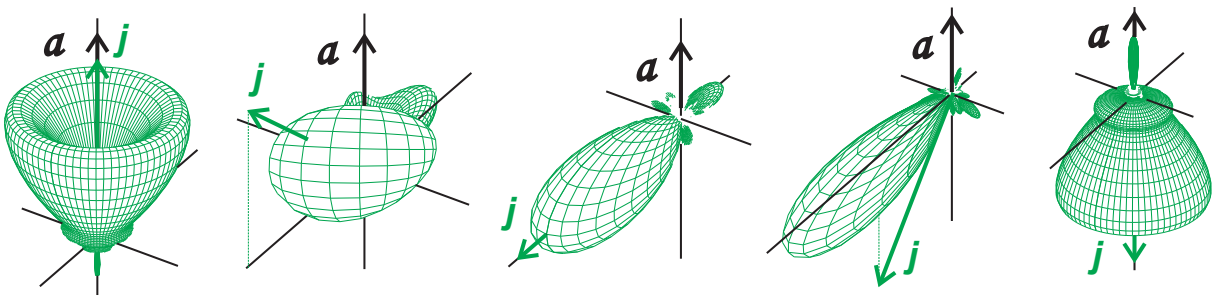


Figure 5.13: The ***a*-*j*-*j*′** distribution for N=2 to N'=3 for superthermal (0.9 eV) OH(A)-Kr . The plots, from left to right are for $\theta_{aj} = 0°$, $\theta_{aj} = 45°$, $\theta_{aj} = 90°$, $\theta_{aj} = 135°$ and $\theta_{aj} = 180°$.

Kr is shown in figure 5.13, for the same values of θ_{aj} as presented in figures 5.11 and 5.12. The plots are again for the transition N=2 to N'=3, but at a collision energy of 0.9 eV. As can be seen, the double lobe structure is lost due to the more impulsive nature of the collisions. The resulting distributions are oriented, as is observed for NO(A)-He [118], NO(A)-Ar and NO(A)-Kr. It should be noted that the same oriented distributions are observed in OH(A)-Ar as the collision energy is increased, and also as N (or N') is increased under thermal conditions, as the attractive regions of the PES play less of a role.

5.10 Summary

A theoretical description of three vector correlations has been presented, with particular emphasis on the ***k*-*j*-*j*′** correlation. It has been shown how lower order vector correlations can be obtained, for example the ***j*-*j*′** correlation, for which experimental results for NO(A)-Kr and OH(A)-Kr were shown in the previous chapter. The ***k*-*k*′-*j*′** correlation was considered [8, 162], which can also be measured experimentally [15–17, 243]. Results for this correlation will be presented in the following chapter for NO(X)-Ar.

A comparative study of these vector correlations in NO(A)-Kr and OH(A)-Kr has been considered, using the results of the fixed energy quasi-classical trajectory calculations, described in section 2.3.2. As has been shown, impulsive collisions dominate in NO(A)-Kr, which do not lead to significant depolarisation, whereas collisions of OH(A) with krypton

result in a larger change in the direction of $\boldsymbol{j}$, supporting the conclusions reached in the previous chapter. However, in both systems the projection of $\boldsymbol{j}$ onto the kinematic apse is conserved throughout the collision, a property that is only strictly observed in the limits of an idealised, impulsive collision between a hard sphere and rigid ellipsoid. As the OH(A)-Kr potential energy surface has significant attractive character, the good conservation of the projection of $\boldsymbol{j}$ onto the apse is not necessarily expected. It has also been shown that the attractive nature of the potential plays a role in the collision under thermal conditions, leading to an aligned distribution of $\boldsymbol{j}'$ with respect to the apse when $\boldsymbol{j}$ lies perpendicular to the apse, and leading to a double lobe structure for different θ_{aj} angles. Therefore, the collisions cannot be considered as impulsive encounters. If the collisions were impulsive, the distribution of $\boldsymbol{j}'$ would be oriented, as is seen to be the case in the $\boldsymbol{a}$-$\boldsymbol{j}$-$\boldsymbol{j}'$ correlations in NO(A)-Kr. Previous studies have also shown that impulsive collisions dominate in the case of NO(A)-He [109, 118] and NO(A)-Ar [109, 119], whereas for OH(A)-Ar the same influence of the attractive part of the potential is seen [116, 119]. However, in all cases there is observed to be good conservation of the projection of $\boldsymbol{j}$ onto the kinematic apse. As the collision energy is increased, the $\boldsymbol{a}$-$\boldsymbol{j}$-$\boldsymbol{j}'$ distributions become oriented for OH(A)-Ar and OH(A)-Kr, as the collisions sample the attractive part of the potential less, and consequently become more impulsive in nature.

Chapter 6

Vector correlations in NO(X)

There has been considerable interest in studying the collisions of NO(X) with the rare gases. These systems have an added degree of complexity compared to the $^2\Sigma$ states considered in the previous chapters due to the two spin-orbit states, both of which can be populated as a result of collisions. This leads to a breakdown in the Born-Oppenheimer approximation. However, it is still possible to perform exact quantum mechanical scattering calculations. There has therefore been much previous work comparing experimentally and theoretically obtained rotational energy transfer cross-sections [28, 72, 97–100, 168, 192–197] and differential cross-sections (DCSs) [9, 12, 19, 21–23, 64–73], as well as considering collisional depolarisation [106, 110]. The majority of these previous studies were performed for a specific initial rotational level of NO(X), but with the Λ-doublet level unresolved.

Previous measurements made using the crossed molecular beam apparatus from which results are presented in this chapter have highlighted the extra information that can be gained by resolving the initial Λ-doublet level as well as the final Λ-doublet level. The role that parity plays in the DCSs has been studied for NO(X)-He [19, 20] and NO(X)-Ar [21–23]. In both systems, there was evidence of so called 'parity pairs', where the rotational states with the same parity (*i.e.* the e Λ-doublet level of the $j' = n - 0.5$ level and the f Λ-doublet level of the $j' = n + 0.5$ level) had similarly structured DCSs. Oscillations were also observed in the DCSs for the collisions of NO(X)-Ar [21–23] where the parity was conserved, but not NO(X)-He [19, 20]. These were shown to be due to interference

between trajectories in which the Ar atom interacts with either end of the NO(X) radical and the side. This was not observed in NO(X)-He due to the smaller momentum (and so longer de Broglie wavelength) associated with the system at the collision energy of the experiment. Without the hexapole state selection exploited here these effects would not be observed, as both Λ-doublet levels would be populated, and these effects would be averaged over both parities.

Collision induced alignment has also been studied previously for the NO(X)-rare gas systems [15, 16, 243–247]. Chandler and co-workers used a polarised pump laser coupled with velocity mapped ion imaging to obtain the $\boldsymbol{k}$-$\boldsymbol{k}'$-$\boldsymbol{j}'$ correlation for NO(X)-Ar [15, 16]. This is similar to the experimental results that will be presented in this chapter for collisions of NO(X) with argon, but those presented here have been recorded with full Λ-doublet resolution of the initial state, allowing the effect that parity has on the collision induced alignment to be determined. Chandler and co-workers have also investigated the collision induced orientation of NO(X) with Ar [17]. This provides information about the handedness with which the molecule is rotating after the collision, *i.e.* either clockwise or anticlockwise, which is complementary to that obtained from the collision induced alignment measurements.

In this chapter, the experimental methods employed to obtain full Λ-doublet resolution of the initial NO(X) state will be described, along with the crossed molecular beam apparatus used to obtain the data shown. The kinematic apse model will be presented, which can be used to account for the collision induced alignment effects considered here. The differential cross-section measurements made for the inelastic scattering of NO(X) with krypton will be presented in section 6.6, before the experimentally obtained collision induced alignment results for NO(X)-Ar. These will be compared with the predictions of the apse model in the final section of the chapter.

6.1 Hexapole state selection

It is possible to select the initial state of a polar symmetric top molecule or linear molecules with non-zero angular momentum using hexapole focussing [248]. A hexapole consists of six electrostatic rods with alternating positive and negative charges [249], and therefore this state selection is achieved by exploiting the Stark effect. In a static electric field, the additional interaction is given by [102, 250]:

$$V_{\text{Stark}} = -\boldsymbol{\mu} \cdot \boldsymbol{E} = -\mu E \cos\theta_{\mu E} \tag{6.1}$$

where $\boldsymbol{\mu}$ is the electric dipole of the NO(X), $\boldsymbol{E}$ is the applied electric field, and $\theta_{\mu E}$ is the angle between the two.

The potential at a point (r, ϕ) in an ideal hexapole is given by:

$$V(r, \phi) = V_0 \left(\frac{r}{r_0}\right)^3 \cos 3\phi \tag{6.2}$$

where V_0 is the potential applied to the rods and r_0 is the radius of the hexapole. The magnitude of the electric field the radical experiences is therefore:

$$E(r) = \frac{3V_0 r^2}{r_0^3} \tag{6.3}$$

Combining equations (6.1) and (6.3) allows the radial force to be calculated as [251, 252]:

$$F(r) = \mu \langle \cos\theta_{\mu E} \rangle \frac{\mathrm{d}E(r)}{\mathrm{d}r} = \frac{6V_0 \mu r}{r_0^3} \langle \cos\theta_{\mu E} \rangle \tag{6.4}$$

where $\langle \cos\theta_{\mu E} \rangle \approx \frac{\epsilon |m\Omega|}{j(j+1)}$. It follows that the e state (ϵ=+1) will be high field seeking and diverge from the path of the hexapole, whereas the f (ϵ=−1), low field seeking state will be focussed along the axis of the hexapole.

6.2 Experimental methods

The experimental ion images presented later in this chapter for the scattering of NO(X) with argon and krypton were obtained using a crossed molecular beam set up, coupled with a (1+1′) REMPI detection scheme and velocity mapped ion imaging. The initial quantum state of NO(X) was selected using hexapole focussing, allowing full Λ-doublet resolution of the molecular wavefunction to be achieved.

6.2.1 Molecular beams

A schematic diagram of the experiment is presented in figure 6.1. A pulsed General valve, operating at 10 Hz produces the NO(X) molecular beam in chamber 1. The NO beam was seeded at 16% in argon to aid adiabatic cooling, so most of the NO is present in its lowest rotational state, Ω=0.5, j=0.5. This passes through a 5 mm diameter skimmer 3 cm away from the source, which further selects the most rotationally cold part of the molecular beam, before entering the hexapole. As outlined above, this state selects the Ω=0.5, j=0.5 f Λ-doublet component of the NO(X). The hexapole also focusses this state into the scattering chamber, shown as chamber 3 in figure 6.1. Here the NO(X) beam is intersected by the secondary molecular beam, travelling at 90° to the primary beam. This secondary beam is also produced by a General valve in chamber 4. This passes through a

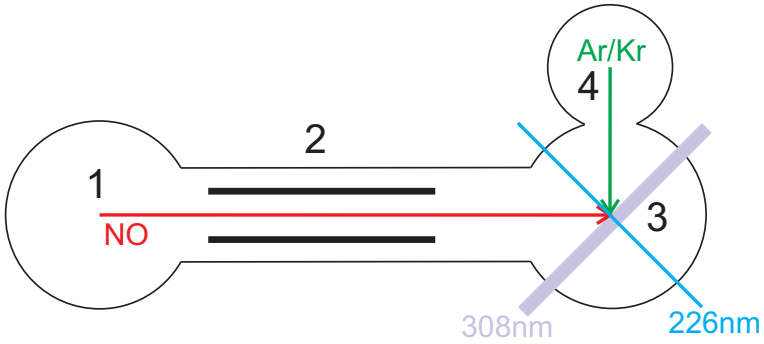


Figure 6.1: Schematic of the crossed molecular beam apparatus used to perform the experimental measurements described in this chapter. Chamber 1 is the NO source chamber, chamber 2 the hexapole, chamber 3 the scattering chamber and chamber 4 the source chamber for the secondary molecular beam. The time of flight tube and imaging detector are perpendicular to the plane containing the lasers and molecular beams.

skimmer with a diameter of 2 mm, 8 cm away from the General valve before entering the scattering chamber.

For the differential cross-section measurements that will be presented later in the chapter, the secondary beam was krypton. This beam operated at 5 Hz to allow the background signal to be recorded simultaneously to minimise the errors associated with experimental fluctuations.

In the limit that the internal energy of the gas is converted to kinetic energy, the velocities ($|\boldsymbol{v}|$) of the molecular beams can be determined using [1, 253, 254]:

$$|\boldsymbol{v}| = \sqrt{\frac{2k_B}{m}\left(\frac{\gamma}{\gamma - 1}\right)T} \tag{6.5}$$

where γ is the ratio of the fixed pressure and fixed volume heat capacities, C_p/C_v, m is the mass of the gas and T is the temperature. At a temperature of 298 K, the velocity of the NO(X) beam is calculated to be 583 ms^{-1} and the krypton beam to be 384 ms^{-1}.

The collision energy can also be obtained using the radii of the ion images that will be presented in section 6.6. The radius of the image is determined by the final centre of mass velocity of the NO(X) after the collision, and therefore as the rotational state of the NO(X) increases, the radius of the image decreases. Figure 6.2 shows a plot of the radius of the resulting ion image as a function of the final rotational state, j'. The best fit to the data gives a collision energy of 64 meV (approximately 520 cm^{-1}). Assuming

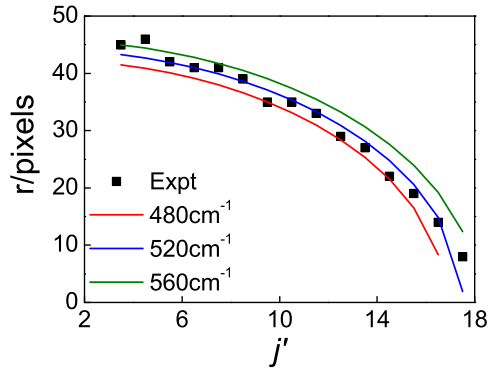


Figure 6.2: A plot of the experimentally determined radius of the Newton spheres from the images presented in section 6.6 vs the final rotational state, j'.

that the velocity of the NO(X) beam is $625\,\mathrm{ms}^{-1}$, as has been determined previously [23] (see below), the velocity of the krypton beam is then $410\,\mathrm{ms}^{-1}$. These values are larger than those obtained from equation (6.5). However, using a temperature of 340 K in the calculated value returns the values of the velocities of the beams obtained from the ion images. It is not unreasonable that the temperature of the General valves will increase during use due to friction of the valve mechanism, or through the resistance to electrical current of the valve. Therefore the velocities of the krypton and NO(X) beams will be considered to be $410\,\mathrm{ms}^{-1}$ and $625\,\mathrm{ms}^{-1}$ respectively.

The same method for obtaining the velocities has been used previously for collisions of NO(X) with argon [23]. The velocities for the NO(X) beam and argon beam obtained were $625\,\mathrm{ms}^{-1}$ and $580\,\mathrm{ms}^{-1}$ respectively. These are again larger than the values calculated using equation (6.5) at a temperature of 298 K. However, using a temperature of approximately 340 K once again produces the molecular beam velocities determined from the radii of the Newton spheres. These velocities give rise to a centre of mass collision energy of 65 meV (approximately $530\,\mathrm{cm}^{-1}$).

6.2.2 Vacuum system

Due to the long flight path of the NO(X) beam, it is necessary to maintain a good vacuum throughout the experiment. For the NO(X)-Ar collision induced alignment experiments, typical operating pressures throughout the NO source chamber (chamber 1), hexapole (chamber 2) and scattering chamber (chamber 3) were of the order of 1×10^{-6} mbar with the molecular beams on. With the argon beam on, the pressure in the corresponding source chamber (chamber 4) was of the order of 1×10^{-5} mbar. The NO source chamber was pumped by a diffusion pump, backed by a roots pump which was then backed with a rotary vane pump. The path between the NO source chamber and scattering chamber was pumped with four diffusion pumps, and there was a further diffusion pump attached to the secondary beam source chamber. Each diffusion pump was backed by a rotary vane pump. The scattering chamber (chamber 3) was pumped using a turbo pump (backed by

a rotary vane pump), to avoid contaminating this chamber with oil.

After making the NO(X)-Ar collision induced alignment measurements, all the diffusion pumps except that on the NO(X) source chamber were replaced with turbo pumps. These are all backed by rotary vane pumps. This modification has improved the vacuum throughout the experiment, resulting in typical pressures of approximately 1×10^{-7} mbar in the hexapole, and 5×10^{-7} mbar in the scattering chamber when both molecular beams are on.

6.2.3 Lasers

A XeCl excimer EMG 201 MSC lasing at 308 nm with a power output of approximately 120 mJ/pulse was passed through a beam splitter. About 90% of the beam was used to pump an FL3002 tunable dye laser. The dye employed was Coumarin 2 in methanol which lases at approximately 452 nm. This was then frequency doubled to about 226 nm, and the wavelength tuned to the rovibrational NO(A $\leftarrow$ X) transition of interest. The output from the dye laser was then passed through a Rochon polariser and photoelastic modulator (PEM) before entering the scattering chamber in the plane of the molecular beams, at an angle of 45° to the secondary molecular beam.

The remaining 10% of the excimer beam was guided into the scattering chamber, again in the plane of the molecular beams, perpendicular to the dye laser and at an angle of 45° to both molecular beams, as shown in figure 6.1. As the excimer beam was slightly divergent, a focussing lens was used to lightly focus the excimer beam into the scattering centre. The resulting detection volume obtained where the dye laser and excimer laser overlapped was of the order of 1.5 mm×1.5 mm×3 mm.

6.2.4 Detection

A (1+1′) REMPI excitation scheme was employed, where the dye laser was used to selectively excite a final Ω', j', Λ' state from the X $^2\Pi$ state to the A $^2\Sigma^+$ state, and the excimer laser then ionises the molecules in the A state. This scheme allows the dye laser power to

be kept low, to avoid saturating the transition [255].

The ions are detected using velocity mapped ion imaging [62, 63]. This is achieved using an inhomogeneous electric field to focus the ions with the same velocity onto the same point on a position sensitive detector. The field was created using a positively charged extractor and repeller and a ground electrode. Typical voltages applied to achieve velocity mapping were approximately 1500 V on the repeller and 1000 V on the extractor. The detector itself comprises of two micro channel plates (MCPs) in front of a P47 phosphor screen. The voltage applied to the front MCP was typically −920 V, and that to the back MCP +920 V. The voltage on the phosphor screen was 3.2 kV. The detector was gated by pulsing the front MCP. Each individual ion that hits the front MCP produces a stream of electrons that travel through the MCPs, amplifying the signal. These electrons then hit the phosphor screen, producing a flash which is recorded using a charge coupled device camera. Each shot of the laser could produce between 5 and 20 ions. Therefore to record the NO(X)-Kr DCS images between 10000 and 20000 laser shots were used, and to produce the final NO(X)-Ar collision induced alignment images presented in this work it was necessary to sum over 300000 laser shots.

The intensity of the detected signal at a point (x, y) on the detector is given by [1, 15, 22, 23]:

$$\begin{aligned} F(x,y,j^\star,j',j,\chi_p) &= \int\int\int\int\int\int\int n_{\mathrm{NO}}(\boldsymbol{r}_{\mathrm{NO}},\boldsymbol{v}_{\mathrm{NO}},t'_{\mathrm{NO}})n_{\mathrm{rg}}(\boldsymbol{r}_{\mathrm{rg}},\boldsymbol{v}_{\mathrm{rg}},t'_{\mathrm{rg}}) \\ &\times f_{t_{\mathrm{NO}}}(v_{\mathrm{NO}})f_{t_{\mathrm{rg}}}(v_{\mathrm{rg}})\frac{v_{\mathrm{rel}}}{v'_{\mathrm{NO}}}\sigma^{(0)}_{jj'}(v_{\mathrm{rel}})P(\boldsymbol{r}_{\mathrm{det}})P(\theta_{kk'})A(x,y,j^\star,j',\chi_p) \\ &\times \delta(t_{\mathrm{NO}}-t'_{\mathrm{NO}})\delta(t_{\mathrm{rg}}-t'_{\mathrm{rg}})\mathrm{d}t'_{\mathrm{NO}}\mathrm{d}t'_{\mathrm{rg}}\mathrm{d}v_{\mathrm{NO}}\mathrm{d}v_{\mathrm{rg}}\mathrm{d}\boldsymbol{t}_{\mathrm{coll}}\mathrm{d}\boldsymbol{r}_{\mathrm{coll}}\mathrm{d}\boldsymbol{r}_{\mathrm{det}} \end{aligned} \quad (6.6)$$

$j^\star$ is the rotational level the molecule is excited to in the A state, j' the final rotational angular momentum of the NO(X) radical after the collision, $\theta_{kk'}$ and $\phi_{kk'}$ the polar and azimuthal angles of the final relative velocity, $\boldsymbol{k}'$, with respect to the initial velocity, $\boldsymbol{k}$, and the plane containing the molecular beams and χ_p the angle between the electric vector of the polarised pump laser, $\boldsymbol{\varepsilon}$, and the molecular beam plane. $A(x, y, j^\star, j', \chi_p)$ incorporates

the polarisation information for the system and $P(\theta_{kk'})$ is the probability that the product is scattered through an angle $\theta_{kk'}$. This is proportional to the differential cross-section, where the proportionality constant is the cross-section for scattering from state j to j', $\sigma^{(0)}_{jj'}$.

The remaining terms in the equation are experimental parameters, which are defined as follows. $n_{\mathrm{NO}}(\boldsymbol{r}_{\mathrm{NO}}, \boldsymbol{v}_{\mathrm{NO}}, t'_{\mathrm{NO}})$ and $n_{\mathrm{rg}}(\boldsymbol{r}_{\mathrm{rg}}, \boldsymbol{v}_{\mathrm{rg}}, t'_{\mathrm{rg}})$ correspond to the number densities in the NO and secondary, rare gas (rg) molecular beams respectively, which depend on the initial position, $\boldsymbol{r}$, velocity $\boldsymbol{v}$ and time t. The vector $\boldsymbol{r}$ is defined perpendicular to the direction of propagation of the molecular beam, and accounts for the variation in the number density across the width of the beam. $f_{t_{\mathrm{NO}}}(v_{\mathrm{NO}})$ and $f_{t_{\mathrm{rg}}}(v_{\mathrm{rg}})$ are the (normalised) velocity distributions in the molecular beams. $P(\boldsymbol{r}_{\mathrm{det}})$ accounts for the probability that the product will be detected at the position $\boldsymbol{r}_{\mathrm{det}}$, which depends on both the laser position and time at which the laser fires. The two Dirac delta functions ensure that the NO and rare gas are at the collision point $\boldsymbol{r}_{\mathrm{coll}}$ at the time of the collision, t_{coll}. The outer two integrals correspond to integrating over the collision volume, defined as the region where the two molecular beams overlap, and the detection volume, which corresponds to the volume where the excimer and dye laser overlap.

Assuming that $A(x, y, j^\star, j', \chi_p)$ does not depend on the experimental parameters mentioned above, the intensity of the signal at the point (x, y) can be written as [23]:

$$F(x, y, j^\star, j', j, \chi_p) = B(x, y, j, j')P(\theta_{kk'})A(x, y, j^\star, j', \chi_p) \tag{6.7}$$

$B(x, y, j, j')$ is an instrument function, which accounts for the probability that the products from a collision from initial state j to final state j' will be detected and contribute to the intensity of the image at point (x, y). This has been discussed in detail previously [21–23], and only a brief summary will be given here in section 6.3.

For the collision induced alignment measurements, the PEM is used to flip the laser polarisation between horizontal (*i.e.* parallel to the plane containing the molecular beams

so $\chi_p = 0°$) and vertical (*i.e.* perpendicular to the same plane so $\chi_p = 90°$) linearly polarised light. To a good approximation, only the $A(x, y, j^\star, j', \chi_p)$ term changes with changing laser polarisation. Taking the normalised difference between the two images therefore allows the polarisation to be separated from the DCS and instrument function *via*:

$$\frac{I_V - I_H}{I_V + I_H} = \frac{F(x, y, j^\star, j', j, 90°) - F(x, y, j^\star, j', j, 0°)}{F(x, y, j^\star, j', j, 90°) + F(x, y, j^\star, j', j, 0°)} \tag{6.8}$$

$$\approx \frac{A(x, y, j^\star, j', 90°) - A(x, y, j^\star, j', 0°)}{A(x, y, j^\star, j', 90°) + A(x, y, j^\star, j', 0°)} \tag{6.9}$$

It follows that $-1 < \frac{I_V - I_H}{I_V + I_H} < +1$, where a value of 0 indicates there is no alignment of $\boldsymbol{j}'$ following the collision.

6.3 Flux-density effects

The first term in equation (6.7), $B(x, y, j, j')$, is the instrument function, which accounts for the variation in intensity of the ion image due to the experimental apparatus used. This can be written as [22]:

$$\begin{aligned} B(x, y, j, j') = & \int\int\int\int\int\int\int n_{\mathrm{NO}}(\boldsymbol{r}_{\mathrm{NO}}, \boldsymbol{v}_{\mathrm{NO}}, t'_{\mathrm{NO}}) n_{\mathrm{rg}}(\boldsymbol{r}_{\mathrm{rg}}, \boldsymbol{v}_{\mathrm{rg}}, t'_{\mathrm{rg}}) \\ & \times f_{t_{\mathrm{NO}}}(v_{\mathrm{NO}}) f_{t_{\mathrm{rg}}}(v_{\mathrm{rg}}) \frac{v_{\mathrm{rel}}}{v'_{\mathrm{NO}}} \sigma^{(0)}_{jj'}(v_{\mathrm{rel}}) P(\boldsymbol{r}_{\mathrm{det}}) \\ & \times \delta(t_{\mathrm{NO}} - t'_{\mathrm{NO}}) \delta(t_{\mathrm{rg}} - t'_{\mathrm{rg}}) \mathrm{d}t'_{\mathrm{NO}} \mathrm{d}t'_{\mathrm{rg}} \mathrm{d}v_{\mathrm{NO}} \mathrm{d}v_{\mathrm{rg}} \mathrm{d}\boldsymbol{t}_{\mathrm{coll}} \mathrm{d}\boldsymbol{r}_{\mathrm{coll}} \mathrm{d}\boldsymbol{r}_{\mathrm{det}} \end{aligned} \tag{6.10}$$

where the variables have been defined in the previous section. It follows that to fully describe the instrument function it is necessary to consider the geometric design of the experiment, the spatial and temporal distributions of the molecular beams and their velocity distributions, the widths of the lasers (from which the detection volume can be calculated), and the laser positions and time delay with respect to the most probable collision time, as has been discussed previously [21–23, 256].

To calculate these instrument functions, a Monte-Carlo simulation is performed. This effectively performs the integral by summing over many trajectories, where the integration variables are randomly sampled from an appropriate distribution. A description of how the experiment is characterised to determine the values of the variables needed for the instrument function is presented below.

The velocities of the molecular beams have already been discussed in section 6.2.1, and determined to have values of 625 ms^{-1} for the NO(X) beam, 410 ms^{-1} for the krypton beam and 580 ms^{-1} for the argon beam. It is possible to estimate the spread in velocities within these molecular beams by recording a velocity mapped ion image of each of the beams. This is shown in figure 6.3 for the NO(X) and krypton beams. To image the krypton beam it

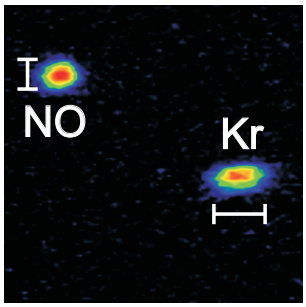


Figure 6.3: Velocity mapped ion images of the NO beam and krypton beam.

was necessary to add a small amount of NO(X) to the valve. As the mass of NO(X) is lower than for krypton, this will effect the resulting velocity of the beam. However, the amount of NO(X) used was kept low, so this should not be a significant perturbation. Therefore, from figure 6.3 it is possible to estimate the full width half maximum (corresponding to the length of the white lines) of the krypton beam as 115 ms^{-1} and the NO(X) as 80 ms^{-1}. Although the initial velocity of the NO(X) is larger, the hexapole also acts as a velocity filter, and therefore the distribution of the velocities in the NO(X) beam is smaller than that in the krypton beam.

The size of the detection volume can be determined by taking a spatially mapped image using either the NO(X) or secondary molecular beam (with a small amount of NO(X) so it can be detected). Spatial mapping is achieved by changing the ratio of voltages on the

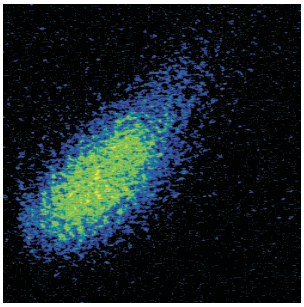


Figure 6.4: A spatial mapped ion image showing the laser overlap region.

ion optics, with the extractor voltage set to 750 V and the repeller remaining at 1500 V. This results in the ions created at the same point in space being mapped to the same point on the detector. A spatial map of the detection volume is shown in figure 6.4. In the figure, the direction of the dye laser is from top right to bottom left, and the excimer from bottom right to top left. The width of the dye laser beam is approximately 1.5 mm, from which it can be determined that the focussed excimer beam is approximately 3 mm wide in the centre of the scattering chamber. It should be noted that the less intense area in the top right of the image is from (1+1) signal, where the dye laser is both exciting the NO(X) to NO(A) and ionising the radicals in the electronically excited state.

The instrument function for j'=8.5 for NO(X)-Ar is shown in the left hand panel of figure 6.5, where the detection volume is assumed to be in the centre of the interaction region, and the time delay of the laser is set at its optimum value. There is a clear asymmetry about the relative velocity (which goes horizontally from right to left). As

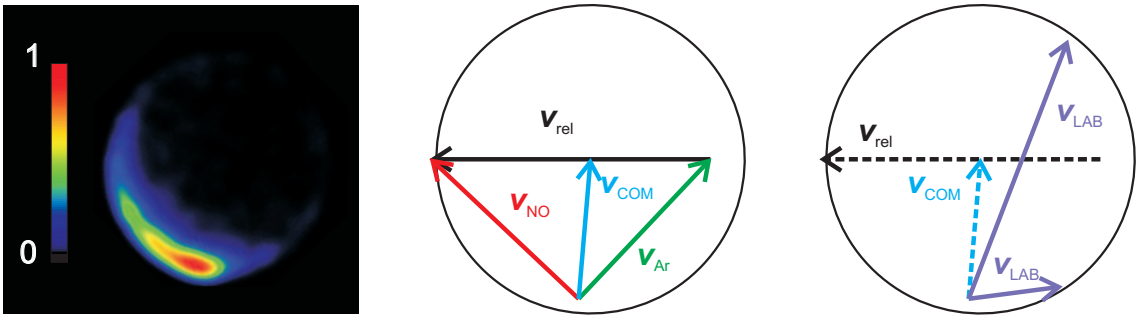


Figure 6.5: The left hand panel presents an example of an instrument function for $j' = 8.5$. The middle panel shows the Newton triangle for the scattering process, and the circle is the outline of the resultant Newton sphere. The right hand panel shows the LAB frame velocity for scattering to two different points on the Newton sphere.

the scattering process is cylindrically symmetric, and therefore has no $\phi_{kk'}$ dependence, the image should be symmetric about v_{rel}. The Newton triangle for the collision is shown in the middle panel of figure 6.5, along with the corresponding Newton sphere associated with the scattering process. The right panel shows the resultant laboratory (LAB) frame velocities for two radicals that have been scattered through the same angle to different points on the Newton sphere. As can be seen, the product scattered to the top right of the image has a larger LAB frame velocity, and so will leave the laser detection volume more quickly than that scattered to the bottom right of the image. Consequently it is less likely to be detected, and therefore the intensity of the image at that point will be smaller. Therefore the bottom half of the images correspond to radicals with slower lab frame velocities, and the top half of the images to those with higher lab frame velocities. These will be referred to as the slow side and fast side of the image respectively. It follows

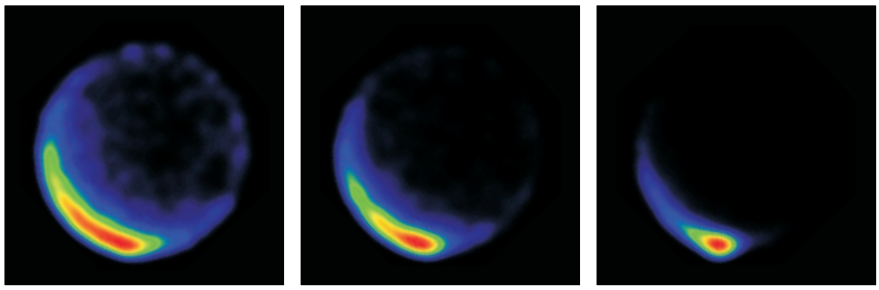


Figure 6.6: The effect of increasing the laser delay on the probability of detection. The middle image corresponds to the laser firing at the most probable collision time, the left hand image to it firing 100 μs earlier and the right hand image it firing 100 μs later. The relative velocity is horizontally from right to left. The scale is the same as in figure 6.5

that if the lasers fire at a later time, as shown in the right hand panel of figure 6.6, only the products with slow LAB frame velocities are likely to be detected, and there is only significant intensity in the slow side of the image. Equally, if the laser fires at an earlier time, as shown in the left hand panel of figure 6.6, there is more intensity on the fast side of the image. Whilst this appears desirable from the instrument functions presented here, this results in a loss of signal experimentally as fewer radicals will have undergone collisions.

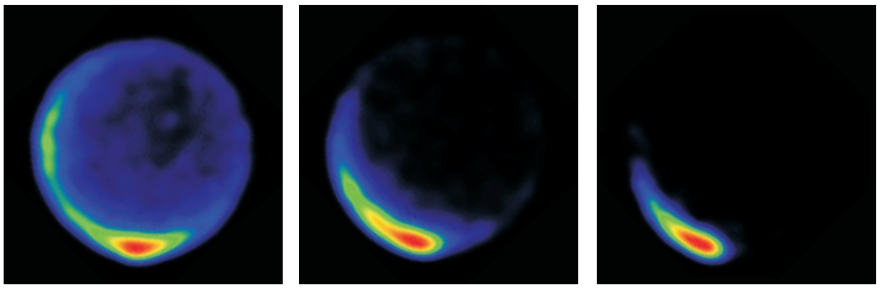


Figure 6.7: The effect of moving the detection volume on the probability of detection. The middle image corresponds to the laser being in the centre of the interaction region, the left hand image it being moved 5 mm towards the fast side of the image, and the right hand image it being moved 5 mm towards the slow side of the image. The relative velocity is horizontally from right to left. The scale is the same as in figure 6.5

The effect of moving the laser position is shown in figure 6.7. The right hand panel again shows the instrument function for j'=8.5 for NO(X)-Ar with the laser in the centre of the interaction region. As is clearly seen, moving the laser detection volume has a significant effect on the probability of detection. Moving the detection volume towards the fast side of the image, as considered in the left hand panel, favours detection of molecules with faster LAB frame velocities. Equally, moving the detection volume to the slow side of the image would favour molecules with slower LAB frame velocities, as shown in the right hand panel.

6.4 Kinematic apse model

In equation (6.7), the term $A(x, y, j^\star, j', \chi_p)$ contains the polarisation information, and accounts for the polarisation dependent probability that the radical will be detected. Previously, the kinematic apse model has been used to account for this [19–23], and this will be considered here. The model has also been shown to explain the product rotational angular momentum alignment in a number of previous studies [15, 244, 257–259], and the results from the model will be compared to those obtained experimentally later in the chapter for the collision induced alignment of NO(X)-Ar.

The concept of the kinematic apse was introduced in section 5.9, and applied to col-

lisions of NO(A) and OH(A) with krypton. As the projection of $\boldsymbol{j}$ onto the apse was observed to be conserved in both systems, it is reasonable to assume that the same approximation will be true for collisions of NO(X) with argon and krypton. As the NO(X) radical is in its rotational ground state, *i.e.* j=0.5 it follows that the initial projection (m_j^a) and final projection ($m_{j'}^a$) of the rotational angular momentum onto the apse are both equal to 0.5. Therefore, if $j' > 0.5$ after the collision, $\boldsymbol{j}'$ must lie perpendicular to the kinematic apse. The results from quantum mechanical calculations have shown that when the apse is taken as the reference axis, the only moment that contributes to the expansion of the $\boldsymbol{j}'$ distribution is the $a_0^{(2)}$ moment [247]. This takes its negative limiting value of -0.5. Therefore the distribution of $\boldsymbol{j}'$ is considered to be perpendicular to the apse, and cylindrically symmetric. This is illustrated in the left hand panel of figure 6.8 for a range of scattering angles. The distribution of $\boldsymbol{j}'$ is different at different scattering angles, and

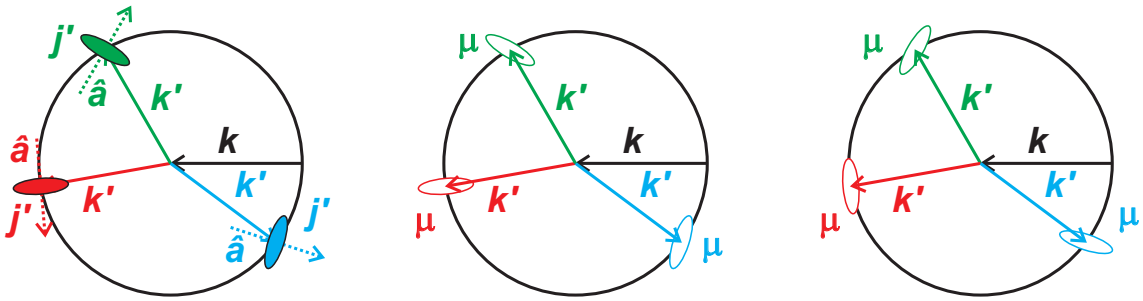


Figure 6.8: The direction of $\hat{\boldsymbol{a}}$ (dashed arrow) and the resultant distribution of $\boldsymbol{j}'$ for a range of scattering angles (left hand panel), and the corresponding distribution of the transition dipole moment, $\boldsymbol{\mu}$, for Q branch excitation (middle panel) and P/R branch excitation (right hand panel).

consequently at different points on the Newton sphere. As discussed in the introduction, for linearly polarised light the probability that a photon is absorbed is proportional to $\cos^2\theta_{\varepsilon\mu}$, where $\boldsymbol{\varepsilon}$ is the electric vector of the light and $\boldsymbol{\mu}$ is the transition dipole moment. For a P or R branch transition, $\boldsymbol{\mu}$ is perpendicular to $\boldsymbol{j}'$ and for a Q branch they are parallel, in the high j limit. The middle and right hand panels of figure 6.8 show the resultant distributions of $\boldsymbol{\mu}$ at different scattering angles for Q branch and P/R branch excitation respectively. Therefore, the probability that a photon is absorbed will be different at different points on the Newton sphere, leading to a variation in intensity throughout the

image. The transition probability is proportional to [19, 20, 23]:

$$A(x, y, j^\star, j', \chi_p) \propto \sum_{m_{j^\star}} |\langle \psi^\star(j^\star, m_{j^\star}) | \boldsymbol{\mu} \cdot \boldsymbol{\varepsilon} | \psi'_a(j', m^a_{j'}) \rangle|^2 \tag{6.11}$$

where $\psi^\star(j^\star, m_{j^\star})$ is the wavefunction following excitation from the $^2\Pi$ to the $^2\Sigma$ state, and $\psi'_a(j', m^a_{j'})$ is the wavefunction after the scattering event. It should be noted that $m_{j^\star}$ is the projection along $\boldsymbol{\varepsilon}$, and $m^a_{j'}$ the projection along $\hat{\boldsymbol{a}}$. It is therefore necessary to rotate $\psi'_a(j', m^{j'}_a)$ through the angle $\theta_{a\varepsilon}$ to transform the wavefunction from the apse frame to the laser frame, where $\theta_{a\varepsilon}$ is the angle between $\hat{\boldsymbol{a}}$ and $\boldsymbol{\varepsilon}$. Therefore [19]:

$$\psi'_a(j', m^a_{j'}) = \sum_{m_{j'}} d^{j'}_{m_{j'} m^a_{j'}}(\theta_{a\varepsilon}) \psi'(j', m_{j'}) \tag{6.12}$$

where $d^{j'}_{m_{j'} m^a_{j'}}(\theta_{a\varepsilon})$ is a reduced Wigner rotation matrix [102]. Substituting this expression for the wavefunction into equation (6.11) yields [19]:

$$A(x, y, j^\star, j', \chi_p) \propto \sum_{m_{j^\star} m_{j'}} |d^{j'}_{m_{j'} m^a_{j'}}(\theta_{a\varepsilon}) \langle \psi^\star(j^\star, m_{j^\star}) | \boldsymbol{\mu} \cdot \boldsymbol{\varepsilon} | \psi'(j', m_{j'}) \rangle|^2 \tag{6.13}$$

The (m dependent) detection probability for absorption of linearly polarised light is given by [260]:

$$|\langle \psi^\star(j^\star, m_{j^\star}) | \boldsymbol{\mu} \cdot \boldsymbol{\varepsilon} | \psi'(j', m_{j'}) \rangle|^2 = S_{jj^\star} \begin{pmatrix} j^\star & 1 & j' \\ m_{j^\star} & 0 & -m_{j'} \end{pmatrix}^2 \delta_{m_{j'} m_{j^\star}} \tag{6.14}$$

where $(\cdots)$ is a 3-j symbol [102], and $S_{jj^\star}$ is the Hönl London factor for the transition [156, 228]. It follows that the intensity for the transition is given by [19, 23, 241, 242]:

$$A(x, y, j^\star, j', \chi_p) \propto S_{jj^\star} \sum_{m_{j'}} \left| d^{j'}_{m_{j'} m^a_{j'}}(\theta_{a\varepsilon}) \begin{pmatrix} j^\star & 1 & j' \\ m_{j^\star} & 0 & -m_{j'} \end{pmatrix} \right|^2 \tag{6.15}$$

As the final relative velocity is known at each point on the Newton sphere, it is possible

to calculate the kinematic apse vector at each point. Therefore, the above expression can be used to calculate the intensity of the image at every point. It should be noted that as $A(x, y, j^\star, j', \chi_p)$ has been assumed to only depend on the laser polarisation and to be independent of the other experimental parameters incorporated into the instrument function (in particular the spread of velocities in the NO(X) and secondary molecular beams), the calculations were performed using a single (fixed) relative velocity.

Figure 6.9 shows the intensity calculated from equation (6.15) for Q branch excitation (left hand panel) and R branch excitation (right hand panel) for NO(X)-Kr for j'=8.5 f. Within each panel the left hand image corresponds to the polarisation vector being vertical

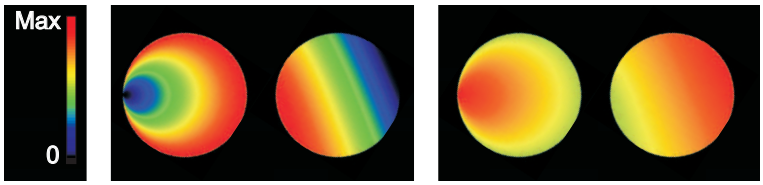


Figure 6.9: The variation in intensity due to collision induced alignment effects calculated using the apse model assuming Q branch (left panel) and R branch (right panel) detection for j'=8.5 f for NO(X)-Kr. Within each panel, the left image shows I_V, and the right hand panel I_H. The scale corresponds to the intensity of the images. The direction of $\boldsymbol{v}_{\mathbf{rel}}$ is horizontal from right to left.

(I_V) to the plane containing the molecular beams, and the right hand panel to horizontal polarisation (I_H) *i.e.* in the plane of the molecular beams. It should be noted that the scales of the I_H and I_V images are the same for both branches, and is shown to the left of the figure. Therefore the difference in the relative intensities of the two images reflects the different sensitivities of the R and Q branch to alignment. It follows that if the NO(X) is forward scattered it is more likely to be detected if horizontally polarised light is used on a Q branch transition, and vertically polarised light on an R branch transition. The converse is true for the backward scattered products.

As for the NO(X)-Ar collision induced alignment images the normalised difference images will be presented, it is also instructive to consider these from the model presented above. The alignment calculated using equation (6.15) is shown in figure 6.10, again for j'=8.5 f. Within each panel the first image corresponds to I_V, the middle to I_H, and the

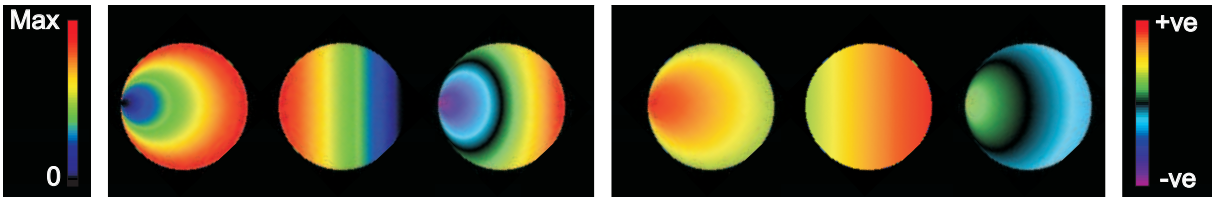


Figure 6.10: The variation in intensity due to collision induced alignment effects calculated using the apse model assuming Q branch (left panel) and R branch (right panel) detection for j'=8.5 f for NO(X)-Ar. Within each panel, the left image shows I_V, the middle I_H and the right hand panel the normalised intensity, $\frac{I_V - I_H}{I_V + I_H}$. The left hand scale corresponds to the I_H and I_V images, and the right hand scale that of the normalised difference images. The direction of $\boldsymbol{v}_{\mathbf{rel}}$ is horizontal from right to left.

right hand panel to the normalised difference $\frac{I_V - I_H}{I_V + I_H}$. As in the previous figure, the scales of the I_H and I_V images are the same for both branches (shown on the left hand side), as is the normalised difference scale (shown on the right hand side). The opposite signs of the difference images for the two branches is due to $\boldsymbol{\mu}$ being parallel to $\boldsymbol{j}$ for a Q branch transition (in the high j limit) and $\boldsymbol{\mu}$ being perpendicular to $\boldsymbol{j}$ for an R (or P) branch transition.

The most striking difference between the collision induced alignment correction for NO(X)-Ar and NO(X)-Kr is that the image corresponding to I_H is symmetric about v_{rel} in the case of NO(X)-Ar, but not for NO(X)-Kr. For NO(X)-Ar, the symmetry is observed because of the experimental geometry employed (*i.e.* the fact the two molecular beams cross at 90°), and because the two beams have very similar velocities. This results in $\boldsymbol{v}_{\mathrm{rel}}$ being at approximately 43° to the direction of the NO(X) beam. The electric vector of the laser, $\boldsymbol{\varepsilon}$ is at 45° to the NO(X) beam, with the result that, to a good approximation, $\boldsymbol{v}_{\mathrm{rel}} \parallel \boldsymbol{\varepsilon}$. As the scattering process is azimuthally symmetric about $\boldsymbol{v}_{\mathrm{rel}}$, it is consequently azimuthally symmetric about $\boldsymbol{\varepsilon}$, and I_H is therefore symmetric. This is shown schematically in figure 6.11. The left hand panel shows the Newton triangle for the collision and the direction of the laser. The middle panel shows the $\boldsymbol{j}'$ distribution for two different scattering angles, when the scattering is considered to be restricted to the plane containing the molecular beams. The distribution of $\boldsymbol{j}'$ lies in a disc perpendicular to the page in the direction shown in the figure. The two red arrows correspond to the

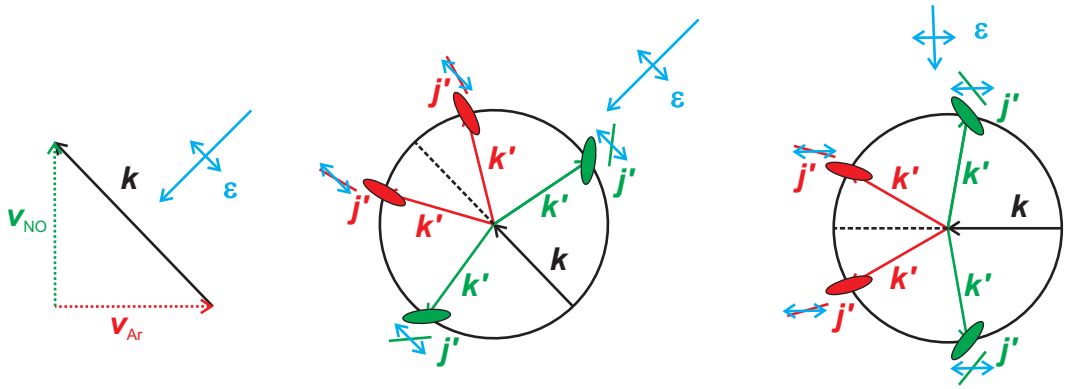


Figure 6.11: The left hand panels show the Newton triangle for the scattering of NO(X) with argon. The middle panels show the resultant $\boldsymbol{j}'$ distribution, and the angle between this and the polarisation of the laser $\boldsymbol{\varepsilon}$. The right hand panel show the same image, but rotated so that $\boldsymbol{v}_{\mathbf{rel}}$ is horizontal, for comparison with the images presented in this chapter.

same scattering angle, as do the two green arrows. As can be seen, the angle between the $\boldsymbol{j}'$ distribution and $\boldsymbol{\varepsilon}$ is the same for the same scattering angle, irrespective of whether the product is scattered to the fast side of the ion image or the slow side. The right hand panel in the figure is the same as the middle panel, but rotated so that $\boldsymbol{v}_{\mathrm{rel}}$ ($\equiv \boldsymbol{k}$) is horizontal, as is considered throughout the rest of the chapter.

Figure 6.12 presents the same three figures as figure 6.11, but for NO(X)-Kr. Due to the more significant difference in velocities between the two molecular beams, $\boldsymbol{v}_{\mathrm{rel}}$ is at an angle of approximately 33° to the direction of the NO(X) beam, meaning it can no longer be approximated to be parallel to $\boldsymbol{\varepsilon}$. The scattering process is therefore no longer cylindrically symmetric about $\boldsymbol{\varepsilon}$, with the result that the angle between $\boldsymbol{j}'$ and $\boldsymbol{\varepsilon}$

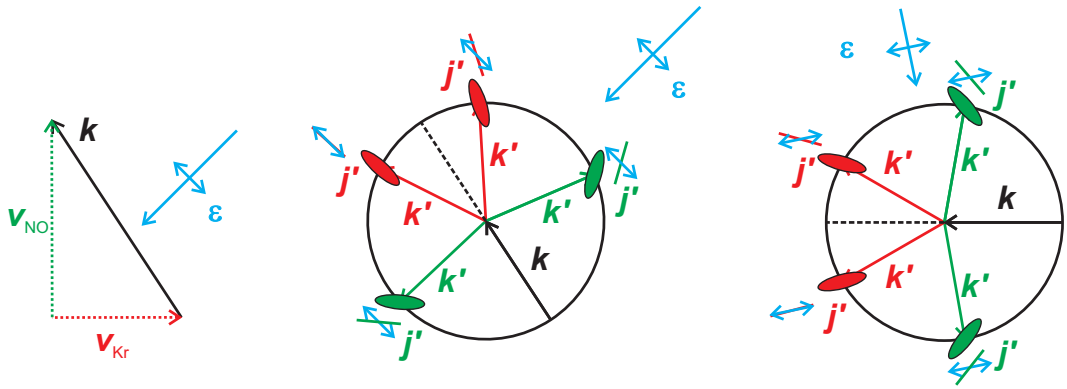


Figure 6.12: As for figure 6.11, but for NO(X)-Kr instead of NO(X)-Ar.

is different for radicals which are scattered through the same scattering angle when they are scattered to the fast side and slow side of the image. The resulting image is therefore no longer symmetric. The I_V images are symmetric in both cases as $\boldsymbol{\varepsilon}$ is perpendicular to $\boldsymbol{v}_{\mathrm{rel}}$ for both NO(X)-Ar and NO(X)-Kr.

It should be noted that the discussion presented in this section has assumed that the scattering of NO(X) with rare gases is an isotropic process (*i.e.* there is a uniform DCS), and that the probability of the radicals being detected only depends on the laser polarisation, and is otherwise independent of scattering angle. As shown in section 6.3, this is not the case, with the probability of detection depending on both the instrument function and DCS. Although the influences of these cancel to a good approximation when considering the normalised difference images (see equation (6.9)), if the DCS, or the instrument function, is small then the NO(X) is unlikely to be detected and there will be little intensity in that region of the image. Consequently, the collision induced alignment information would be lost. Therefore, the instrument functions and DCS do influence the appearance of the experimental collision induced alignment images that will be considered for NO(X)-Ar.

6.5 Data analysis: Differential cross-sections

As discussed previously, the intensity of the ion image at a position (x, y) is given by (as given by equation (6.7)) [1, 15, 22, 23]:

$$F(x, y, j^\star, j', j, \chi_p) = B(x, y, j, j')P(\theta_{kk'})A(x, y, j^\star, j', \chi_p) \tag{6.16}$$

where [22, 23]:

$$P(\theta_{kk'}) = \frac{1}{2}\sum_k [k]a^{(k)}(k, k')P_k(\cos\theta_{kk'}) \tag{6.17}$$

where $[k] = 2k + 1$ and the expansion coefficients, $a^{(k)}(k, k')$, are the associated Legendre moments of the DCS. Considering a given j to j' transition excited on a given branch, and a fixed laser polarisation, the experimental image can be written as a sum of basis

functions, $F_k(x,y)$ as [22, 23]:

$$F_{\exp}(x,y) = \frac{1}{2}\sum_k [k]a^{(k)}(k,k')F_k(x,y) \tag{6.18}$$

where $F_k(x,y) = B(x,y)A(x,y)P_k(\cos\theta_{kk'})$ *i.e.* the product of the instrument function and collision induced alignment correction considered previously, weighted by the k^{th} Legendre polynomial to account for the angular distribution of scattered products.

Instead of fitting the ion images in two dimensions the fit can be performed in Fourier space, where the image can be fit using one dimensional Fourier moments. To do this, both the experimental ion image and corresponding basis sets were converted into polar co-ordinates, $F(r,\phi_r)$, and written as a sum of their Fourier moments [77, 261, 262]:

$$F(r,\phi_r) = f_0(r) + 2\left(\sum_{-m}^{0} f_m(r)\sin(m\phi_r) + \sum_{0}^{m} f_m(r)\cos(m\phi_r)\right) \tag{6.19}$$

where the Fourier moments are given by [22, 23]:

$$\begin{aligned} f_m(r) &= (2-\delta_{0m})\int_0^{2\pi} F(r,\phi_r)\cos(m\phi_r)r\mathrm{d}\phi_r \qquad m \geq 0 \\ f_{-m}(r) &= 2\int_0^{2\pi} F(r,\phi_r)\sin(m\phi_r)r\mathrm{d}\phi_r \qquad m < 0 \end{aligned} \tag{6.20}$$

The Fourier moments describe the angular anisotropy of the image as a function of r. For example, the $f_{+1}(r)$ and $f_{+2}(r)$ moments describe the orientation and alignment of the image parallel to $\boldsymbol{v}_{\text{rel}}$, whereas $f_{-1}(r)$ and $f_{-2}(r)$ describe the orientation and alignment perpendicular to $\boldsymbol{v}_{\text{rel}}$.

These Fourier moments are then fit using a genetic algortihm to minimise the value of χ^2, which is evaluated according to [22, 23]:

$$\chi^2 = \frac{1}{2m_{\max}+1}\sum_{-m_{\max}}^{+m_{\max}}\int \frac{\left(f_m^{\exp}(r) - \frac{1}{2}\sum[k]a^{(k)}(k,k')f_m^k(r)\right)^2}{f_{m=0}^{\exp}(r)}\mathrm{d}r \tag{6.21}$$

where $f_m^{\exp}(r)$ are the m^{th} Fourier moments of the experimental image, $f_m^k(r)$ the m^{th}

Fourier moments of the basis image, and $a^{(k)}(k,k')$ the expansion coefficients of the DCS. It is the value of the moments that are allowed to vary and are optimised in the fitting procedure. Using the values of $a^{(k)}(k,k')$ output from the fit, it is then possible to write the DCS from the experimental image using equation (6.17) [22, 23].

6.6 Differential cross-sections: NO(X)-Kr

6.6.1 Calculation details

The quantum mechanical (QM) calculation results presented in this section were performed using the HIBRIDON suite of codes [176], using the NO(X)-Kr potential energy surface (PES) of Alexander and co-workers [170] presented in section 2.3.1. The Log-Derivative propagation [178] was performed from 4.5 a_0 to 15 a_0 and Airy propagation [179, 180] to 60 a_0. To converge the cross-sections, it was necessary to include partial waves up to J=300, and a rotational basis set of NO(X) up to and including j=20.5. The calculations were run at a collision energy of 520 cm^{-1}, which corresponds to that obtained from the experimental data in section 6.2.1.

6.6.2 Results

The full set of ion images obtained for the spin-orbit conserving and Λ-doublet conserving collisions of NO(X) with krypton are presented in figure 6.13. The images for these f-f transitions were recorded using either R_{21} branch excitation, or for the higher rotational states ($j' \geq$14.5) where the signal levels were lower, the overlapping Q_{11}+P_{21} branches. Although all the transitions were recorded using both horizontally and vertically polarised light, only the images obtained using horizontally polarised light are presented here. In all the images, the relative velocity is horizontal from right to left.

As can be seen, as j' increases the radius of the resulting Newton sphere decreases. The size of the image is proportional to the final centre of mass velocity of the NO(X).

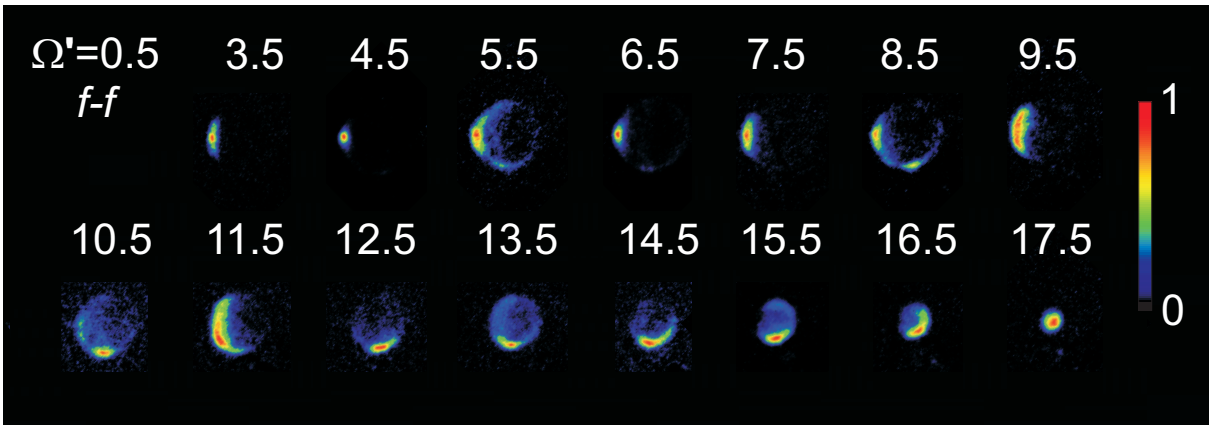


Figure 6.13: State to state resolved ion images for collisions of NO(X, Ω=0.5, j=0.5 f) with krypton. All transitions preserve the initial spin-orbit level and the initial Λ-doublet level. The relative velocity is horizontal from right to left.

This is given by:

$$|\boldsymbol{v}'_{\mathrm{NO}}| = \frac{m_{\mathrm{Kr}}}{m_{\mathrm{Kr}} + m_{\mathrm{NO}}} \sqrt{\frac{2(E_{\mathrm{coll}} - \Delta E_{\mathrm{rot}})}{\mu}} \tag{6.22}$$

where E_{coll} is the initial collision energy and ΔE_{rot} is the change in rotational energy brought about by the collision, m_{X} is the mass of X and μ is the reduced mass of the NO(X)-Kr system. It follows that as j' increases, ΔE_{rot} increases and consequently $|\boldsymbol{v}'_{\mathrm{NO}}|$ decreases, leading to a decrease in the radius of the ion image.

It is also apparent that at low j' the NO(X) is predominantly forward scattered, whereas as j' increases the radical becomes increasingly sideways and the backwards scattered. At low j', ΔE_{rot} is relatively small, and so the transition can be brought about by a more glancing blow collision, leading to forward scattering. As j' increases (and consequently ΔE_{rot}), a more 'head-on' collision is necessary to bring about the change in rotational energy required for the transition. These collisions tend to sample the more repulsive core of the PES, and therefore lead to sideways and backward scattered products.

The lowest level it was possible to record was j'=3.5. This is because the NO(X) in the molecular beam is not exclusively in the Ω=0.5, j=0.5 state, and a small amount is in other, low rotational levels. Although the effect of this is accounted for through the background subtraction, where the unscattered background NO(X) is subtracted from the scattered signal on alternate laser shots, in the forward scattered region of the image the unscattered

signal is more intense than the scattered signal, resulting in a lack of intensity in that part of the image. As can be seen from the trends discussed above, for the lowest j' the DCS is strongly forward scattered. Therefore, the NO(X) that is scattered through collisions with krypton is scattered into the same region as the unscattered NO(X), meaning it is not possible to record images for the very lowest j' states. However, it was possible to record all higher j' states, up to the maximum that is energetically accessible, j'=17.5.

The total parity of the NO(X) wavefunction is given by $(-1)^{j'-\epsilon/2}$, where ϵ=−1 for the f Λ-doublet level, and ϵ=+1 for the e Λ-doublet level. Therefore, considering just the f-f transitions shown above, transitions where Δj ($\Delta j = j' - j$) is even conserve the parity of the wavefunction, and for transitions where Δj is odd the parity changes. In collisions of NO(X) with argon, oscillations were observed in the DCSs which conserved the overall parity of the wavefunction, but not in those where the parity changes [21–23, 73]. Although a full analysis of the images has yet to be performed, the same trend is observable in the ion images presented here for NO(X) with krypton, where even Δj transitions have multiple peaks in the images (most noticeable for j'=8.5 and j'=10.5), whereas those for odd Δj (for example j'=9.5 and j'=11.5) have only a single peak.

Another parity effect observed in both the NO(X)-He [19, 20] and NO(X)-Ar [21–23, 73] DCSs were the presence of 'parity pairs'. It was shown that the structure of the DCSs

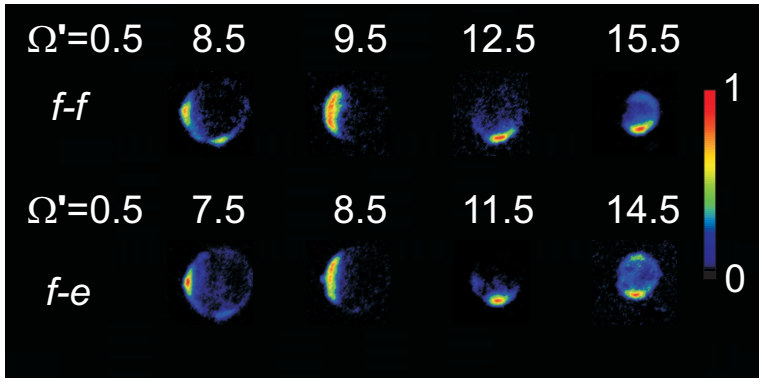


Figure 6.14: Spin-orbit conserving state to state resolved ion images for collisions of NO(X, $\Omega = 0.5$, j=0.5 f) with krypton. The top row corresponds to transitions which preserve the initially populated Λ-doublet level, and the bottom row to those that change the initial Λ-doublet level. The relative velocity is horizontal from right to left.

for the transitions corresponding to $j' = n + 0.5, f$ and $j' = n - 0.5, e$ were very similar. These final states have the same parity. A selection of the ion images corresponding to Λ-doublet conserving transitions are reproduced in the top row of figure 6.14, and the ion image for the corresponding 'parity pair' from the Λ-doublet changing (f-e transition) is shown beneath them. The f-e transitions were recorded using Q_{21}+R_{11} excitation, and again only the images recorded using horizontally polarised light are presented. As can be clearly seen, the ion images for the 'parity pairs' also have similar structures for the inelastic scattering of NO(X) with krypton. The reasons that these 'parity pairs' are observed has been discussed in detail previously [23, 73, 166, 263, 264], and can be attributed to the different potential matrix elements ($\langle V_{l0} \rangle$) that couple different Δj transitions. In the limit where the Hund's case (a) coupling scheme applies, $\langle V_{l0} \rangle$ for spin-orbit conserving transitions are given by [150, 166, 263]:

$$\langle V_{l0} \rangle \propto \frac{1}{2} \left[1 + \epsilon\epsilon'(-1)^{\Delta j + l} \right] \begin{pmatrix} j' & l & j \\ -\Omega & 0 & \Omega \end{pmatrix} \begin{pmatrix} \ell' & l & \ell \\ 0 & 0 & 0 \end{pmatrix} \begin{Bmatrix} j & \ell & J \\ \ell' & j' & l \end{Bmatrix} \tag{6.23}$$

where ℓ is the orbital angular momentum quantum number, and $(\cdots)$ and $\{\cdots\}$ are a 3-j and 6-j symbol respectively [102]. When the initial state is j=0.5 f, as considered here, the transitions to the final states $j' = n + 0.5, f$ and $j' = n - 0.5, e$ for small values of Δj are coupled by the same, single, potential matrix element, $\langle V_{n0} \rangle$ [195, 263]. This directly gives rise to the similar structures of the DCSs for the two states that make up the 'parity pair'. For larger Δj transitions, scattering has to be considered to proceed *via* (one or more) virtual states [263]. In this case, parity conserving transitions are governed by potential matrix elements where l is either always odd or always even, whereas the potential matrix elements that govern parity changing transitions take a combination of both odd and even values of l [263]. Again, the set of potential matrix elements that couple larger Δj transitions will be the same for transitions which make up a 'parity pair', and therefore the DCSs have a similar structure.

As the first three images for the f-f transitions shown in figure 6.14 were recorded

using R_{21} excitation, and the f-e transitions were recorded using Q_{21}+R_{11} excitation, the collision induced alignment correction will be different for the two sets of images, and will contribute to the variations in intensity observed in the two images. This is particularly apparent in the top right region, where there tends to be more intensity in the f-e images which were recorded using Q branch excitation compared to the f-f images which were recorded with R branch excitation. Looking back at the collision induced alignment corrections in figure 6.9, this is as expected. Both the j'=15.5 f and j'=14.5 e transitions were recorded using Q branch transitions, and therefore the collision induced alignment correction would be the same for both images.

Although a full analysis of all the ion images has yet to be performed, some of the data have been analysed using the method outlined in section 6.5. The results of this are shown in figure 6.15. The left hand panels show the data for transitions which conserve the initial Λ-doublet level, and the right those that change the initial Λ-doublet level, for a range of j'. Within each panel, the left hand ion image is that obtained experimentally using horizontally polarised light, and the right hand image the fit to the data. As can be seen, all the features that are observed in the experimentally recorded ion images are reproduced in the fitted images. The plots on the right show the experimentally determined DCS, where the red and green lines correspond to the parity conserving and parity changing DCSs respectively. The structures of the DCSs display all the features that were discussed above.

The black lines in the figure show the DCSs obtained from the QM calculations. Considering the preliminary nature of the experimentally determined DCSs, the agreement between the experimental and theoretical DCSs is reasonable. There is evidence that the experimental DCSs show more backward scattering than their QM counterparts in the case of parity conserving collisions (red lines). This could be an artifact due to the basis sets used to fit the data, although the parity changing transitions fit using the same parameters in the basis sets do not show the same systematic feature. Therefore this could highlight an inaccuracy in the PES used for the calculations. As discussed above,

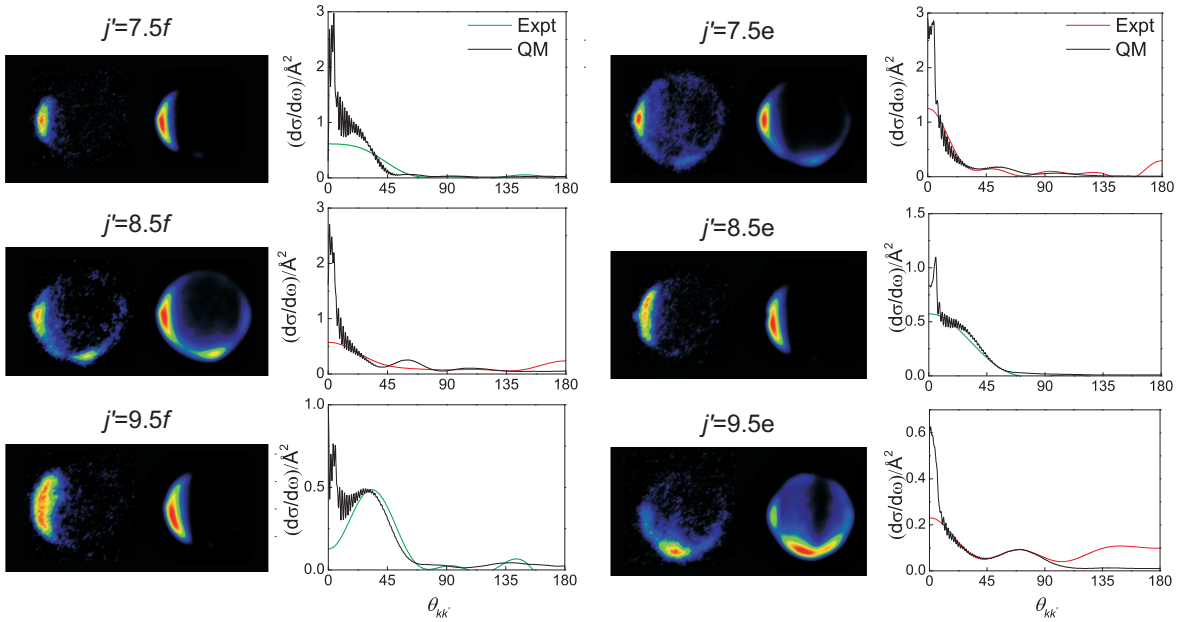


Figure 6.15: Fits of the spin-orbit conserving NO(X)-Kr DCS data for a range of j', for Λ-doublet conserving (left column) and changing (right hand column) transitions. Within each panel, the left hand ion image shows the experimentally recorded data, and the right hand the fit to the data. The corresponding DCSs are shown in the plots on the right, where the red and green lines show the parity conserving and parity changing DCSs, and the black lines the DCS obtained from QM calculations. The intensity scale on the ion images is the same as that in figure 6.14.

parity conserving transitions are governed either by solely even or odd potential matrix elements, and parity changing by a mixture of both odd and even potential matrix elements. In previous studies for NO(X)-Ar [21, 23, 73], it has been shown that parity changing transitions are strongly influenced by $\langle V_{10} \rangle$ and $\langle V_{30} \rangle$, whereas the even potential matrix elements influence parity conserving transitions more, to the point where in the limit of a homonuclear diatomic, only the terms where l is even contribute to the expansion given in equation (2.28), and only parity conserving transitions are observed. As the NO(X)-Kr V_{sum} PES is more homonuclear (*i.e.* more symmetric) in character than that for NO(X)-Ar, as shown in chapter 2, and as the discrepancy between the QM and experimental DCSs is observed only in the case of parity conserving transitions, this would suggest if there is an inaccuracy in the NO(X)-Kr PES used, it is likely to be with the even expansion coefficients. However the source of the disagreement requires further investigation before any conclusions can be reached.

6.7 Collision induced alignment: NO(X)-Ar

6.7.1 Spin-orbit conserving transitions

The collision induced alignment results for spin-orbit conserving transitions are presented in figure 6.16. The experimental results are shown in the top row of the figure. For these images, black shows that I_V=I_H, areas of red/green corresponds to positive intensity and shows $I_V > I_H$, and areas of negative intensity corresponding $I_V < I_H$ are blue/purple. The f-f transitions were recorded using R_{21} branch excitation, and the f-e transition using the Q_{21}+R_{11} branch.

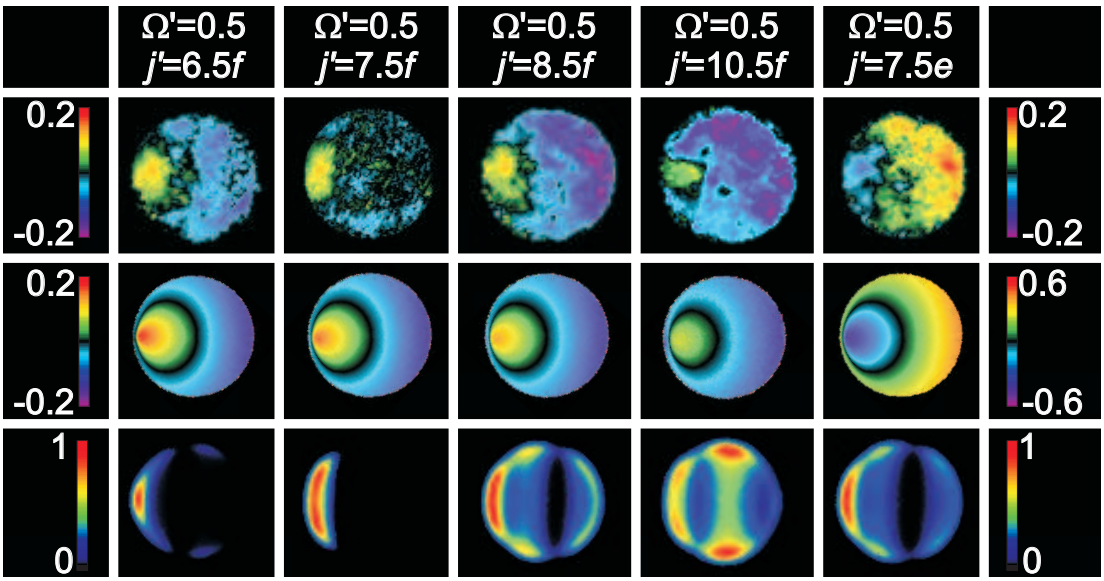


Figure 6.16: Spin-orbit conserving collision induced alignment difference images recorded experimentally (top row) and those simulated using the apse model (middle row), and simulated DCSs (bottom row). The scales in the left hand column correspond to the scales of the images in the four left hand columns, showing transitions recorded experimentally with the R_{21} branch, and the scales in the right hand column shows the scale of the images in the final column, where the experimental image was recorded using Q_{21}+R_{11} excitation. The direction of $\boldsymbol{v}_{\mathbf{rel}}$ is horizontal from right to left.

In the case of R branch excitation for a $\Sigma \leftarrow \Pi$ transition, the transition dipole moment, $\boldsymbol{\mu}$ is perpendicular to both $\boldsymbol{j}$ and the bond axis (in the high j limit). As the probability that a photon is absorbed is maximum when the electric vector of the light, $\boldsymbol{\varepsilon}$ is parallel to $\boldsymbol{\mu}$ and minimum when they are perpendicular, it follows that I_V will be greatest if $\boldsymbol{j}'$ lies

in the scattering plane, corresponding to 'propeller' or 'cartwheel' like rotation, and I_H will be greatest if $\boldsymbol{j}'$ is perpendicular to the scattering plane, corresponding to 'frisbee' like rotation. In all the images recorded with R branch excitation, the forward scattered region has a positive intensity, corresponding to $I_V > I_H$ and therefore the NO(X) is rotating like a propeller. As the scattering angle increases, the intensity becomes less positive, and in the sideways and backward scattered regions, the intensity is negative corresponding to the NO(X) bond axis rotating in the scattering plane, like a 'frisbee'. This is the same trend as has been observed in the previous studies by Chandler and co-workers [15, 16].

The final image in the column was recorded using a mixed Q and R branch transition. The intensity of the Q branch is approximately twice as sensitive to the alignment as the R branch, and therefore the contribution from the Q branch will dominate. In this case, $\boldsymbol{\mu}$ is parallel to $\boldsymbol{j}$ and perpendicular to the bond axis in the high j limit, and therefore when $I_V > I_H$ $\boldsymbol{j}'$ lies out of the scattering plane and the NO(X) rotates like a frisbee, and when $I_H > I_V$ $\boldsymbol{j}'$ lies in the scattering plane, and the rotation of the radical resembles a propeller. Therefore, the negative intensity in the forward scattered direction of this image shows the NO(X) is again rotating like a propeller, and the positive intensity as the scattering angle increases that the radical is rotating like a frisbee.

To rationalise the observed direction of $\boldsymbol{j}'$ following the collision in the forward and backward scattered directions, it is necessary to consider the azimuthal dependence of the scattering process, and where the kinematic apse lies in each case. This is shown

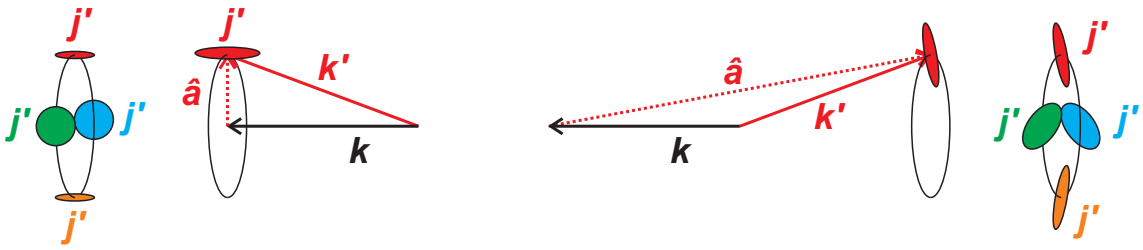


Figure 6.17: The azimuthal dependence of the distribution of $\boldsymbol{j}'$ in the forward scattered (left hand panels) and backward scattered (right hand panels) directions. The outer two panels show the $\boldsymbol{j}'$ distributions considering scattering through $\phi_{kk'} = 0°$, 90°, 180° and 270°, and the inner two the direction of the apse and $\boldsymbol{j}'$ distribution considered at $\phi_{kk'} = 90°$.

schematically for forward scattering in the left hand panels of figure 6.17, and for backward scattering in the right hand panels. For forward scattering, $\boldsymbol{a}$ can be considered to (approximately) lie perpendicular to $\boldsymbol{k}$. Therefore, to conserve the projection of $\boldsymbol{j}$ onto the kinematic apse, the resulting distribution of $\boldsymbol{j'}$ has a component parallel to $\boldsymbol{k}$ at all azimuthal angles (denoted $\phi_{kk'}$), as shown in the very left hand panel of the figure. It follows that when the azimuthal angle is averaged over, the $\boldsymbol{j'}$ distribution is most strongly polarised parallel to $\boldsymbol{k}$, which corresponds to the radical rotating like a propeller. In the backward scattered direction, the apse has a greater component parallel to $\boldsymbol{k}$, with the result that the $\boldsymbol{j'}$ distribution will be more strongly polarised perpendicular to $\boldsymbol{k}$. Therefore, when the $\boldsymbol{j'}$ distribution is averaged over $\phi_{kk'}$, $\boldsymbol{j'}$ is found to be perpendicular to $\boldsymbol{k}$, corresponding to the radical rotating like a frisbee.

As j' increases, the range of scattering angles over which the radical is rotating like a propeller out of the scattering plane decreases. To conserve energy, an increase in j' leads to a decrease in k', and as discussed in section 6.6.2, the radius of the Newton sphere decreases as the magnitude of $\boldsymbol{k'}$ decreases. It follows that for a given scattering angle, the direction of $\boldsymbol{a}$ is different for a low Δj and large Δj transition, resulting in a different distribution of $\boldsymbol{j'}$ at that scattering angle. As Δj increases, the component of $\boldsymbol{a}$ parallel to $\boldsymbol{k}$ increases, with the result that the distribution of $\boldsymbol{j'}$ becomes more perpendicular to $\boldsymbol{k}$ (due to the conservation of the projection of $\boldsymbol{j}$ onto the kinematic apse). This is shown schematically in figure 6.18, where the left hand panel corresponds to a small Δj transition, and the right hand panel a large Δj transition. As can be seen, this effect is the

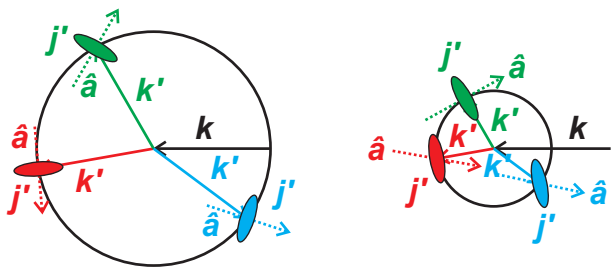


Figure 6.18: The direction of the kinematic apse (dashed arrow), and the resultant distribution of $\boldsymbol{j'}$ at a range of scattering angles for a low Δj transition (left) and a large Δj transition (right). The distributions of $\boldsymbol{j'}$ are cylindrically symmetric about the apse.

most pronounced in the forward scattered direction, where the collision induced alignment is seen to vary most rapidly experimentally. For an R branch transition, where $\boldsymbol{\mu} \perp \boldsymbol{j'}$, $\boldsymbol{\mu}$ will also be more strongly polarised parallel to $\boldsymbol{k}$ for a large Δj transition. As $\boldsymbol{\varepsilon}$ is parallel to $\boldsymbol{k}$ (to a good approximation), the probability of a photon being absorbed when the probe laser is horizontally polarised will be greater for a large Δj transition than a small Δj transition. Consequently, the value of $\frac{I_V - I_H}{I_V + I_H}$ will be more negative, as is observed in figure 6.16.

It should also be noted that as j' increases, $|\boldsymbol{j'}|$ will increase, and therefore to conserve the projection of $\boldsymbol{j}$ onto the apse, the distribution of $\boldsymbol{j'}$ will be more strongly polarised perpendicular to the apse. Consequently the distribution of $\boldsymbol{\mu}$ would be more strongly polarised, which would enhance the difference in intensity observed in the images recorded with each polarisation discussed.

The j'=7.5 e and j'=8.5 f images make up a so called 'parity pair'. As shown previously in NO(X)-He [19, 20] and NO(X)-Ar [21–23, 73], and as discussed above for NO(X)-Kr, the DCSs for the $j' = n + 0.5, f$ and $j' = n - 0.5, e$ states have very similar structures, as they have the same parity. This is also seen in the collision induced alignment results presented here for these two states. As can be seen, they qualitatively have the same structure, and the intensities are opposite as the j'=8.5 f image was recorded using the R_{21} branch, and the j'=7.5 e image with effectively a Q branch.

The second row in figure 6.16 presents the product rotational alignment calculated using the apse model described in section 6.4. There is good agreement between the experimental images and those simulated using the apse model. As discussed in section 2.3.1, spin-orbit conserving collisions are governed by the V_{sum} PES [166, 167], which has a well depth of approximately 110 cm^{-1} [168]. The collision energy is 530 cm^{-1}, and therefore the collisions will be impulsive in nature, and the assumption that the projection of $\boldsymbol{j}$ onto the kinematic apse is conserved is likely to be valid.

For the R branch transitions shown in the first four columns, there is also good quantitative agreement, with the simulated images and experimental images shown with the

same intensity scales. This good agreement suggests that the experimental laser powers were kept sufficiently low to not be saturating the transitions. However, the magnitude predicted using the simple apse model in the case of the j'=7.5 e state is larger than that observed experimentally. The calculations were performed assuming pure Q branch excitation. Experimentally, there is an unresolved R branch satellite line, which is sensitive to alignment in the opposite sense to the Q branch, and so will reduce the magnitude of alignment observed. If the wavelength for the two transitions were identical, it would be possible to take a weighted sum of the two contributions (where the weight would be the sensitivity of the two branches to alignment) to obtain the simulated image. However, the wavelengths for the transitions are shifted slightly relative to one another, and so the extent to which the two branches contribute to the signal is not known, meaning a simple analysis is not possible.

The calculated images assume an isotropic DCS, *i.e.* that scattering through any angle is equally likely. This is obviously not the case experimentally, and whilst taking the normalised difference between the two images removes any influence of the DCS and flux-density correction to a good approximation [22, 23], the intensity of the experimental images will be lower where the DCS is small. The final row in the image shows the simulated DCSs. As can be seen, for images where the DCS is large over all scattering angles, the experimental image has good intensity throughout. However, when the DCS falls to zero, there is little intensity in the experimental images. This is particularly apparent in the j'=7.5 f image, where the DCS is predominantly forward scattered, and consequently the highest intensity is observed experimentally in the forward scattered direction.

Another significant difference between the experimental and simulated images is the asymmetry present in the images recorded experimentally. The symmetry present in the simulated images has been discussed in section 6.4, and this will not be repeated here. The source of the asymmetry in the experimental images is yet to be determined, but the magnitude of the polarisation on the slow side of the image (the bottom half) tends to

be smaller than that on the fast side of the image (the top half). This is the opposite of what would be expected if it was due to flux-density effects, where the experimental images would be subject to larger errors and less signal on the fast side of the image. One possible explanation is that the magnetic dipole moment of the NO(X) interacts with the earths magnetic field causing the radical to precess. Radicals on the slow side of the image remain in the detection volume longer, and so can become disaligned before being detected. This disalignment would also occur in radicals with a faster LAB velocity, but they would fly out of the detection volume and so would not contribute to the signal. Another possible explanation is that the aligned NO(X) molecules on the slow side of the images could remain in the detection volume for sufficient time to undergo secondary collisions. These collisions would lead to depolarisation, and again reduce the extent to which the molecules are aligned on the slow side of the image.

6.7.2 Spin-orbit changing transitions

The collision induced alignment results for spin-orbit changing transitions are presented in figure 6.19. The experimental results are shown in the top row of the figure, the results from the apse model calculation in the middle row and the DCSs in the bottom row of the figure. The images were recorded using the mixed Q_{22}+R_{12} branch. As can be seen from the images, the trends in the alignment as a function of scattering angle are similar to those observed in the spin-orbit conserving case. There is also evidence of the same asymmetry. As these trends have been discussed in the previous section, the same arguments will not be repeated here.

A comparison of the images obtained experimentally in the top row and those calculated using the apse model shows that the agreement between the two is still reasonable. Again, the calculated images predict more alignment than is observed experimentally, but these were calculated as previously assuming pure Q branch excitation, and ignoring the effects of the satellite line. Spin-orbit changing transitions are governed by the V_{diff} PES [166, 167], which is significantly more anisotropic than the V_{sum} PES, with the potential

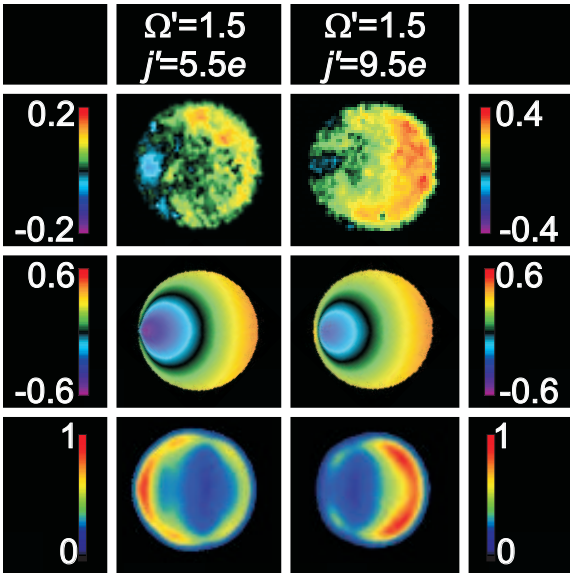


Figure 6.19: Spin-orbit changing collision induced alignment difference images recorded experimentally (top row) and those simulated using the apse model (middle row), and simulated DCSs (bottom row). The scales in the left and right hand column correspond to the images in the second and third column respectively. The experimental images were recorded using the Q_{22}+R_{12} branch. The direction of $\boldsymbol{v}_{\mathbf{rel}}$ is horizontal from right to left.

varying more rapidly as a function of the distance between the NO(X)-Ar, and the angle of approach. Regions of the V_{diff} potential are also highly attractive in nature, with the result that the collisions are expected to be less impulsive. Therefore the assumptions of the kinematic apse model are less applicable. Consequently the kinematic apse calculations agree less well with the experimental images compared to the spin-orbit conserving case. It should be noted that a full analysis of the images is currently being performed to obtain the $a_q^{(k)}$ moments (as discussed in sections 2.2.2 and 5.4), which can be compared with those obtained from full QM scattering calculations. The provisional fits show that the experimental and theoretical moments are in excellent agreement for both the spin-orbit conserving and spin-orbit changing transitions considered throughout this section [243].

6.8 Summary

In the first part of the chapter, the experimental methods employed to measure the scattering dynamics of fully Λ-doublet state resolved NO(X) with argon and krypton have been

described, with a particular emphasis on measuring the resulting differential cross-sections and the collision induced alignment. The kinematic apse model was also introduced to help to rationalise the NO(X)-Ar collision induced alignment results obtained experimentally.

The fully Λ-doublet state resolved differential cross-sections for collisions of NO(X) with krypton, are presented in section 6.6. A set of ion images for spin-orbit conserving and Λ-doublet conserving transitions (*i.e.* f-f transitions) up to and including j'=17.5, the highest rotational state energetically accessible have been shown. A selection of ion images were also presented for collisions which conserved the spin-orbit level, but resulted in a change of Λ-doublet level (*i.e.* f-e transitions). As has been seen previously for collisions of fully Λ-doublet state resolved NO(X) with helium and argon, the structure of the DCSs for the $j' = n + 0.5, f$ and $j' = n - 0.5, e$ states are very similar, due to the transitions having the same parity. Provisional fits of a selection of ion images have been presented, and the agreement between the experimental DCSs and those obtained from QM scattering calculations is reasonable.

In the final section of the chapter, collision induced alignment results for collisions of NO(X) with argon have been presented. Again these were measured with full Λ-doublet state resolution of the initial and final state of the NO(X), for a selection of spin-orbit conserving and spin-orbit changing transitions. The experimental results were then compared with the kinematic apse model. There is a propensity for the NO(X) to rotate out of the scattering plane in a 'propeller' like motion in the forward scattered direction, whilst the products at larger scattering angles rotate in the scattering plane like a 'frisbee'. The product rotational alignment has been shown to be well described by a simple model where the projection of $\boldsymbol{j}$ onto the kinematic apse is rigorously conserved. The agreement between the apse model and the experimental images is less good for spin-orbit changing transitions, which are governed by the more anisotropic V_{diff} PES. Despite this, the agreement between the two sets of data is still reasonable.

Chapter 7

Conclusions and future work

7.1 Conclusions

A joint experimental and theoretical study of the vector correlations that characterise the stereodynamics of atom-diatom collisions has been presented. The inelastic scattering of NO(X) with argon and krypton, and of NO(A) and OH(A) with krypton has been considered. It has been shown that for collisions of NO with the rare gases, the collisions are impulsive, both in the ground and excited electronic state of NO. In comparison, the collisions of OH(A) with krypton are strongly influenced by the attractive nature of the potential energy surface (PES), leading to the formation of complexes which can survive for many rotational periods.

Zeeman and hyperfine quantum beat spectroscopy was used to determine the collisional depolarisation cross-sections for collisions of NO(A) and OH(A) with krypton. For NO(A)-Kr, the total 'disorientation' and 'disalignment' cross-sections measured experimentally under thermal conditions decreased with increasing initial rotational quantum number, N, and were found to be in excellent agreement with those obtained from quasi-classical trajectory calculations. This agreement between the experimental and theoretical calculations was not seen in OH(A)-Kr, where the experimentally determined total depolarisation cross-sections were less dependent on N. The unusual trend in the total depolarisation cross-sections has been attributed to the importance of elastic depolarisation

in OH(A)-Kr, cross-sections for which have also been presented. As the collision energy is increased for OH(A)-Kr, it has been shown that the agreement between the experimental and theoretical depolarisation cross-sections is improved, although the agreement is not as good as in the case of NO(A)-Kr. Reasons for the disagreement between the results of the experimental and theoretical depolarisation cross-sections have been suggested. The most likely explanation is due to the importance of electronic quenching in OH(A)-Kr, which has also been studied experimentally here. The associated cross-sections are largest at low N, where the greatest disagreement is observed between the experimental and theoretical depolarisation cross-sections. The theoretical calculations performed in this study do not include the effects of electronic quenching, and assume adiabatic behaviour.

The contrasting mechanisms of depolarisation in NO(A)-Kr and OH(A)-Kr have also been considered. For NO(A)-Kr, the rotational energy transfer cross-sections (RET) are large, but depolarisation is inefficient compared to RET. Collisions of NO(A) with krypton are governed by an isotropic PES [171] that is only weakly attractive, and therefore impulsive encounters dominate. This results in the direction of the final rotational angular momentum, $\boldsymbol{j}'$, being similar to that of the initial rotational angular momentum $\boldsymbol{j}$. In contrast, the significantly more anisotropic and attractive OH(A)-Kr PES [172] effectively randomises the direction of $\boldsymbol{j}$ in every collision, with the result that depolarisation is efficient compared to RET. It has also been shown that there are orbiting trajectories where the krypton is trapped by the OH(A). These lead to efficient elastic depolarisation, and therefore the trends in the elastic depolarisation cross-sections can be attributed to the highly attractive nature and anisotropy of the PES.

Higher order vector correlations have been considered, with a particular emphasis on the $\boldsymbol{k}$-$\boldsymbol{j}$-$\boldsymbol{j}'$ correlation. Making use of the quasi-classical trajectory (QCT) calculations, these distributions were shown for NO(A)-Kr and OH(A)-Kr. The results again reflect the differences in the mechanisms of depolarisation discussed above. The $\boldsymbol{a}$-$\boldsymbol{j}$-$\boldsymbol{j}'$ correlation was also discussed, where $\boldsymbol{a}$ is the kinematic apse. For both NO(A)-Kr and OH(A)-Kr there was shown to be good conservation of the projection of $\boldsymbol{j}$ onto the kinematic apse

throughout the collision. This propensity rule is only strictly observed in the limit of a purely impulsive collision, and as shown, the collisions of OH(A)-Kr cannot be considered to be impulsive, with the attractive interactions leading to double lobes in the $\boldsymbol{a}$-$\boldsymbol{j}$-$\boldsymbol{j}'$ distributions under thermal conditions. These are also observed in the case of OH(A)-Ar [119], although the structure is lost as the collision energy is increased. Therefore it is perhaps surprising that the projection of $\boldsymbol{j}$ onto the kinematic apse is conserved in these systems.

It has also been shown that in collisions of NO(X) with argon, the projection of $\boldsymbol{j}$ onto the kinematic apse is conserved throughout the collision, as the kinematic apse model described in section 6.4 agrees well with the collision induced alignment results obtained experimentally. These measurements were performed with full Λ-doublet level resolution of both the initial and final state of the NO(X) for the first time, using hexapole focussing to select the Ω=0.5, j=0.5 f level. The results presented show that the forward scattered products rotate out of the horizontal plane defined by the molecular beams, like a propeller, whereas those that are backward scattered rotate in the scattering plane, like a frisbee. The agreement between the experimental results and apse model is excellent, showing that the collision induced alignment effects can be accounted for classically.

Differential cross-sections (DCSs) for the inelastic scattering of NO(X) with krypton have been presented. The results were again measured using hexapole focussing to obtain a single Λ-doublet level of the NO(X). It has been shown that those transitions where the parity is conserved have multiple peaks in the DCS, whereas those where the parity changes only have a single peak, as has been observed in NO(X)-Ar previously [21–23, 73]. There is also evidence of the same 'parity pairs' as have been observed in NO(X)-He [19, 20] and NO(X)-Ar [21–23, 73], corresponding to the DCSs for the $j' = n + 0.5, f$ and $j' = n - 0.5, e$ states having similar structures. Provisional fits to the ion images have also shown that there is reasonable agreement between the experimentally determined DCSs, and those from quantum mechanical calculations.

7.2 Future work

7.2.1 Atom-diatom scattering

Electronic quenching of OH(A) with krypton

Further characterisation of the electronic quenching of OH(A) to OH(X) by krypton could provide insight into the role that non-adiabatic effects play in this system. Therefore, it would be interesting to determine the rotational and vibrational populations produced in OH(X) through electronic quenching. This could be achieved with the addition of a third laser to the experimental set up described in chapter 3 for the OH(A)-Kr Zeeman quantum beat experiments. The first would be used to photolyse the precursor, and the second to excite the OH(X) to OH(A). The third would then be used to excite the quenched radicals to a vibrationally excited state of OH(A), from which the fluorescence intensity could be measured to determine the relative population of the rotational level.

A theoretical study could also be performed to model the electronic quenching of OH(A) with krypton. It would be possible to perform a crude analysis using the adiabatic PES and QCT calculations presented in chapter 2 by assuming that the trajectories that sample the global minimum of the PES in the HO-Kr geometry are quenched. A better method would be to employ the non-adiabatic potential energy surfaces introduced in figure 4.21 [238]. If QCT calculations were used, the probability that the radical will be quenched would be considered at each point in the trajectory, and the trajectory propagated accordingly. This would allow the radical to 'hop' between the potential energy surfaces that describe the interaction. It would also be possible to run non-adiabatic quantum mechanical calculations to characterise the electronic quenching [265].

The k-k' correlation: NO(X) with rare gases

As has been mentioned previously, oscillations have been observed in the DCSs for collisions of fully Λ-doublet resolved NO(X) with argon [21–23], but not for NO(X) with helium [19, 20]. This was attributed to the interference of trajectories that sampled the end of

the NO(X) radical and the side. Due to the light mass of helium, the total momentum for the system is small, and the associated de Broglie wavelength is longer than that for NO(X)-Ar (at a fixed collision energy), so the interference effects are not seen. Increasing the mass of the rare gas to krypton, as considered here in chapter 6, also decreases the de Broglie wavelength which would lead to oscillations in the DCS. Although a full analysis has yet to be performed, there is evidence of these in the parity conserving DCSs shown. It would also be possible to measure the DCSs for collisions of NO(X) with xenon, which would be expected to have the same effect.

An alternative method for increasing the associated momentum (and so decreasing the associated de Broglie wavelength) would be to increase the collision energy. This could be done, as previously [9, 65, 68, 69], by seeding the primary NO(X) beam in helium instead of argon. As discussed in section 6.2.1, the resultant beam velocity can be calculated using [253, 254]:

$$|\boldsymbol{v}| = \sqrt{\frac{2k_B}{m}\left(\frac{\gamma}{\gamma-1}\right)T} \tag{7.1}$$

where γ is the ratio of the heat capacities measured at fixed pressure and fixed volume C_p/C_v, m is the mass of the gas and T is the temperature at which the valve operates. Using a mix of 15 % NO(X) and 85 % helium would result in a primary beam velocity of approximately 1370 ms^{-1} (taking T=340 K, as discussed in section 6.2.1), and therefore the collision energy of the NO(X)-Ar collisions would be increased to 200 meV (approximately 1590 cm^{-1}). Although it would also be possible to seed the rare gas in the secondary beam with helium to increase the collision energy, the resulting ion image would contain two overlapping Newton spheres, one due to collisions of the rare gas with NO(X), and the other due to collisions of helium with NO(X). This would result in a loss of information in the forward scattered direction, where the two Newton spheres would overlap.

The $\boldsymbol{k}$-$\boldsymbol{k}'$-$\boldsymbol{j}'$ correlation: NO(X) with rare gases

The experiments described in chapter 6 for determining the $\boldsymbol{k}$-$\boldsymbol{k}'$-$\boldsymbol{j}'$ correlation for NO(X)-Ar could be extended to a wider range of collision partners. The collision induced alignment could be measured for NO(X) with krypton and xenon. As the rare gas becomes heavier, the interaction potential becomes more attractive and the apse model would be expected to be less applicable. Therefore, measuring the collision induced alignment for these systems and comparing the results to the apse model would provide a test of the model.

It would also be possible to measure the collision induced orientation for NO(X)-Ar (and the heavier rare gases suggested above). This would complement the results presented here in chapter 6 by showing the sense of rotation of the radical after the collision (*i.e.* whether it is rotating clockwise or anticlockwise), instead of the plane of rotation of the radical. Lorenz *et al.* [17] have measured this for NO(X)-Ar, but without full Λ-doublet resolution. The experiments suggested here would allow the effect that parity has on the collision induced orientation to be determined. These effects may be important, as preliminary work suggests that unlike the collision induced alignment results presented in this work, the collision induced orientation cannot be explained classically, and therefore quantum mechanical effects play a role.

For these experiments, it would be necessary to use circularly polarised light, which can be obtained by passing linearly polarised light through a quarter waveplate. A further complication arises from the need to direct the tunable dye laser up the time of flight tube towards the detector, which is necessary as the collision induced orientation is created perpendicular to the plane containing the molecular beams. The optics for achieving this are shown schematically in figure 7.1. The current path of the dye laser used in the measurements presented in chapter 6 is simply from left to right at the level of the first prism. Note that it will also be necessary to create a hole in the repeller plate to guide the laser through, and also create a beam block to prevent the laser from hitting the detector. This geometry has the added advantage that the position of the detection volume will be

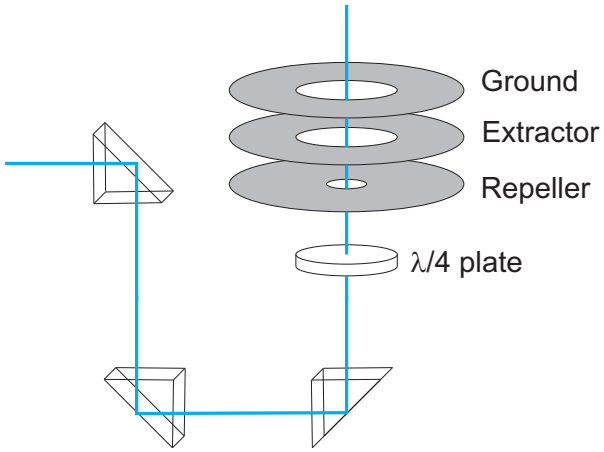


Figure 7.1: The optics arrangement required for guiding the laser up the time of flight tube as is necessary for the collision induced orientation measurements.

well-defined as being in the centre of the scattering chamber, making it easier to account for any flux-density effects that may need to be considered.

An alternative method that could be used to detect the orientation is to use a magnetic field to rotate the polarised distribution into the plane of the molecular beams so it could be detected without directing the laser towards the detector, as is used in the Zeeman quantum beat measurements described in chapter 3. However, the magnetic field would interfere with the ion optics required to velocity map the ions onto the detector.

The k-k'-r-j' correlation: NO(X) with rare gases

Measurement of the four vector $\boldsymbol{k}$-$\boldsymbol{k}'$-$\boldsymbol{r}$-$\boldsymbol{j}'$ correlation (or $\boldsymbol{k}$-$\boldsymbol{k}'$-$\boldsymbol{j}$-$\boldsymbol{j}'$ correlation) would allow the stereodynamics of an atom-diatom collision to be fully characterised. The control of the orientation of the bond axis, $\boldsymbol{r}$, (or initial rotational angular momentum $\boldsymbol{j}$) of the NO(X) before the collision could be achieved by using an applied electric (or magnetic) field. Previous studies have used a quadrupole to orient the bond axis of NO(X) to measure the steric asymmetry of collisions with helium and argon [20, 47, 97–100]. This could be added to the crossed molecular beam experiment described in chapter 6. These experiments would be challenging to perform because, as mentioned above, the addition of an electric (or magnetic) field would interfere with the electric field created by the ion optics which

allows velocity mapping of the ions to be achieved. However, if the fields required could be switched on a fast enough timescale [83], and the polarised lasers described previously for the detection of the direction of $\boldsymbol{j}'$ were used, the four vector correlation would be amenable to experimental measurement.

7.2.2 Diatom-diatom scattering

Replacing the atomic collision partner with a diatom adds an extra degree of complexity to the scattering process, as internal vibrational and rotational states of the collision partner can be populated by the collision. There is also another source of rotational angular momentum associated with the second diatom, meaning the four vector correlation considered above is no longer adequate to fully describe the collision dynamics. However, this allows new correlations between the rotational angular momenta associated with the two diatoms to be considered.

The j-j' correlation: OH(A)+H_2

The Zeeman quantum beat spectroscopy experiments described in chapter 3 could be used to determine the rotational energy transfer (RET), electronic quenching and depolarisation cross-sections for OH(A)-H_2, as have been presented for OH(A)-Kr in chapter 4. In OH(A)+H_2, both non-reactive quenching to produce OH(X), and reactive quenching to produce H+H_2O, would compete with the RET and collisional depolarisation processes of interest. As the quenching has been well characterised [265–270], it would be interesting to determine if this has a similar effect on the depolarisation cross-sections for OH(A)-H_2 as has been observed in OH(A)-Kr.

It would also be interesting to determine whether the depolarisation cross-sections for OH(A)-H_2 are most influenced by kinematic or dynamic effects. The potential energy surface for OH(A)-H_2 [271] is significantly more attractive and anisotropic than that for OH(A)-Kr, and therefore it might be anticipated that the collisions will be very depolarising leading to a randomisation of the direction of $\boldsymbol{j}$. However, the kinematics of H_2 as

a collision partner are very different to those for krypton. Due to the light mass of the hydrogen, it will only have a very small associated momentum, meaning it has less momentum to transfer. It will also be travelling at a much greater speed than the krypton, and so will have less time to sample the attractive parts of the potential. Therefore, it would be expected from the kinematics that the extent to which collisions cause depolarisation to be small.

Quasi-classical trajectory calculations

The theoretical calculations for diatom-diatom scattering would also provide a challenge, which including the extra degrees of freedom that an additional diatom introduces. This addition of an extra atom from the three atom scattering considered earlier makes quantum mechanical scattering calculations too computationally expensive to perform. However, it would be possible to develop a quasi-classical trajectory (QCT) code, which has been shown to provide an adequate description of the systems considered here.

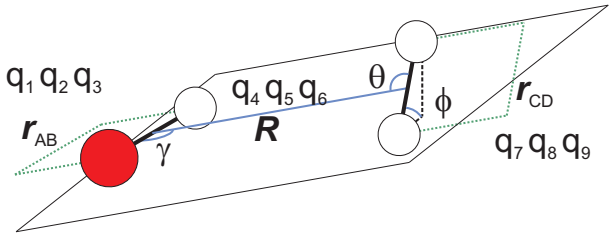


Figure 7.2: The reference frame that describes a diatom-diatom collision in the QCT calculations.

It is necessary to use six variables to fully describe the positions of all four atoms throughout the scattering process. These are shown in figure 7.2 and correspond to the bonds of the two diatoms ($\boldsymbol{r}_{\mathrm{AB}}$ and $\boldsymbol{r}_{\mathrm{CD}}$, where $\boldsymbol{r}_{\mathrm{AB}} \equiv \boldsymbol{r}$ in section 2.3.2), the vector that connects the centre of mass of AB to the centre of mass of CD ($\boldsymbol{R}$), the angle between $\boldsymbol{r}_{\mathrm{AB}}$ and $\boldsymbol{R}$ (γ), the angle between $\boldsymbol{r}_{\mathrm{CD}}$ and $\boldsymbol{R}$ (θ) and the azimuthal angle between $\boldsymbol{r}_{\mathrm{CD}}$ and the plane containing the vectors $\boldsymbol{r}_{\mathrm{AB}}$ and $\boldsymbol{R}$ (ϕ). Therefore, to include the fourth atom, it has been necessary to define an additional three co-ordinates $\boldsymbol{r}_{\mathrm{CD}}$, θ and ϕ.

Analogously to equation (2.32), the Hamiltonian for diatom-diatom scattering is given

by:

$$\mathcal{H} = \sum_{i=1}^{3} \frac{p_{qi}}{2\mu_{AB}} + \sum_{i=4}^{6} \frac{p_{qi}}{2\mu_{AB,CD}} + \sum_{i=7}^{9} \frac{p_{qi}}{2\mu_{CD}} + V(R, r_{\mathrm{AB}}, r_{\mathrm{CD}}, \gamma, \theta, \phi) \tag{7.2}$$

where q_i are the Jacobi co-ordinates that describe the position of atom B with respect to atom A (i=1,2,3), the centre of mass of CD with respect to the centre of mass of AB (i=4,5,6) and the position of atom D with respect to atom C (i=7,8,9), and p_{qi} are the associated momenta. It follows that the first and third terms describe the kinetic energy of the diatoms AB and CD respectively, and the second the kinetic energy associated with the relative motion of CD with respect to AB. The final term is the potential energy determined by the relative positions of the two diatoms and their bond lengths. The trajectories will again be propagated by solving Hamilton's equations of motion, given in section 2.3.2.

The first system that will be studied using the four atom scattering code will be OH(A)-H_2. These calculations will provide theoretical values of the RET and depolarisation cross-sections that can be compared with those obtained experimentally from the Zeeman quantum beat measurements. The calculations will also allow the role of the second diatom on the collision dynamics to be determined, something which would be difficult to measure experimentally. Not only would these allow the vector correlations and mechanism of depolarisation to be investigated, as considered here for NO(A)-Kr and OH(A)-Kr in chapters 4 and 5, but information could also be obtained about the correlations between the internal excitation of the two species. Additional vector correlations could also be considered, for example the $\boldsymbol{j}_{\mathrm{AB}}$-$\boldsymbol{j}_{\mathrm{CD}}$ correlation would show if the direction of the initial rotational angular momentum of both diatoms determines the outcome of the collision.

The $\boldsymbol{k}$-$\boldsymbol{k}'$ correlation: NO(X) with diatoms

It would be possible to replace the gas in the secondary beam of the crossed molecular beam apparatus described in chapter 6 with a diatomic collision partner, for example N_2, O_2 or HD. These diatoms have vibrational and rotational states that could be populated by the collision. In this case the final centre of mass velocity of the NO(X) would be given

by:

$$|\boldsymbol{v}'_{\mathrm{NO}}| = \frac{m_{\mathrm{AB}}}{m_{\mathrm{AB}} + m_{\mathrm{NO}}} \sqrt{\frac{2(E_{\mathrm{coll}} - \Delta E_{\mathrm{rot}} - \Delta E_{\mathrm{AB}})}{\mu_{\mathrm{NO,AB}}}} \tag{7.3}$$

where m_{X} is the mass of species X, E_{coll} the collision energy, ΔE_{rot} the change in rotational energy of the NO(X), ΔE_{AB} the change in internal energy of the diatom AB, and $\mu_{\mathrm{NO,AB}}$ the reduced mass of the system. It follows that if the states are sufficiently well separated in energy (*i.e.* ΔE_{AB} is large), it would be possible to resolve the states in the resulting ion image as they would give rise to different sized Newton spheres. Therefore, this structure would be most likely to be observed in the collisions of NO(X) with HD, where the rotational spacing is large due to the small moment of inertia associated with the diatom.

Unlike the initial state of the NO(X), which is selected through hexapole focussing, many initial states of the diatomic collision partner could be populated in the molecular beam. Again, this would be least significant for HD due to the larger rotational constant associated with a lighter diatom. Therefore to achieve fully resolved state to state DCSs, where only one initial state of each diatom is populated, it may be necessary to cool the General valve that produces the molecular beam [39, 272].

As discussed above, population of the internal states of the diatomic collision partner would lead to the NO(X) having a different outgoing velocity, which would lead to different size Newton spheres. To increase the resolution of the experiment to aid in resolving the final state of the diatomic collision partner, a sliced imaging technique can be used [31–

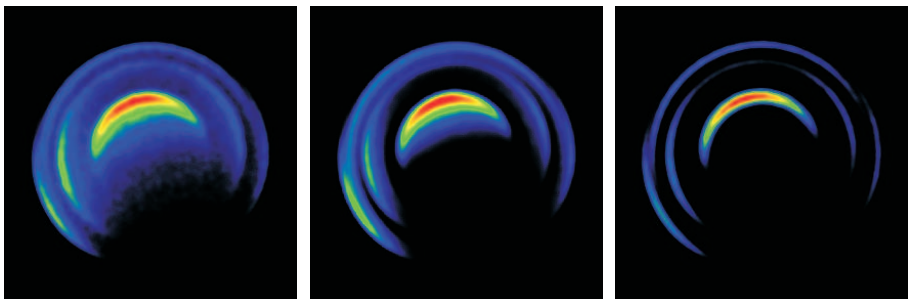


Figure 7.3: Simulated images for the collisions of NO(X) with HD, where the whole Newton sphere is detected (left panel), 50% of the Newton sphere (middle panel) and 5% of the Newton sphere (right panel). Figure adapted from reference [273].

33, 81–84]. This involves using a short pulse to trigger the detector so that it only detects a 'slice' of the Newton sphere, as opposed to the whole Newton sphere. An illustration of this is shown in figure 7.3 for simulated images of collisions of NO(X) with HD. The left hand panel of the figure corresponds to the image obtained when the whole Newton sphere is detected, and those in the middle and right panels to when a slice is taken through the Newton sphere. This increased resolution would allow correlations between the internal excitation of the two diatoms to be obtained, as well as the dependence of these correlations on scattering angle.

Bibliography

[1] M. Brouard and C. Vallance, *Tutorials in Molecular Reaction Dynamics*, Royal Society of Chemistry, Cambridge, 2010.

[2] M. P. de Miranda and D. C. Clary, *J. Chem. Phys.*, **106**, 4509 (1997).

[3] D. A. Case and D. R. Herschbach, *Mol. Phys.*, **30**, 1537 (1975).

[4] D. A. Case and D. R. Herschbach, *J. Chem. Phys.*, **64**, 4212 (1976).

[5] D. A. Case, G. M. McClelland, and D. R. Herschbach, *Mol. Phys.*, **35**, 541 (1978).

[6] G. M. McClelland and D. R. Herschbach, *J. Phys. Chem.*, **83**, 1445 (1979).

[7] J. D. Barnwell, J. G. Loeser, and D. R. Herschbach, *J. Phys. Chem.*, **87**, 2781 (1983).

[8] F. J. Aoiz, M. Brouard, and P. A. Enriquez, *J. Chem. Phys.*, **105**, 4964 (1996).

[9] A. A. Dixit, P. J. Pisano, and P. L. Houston, *J. Phys. Chem. A*, **105**, 11165 (2001).

[10] L. J. Rawluk, Y. B. Fan, Y. Apelblat, and M. Keil, *J. Chem. Phys.*, **94**, 4205 (1991).

[11] R. Schinke and J. M. Bowman, *Molecular collision dynamics*, Springer-Verlag, Heidelberg, 1982.

[12] F. J. Aoiz, J. E. Verdasco, V. J. Herrero, V. S. Rábanos, and M. H. Alexander, *J. Chem. Phys.*, **119**, 5860 (2003).

[13] G. Hall, K. Liu, M. J. McAuliffe, C. F. Giese, and W. R. Gentry, *J. Chem. Phys.*, **78**, 5260 (1983).

[14] R. G. Macdonald and K. Liu, *J. Chem. Phys.*, **91**, 821 (1989).

[15] E. A. Wade, K. T. Lorenz, D. W. Chandler, J. W. Barr, G. L. Barnes, and J. I. Cline, *Chem. Phys.*, **301**, 261 (2004).

[16] J. I. Cline, K. T. Lorenz, E. A. Wade, J. W. Barr, and D. W. Chandler, *J. Chem. Phys.*, **115**, 6277 (2001).

[17] K. T. Lorenz, D. W. Chandler, J. W. Barr, W. Chen, G. L. Barnes, and J. I. Cline, *Science*, **293**, 2063 (2001).

[18] A. J. McCaffery, M. J. Proctor, and B. J. Whitaker, *Annu. Rev. Phys. Chem.*, **37**, 223 (1986).

[19] A. Gijsbertsen, H. Linnartz, G. Rus, A. E. Wiskerke, S. Stolte, D. W. Chandler, and J. Kłos, *J. Chem. Phys.*, **123**, 224305 (2005).

[20] A. Gijsbertsen, *Towards a Better Understanding of Inelastic Atom-Molecule Collisions*, PhD Thesis, Vrije Universiteit, Amsterdam, 2006.

[21] C. J. Eyles, M. Brouard, C.-H. Yang, J. Kłos, F. J. Aoiz, A. Gijsbertsen, A. E. Wiskerke, and S. Stolte, *Nature Chemistry*, **3**, 597 (2011).

[22] C. J. Eyles, M. Brouard, H. Chadwick, B. Hornung, B. Nichols, C.-H. Yang, J. Kłos, F. J. Aoiz, A. Gijsbertsen, A. E. Wiskerke, and S. Stolte, *Phys. Chem. Chem. Phys.*, **14**, 5403 (2012).

[23] C. J. Eyles, *An Experimental and Theoretical Study of the Dynamics of Atom-Molecule Scattering*, DPhil Thesis, University of Oxford, 2010.

[24] C. P. Fell, A. J. McCaffery, K. L. Reid, and A. Ticktin, *J. Chem. Phys.*, **95**, 4948 (1991).

[25] M. C. van Beek, J. J. ter Meulen, and M. H. Alexander, *J. Chem. Phys.*, **113**, 637 (2000).

[26] M. C. van Beek and J. J. ter Meulen, *J. Chem. Phys.*, **115**, 1843 (2001).

[27] M. C. van Beek, G. Berden, H. L. Bethlem, and J. J. ter Meulen, *Phys. Rev. Lett.*, **86**, 4001 (2001).

[28] M. J. L. de Lange, S. Stolte, C. A. Taajtes, J. Kłos, G. C. Groenenboom, and A. van der Avoird, *J. Chem. Phys.*, **121**, 11691 (2004).

[29] M. L. Costen, S. Marinakis, and K. G. McKendrick, *Chem. Soc. Rev.*, **37**, 732 (2008).

[30] K. Schreel and J. J. ter Meulen, *J. Phys. Chem. A*, **101**, 7639 (1997).

[31] J. J. Lin, J. Zhou, W. Shiu, and K. Liu, *Science*, **300**, 966 (2003).

[32] J. Zhou, J. J. Lin, and K. Liu, *Mol. Phys.*, **108**, 957 (2010).

[33] F. Wang and K. Liu, *J. Phys. Chem. Lett.*, **2**, 1421 (2011).

[34] S.-H. Lee, F. Dong, and K. Liu, *J. Chem. Phys.*, **125**, 133106 (2006).

[35] S.-H. Lee, F. Dong, and K. Liu, *J. Chem. Phys.*, **116**, 7839 (2002).

[36] R. T. Skodje, D. Skouteris, D. E. Manolopoulos, S.-H. Lee, F. Dong, and K. Liu, *Phys. Rev. Lett.*, **85**, 1206 (2000).

[37] C.-H. Yang, G. Sarma, J. J. ter Meulen, D. H. Parker, U. Buck, and L. Wiesenfield, *J. Phys. Chem. A*, **114**, 9886 (2010).

[38] C.-H. Yang, G. Sarma, J. J. ter Meulen, D. H. Parker, G. C. McBane, L. Wiesenfield, A. Faure, Y. Scribano, and N. Feautrier, *J. Chem. Phys.*, **133**, 131103 (2010).

[39] C.-H. Yang, G. Sarma, D. H. Parker, J. J. ter Meulen, and L. Wiesenfield, *J. Chem. Phys.*, **134**, 204308 (2011).

[40] X. Wang, W. Dong, M. Qiu, Z. Ren, L. Che, D. Dai, X. Wang, X Yang, Z. Sun, B. Fu, S.-Y. Lee, X. Xu, and D. H. Zhang, *PNAS*, **105**, 6227 (2008).

[41] L. Che, Z. Ren, X. Wang, W. Dong, D. Dai, X. Wang, D. H. Zhang, X. Yang, L. Sheng, G. Li, H.-J. Werner, F. Lique, and M. H. Alexander, *Science*, **317**, 1061 (2007).

[42] A. Lin, S. Antonova, A. P. Tsakotellis, and G. C. McBane, *J. Phys. Chem. A*, **103**, 1198 (1999).

[43] U. Hefter, P. L. Jones, A. Mattheus, J. Witt, K. Bergmann, and R. Schinke, *Phys. Rev. Lett.*, **46**, 915 (1981).

[44] P. L. Jones, U. Hefter, A. Mattheus, J. Witt, K. Bergmann, W. Müller, W. Meyer, and R. Schinke, *Phys. Rev. A*, **26**, 1283 (1982).

[45] P. L. Jones, E. Gottwald, U. Hefter, and K. Bergmann, *J. Chem. Phys.*, **78**, 3838 (1983).

[46] A. Mattheus, A. Fischer, G. Ziegler, E. Gottwald, and K. Bergmann, *Phys. Rev. Lett.*, **56**, 712 (1986).

[47] M. J. L. de Lange, J. J. van Leuken, M. M. J. E. Drabbels, J. Bulthuis, J. G. Snijders, and S. Stolte, *Chem. Phys. Lett.*, **294**, 332 (1998).

[48] P. Casavecchia, *Rep. Progr. Phys.*, **63**, 355 (2000).

[49] Y. T. Lee, J. D. McDonald, P. R. LeBreton, and D. R. Herschbach, *Rev. Sci. Instrum.*, **40**, 1402 (1969).

[50] W. D. Geppert, C. Naulin, and M. Costes, *Chem. Phys. Lett.*, **333**, 51 (2001).

[51] G. Capozza, E. Segolini, F. Leonori, G. G. Volpi, and P. Casavecchia, *J. Chem. Phys.*, **120**, 4557 (2004).

[52] M. N. R. Ashfold and J. D. Howe, *Annu. Rev. Phys. Chem.*, **45**, 57 (1994).

[53] X. Liu, J. J. Lin, S. Harich, G. C. Schatz, and X. Yang, *Science*, **289**, 1536 (2000).

[54] S. A. Harich, D. Dai, C. C. Wang, X. Yang, S. D. Chao, and R. T. Skodje, *Nature*, **419**, 281 (2002).

[55] J. Zhang, D. Dai, C. C. Wang, S. A. Harich, X. Wang, X. Yang, M. Gustafsson, and R. T. Skodje, *Phys. Rev. Lett.*, **96**, 093201 (2006).

[56] D. Dai, C. C. Wang, S. A. Harich, X. Wang, X. Yang, S. D. Chao, and R. T. Skodje, *Science*, **300**, 1730 (2003).

[57] M. Qiu, Z. Ren, L. Che, D. Dai, S. A. Harich, X. Wang, X. Yang, C. Xu, D. Xie, M. Gustafsson, R. T. Skodje, Z. Sun, and D. H. Zhang, *Science*, **311**, 1440 (2006).

[58] L. Schnieder, W. Meier, K. H. Welge, M. N. R. Ashfold, and C. M. Western, *J. Chem. Phys.*, **92**, 7027 (1990).

[59] L. Schnieder, K. Seekamp-Rahn, E. Wrede, and K. H. Welge, *J. Chem. Phys.*, **107**, 6175 (1997).

[60] C. Lin, M. F. Witinski, and H. F. Davis, *J. Chem. Phys.*, **119**, 251 (2003).

[61] B. Jones, J. Zhou, L. Yang, and C. Y. Ng, *Rev. Sci. Instrum.*, **79**, 123106 (2008).

[62] D. H. Parker and A. T. J. B. Eppink, *J. Chem. Phys.*, **107**, 2357 (1997).

[63] D. W. Chandler and P. L. Houston, *J. Chem. Phys.*, **87**, 1445 (1987).

[64] M. S. Westley, K. T. Lorenz, D. W. Chandler, and P. L. Houston, *J. Chem. Phys.*, **114**, 2669 (2001).

[65] A. G. Suits, L. S. Bontuyan, P. L. Houston, and B. J. Whitaker, *J. Chem. Phys.*, **96**, 8618 (1992).

[66] P. Casavecchia, A. Laganà, and G. G. Volpi, *Chem. Phys. Lett.*, **112**, 445 (1984).

[67] S. D. Jons, J. E. Shirley, M. T. Vonk, C. F. Giese, and W. R. Gentry, *J. Chem. Phys.*, **97**, 7831 (1992).

[68] L. S. Bontuyan, A. G. Suits, P. L. Houston, and B. J. Whitaker, *J. Phys. Chem.*, **97**, 6342 (1993).

[69] S. D. Jons, J. E. Shirley, M. T. Vonk, C. F. Giese, and W. R. Gentry, *J. Chem. Phys.*, **105**, 5397 (1996).

[70] H. Kohguchi, T. Suzuki, and M. H. Alexander, *Science*, **294**, 832 (2001).

[71] M. S. Elioff and D. W. Chandler, *J. Chem. Phys.*, **117**, 6455 (2002).

[72] M. H. Alexander, *J. Chem. Phys.*, **99**, 7725 (1993).

[73] C. J. Eyles, M. Brouard, H. Chadwick, F. J. Aoiz, J. Kłos, A. Gijsbertsen, X. Zhang, and S. Stolte, *Phys. Chem. Chem. Phys.*, **14**, 5420 (2012).

[74] J. J. Kay, G. Paterson, M. L. Costen, K. E. Strecker, K. G. McKendrick, and D. W. Chandler, *J. Chem. Phys.*, **134**, 091101 (2011).

[75] T. N. Kitsopoulos, M. A. Buntine, D. P. Baldwin, R. N. Zare, and D. W. Chandler, *Science*, **260**, 1605 (1993).

[76] M. A. Buntine, D. P. Baldwin, R. N. Zare, and D. W. Chandler, *J. Chem. Phys.*, **94**, 4672 (1991).

[77] M. J. Bass, M. Brouard, C. Vallance, T. N. Kitsopoulos, P. C. Samartzis, and R. L. Toomes, *J. Chem. Phys.*, **119**, 7168 (2003).

[78] D. D. Parish and D. R. Herschbach, *J. Am. Chem. Soc.*, **95**, 6133 (1973).

[79] K. T. Gillen, A. M. Rulis, and R. B Bernstein, *J. Chem. Phys.*, **54**, 2831 (1971).

[80] A. M. Rulis and R. B Bernstein, *J. Chem. Phys.*, **57**, 5497 (1972).

[81] C. R. Gebhardt, T. P. Rakitzis, P. C. Samartzis, V. Ladopoulos, and T. N. Kitsopoulos, *Rev. Sci. Instrum.*, **72**, 3848 (2001).

[82] M. L. Lipciuc and M. H. M. Janssen, *Phys. Chem. Chem. Phys.*, **8**, 3007 (2006).

[83] M. L. Lipciuc, A. J. van den Brom, L. Dinu, and M. H. Janssen, *Rev. Sci. Instrum.*, **76**, 123103 (2005).

[84] J. J. Lin, J. Zhou, W. Shiu, and K. Liu, *J. Chem. Phys.*, **74**, 2495 (2003).

[85] U. Fano and J. H. Macek, *Rev. Mod. Phys.*, **45**, 553 (1973).

[86] H. J. Loesch and A. Remscheid, *J. Chem. Phys.*, **93**, 4779 (1990).

[87] H. J. Loesch, *Annu. Rev. Phys. Chem.*, **46**, 555 (1995).

[88] G. Xing, T. Kasai, and P. R. Brooks, *J. Am. Chem. Soc.*, **117**, 2581 (1995).

[89] S.-M. Wu, D. C̃. Radenovic, W. J. van der Zande, G. C. Groenenboom, D. H. Parker, C. Vallance, and R. N. Zare, *Nature Chemistry*, **3**, 28 (2011).

[90] D. H. Parker and R. B. Bernstein, *Annu. Rev. Phys. Chem.*, **40**, 561 (1989).

[91] D. H. Parker, H. Jalink, and S. Stolte, *J. Phys. Chem.*, **91**, 5427 (1987).

[92] T. P. Rakitzis, A. J. van den Brom, and M. H. M. Janssen, *Science*, **303**, 1852 (2004).

[93] D. H. Parker, K. K. Chakravorty, and R. B. Bernstein, *J. Phys. Chem.*, **85**, 466 (1981).

[94] P. W. Harland and P. R. Brooks, *J. Am. Chem. Soc.*, **125**, 13191 (2003).

[95] C. G. Aitken, D. A. Blunt, and P. W. Harland, *Int. J. Mass. Spec. and Ion Processes*, **149**, 279 (1995).

[96] P.-Y. Tsai, D.-C. Che, M. Nakamura, K.-C. Lin, and T. Kasai, *Phys. Chem. Chem. Phys.*, **12**, 2532 (2010).

[97] M. J. L. de Lange, M. Drabbels, P. T. Griffiths, J. Bulthuis, S. Stolte, and J. G. Snijders, *Chem. Phys. Lett.*, **313**, 491 (1999).

[98] M. J. L. de Lange, *Steric and State-to-State Dependence of Rotationally Inelastic Scattering of NO*, PhD Thesis, Vrije Universiteit, Amsterdam, 2003.

[99] J. J. van Leuken, J. Bulthuis, S. Stolte, and J. G. Snijders, *Chem. Phys. Lett.*, **260**, 595 (1996).

[100] A. Gijsbertsen, M. J. de Lange, A. E. Wiskerke, H. Linnartz, M. Drabbels, J. Kłos, and S. Stolte, *Chem. Phys.*, **301**, 293 (2004).

[101] A. J. Orr-Ewing and R. N. Zare, *Annu. Rev. Phys. Chem.*, **45**, 315 (1994).

[102] R. N. Zare, *Angular Momentum, Understanding Spatial Aspects in Chemistry and Physics*, John Wiley and Sons, 1988.

[103] R. N. Zare, *J. Chem. Phys.*, **45**, 4510 (1966).

[104] P. J. Dagdigian and M. H. Alexander, *J. Chem. Phys.*, **130**, 094303 (2009).

[105] P. J. Dagdigian and M. H. Alexander, *J. Chem. Phys.*, **130**, 164315 (2009).

[106] P. J. Dagdigian and M. H. Alexander, *J. Chem. Phys.*, **130**, 204304 (2009).

[107] A. J. McCaffery, *J. Phys. Chem.*, **91**, 5451 (1987).

[108] M. L. Costen, R. Livingstone, K. G. McKendrick, G. Paterson, M. Brouard, H. Chadwick, Y.-P. Chang, C. J. Eyles, F. J. Aoiz, and J. Kłos, *J. Phys. Chem. A*, **113**, 15156 (2009).

[109] M. Brouard, H. Chadwick, Y.-P. Chang, R. Cireasa, C. J. Eyles, A. O. La Via, N. Screen, F. J. Aoiz, and J. Kłos, *J. Chem. Phys.*, **131**, 104307 (2009).

[110] G. Paterson, A. Relf, M. L. Costen, K. G. McKendrick, M. H. Alexander, and P. J. Dagdigian, *J. Chem. Phys.*, **135**, 234304 (2011).

[111] G. Paterson, M. L. Costen, and K. G. McKendrick, *Mol. Phys.*, **109**, 2565 (2011).

[112] S. Marinakis, G. Paterson, G. Richmond, M. Rockingham, M. L. Costen, and K. G. McKendrick, *J. Chem. Phys.*, **128**, 021101 (2008).

[113] S. Marinakis, G. Paterson, J. Kłos, M. L. Costen, and K. G. McKendrick, *Phys. Chem. Chem. Phys.*, **9**, 4414 (2007).

[114] M. L. Costen, H. J. Crichton, and K. G. McKendrick, *J. Chem. Phys.*, **120**, 7910 (2004).

[115] M. Brouard, A. Bryant, I. Burak, S. Marinakis, F. Quadrini, I. Anton Garcia, and C. Vallance, *Mol. Phys.*, **103**, 1693 (2005).

[116] M. Brouard, A. Bryant, Y.-P. Chang, R. Cireasa, C. J. Eyles, A. M. Green, S. Marinakis, F. J. Aoiz, and J. Kłos, *J. Chem. Phys.*, **130**, 044306 (2009).

[117] M. Brouard, H. Chadwick, Y.-P. Chang, R. Cireasa, and C. J. Eyles, *Phys. Scr.*, **80**, 048120 (2009).

[118] M. Brouard, H. Chadwick, C. J. Eyles, F. J. Aoiz, and J. Kłos, *J. Chem. Phys.*, **135**, 084305 (2011).

[119] M. Brouard, H. Chadwick, Y.-P. Chang, C. J. Eyles, F. J. Aoiz, and J. Kłos, *J. Chem. Phys.*, **135**, 084306 (2011).

[120] H. Chadwick, M. Brouard, Y.-P. Chang, C. J. Eyles, T. Perkins, S. A. Seamons, J. Kłos, M. H. Alexander, and F. J. Aoiz, *To be submitted.*

[121] H. J. Crichton, M. L. Costen, and K. G. McKendrick, *J. Chem. Phys.*, **119**, 9461 (2003).

[122] G. Paterson, S. Marinakis, M. L. Costen, K. G. McKendrick, J. Kłos, and R. Toboła, *J. Chem. Phys.*, **129**, 074304 (2008).

[123] L. D. Snow, R. N. Compton, and J. C. Miller, *J. Chem. Phys.*, **88**, 1652 (1988).

[124] E. A. Brinkman and D. R. Crosley, *J. Phys. Chem. A*, **108**, 8084 (2004).

[125] A. Brockhinke, U. Lenhard, A Bülter, and K. Kohse-Höinghaus, *Phys. Chem. Chem. Phys.*, **7**, 874 (2005).

[126] G. Sha, W. Sun, B. Jiang, E. Hintsa, and C. Zhang, *J. Chem. Phys.*, **98**, 9487 (1993).

[127] G. O. Sitz and R. L. Farrow, *J. Chem. Phys.*, **101**, 4682 (1994).

[128] A. D. Rudert, J. Martin, W.-B. Gao, J. B. Halpern, and H. Zacharias, *J. Chem. Phys.*, **111**, 9549 (1999).

[129] A. D. Rudert, J. Martin, W.-B. Gao, H. Zacharias, and J. B. Halpern, *J. Chem. Phys.*, **112**, 9749 (2000).

[130] M. L. Costen and K. G. McKendrick, *J. Chem. Phys.*, **122**, 164309 (2005).

[131] L. Ma, M. H. Alexander, and P. J. Dagdigian, *J. Chem. Phys.*, **134**, 154307 (2011).

[132] G. Paterson, S. Marinakis, M. L. Costen, and K. G. McKendrick, *Phys. Scr.*, **80**, 048111 (2009).

[133] G. Paterson, S. Marinakis, M. L. Costen, and K. G. McKendrick, *Phys. Chem. Chem. Phys.*, **11**, 8813 (2009).

[134] G. Paterson, S. Marinakis, J. Kłos, M. L. Costen, and K. G. McKendrick, *Phys. Chem. Chem. Phys.*, **11**, 8804 (2009).

[135] H. Katô, S. R. Jeyes, A. J. McCaffery, and M. D. Rowe, *Chem. Phys. Lett.*, **39**, 573 (1976).

[136] S. R. Jeyes, A. J. McCaffery, and M. D. Rowe, *Mol. Phys.*, **36**, 1865 (1978).

[137] S. R. Jeyes, A. J. McCaffery, and M. D. Rowe, *Mol. Phys.*, **36**, 845 (1978).

[138] Y.-P. Chang, *Novel probing of angular momentum polarization*, DPhil thesis, University of Oxford, 2010.

[139] M. Brouard, *Reaction Dynamics*, Oxford University Press, Oxford, 1998.

[140] Y. Sumiyoshi, I. Funahara, K. Sato, Y. Ohshima, and Y. Endo, *Mol. Phys.*, **108**, 2207 (2010).

[141] J. C. Polanyi, *Accounts of Chemical Research*, **5**, 161 (1972).

[142] C. C. Carter, H. S. Lee, A. B. McCoy, and T. A. Miller, *J. Mol. Struct.*, **525**, 1 (2000).

[143] S. Fei, X. Zheng, and M. C. Heaven, *J. Chem. Phys.*, **97**, 1655 (1992).

[144] F. J. Aoiz, L. Bañares, and V. J. Herrero, *J. Chem. Soc. Faraday. Trans.*, **94**, 2483 (1998).

[145] F. J. Aoiz, M. Brouard, C. J. Eyles, J. F. Castillo, and V. Sáez Rábanos, *J. Chem. Phys.*, **125**, 144105 (2006).

[146] C. Amiot, *J. Mol. Spectrosc.*, **94**, 150 (1982).

[147] R. D. Levine, *Molecular Reaction Dynamics*, Cambridge University Press, 2005.

[148] J. M. Brown, J. T. Hougen, K.-P. Huber, J. W. C. Johns, I. Kopp, H. Lefebvre-Brion, A. J. Merer, D. A. Ramsey, J. Rostas, and R. N. Zare, *J. Mol. Spectrosc.*, **55**, 500 (1975).

[149] M. H. Alexander, P. Andresen, R. Bacis, R. Bersohn, F. J. Comes, P. J. Dagdigian, R. N. Dixon, R. W. Field, G. W. Flynn, K.-H. Gericke, E. R. Grant, B. J. Howard, J. R. Huber, D. S. King, J. L. Kinsey, K. Kleinermanns, K. Kuchitsu, A. C. Luntz, A. J. McCaffery, B. Pouilly, H. Reisler, S. Rosenwaks, E. W. Rothe, M. Shapiro, J. P. Simons, R. Vasudev, J. R. Wiesenfeld, C. Wittig, and R. N. Zare, *J. Chem. Phys.*, **1749**, 89 (1988).

[150] P. J. Dagdigian, M. H. Alexander, and K. Liu, *J. Chem. Phys.*, **91**, 839 (1989).

[151] L. Bigio and E. R. Grant, *J. Chem. Phys.*, **87**, 5589 (1987).

[152] R. N. Neumann, *Astrophys. J.*, **161**, 779 (1970).

[153] C. Amiot, R. Bacis, and G. Guelachvili, *Can. J. Phys.*, **56**, 251 (1978).

[154] C. A. Burrus and W. Gordy, *Phys. Rev.*, **92**, 1437 (1953).

[155] W. L. Meerts and A. Dymanus, *J. Mol. Spectrosc.*, **44**, 320 (1972).

[156] "J. Luque and D.R. Crosley, "LIFBASE: Database and spectral simulation (version 1.5)", SRI International Report MP 99-009 (1999).

[157] G. Herzberg, *Molecular Spectra and Molecular Structure, Volume I, Spectra of diatomic molecules, 2nd edition*, D. Van Nostrand Company, 1950.

[158] R. F. Barrow and E. Miescher, *Proc. Phys. Soc. London Sect. A*, **70**, 219 (1957).

[159] G. H. Dieke and H. M. Crosswhite, *J. Quant. Spectrosc. Radiat. Transf.*, **2**, 97 (1961).

[160] K. Blum, *Density Matrix Theory and Applications, 2nd Ed.*, Plenum Press, New York, 1996.

[161] M. P. de Miranda and F. J. Aoiz, *Phys. Rev. Lett.*, **93**, 083201 (2004).

[162] M. P. de Miranda, F. J. Aoiz, L. Bañares, and V. Sáez Rábanos, *J. Chem. Phys.*, **111**, 5368 (1999).

[163] I. V. Hertel and W. Stoll, *Adv. At. Mol. Phys*, **13**, 113 (1978).

[164] M. P. de Miranda, F. J. Aoiz, M. Brouard, and V. Sáez-Rábanos, *J. Chem. Phys.*, **121**, 9830 (2004).

[165] D. A. Varsholovich, A. N. Moskalev, and V. K. Khersonskii, *Quantum Theory of Angular Momentum*, World Scientific, Singapore, 1988.

[166] M. H. Alexander, *J. Chem. Phys.*, **76**, 5974 (1982).

[167] M. H. Alexander, *Chem. Phys.*, **92**, 337 (1985).

[168] M. H. Alexander, *J. Chem. Phys.*, **111**, 7426 (1999).

[169] K. P. Huber and G. Herzberg, *Molecular Spectra and Molecular Structure, Volume IV, Constants of diatomic molecules*, D. Van Nostrand Company, 1979.

[170] B. Wen, H. Meyer, J. Kłos, and M. H. Alexander, *J. Phys. Chem. A*, **113**, 7366 (2009).

[171] J. Kłos, M. H. Alexander, R. Hernández-Lamoneda, and T. G. Wright, *J. Chem. Phys.*, **129**, 244303 (2008).

[172] H. Chadwick, M. Brouard, Y.-P. Chang, C. J. Eyles, T. Perkins, S. A. Seamons, J. Kłos, M. H. Alexander, and F. J. Aoiz, *To be submitted.*

[173] M. Karplus, R. N. Porter, and R. D. Sharma, *J. Chem. Phys.*, **43**, 3259 (1965).

[174] N. M. J. Woodhouse, *Introduction to Analytical Dynamics*, Oxford Science Publications, 1987.

[175] F. J. Aoiz, M. Brouard, C. J. Eyles, J. Kłos, and M. P. de Miranda, *J. Chem. Phys.*, **130**, 044305 (2009).

[176] HIBRIDON is a package of programs for the time-independent quantum treatment of inelastic collisions and photodissociation written by M. H. Alexander, D. Manolopoulos, H. -J. Werner, and B. Follmeg, with contributions by P. F. Vohralik, D. Lemoine, G. Corey, R. Gordon, B. Johnson, T. Orlikowski, A. Berning, A. Degli-Esposti, C. Rist, P. Dagdigian, B. Pouilly, G. van der Sanden, M. Yang, F. de Weerd, S. Gregurick, and J. Kłos.

[177] A. M. Arthurs and A. Dalgarno, *Proc. R. Soc. Lond.*, **256**, 540 (1960).

[178] D. E. Manolopoulos, *J. Chem. Phys.*, **85**, 6425 (1986).

[179] M. H. Alexander and D. E. Manolopoulos, *J. Chem. Phys.*, **86**, 2044 (1987).

[180] M. H. Alexander, *J. Chem. Phys.*, **81**, 4510 (1984).

[181] M. S. Child, *Molecular Collision Theory*, Dover Publications Inc., 1996.

[182] G. C. Corey and A. D. Smith, *J. Chem. Phys.*, **83**, 5663 (1985).

[183] G. C. Corey, M. H. Alexander, and J. Schaefer, *J. Chem. Phys.*, **85**, 2726 (1986).

[184] M. H. Alexander and P. J. Dagdigian, *J. Chem. Phys.*, **83**, 2191 (1985).

[185] M. H. Alexander and S. L. Davis, *J. Chem. Phys.*, **78**, 6754 (1983).

[186] B. Follmeg, P. Rosmus, and H.-J.Werner, *J. Chem. Phys.*, **93**, 4687 (1990).

[187] G. C. Corey and F. R. McCourt, *J. Phys. Chem.*, **87**, 2723 (1983).

[188] M. H. Alexander, J. E. Smedley, and G. C. Corey, *J. Chem. Phys.*, **84**, 3049 (1986).

[189] A. R. Edmonds, *Angular Momentum in Quantum Mechanics*, Princeton University Press, Princeton, NJ, 1974.

[190] L. Scharfenberg, K. B. Gubbels, M. Kirste, G. C. Groenenboom, A. van der Avoird, G. Meijer, and S. Y. T. van der Meerakker, *Eur. Phys. J. D*, **65**, 189 (2011).

[191] K. Schreel, J. Schleipen, A. Eppink, and J. J. ter Meulen, *J. Chem. Phys.*, **99**, 8713 (1993).

[192] P. Andreson, H. Joswig, H. Pauly, and R. Schinke, *J. Chem. Phys.*, **77**, 2204 (1982).

[193] C. R. Bieler, A. Sanov, and H. Reisler, *Chem. Phys. Lett.*, **235**, 175 (1995).

[194] G. C. Corey and M. H. Alexander, *J. Chem. Phys.*, **85**, 5652 (1986).

[195] M. Yang and M. H. Alexander, *J. Chem. Phys.*, **103**, 6973 (1995).

[196] T. Orlikowski and M. H. Alexander, *J. Chem. Phys.*, **79**, 6006 (1983).

[197] J. J. van Leuken, F. H. W. van Ameron, J. Bulthuis, J. G. Snijders, and S. Stolte, *J. Phys. Chem.*, **99**, 15573 (1995).

[198] A. Jörg, A. D. Esposti, and H.-J. Werner, *J. Chem. Phys.*, **93**, 8757 (1990).

[199] S. C. Farantos and A. Vegiri, *J. Phys. Chem.*, **2719**, 92 (1988).

[200] A. Jörg, U. Meier, and K. Kohse-Höinghaus, *J. Chem. Phys.*, **93**, 6453 (1990).

[201] R. K. Lengel and D. R. Crosley, *J. Chem. Phys.*, **67**, 2085 (1977).

[202] A. D. Esposti and H.-J. Werner, *J. Chem. Phys.*, **93**, 3351 (1990).

[203] T. Imajo, K. Shibuya, and K. Obi, *Chem. Phys. Lett.*, **137**, 139 (1987).

[204] T. Ebata, Y. Anezaki, M. Fujii, N. Mikami, and M. Ito, *Chem. Phys.*, **84**, 151 (1984).

[205] A. V. Smith and A. W. Johnson, *Chem. Phys. Lett.*, **93**, 608 (1982).

[206] J. Kłos, M. H. Alexander, M. Brouard, C. J. Eyles, and F. J. Aoiz, *J. Chem. Phys.*, **129**, 054301 (2008).

[207] I. Ballingall, M. F. Rutherford, K. G. McKendrick, and M. L. Costen, *Mol. Phys.*, **108**, 847 (2010).

[208] R. T. Carter and J. R. Huber, *Chem. Soc. Rev.*, **29**, 305 (2000).

[209] E. Hack and J. R. Huber, *Int. Rev. Phys. Chem.*, **10**, 287 (1991).

[210] H. Bitto and J. R. Huber, *Acc. Chem. Res.*, **25**, 65 (1992).

[211] M. P. Docker, *Chem. Phys.*, **125**, 185 (1988).

[212] R. N. Dixon, *J. Chem. Phys.*, **85**, 1866 (1986).

[213] C. H. Greene and R. N. Zare, *J. Chem. Phys.*, **78**, 6741 (1983).

[214] A. C. Kummel, G. O. Sitz, and R. N. Zare, *J. Chem. Phys.*, **85**, 6874 (1986).

[215] A. C. Kummel, G. O. Sitz, and R. N. Zare, *J. Chem. Phys.*, **88**, 7357 (1988).

[216] P. Lebow, F. Raab, and H. Metcalf, *Phys. Rev. Lett.*, **42**, 85 (1979).

[217] F. Raab, T. Bergeman, D. Lieberman, and H. Metcalf, *Optics Lett.*, **5**, 427 (1980).

[218] F. Raab, T. Bergeman, D. Lieberman, and H. Metcalf, *Phys. Rev. A*, **24**, 3120 (1981).

[219] J. Xin, I. Ionescu, D. Kuffel, and S. A. Reid, *Chem. Phys.*, **291**, 61 (2003).

[220] L. Rubio-Lago, D. Sofikitis, A. Koubenakis, and T. P. Rakitzis, *Phys. Rev. A*, **74**, 042503 (2006).

[221] A. U. Grunewald, K.-H. Gericke, and F. J. Comes, *J. Chem. Phys.*, **89**, 345 (1988).

[222] K.-H. Gericke, H. G. Gläser, C. Maul, and F. J. Comes, *J. Chem. Phys.*, **92**, 411 (1990).

[223] Y.-P. Chang, M. Brouard, R. Cireasa, T. Perkins, and S. A. Seamons, *Phys. Chem. Chem. Phys.*, **13**, 8213 (2011).

[224] M. Baba, M. Brouard, S. P. Rayner, and J. P. Simons, *Chem. Phys. Lett.*, **220**, 411 (1994).

[225] D. Case, *Faraday rotation studies of collisional depolarization*, Part II Thesis, University of Oxford, 2006.

[226] A. Green, *Zeeman quantum beat spectroscopy as a tool for studying collisional depolarisation*, Part II Thesis, University of Oxford, 2007.

[227] B. L. Hemming, D. R. Crosley, J. E. Harrington, and V. Sick, *J. Chem. Phys.*, **115**, 3099 (2001).

[228] L. T. Earls, *Phys. Rev.*, **48**, 423 (1935).

[229] H.-S. Lee, A. B. McCoy, R. R. Toczyłowski, and S. M. Cybulski, *J. Chem. Phys.*, **113**, 5736 (2000).

[230] B. L. Hemming and D. R. Crosley, *J. Phys. Chem. A*, **106**, 8992 (2002).

[231] P. H. Paul, J. L. Durant Jr, J. A. Gray, and M. R. Furlanetto, *J. Chem. Phys.*, **102**, 8378 (1995).

[232] P. H. Paul, *J. Quant. Spectrosc. Radiat. Transf.*, **51**, 511 (1994).

[233] H. Chadwick, *The Collision Dynamics of NO(A): Experiment versus Theory*, Part II Thesis, University of Oxford, 2008.

[234] J. B. Nee, C. Y. Yuan, J. Y. Hsu, J. C. Yang, and W. J. Chen, *Chem. Phys.*, **300**, 85 (2004).

[235] G. D. Greenblatt and A. R. Ravishankara, *Chem. Phys. Lett.*, **136**, 501 (1987).

[236] P. H. Paul, *J. Phys. Chem.*, **99**, 8472 (1995).

[237] L. R. Williams and D. R. Crosley, *J. Chem. Phys.*, **104**, 6507 (1996).

[238] J. Kłos, *Private communication*, 2011.

[239] J. Aldegunde, M. P. de Miranda, J. M. Haigh, B. K. Kendrick, V. Sáez-Rábanos, and F. J. Aoiz, *J. Phys. Chem. A*, **109**, 6200 (2005).

[240] N. E. Shafer-Ray, A. J. Orr-Ewing, and R. N. Zare, *J. Phys. Chem.*, **99**, 7591 (1995).

[241] V. Khare, D. J. Kouri, and D. K. Hoffman, *J. Chem. Phys.*, **74**, 2275 (1981).

[242] D. K. Hoffman, J. W. Evans, and D. J. Kouri, *J. Chem. Phys.*, **80**, 144 (1984).

[243] M. Brouard, H. Chadwick, C. J. Eyles, B. Hornung, B. Nichols, and S. Stolte, *To be submitted.*

[244] Y. Kim and H. Meyer, *Chem. Phys.*, **301**, 273 (2004).

[245] Y. Kim, H. Meyer, and M. H. Alexander, *J. Chem. Phys.*, **121**, 1339 (2004).

[246] S. Marinakis, B. J. Howard, F. J. Aoiz, and J. Kłos, *Chem. Phys. Lett.*, **512**, 161 (2011).

[247] M. Brouard, C. J. Eyles, B. Hornung, F. J. Aoiz, P. G. Jambrina, S. Stolte, and M. P. de Miranda, *To be submitted.*

[248] R. W. Anderson, *J. Phys. Chem. A*, **101**, 7664 (1997).

[249] J. Bulthuis, J. J. van Leuken, and S. Stolte, *J. Chem. Soc. Faraday Trans*, **91**, 205 (1995).

[250] B. J. Bichsel, M. A. Morrison, N. Shafer-Ray, and E. R. I. Abraham, *Phys. Rev. A*, **75**, 024310 (2007).

[251] S. R. Gandhi and R. B. Bernstein, *J. Chem. Phys.*, **93**, 4024 (1990).

[252] K. H. Kramer and R. B. Bernstein, *J. Chem. Phys.*, **42**, 767 (1965).

[253] G. Scoles, *Atomic and Molecular Beam Methods, Volume 1*, Oxford University Press, New York, USA, 1988.

[254] G. Scoles, *Atomic and Molecular Beam Methods, Volume 2*, Oxford University Press, New York, USA, 1988.

[255] R. Uberna, R. D. Hinchliffe, and J. I. Cline, *J. Chem. Phys.*, **105**, 9847 (1996).

[256] K. T. Lorenz, D. W. Chandler, and G. C. McBane, *J. Phys. Chem. A*, **106**, 1144 (2002).

[257] Y. Kim and H. Meyer, *Chem. Phys. Lett.*, **387**, 339 (2004).

[258] M. A. Treffers and J. Korving, *Chem. Phys. Lett.*, **97**, 342 (1983).

[259] H. Meyer, *J. Phys. Chem.*, **99**, 1101 (1995).

[260] D. C. Jacobs and R. N. Zare, *J. Chem. Phys.*, **85**, 5457 (1986).

[261] M. J. Bass, M. Brouard, A. P. Clark, and C. Vallance, *J. Chem. Phys.*, **117**, 8723 (2002).

[262] M. J. Bass, M. Brouard, A. P. Clark, C. Vallance, and B. Martínez-Haya, *Phys. Chem. Chem. Phys.*, **5**, 856 (2003).

[263] J. Kłos, F. J. Aoiz, J. E. Verdasco, M. Brouard, S. Marinakis, and S. Stolte, *J. Chem. Phys.*, **127**, 031102 (2007).

[264] F. J. Aoiz, J. E. Verdasco, M. Brouard, J. Kłos, S. Marinakis, and S. Stolte, *J. Phys. Chem. A*, **113**, 14636 (2009).

[265] P.-Y. Zhang, R.-F. Lu, T.-S. Chu, and K.-L. Han, *J. Phys. Chem. A*, **114**, 6565 (2010).

[266] L. P. Dempsey, C. Murray, P. A. Cleary, and M. I. Lester, *Phys. Chem. Chem. Phys.*, **10**, 1424 (2008).

[267] L. P. Dempsey, C. Murray, and M. I. Lester, *J. Chem. Phys.*, **127**, 151101 (2007).

[268] P. A. Cleary, L. P. Dempsey, C. Murray, M. I. Lester, J. Kłos, and M. H. Alexander, *J. Chem. Phys.*, **126**, 204316 (2007).

[269] I. B. Pollack, Y. Lei, T. A. Stephenson, and M. I. Lester, *Chem. Phys. Lett.*, **421**, 324 (2006).

[270] M. I. Lester, R. A. Loomis, R. L. Schwartz, and S. P. Walch, *J. Phys. Chem. A*, **101**, 9195 (1997).

[271] B. Fu, E. Kamarchik, and J. M. Bowman, *J. Chem. Phys.*, **133**, 164306 (2010).

[272] U. Buck, F. Huisken, and J. Schleusener, *J. Chem. Phys.*, **68**, 5654 (1978).

[273] B. Nichols, *Inelastic scattering of hexapole state selected NO(X)*, Part II Thesis, University of Oxford, 2011.